

University of Brighton

**SOOT CHARACTERISATION
IN DIESEL ENGINES USING
LASER-INDUCED INCANDESCENCE**

BENOIT OGER

A thesis submitted in partial fulfilment of the
requirements of the University of Brighton
for the degree of Doctor of Philosophy

Ph.D.

April 2012

COPYRIGHT

Attention is drawn to the fact that copyright of this thesis rests with its author. This copy of the thesis has been supplied on condition that anyone who consults it is understood to recognise that its copyright rests with its author and that no quotation from the thesis and no information derived from it may be published without the prior written consent of the author.

This thesis may be made available for consultation within the University Library and may be photocopied or lent to other libraries for the purposes of consultation.

ABSTRACT

Nowadays, the European automotive market is dominated by Diesel engines. Despite their high efficiency, these produce significant levels of pollutants. Among the various pollutants released, nitrogen oxides and soot are the main issues. Their formation is linked to the combustion process and attempts to reduce one often lead to an increase of the other. Laser diagnostics are among the best tools for experimental, non-intrusive studies inside combustion chambers for a better understanding of the complex combustion processes. Depending on the optical diagnostic, numerous combustion characteristics and processes can be investigated. The work presented here intends initially to develop a quantitative laser technique for characterising soot and, secondly, to further the knowledge on soot formation in Diesel engines by the application of this technique in an optical combustion chamber. Some of the main characteristics describing soot formation are the soot volume fraction, number density and particle sizes. Soot volume fraction is the major one as it is representative of the volume of soot produced.

Planar characterisation of soot volume fraction, number density and particle size were achieved for the first time by simultaneous recording laser-induced incandescence (LII), laser scattering and two-colour time-resolved (2C-TiRe) LII signals. Qualitative planar distributions of particle diameter and soot volume fraction were derived from the image ratio of scattering and incandescence signals. 2C-TiRe LII technique allowed the simultaneous recording of the temporal LII signal for two different wavelengths in order to obtain quantitative values of the laser-heated particles temperature, soot volume fraction and particle size for a local or global part of the flame. These were used to recalibrate relative size and soot volume distributions.

An initial development of the technique was performed on a laminar diffusion flame (Santoro burner) to validate its viability and performance. Equivalent temperature, soot volume fraction and particle diameter were determined throughout the flame. The results were found to be in good agreement with the ones published in the literature.

The diagnostic was subsequently applied to an optical Diesel rapid compression machine, and further refinements were undertaken to cope with the higher soot concentration and lower LII signal. Tests were conducted for in-cylinder pressures ranging from 4 to 10 MPa, and injection pressures up to 160 MPa. A fixed injection timing and injected fuel quantity were used. Effects of in-cylinder pressure, fuel injection pressure and cetane number on soot formation and characteristics were observed. High injection pressure, cetane number and in-cylinder pressure caused a reduction of soot particle size and volume fraction but an increase of the soot particle density.

Keywords: Soot, Laser-Induced Incandescence, Elastic-Laser Scattering, combustion, Diesel

CONTENT

COPYRIGHT	ii
ABSTRACT	iii
CONTENT	iv
LIST OF FIGURES	viii
LIST OF TABLES	xiv
NOMENCLATURE	xv
ACKNOWLEDGEMENT	xviii
1 CHAPTER I: INTRODUCTION	1
1.1 Background of the study	1
2 CHAPTER II: SOOT FORMATION REVIEW	6
2.1 Soot characteristics	6
2.2 Soot formation mechanisms.....	8
2.2.1 Oxidation.....	8
2.2.2 Fuel pyrolysis	9
2.2.3 Nucleation	11
2.2.4 Surface growth	13
2.2.5 Coalescence and agglomeration.....	13
2.3 Soot formation in a direct injection engine.....	15
2.3.1 Introduction to the combustion of compression-ignition engine	15
2.3.2 Soot formation model.....	20
2.3.3 Physical parameters influencing the soot formation	23
2.3.4 Diesel engine parameters influencing soot formation.....	25
2.4 Soot formation modelling	28
2.5 Conclusions.....	29
3 CHAPTER III: SOOT MEASUREMENT TECHNIQUES	30
3.1 Laser-induced incandescence	30
3.1.1 Time-resolved LII	35
3.1.2 Two-colour time-resolved LII.....	36
3.2 Elastic light scattering.....	37
3.3 LII / ELS technique.....	39
3.3.1 Aggregate effects	41
3.4 Soot analysis by TEM or SEM Images.....	42

3.5	Laser-induced fluorescence	43
3.6	Calibration	43
3.6.1	Light extinction	44
3.6.2	Self-calibration	47
3.6.3	Gravimetric measurements	50
3.7	Technique assumptions	51
3.8	Conclusions	51
4	CHAPTER IV: THEORETICAL MODELS OF SOOT HEAT TRANSFER	53
4.1	Theoretical models	53
4.1.1	Main theoretical assumptions	55
4.1.2	Internal energy	56
4.1.3	Absorption of laser light energy	56
4.1.4	Heat conduction to the surrounding gas	57
4.1.5	Heat losses by carbon cluster sublimation	60
4.1.6	Radiative heat transfer	63
4.1.7	Oxidation	64
4.1.8	Particle size distribution	65
4.2	Modelling examples of LII signals	66
4.2.1	Laser fluence	66
4.2.2	Particle diameter distribution	67
4.2.3	Particle diameter	67
4.2.4	Pressure effect	70
4.3	Conclusions	71
5	CHAPTER V: EXPERIMENTAL CONSIDERATIONS AND APPARATUS	73
5.1	Experimental parameters	73
5.1.1	Excitation wavelength	73
5.1.2	Laser fluence, spatial energy distribution and pulse duration	74
5.1.3	Detection wavelength	76
5.1.4	Temporal detection strategy	78
5.1.5	Calibration method	79
5.2	Set-up configurations	79
5.3	Laser	81
5.3.1	Description	81
5.3.2	Synchronisation	81

5.3.3	Beam profile.....	81
5.4	Light collection system.....	83
5.5	Spatial signal acquisition.....	84
5.5.1	CCD Camera.....	85
5.6	Temporal detection system.....	86
5.6.1	Photomultipliers.....	86
5.6.2	Oscilloscope.....	87
5.7	Calibration method.....	88
5.7.1	Absolute light calibration.....	88
5.8	Camera spatial calibration.....	92
5.9	Spatial calibration of the local measurement 2C-TiRe-LII.....	94
5.10	Conclusions.....	95
6	CHAPTER VI: QUANTITATIVE STUDY OF SOOT FORMATION UPON A LAMINAR DIFFUSION FLAME.....	96
6.1	Santoro Burner.....	96
6.1.1	Set-up.....	97
6.2	Soot quantification by Auto-calibrated-2C-TiRe-LII.....	99
6.2.1	Measurement volume.....	99
6.3	Global 2C-TiRe-LII measurements.....	102
6.3.1	Time-resolved LII signals.....	102
6.3.2	Particle sizing.....	106
6.3.3	Soot volume fraction.....	115
6.3.4	Particle number density.....	117
6.4	Local 2C-TiRe-LII measurements.....	118
6.4.1	Result summary.....	120
6.5	Quantitative spatial soot distribution study.....	121
6.5.1	Comparison between sampling approaches.....	126
6.5.2	Results and discussion.....	128
6.5.3	Profiles.....	130
6.5.4	Particle size distribution.....	134
6.5.5	Errors due to the technique.....	136
6.6	Conclusions.....	137
7	CHAPTER VII SOOT FORMATION IN A DIESEL ENGINE.....	140
7.1	Experimental set-up.....	141

7.2	Optical engine transposition challenges	144
7.3	Post-processing	148
7.3.1	Heat release rate analysis	152
7.4	Experimental results and discussion	154
7.4.1	Influence of injection pressure	155
7.4.2	Influence of in-cylinder pressure	163
7.4.3	Influence of cetane number	168
7.5	Conclusions.....	172
8	CHAPTER VIII: CONCLUSION	175
8.1	Research outcomes	175
8.2	Recommendations for future work	179
9	REFERENCES	182
10	APPENDIX	210
10.1	Appendix A – Emission Standards	211
10.2	Appendix B – Fitting coefficients for soot sublimation rate properties	215
10.3	Appendix C – Burner’s drawings	216
10.4	Appendix D – Heat Release Rate	218
10.5	Appendix E – Santoro burner data in the literature	220

LIST OF FIGURES

Figure 1-1 – Schema of the relation between the particle sizes and their deposition on the pulmonary system ((Kreyling et al., 2005) adapted from (ICRP, 1994) and (Price OT et al., 2002))	2
Figure 1-2 – Typical composition (by mass) of Diesel particulate matter (adapted from Murphy et al. 1998)	2
Figure 2-1 – TEM images of agglomerates and primary particles (Vander Wal et al., 1999, Smith, 1981)	6
Figure 2-2 – Onion-shell structure of nanocrystalline graphite forming the soot particles (Ivleva et al., 2007)	7
Figure 2-3 – Schematic of substructure of carbon particle (Vander Wal et al., 1999, Smith, 1981)	7
Figure 2-4 – Schematic diagram of the soot formation steps (adapted from (Tree and Svensson, 2007))	8
Figure 2-5 – Pathways of benzene formation	10
Figure 2-6 – HACA mechanism of polycyclic aromatic hydrocarbon formation [adapted from (Wang and Frenklach, 1997)]	11
Figure 2-7 – Combination of benzyl with propargyl	12
Figure 2-8 – Combination of two cyclopentadienyl	12
Figure 2-9 – Combination of cyclopentadienyl and indenyl	12
Figure 2-10 – Propargyl radical leading to the phenanthrene formation	12
Figure 2-11 - TEM image of soot agglomerates at Diesel engine exhaust (Wentzel et al., 2003)	14
Figure 2-12 - Number of particles in an aggregate as function of the nondimensional length (L/d_p) (Koylu et al., 1997)	14
Figure 2-13 – P-V diagram for ideal Diesel cycle	15
Figure 2-14 – Typical heat release rate and pressure diagram of a Diesel combustion engine	19
Figure 2-15 – Sandia’s conceptual model of Diesel combustion (Dec, 1997, Siebers and Higgins, 2001)	20
Figure 2-16 – Conceptual model of soot formation and oxidation processes in a Diesel spray flame (Kosaka et al., 2005).	21

Figure 2-17 – ϕ -T map (Akihama et al., 2001, Idicheria and Pickett, 2005)	22
Figure 3-1 – Spectral radiance of a blackbody for different temperatures	32
Figure 3-2 – Diagram of optical diagnostics.....	52
Figure 4-1 – Schematically representation of the energy balance of a laser heated particle (Will et al., 1998)	53
Figure 4-2 – Evolution of particle temperature and the different heat transfers during the LII process (Schraml et al., 2000).....	54
Figure 4-3 – Evolution of vaporization heat and molecular mass with temperature	61
Figure 4-4 – Evolution of soot vapour pressure with temperature.....	62
Figure 4-5 – Temporal laser profile distribution.....	66
Figure 4-6 – Particle lognormal size distribution for different standard deviations	67
Figure 4-7 – Normalised LII signals for various particle diameters.	68
Figure 4-8 – Particle’s temperature profiles during LII process for various particle diameters.	68
Figure 4-9 – Particle’s maximal temperature profiles during LII process for various particle diameters.	69
Figure 4-10 – Normalized LII signal for various pressures	70
Figure 5-1 – Dependence of laser profile and fluence on LII signal for 100 nm particles radius (Tait and Greenhalgh, 1993b).....	75
Figure 5-2 – Dependence of LII signal peak on laser fluence. Measurement were carried out at 532 nm excitation wavelength with a top-hat beam profile on Santoro burner flame conditions (Michelsen, 2003, Michelsen et al., 2003).....	76
Figure 5-3 – Spectrum of a laminar blue flame showing Swan bands	77
Figure 5-4 – Different temporal detection strategies for camera acquisition.....	78
Figure 5-5 – Optical set-ups.....	80
Figure 5-6 – Laser excitation optical equipment layout.....	82
Figure 5-7 – Laser beam print before the sheet-forming optics on photographic paper (single shot)	82
Figure 5-8 – Laser beam profile (single shot) after the sheet-forming optics on photographic paper (true and false colour) (top) and from the camera fitted with the LII and ND filters (bottom).....	82
Figure 5-9 – Laser beam profile in three dimensions recorded by the camera	83
Figure 5-10 – Optical detection equipment layout.....	83

Figure 5-11 – Transmittance and reflectance ratio of the beamsplitters (Melles-Griot).....	84
Figure 5-12 – ELS and PLII transmittance filter profiles	85
Figure 5-13 – PMTS temporal characteristics	86
Figure 5-14 – Sensitivity and efficiency of the PMTs	87
Figure 5-15 – Drawing of the calibration lamp (source: Oriel™)	88
Figure 5-16 – Calibrated spectral irradiance of the Oriel lamp (full spectrum equivalent to a blackbody radiating at 3221 K)	89
Figure 5-17 – Calibrated spectral irradiance of the Oriel lamp	89
Figure 5-18 – Calibration curves of the Photomultipliers (from Santoro burner and global 2C-TiRe-LII conditions).....	91
Figure 5-19 – Blackbody radiation at 400 nm and 700 nm wavelengths as function of the temperature and the corresponding signal ratio	92
Figure 5-20 – Camera calibration patterns for the ELS (left) and PLII images (right).....	93
Figure 5-21 – Camera image correction (DaVis processing).....	93
Figure 6-1 –Laminar diffusion flame produced by the Santoro burner	98
Figure 6-2 – Illustration of the different 2c-TiRe-LII sampling locations within the flame and the two laser planes	100
Figure 6-3 – Post-processing diagram for the Santoro burner	101
Figure 6-4 – Raw and averaged temporal LII signals recorded at 400 nm and 700 nm (vertical slice of the flame sampled)	102
Figure 6-5 –Image representing 1000 LII temporal signals.....	103
Figure 6-6 – Laser fluence effect on LII signal (experimental)	104
Figure 6-7 – Laser fluence effect on LII signal peak (experimental)	104
Figure 6-8 – Laser fluence effect on normalized LII signal (experimental)	105
Figure 6-9 –Averaged experimental temporal LII signals with their best fitting by theoretical curves (entire flame sampled)	107
Figure 6-10 – Fit quality between experimental and theoretical signals	108
Figure 6-11 – Temperature decay curves, comparison between experimental and simulated	109
Figure 6-12 – Temperature curves corresponding to data of Figure 6-9	110
Figure 6-13 – Effect of λ -dependency of $E(m)$ on the quality fit of the temporal LII.....	111

Figure 6-14 – Temperature and soot volume fraction from the averaged LII signals from the entire flame.....	115
Figure 6-15 – Particle number densities and temperature from 2C-Tire LII measurements	117
Figure 6-16 – Averaged temporal LII decay signals for different flame locations.....	118
Figure 6-17 – Temporal LII decay signals for different flame locations.....	119
Figure 6-18 – Typical image acquisitions.....	122
Figure 6-19 – Flame soot mapping for single shot measurement and two laser plans - ELS and LII images, soot volume fraction, particle size and density are calibrated by 2C-TiRe-LII	123
Figure 6-20 – Flame soot mapping - Averaged ELS and LII images over 1000 images, the average soot volume fraction, particle size and density are calibrated by 2C TiRe-LII.....	125
Figure 6-21 – Soot formation model in a laminar diffusion flame	129
Figure 6-22 – Soot volume fraction profiles across the flame for different heights above burner (averaged measurement)	130
Figure 6-23 – Longitudinal soot volume fraction profiles across the flame for different radial positions (single measurement).....	131
Figure 6-24 – Particle diameter profiles at different heights above burner across the flame.....	133
Figure 6-25 – Number density profiles for different heights above burner across the flame.....	134
Figure 6-26 – Histograms of the spatial particle size distribution	135
Figure 7-1 – CAD drawings of the Proteus design	141
Figure 7-2 – Crank angle degree and time ASOI correspondence.....	142
Figure 7-3 – Injection duration and end of injection for the different injection rail pressure	143
Figure 7-4 –Soot cloud absorption.....	144
Figure 7-5 – Illustration of cycle to cycle variations of soot clouds by PLII measurements in a combustion chamber.....	147
Figure 7-6 – Background noise from flame luminescence and cylinder-wall	148
Figure 7-7 – Post-processing diagram.....	149
Figure 7-8 – RCM acquisition image example	150
Figure 7-9 – Example of image post processing.....	151

Figure 7-10 – Typical experimental temporally resolved LII decay curves with their best theoretical best fits (for 8 MPa in-cylinder pressure and 160 MPa injection pressure).....	151
Figure 7-11 – In-cylinder pressure traces for 8 MPa in-cylinder pressure and 160 MPa injection pressure for motored or fired condition.....	153
Figure 7-12 – Heat release rates for different injection pressures (for 6 MPa in-cylinder pressure).....	153
Figure 7-13 – Heat release rates for different in-cylinder pressures (for 160 MPa in-cylinder pressure).....	154
Figure 7-14 – Results for 160 MPa IP/10 MPa ICP/55.3 CN.....	156
Figure 7-15 – Results for 120 MPa IP/10 MPa ICP/55.3 CN.....	157
Figure 7-16 – Results for 160 MPa IP/8 MPa ICP/55.3 CN.....	158
Figure 7-17 – Results for 120 MPa IP/8 MPa ICP/55.3 CN.....	159
Figure 7-18 – Mean particle diameters obtained from 2C-TiRe LII measurements for different injection pressures	161
Figure 7-19 – Soot volume fractions obtained from 2C-TiRe LII measurements for different injection pressures	162
Figure 7-20 – Results for 100 MPa IP/8 MPa ICP/59.3 CN.....	163
Figure 7-21 – Results for 100 MPa IP/6 MPa ICP/59.3 CN.....	164
Figure 7-22 – Results for 120 MPa IP/6 MPa ICP/55.3 CN.....	165
Figure 7-23 – Mean particle diameters by 2C-TiRe LII for different in-cylinder pressures.....	167
Figure 7-24 – Soot volume fractions obtained from 2C-TiRe LII measurements for different injection pressures	167
Figure 7-25 – Results for 120 MPa IP/8 MPa ICP/59.3 CN.....	169
Figure 7-26 – Results for 100 MPa IP/8 MPa ICP/61.3 CN.....	170
Figure 7-27 – Mean particle diameters obtained by 2C-TiRe LII for different cetane numbers.....	171
Figure 7-28 – Soot volume fractions obtained by 2C-TiRe LII for different cetane numbers	171
Figure A-1 – EU emissions standards for passenger cars (category M1), g.km ⁻¹	211
Figure A-2 – EU emissions standards for light commercial vehicle [g.km ⁻¹]	213
Figure A-3 – Schematics of the Santoro burner.....	216
Figure A-4 – Schematic of the Santoro burner - Plates	217

Figure A-5 – Soot volume fraction profiles for Santoro burner from NIST	220
Figure A-6 – Soot volume fraction profiles for Santoro burner (Lebourgeois, 2010)	221
Figure A-7 – CFD simulations and experimental results from NRC group	222

LIST OF TABLES

Table 1 – Table of pollutant emission limits for passenger car adopted by the European Union (adapted from the Directive 70/220/EEC)	3
Table 2 – Non-exhaustive list of fuel tested for their effects on soot	25
Table 3 – Main theoretical parameter for LII signal computation	66
Table 4 – Table summarizing the different heat transfers used in the condition of atmospheric flame and high pressure condition (Diesel combustion chamber).....	72
Table 5 – Intensified camera’s characteristics	85
Table 6 – Published results for the Santoro burner	97
Table 7 – Gas temperature optimization	112
Table 8 – Laser fluence optimization.....	113
Table 9 – Size distribution optimization	114
Table 10 – Equivalent diameters and error fits depending on $E(m)$, α and β	114
Table 11 – Peak temperatures from 30 to 60 mm HAB.....	119
Table 12 – Results from 2C-TiRe-LII.....	120
Table 13 – Comparison of the different results from two measurement approaches....	127
Table 14 – Optimal fitting parameters	138
Table 15 – Main engine characteristic and operating conditions.....	142
Table 16 – Suitable operating conditions.....	146
Table 17 –Fitting parameters for RCM conditions	152
Table A-18 – Fitting coefficients for the vapour pressure [atm], mean molecular weight [Kg.mol ⁻¹] and the heat of vaporization [J.K ⁻¹ .mol ⁻¹] (Leider et al, 1973).....	215

NOMENCLATURE

Roman Symbols

c_p	particle heat capacity [$\text{J}\cdot\text{g}^{-1}\cdot\text{K}^{-1}$]
c_s	specific heat of soot [$\text{J}\cdot\text{g}^{-1}\cdot\text{K}^{-1}$]
d_p	particle diameter [m]
d_{p0}	initial particle diameter [m]
$f(d_{p0})$	particle size distribution function
f_L	focal length [m]
f_v	particle volume fraction [-]
I/I_0	transmittance [-]
Kn, Kn_c, Kn_h	different Knudsen numbers [-]
L	optical path length [m]
$L_{b,\lambda}$	spectral radiance [$\text{W}\cdot\text{m}^{-3}\cdot\text{Sr}^{-1}$]
M_v	molar mass of vapour [$\text{kg}\cdot\text{mol}^{-1}$]
m	complex refractive index [-]
m_g	molecular mass of the gas [kg]
m_v	molecular mass of the vapour [kg]
m_p	particle mass [kg]
n_p	particle number concentration [m^{-3}]
p_g	gas pressure [Pa]
p_s	vapour pressure [Pa]
p^*	corresponding pressure at the vapour pressure curve [Pa]
Q_{abs}	rate of absorbed laser-energy [W]
Q_{cond}	conductive heat [W]
Q_{sub}	sublimation heat [W]
Q_{rad}	radiative heat [W]
r_p	particle radius [m]
t	time [s]
T^*	corresponding temperature at the vapour pressure curve [K]
T_{bb}	temperature of black-body source during calibration [K]
T_g, T_p, T_v	temperature of gas, particle and vapour [K]
T_{p0}	particle heat-up temperature [K]
U_{sub}	sublimation rate [$\text{kg}\cdot\text{s}^{-1}$]

V_m observed test volume [m^3]

Greek symbols

β	sublimation constant [-]
γ	heat capacity ratio [-]
Δh_v	sublimation enthalpy of the particle material [$J.kg^{-1}$]
$\varepsilon_p, \varepsilon_{pt}$	particle spectral emissivity, total emissivity [-]
$\lambda_1, \lambda_2, \lambda_{detect}$	detection wavelength [m]
λ_{cond}	thermal conductivity of the gas [$W.m^{-1}.K^{-1}$]
λ_g	mean free path of the gas molecules [m]
λ_{laser}	laser wavelength [m]
ϕ	fuel/air equivalence ratio [-]
ρ_p	density of the particle material [$kg.m^{-3}$]
ρ_s	density of soot [$kg.m^{-3}$]
ρ_s, ρ_∞	vapour density at particle surface and at infinity [$kg.m^{-3}$]
σ_g	geometric standard deviation [-]
χ^2	least-squares error [varying]

Constants

c	speed of light, 299,792,458 [$m.s^{-1}$]
h	Planck's constant, $6.6260689633 \times 10^{-34}$ [J.s]
k_B	Boltzmann's constant, $1.380650424 \times 10^{-23}$ [J.K ⁻¹]
N_A	Avogadro number, $6.02214179 \times 10^{23}$ [mol ⁻¹]
R_m	universal gas constant, 8.314472 [J.K ⁻¹ .mol ⁻¹]
σ_{SB}	Stefan-Boltzmann constant, $5.67040040 \times 10^{-8}$ [$W.m^{-2}.K^{-4}$]

Subscripts

c	continuum regime
fm	free molecular regime
g	gas
p	particle
v	vapour
tr	transition regime

Acronyms

2C-TiRe	2-Colour Time-Resolved
ASOI	After Start Of Injection
CCD	Charge Coupled Device
CFD	Computational Fluid Dynamics
CN	Cetane Number
DI	Direct Injection
DNS	Direct Numerical Simulation
EGR	Exhaust Gas Recirculation
FMR	Free Molecular Regime
FWHM	Full Width at Half Maximum
IC	Internal Combustion
ICCD	Intensified Charge Coupled Camera
ICP	In-Cylinder Pressure
IP	Injection Pressure
LIF	Laser-Induced Fluorescence
LII	Laser-Induced Incandescence
ELS	Elastic Light Scattering
LES	Large Eddy Simulation
MFP	Mean Free Path
Nd:YAG	Neodymium Yttrium-Aluminium Garnet
NO _x	Nitric Oxides
PAH	Polycyclic Aromatic Hydrocarbons
PLII	Planar Laser-Induced Incandescence
ppm	Particles Per Million
PMT	Photo Multiplier Tube
RCM	Rapid Compression Machine
slm	Standard litres per minute
SOF	Soluble Organic Fraction
VCO	Valve-Covered Orifice
UV	Ultra Violet

ACKNOWLEDGEMENT

First of all, I would like to acknowledge with many thanks my supervisors, Doctor Cyril Crua and Professor Morgan Heikal for the support and assistance during this research project.

I wish to express my deepest gratitude to the mechanical and electrical technicians of the School of Engineering, William Whitney, Ken Maris, Brian Maggs, David Stansbury and Tony Brown.

I want to particularly grateful Lyndon Delauray for his help during difficult times in gathering data on these experiments and also for the valuable talks I had with him.

I want to thank Tiago Peres Lourenco Cardoso, Steve Higginson, Doctor Steven Begg and Doctor Romain Demory and all the members of the CAE research group as well as the research group from CORIA, Professor Gerard Gréhan, Doctor Annie Garo, Doctor Sawitree Saengkaew for their useful suggestions and comments. Without forgetting Doctor Guillaume de Sercey aka “the king of macro” who I worked with on the Vertigo project and for his precious help on Davis.

I gratefully acknowledge the European Union for the financial support on the C5 project and the Ricardo UK Plc. for the equipment and technical support.

Particular thoughts go to my wife Yong Yan Tan, parents and grandparents who have supported me for all these years and Marj Ballinger for helping me with my Franco-English writing.

DECLARATION

I declare that the research contained in this thesis, unless otherwise formally indicated within the text, is the original work of the author. The thesis has not been previously submitted to this or any other university for a degree, and does not incorporate any material already submitted for a degree.

Benoît Oger

1 CHAPTER I: INTRODUCTION

1.1 *Background of the study*

The ideal combustion producing only carbon dioxide (CO₂) and water (H₂O) exists only in theory. Diesel engines are far from “clean” or “green”, at their exhaust many pollutants are released, on the one hand: nitrogen oxides, (NO_x), unburned hydrocarbons (HC) carbon monoxide (CO) and particulates (PM) for the incomplete combustion species and on the other hand the CO₂ for a complete combustion product (average production is around 3.14 kg of CO₂ per kg of diesel fuel burnt). Moreover, CO₂ is a greenhouse gas, unwholesome for the ozone layer, and the main component of the increase of greenhouse effect (Arrhenius, 1896, Kasting and Ackerman, 1986).

Diesel combustion releases into the atmosphere numerous small carbon particles known as ‘soot’. Soot particles attract much attention from scientific communities as they are the evident demonstration of low efficiency combustion, play a main role in global warming (Jacobson, 2002) and have a harmful impact on human health (carcinogenic).

Soot coming from natural sources, such as forest fire, or from human activities end up in the atmosphere where high concentrations can be found in urban areas. Their average size is under 10 μm , hence their classification name as “Particle Matter 10 μm ” or “PM₁₀”. The smallest particles are under 1 μm . Soot particles can be also classified as PM₁ (ultrafine particles) and PM_{2.5}. Their lightness confers them the ability to stay longer in suspension in the atmosphere due to their insignificant falling speed.

Particle size determines how deeply they will penetrate the respiratory system. The smaller the particles, the deeper they permeate the lung (Figure 1-1) and the more harmful they are for individual’s health, especially the ultrafine particles under 2.5 μm which can reach the alveoli (Oberdörster, 2000). Modern diesel combustion strategies successfully reduced the overall particle matter emissions to meet legislations, but resulted in the production of more harmful ultrafine particles.

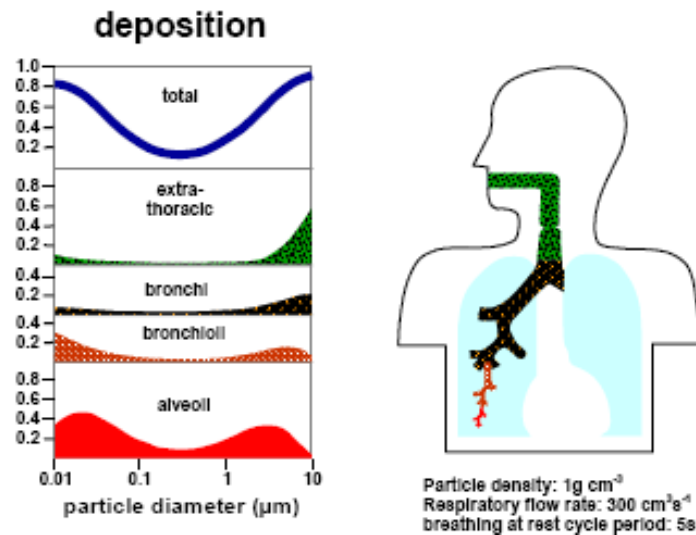


Figure 1-1 – Schema of the relation between the particle sizes and their deposition on the pulmonary system ((Kreyling et al., 2005) adapted from (ICRP, 1994) and (Price OT et al., 2002))

The influence of these particles is well-known. They increase the risk of cancers, respiratory and cardiovascular diseases, asthma and reduce the pulmonary capacity of young persons (World Health Organization, 2004). The toxicity of the soot particles does not come from the carbon but from the hydrocarbon compounds, sulphur and metallic ashes trapped inside the particle (Figure 1-2) (Murphy et al. 1998).

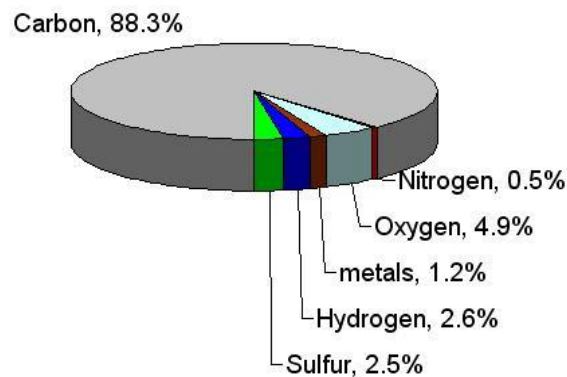


Figure 1-2 – Typical composition (by mass) of Diesel particulate matter (adapted from Murphy et al. 1998)

The World Health Organization has estimated the present particle concentration in the atmosphere is a factor reducing life expectancy by 8.2 months in Europe and 10.3 for the 10 new counties entering the European Union (more polluted) and 348,000 deaths per year can be attributed to this pollutant.

As a result, government authorities have wished to reduce particle matter emissions principally from internal combustion engines.

In a relatively short time, the particle matter emission limit for passenger cars in Europe (Table 1) was reduced from $140 \text{ mg}\times\text{km}^{-1}$ (Euro 1) to $5 \text{ mg}\times\text{km}^{-1}$ (Euro 5). The next legislation, Euro 6, will lower even further this limit; at a level that becomes difficult for engine manufacturers to meet these emissions levels. The use of after-treatment will not be sufficient. European countries are not the only ones to restrict emissions. USA and Japan have also adopted emission limits, and emerging countries in Asia, Africa and South America are following this path. The emission regulations have been the trigger for engine manufacturers to produce “cleaner” cars. Nowadays, pollutant emissions have become a critical economic and marketing issue for manufacturers.

Emissions standard	Particulate matters (PM) [$\text{mg}\times\text{km}^{-1}$]		Oxides of nitrogen (NO_x) [$\text{mg}\times\text{km}^{-1}$]		Hydrocarbons (HC) [$\text{mg}\times\text{km}^{-1}$]	
	Diesel	Petrol	Diesel	Petrol	Diesel	Petrol
Euro 1 (1992)	140	-	970 (HC included)	970 (HC included)-	970 (NO_x included)	970 (NO_x included)-
Euro 2 (1996)	100	-	700 (HC included)	500 (HC included)	700 (NO_x included)	500 (NO_x included)
Euro 3 (2000)	50	-	500	150	-	200
Euro 4 (2005)	25	-	250	80	-	100
Euro 5 (2009)	5	5	180	60	-	100
Euro 6 (2014)	5	5	80	60	-	100

Table 1 – Table of pollutant emission limits for passenger car adopted by the European Union (adapted from the Directive 70/220/EEC)

In the past, limits were easily reached by the addition of after-treatment systems such as catalyst converters. However, more recent limits have generated the creation and implementation of new combustion strategies, principally the increase of injection pressure and the use of exhaust gas recirculation (EGR).

Nevertheless, for a reduction of engine-out particle matter, a better understanding of the soot formation processes is essential. There have been numerous research studies on soot emitted by Diesel engines to investigate:

- Soot formation processes
- Soot volume fraction
- Number of particles
- Average particle size and size distribution
- Soot properties, structure and chemical composition
- Their influences on health and environment

In order to reduce pollutant emissions and reduce the developing time of new engines, engine manufacturers need to develop computational codes able to simulate the combustion processes inside the combustion chamber. To be valid, the results of these computational models need to be reliable and comparable to the experimental ones. Thus, experimental results need to be as much spatially and temporally accurate as possible.

The main objective of this research is to establish a quantitative technique to measure soot volume fraction and particle size in two-dimensions. The technique was first applied on a laminar diffusion flame at atmospheric pressure (ethylene/air). Once the method was validated, the technique was carried out on a Diesel combustion chamber. The optical engine can run under different parameters, for instance: injection pressure, EGR ratio, in-cylinder pressure, fuel type, air intake temperature to identify their influence on soot formation.

This introduction has presented the general background of this research project. The thesis is structured on the following way:

Chapter two reviews previous works concerning the fundamental mechanisms of soot formation and the current understanding of the formation in Diesel direct injection engines. The third chapter reports the different laser diagnostics used to visualize and quantify soot and especially describes the optical techniques used in the experiments.

The fourth chapter describes heat transfer models used for the determination of primary particle diameters. Models are tested for different parameters to understand their effects on the LII signal.

The fifth chapter describes the experimental conditions, apparatus but also the special requirements needed to carry out state of the art laser techniques.

The sixth chapter is the application of the technique to a laminar diffusion flame in order to validate the diagnostic and further understand and characterize the soot formation in a diffusion flame.

The seventh chapter describes the effect of different parameters (injection and in-cylinder pressure and cetane number) on soot formation.

The last chapter provides the conclusion on the atmospheric flame and on the optical combustion chamber experimental studies. A critical discussion on the results ends this work.

2 CHAPTER II: SOOT FORMATION REVIEW

This chapter reviews the knowledge on soot: characteristics, properties, formation processes and the influence of the main parameters in an internal combustion engine on soot formation.

2.1 *Soot characteristics*

Soot is a harmful pollutant and an indicator of low combustion efficiency. It can be defined as an agglomeration of spherical carbon particles formed during an incomplete combustion for high fuel to air ratios. The soot particles contain mostly carbon atoms, with a C/H ratio around 10:1. From electron microscopy studies, soot particles have a chain structure composed up to 4000 of smaller spherical particles (Spherules). These primary particles are agglomerated in clusters and can contain between 10^5 to 10^6 carbon atoms.



**Figure 2-1 – TEM images of agglomerates and primary particles
(Vander Wal et al., 1999, Smith, 1981)**

The agglomerate size can vary from 10 to 1000 nm with a surface area around $200 \text{ m}^2 \times \text{g}^{-1}$. Nanoparticles constituting the agglomerate are more or less spherical with a diameter typically from 10 to 80 nm but most of them are between 15-30 nm (Amann and Siegl, 1981).



Figure 2-2 – Onion-shell structure of nanocrystalline graphite forming the soot particles
(Ivleva et al., 2007)

The spherules are composed of concentric lamellate structure arranged around the centre (similar to the carbon black or graphite structure). The carbon atoms are bonded together in hexagonal face-centred plane arrays (platelet). The space between two platelets is 0.355 nm in average (slightly higher than graphite). 2 to 5 platelets overlay in layers to form crystallites. Thousands of crystallites in unordered layers (turbostratic) constitute a spherule (Figure 2-3) (Amann and Siegl, 1981, Smith, 1981). Soot density is estimated to be close to the graphite i.e. around $2 \text{ g}\times\text{cm}^{-3}$.



Figure 2-3 – Schematic of substructure of carbon particle
(Vander Wal et al., 1999, Smith, 1981)

The particle size is dependent of many factors such as fuel, flame, engine, injector types and operating conditions, where and how the soot particles have been sampled and measured. In diesel engine conditions, at the exhaust, primary particle size has been found to be from 20 to 50 nm with a mean diameter around 30 nm (Lee et al., 2001). A different research group have estimated their size to 30 to 70 nm (Bruce et al., 1991), using sampling probe and scattering technique. In-cylinder light scattering experiments have resulted to 30-50 nm (Tree and Foster, 1994) and 40-65 nm (Pinson et al., 1994). The soot agglomerate size has been determined to be between 100 nm and $2\mu\text{m}$ at the end of combustion (Ladommatos and Zhao, 1994, Desantes et al., 2005, Vander Wal et al., 1999).

2.2 Soot formation mechanisms

The evolution from liquid or vapour phase hydrocarbons to solid soot particles involves five processes: pyrolysis, nucleation, coalescence/surface growth, agglomeration and oxidation (Figure 2-4). These mechanisms occur in the previously cited sequence order; only the oxidation can convert hydrocarbons to CO, CO₂ and H₂O at any time in the sequence. The term “net soot formation” includes the formation and the oxidation of soot. The full process can proceed in a spatially and separated sequence in a laminar flame or simultaneously in a well-stirred reactor. In a combustion engine, the sequence varies between these two limits.

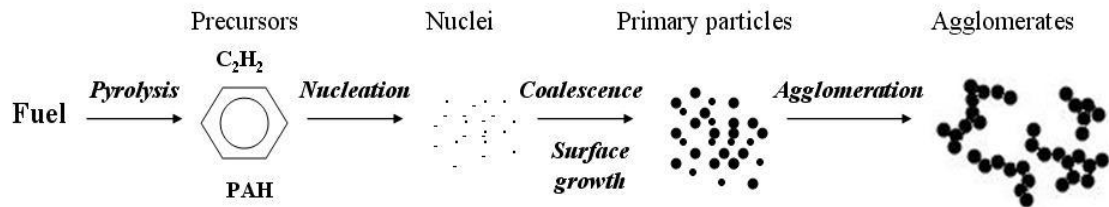


Figure 2-4 – Schematic diagram of the soot formation steps
(adapted from (Tree and Svensson, 2007))

2.2.1 Oxidation

Oxidation is the transformation of carbon or hydrocarbon into combustion products. If a carbon has been partially oxidized, it will not evolve into a soot particle even if the molecule goes through a fuel-rich zone. This phenomenon can occur anytime starting from pyrolysis through agglomeration. It depends on the species present and on the temperature conditions. The soot oxidation occurs at high temperatures, above 1300 K (Glassman, 1989). O₂, O, OH, CO₂ and H₂O species can conduct to soot oxidation.

The process of oxidation of the small particles starts with the chemical attachment of oxygen to the surface (absorption) followed by desorption of the molecule composed by the oxygen linked to the fuel component extracted from the surface (Glassman, 1998a). OH dominates soot oxidation under fuel rich and stoichiometric conditions while OH and O₂ prevail under lean conditions (Bartok and Sarofim, 1991). It is estimated that 10-20% of all OH collisions with soot particles are followed by the gasifying of a carbon atom (Haynes and Wagner, 1981).

The graphite like structure of soot causes higher resistance to oxidation (Smith, 1981). More agglomerated the particles, more the specific area is reduced and the less the soot particles are oxidized.

The net soot production is highly dependent on the oxidation process. The net soot production is highly dependent on the temperature influencing soot formation rate but also oxidation rate. The study of methane/air and methane/oxygen flames (Lee et al., 2000) showed the shortened flame height and higher flame temperature while oxygen is used as combustive which should have increased the soot formation but this did not occur. Soot volume fraction and particle diameters have been found to be lower in the methane/air flame. This is due to a higher oxidation but also because of a shorter resident time in the flame reducing the effect of surface growth.

2.2.2 Fuel pyrolysis

During pyrolysis, high temperatures alter the molecular structure of the fuel. The alteration starts with the wrenching of aromatic carbon bonds, followed by the recombination of radicals. Even if oxygen is present, there is no significant oxidation. The result of the pyrolysis is the production of soot precursors or “building blocks” for soot. All fuels under pyrolysis produce essentially the same species such as polycyclic aromatic hydrocarbons (PAH) and acetylene.

The soot precursor formation depends on the fuel pyrolysis rate compared to fuel and precursor oxidation rate by OH. All of these rates increase with the temperature but not as much as the oxidation one. This explains the fact that premixed flames (large quantity of oxygen present) are less sooty than diffusion flames (absence of oxygen in the pyrolysis region) although the temperature increases. Pyrolysis is an endothermic reaction with its rate dependent upon temperature value and concentrations (Smith, 1981). Radical diffusion is important in diffusion flames. Radicals like OH diffused into the fuel-rich zone can accelerate the pyrolysis. Smith also mentions that a small amount of O, O₂ or OH can lead to an increase of the pyrolysis rate, since many of the reactions take place by means of a free radical mechanism.

The typical pyrolysis products in a laminar diffusion flame are C₂H₂, C₂H₄, CH₄, C₃H₆ and benzene. Acetylene is largely present in fuel rich combustions; its polymerisation is thought to be a cause of the PAHs formation and is considered to be the main soot precursor. Furthermore, the first aromatic rings may be produced from non-aromatic

species such as phenyl or acetylene (Wang and Frenklach, 1997) and will also play a major role for the polycyclisation of the molecules (Figure 2-5).

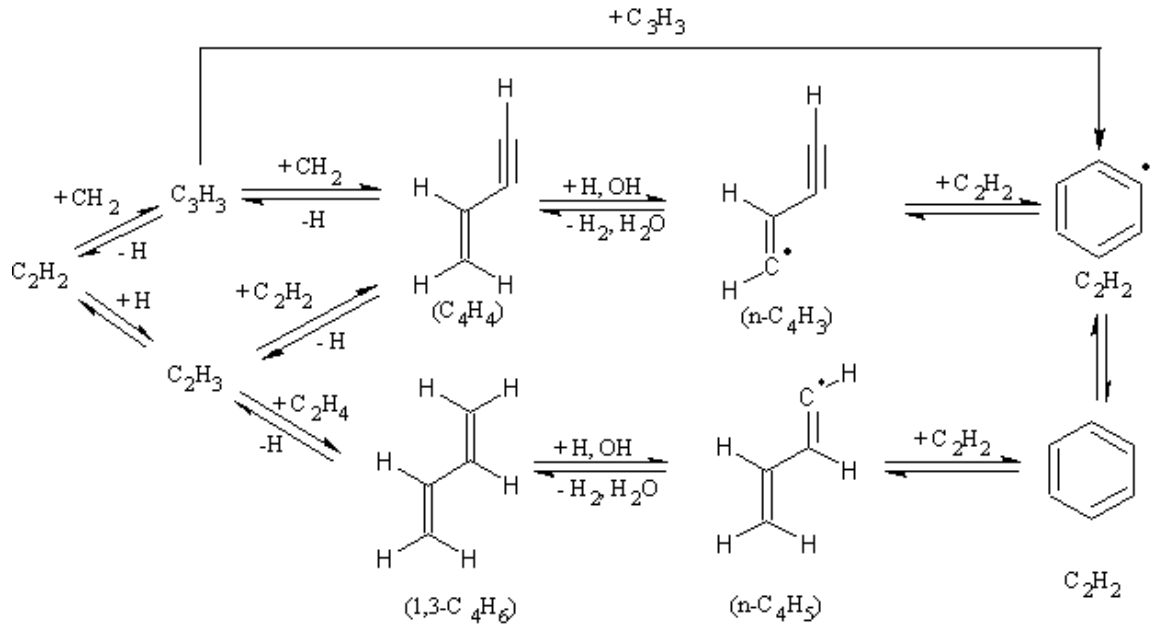
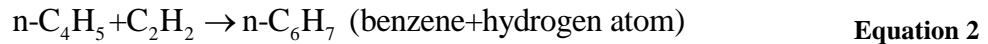
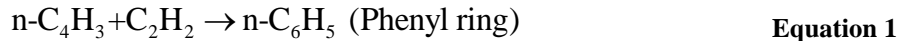
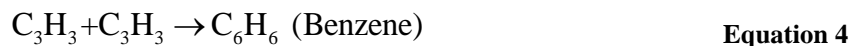
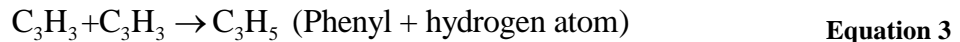


Figure 2-5 – Pathways of benzene formation

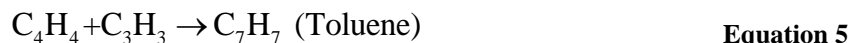
The first way of the formation of benzene (Equation 1, Equation 2) according to Frenklach and Wang (Wang and Frenklach, 1997)



A second way (Equation 3, Equation 4) can possibly happen due to the insufficient quantity of n-C₄H₃ and C₄H₅ to form all the phenyl and benzene (Miller and Melius, 1992).



A third way possible is (Pfefferle et al., 1994):



These formation rates are highly influenced by temperature, the formation rate is maximum for temperatures around 700 K for the first way but higher temperatures for the second way (around 1600 K) while for the third way, it is at low local temperature.

2.2.3 Nucleation

Nucleation, also called soot particle inception, is the formation of solid particles (nuclei) from gas-phase reactants (Bartok and Sarofim, 1991). It is an irreversible mechanism. The smallest detectable nuclei in a luminous flame are in the range of 1.5-2 nm in diameter (Bartok and Sarofim, 1991). These researches also stated that the nucleation is possibly due to the addition of small, probably aliphatic, hydrocarbons to larger aromatic particles at 1300 to 1600 K (Glassman, 1998a).

If the nuclei mass has a negligible contribution to the total mass of soot, they have a major role in the mass added later by providing sites for surface growth. The nucleation only occurs near the primary reaction zone where temperatures and concentrations of ions and radicals are the highest.

The firsts monocyclic hydrocarbons produced will evolve into polycyclic aromatics. The growth of the aromatics is realised through the hydrogen-abstraction-acetylene-addition (HACA) mechanism (Wang and Frenklach, 1997). In this process (Figure 2-6), the first step is the release of a hydrogen atom, followed by the addition of acetylene to the aromatic radical such as phenyl leading to the bonding of an ethynyl ($-C_2H$) group to the aromatic ring. This mechanism continues and leads to long plain condensed aromatic rings which are stable and therefore irreversible.

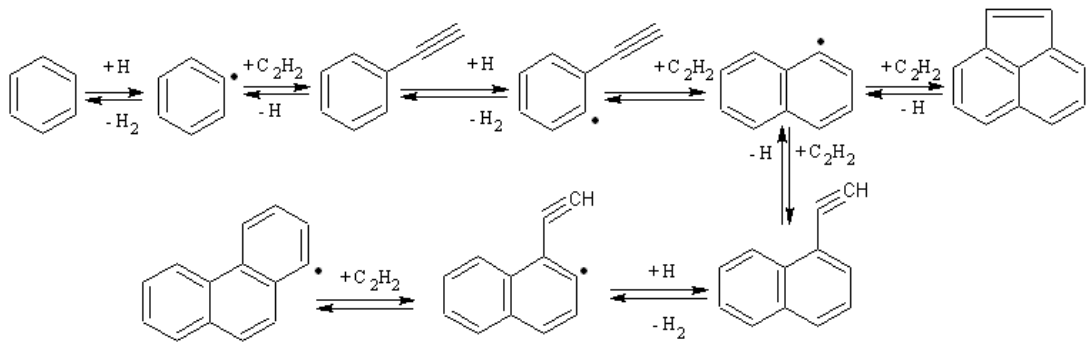


Figure 2-6 – HACA mechanism of polycyclic aromatic hydrocarbon formation
[adapted from (Wang and Frenklach, 1997)]

The competition between the two mechanisms is determined by the ratio of acetylene to benzene. If the concentrations of aromatic species are sufficiently high, PAH can grow through the direct ring-ring condensation (Wang and Frenklach, 1997). However, when the acetylene concentration equals that of benzene then the HACA mechanism becomes dominant. The presence of alternative formation paths have been described and reviewed previously (Violi et al., 1999):

- Combination of benzyl and propargyl leading to the naphthalene formation (Colket and Seery, 1994):

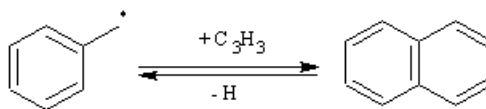


Figure 2-7 – Combination of benzyl with propargyl

- Combination of two cyclopentadienyl radicals (from benzene oxidised) making a naphthalene molecule (Castaldi et al., 1996):

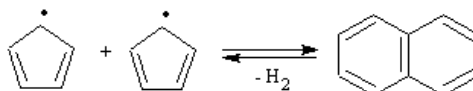


Figure 2-8 – Combination of two cyclopentadienyl

- Combination of cyclopentadienyl and indenyl (from naphthalene oxidised) (Castaldi et al., 1996):

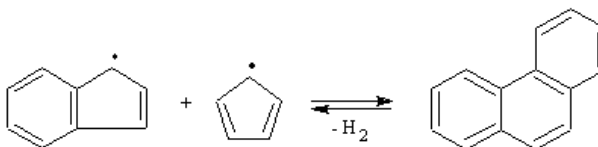


Figure 2-9 – Combination of cyclopentadienyl and indenyl

- Sequential addition of propargyl radicals leading to the formation of phenyl radicals and bi-phenyl. The polycyclisation in phenanthrene is achieved with the addition of acetylene:

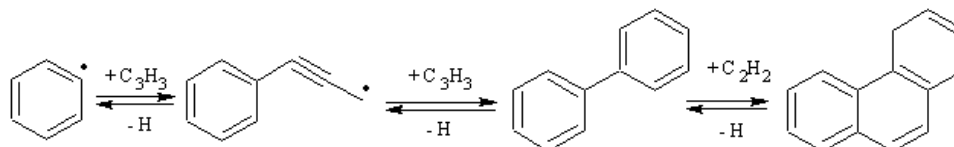


Figure 2-10 – Propargyl radical leading to the phenanthrene formation

2.2.4 Surface growth

Surface growth is the process wherein mass is added to the nuclei which are in numerous number but with an insignificant load of soot. There is no clear distinction between the nucleation end and surface growth beginning. Gas-phase hydrocarbons (mainly acetylene) are deposited on the hot reactive surface of the nuclei. Surface growth continues to occur after leaving the primary reaction zone into cooler and less reactive regions. The number of particles remains the same but the weight of soot and the soot volume fraction increase. The major part of the soot mass is produced during this step. Thus the time of surface growth process is important for reducing the soot production. The smaller the nuclei, the higher is the surface growth because smaller nuclei have more reactive radical sites (Bartok and Sarofim, 1991). The formation of first carbonic particles begins with the growth of the PAH in three dimensions (Heywood, 1988).

2.2.5 Coalescence and agglomeration

Coalescence and agglomeration are both processes where the particles meld. Coalescence (also called coagulation) occurs when the particles collide and coalesce, reducing the number of particles but the soot mass remains constant as the mass of the new spherical particle is equal to the sum of the two collided ones.

Agglomeration occurs when primary particles stick together to form a cluster. The aggregate has a chain-like form being composed of spherical particles (primary particle shapes remain the same, even if sometimes clumping has been observed). The number of particles is reduced but the weight and soot volume fraction remain the same. The length of the agglomerate depends on the residence time in the flame (Sunderland and Faeth, 1996, Xu and Faeth, 2001). The agglomeration process of soot particles can be characterized by the mass fractal concept, using the fractal dimension D_f (Koylu et al., 1995, Koylu et al., 1997, Lee et al., 2000) which is determined through the following equation:

$$N = K_{fr} \left(\frac{2R_g}{d_p} \right)^{D_f} \quad \text{Equation 6}$$

N number of primary particles

K_{fr} fractal prefactor

R_g radius of gyration [m], equivalent to half of the projected maximum diameter of the aggregate (L)

d_p mean primary particle diameter [m]

The average fractal dimension is often determined from TEM images or by scattering (Figure 2-12). N is linear with R_g/d_p and the average value found for Diesel engine condition (at exhaust) is 1.7 (Wentzel et al., 2003).

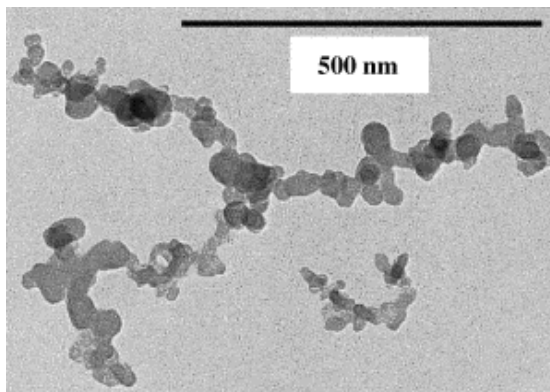


Figure 2-11 - TEM image of soot agglomerates at Diesel engine exhaust (Wentzel et al., 2003)

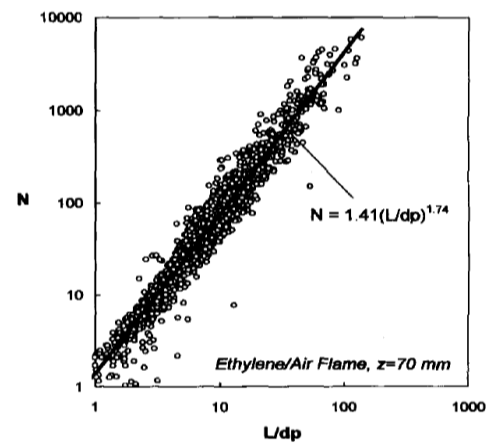


Figure 2-12 - Number of particles in an aggregate as function of the nondimensional length (L/d_p) (Koylu et al., 1997)

2.3 Soot formation in a direct injection engine

2.3.1 Introduction to the combustion of compression-ignition engine

In a compression ignition engine, air alone is induced into the combustion chamber. The fuel is injected after the air has been compressed, slightly before Top Dead Centre (TDC). The high pressure and temperature cause the fuel to self-ignite. The Diesel cycle is a thermodynamic cycle (Figure 2-13), invented by Rudolph Diesel in 1897.

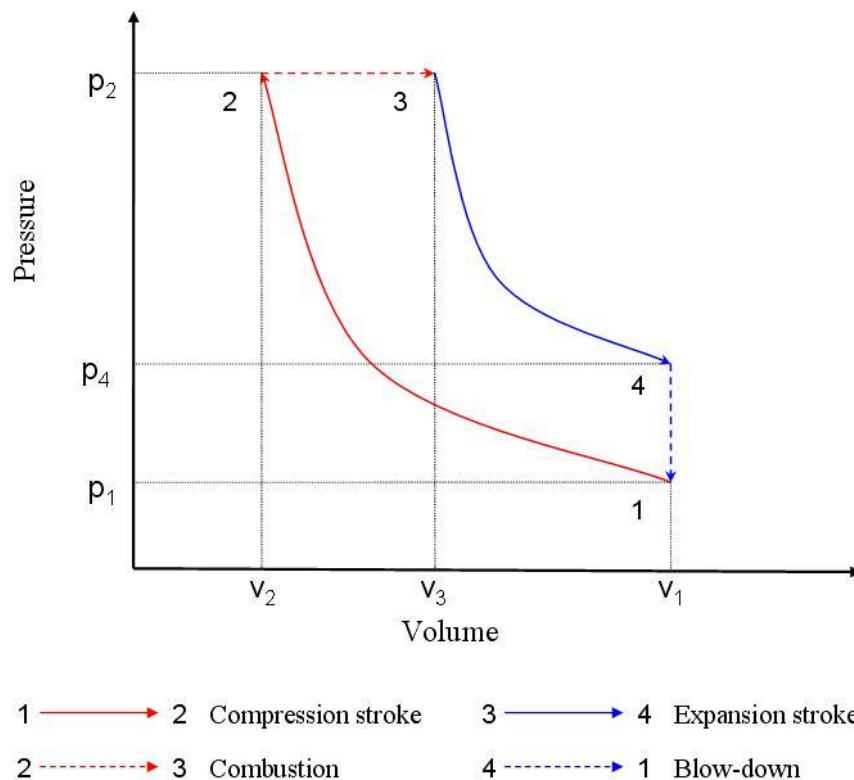


Figure 2-13 – P-V diagram for ideal Diesel cycle

Two categories of Diesel engine can be distinguished between indirect and direct-injection engines according to where the fuel is injected.

In an indirect injection Diesel engine, the fuel is not directly injected into the combustion chamber but into another chamber (prechamber) off the combustion chamber. The combustion starts in the prechamber and spreads to the main chamber. The prechambers are designed to obtain a better air - fuel mixing and reduce the rate of combustion and audible noise but increases heat loss. Thus the engine efficiency is diminished. To promote a good mixing, air flow has to be very high but the fuel does

not need to have a high velocity. The design and manufacture of indirect injection engines has been easier than direct injection engines which require high fuel velocity (high pressure injection) and high in-cylinder gas velocity flow. With the progress on injectors and design of combustion chambers (thanks to the CFD), accomplishment of direct injection has become possible. This is the reason why in the past, cars were manufactured with an indirect injection engine while nowadays all recent vehicles have direct injection engine. On the other hand, in the direct injection engine, fuel injections take place directly in the combustion chamber. Injectors are usually multi-holes and located at the top of the chamber. Compared to previous types of engines, these versions are more efficient, noisier, use higher injection pressures and run at lower rpm.

The recent technology High-pressure-Direct Injection (HDI) has become widespread and is implemented in almost all new Diesel passenger vehicles. This technique has improved the power, torque, pollutant emissions and noise by the increase of injection pressure. The high pressure (>1000 bar) going to the electronic injector is generated via an injection pump supplying the common rail. The high pressure injection has allowed a better atomization of the fuel and the possibility of controlling the injection (start, duration, multi-injections) has opened the path to new combustion strategies.

In a Diesel engine, fuel is injected just before TDC. High pressure and temperature occur in the combustion chamber, causing the auto-ignition of the air/fuel mixture. The mixture does not ignite instantaneously; a delay exists between injection and the beginning of combustion. After the liquid fuel injection in the chamber, the condition inside leads to the heating-up of the fuel liquid droplets and the subsequent evaporation of the liquid fuel into gas-phase. Fuel vapour and oxygen mix together and react, producing radical intermediate concentration sufficient to initialize the combustion at certain places. The auto-ignition delay is dependent upon the fuel properties (cetane number), injection (fuel vaporization) and in-cylinder conditions (temperature and pressure). An increase of the in-cylinder temperature or pressure shortens the auto-ignition delay (Haupais, 1993). The oxygen concentration in the fuel/air mixture (coming from the oxygen contained in fuel or with a better mixing) is important as a higher concentration increases the pyrolysis and oxidation rates of the fuel and, therefore shortens the auto-ignition delay. The auto-ignition delay is reduced by the use of swirl which allows a better air/fuel mixing, but the EGR has the opposite effect as it decreases the oxygen concentration.

The start of combustion can be determined in two ways. The common method is to use the in-cylinder pressure curve (via a pressure sensor) or Heat Release Rate (HRR) obtained from pressure curve (Figure 2-14) but an alternative way is to use the chemiluminescence of some specific species (detected via a photomultiplier). The increase of pressure around TDC or the start of the HRR raise, reveal the start of internal combustion.

The HRR diagram (Figure 2-14) shows the different combustion processes in chamber. The fuel does not burn instantaneously after injection. The liquid is heated-up and vaporized due to the temperature of the surrounding gas before starting to ignite. These phenomena need energy. That is why the heat release is negative before the auto-ignition. Then the fuel vapours burn in a pre-mixed combustion phase. This phase lasts only a few crank angles but it is a curt combustion (greatly increasing the energy released) involving a high pressure and HRR peak (first peak on the HRR diagram) and the noise (knock) proper to Diesel engines. Once the pre-mixed mixture has been burnt, the heat release rate decreases. A second type of combustion by diffusion takes over afterwards for approximately 40 crank angles. During this period, pressure and HRR decrease. The flame propagates upstream to the unburned fuel (which has not been burnt in the premixed flame) and to the incoming fuel. The combustion finally ends in unfavourable conditions (low pressure and temperature) where fuel and combustion products are mixed with the low level of remaining air.

To characterize the combustion of an internal combustion engine, the equivalence ratio and the HRR are often used.

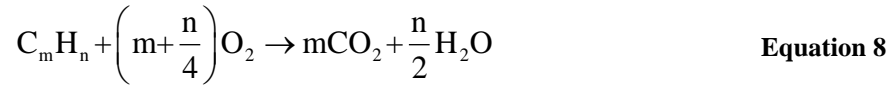
The equivalence ratio Φ (dimensionless number) helps to characterize the fuel mixture (*From p71 Heywood, 1988*).

$$\Phi = \frac{\left(\frac{\text{Quantity of fuel}}{\text{Quantity of air}} \right)_{\text{real mixture}}}{\left(\frac{\text{Quantity of fuel}}{\text{Quantity of air}} \right)_{\text{Stoichiometric mixture}}} \quad \text{Equation 7}$$

If $\Phi > 1$, more fuel than in a stoichiometric mixture: rich mixture

If $\Phi < 1$, more air than in a stoichiometric mixture: lean mixture

If $\Phi = 1$, the reaction is stoichiometric, in an ideal combustion case, hydrocarbons are totally burnt, theoretically resulting water and carbon dioxide as combustion products:

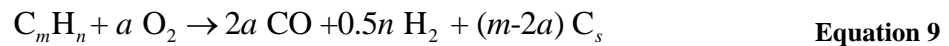


Two other ratios are useful to define the engine operating conditions:

$$\text{Air/fuel ratio, (A/F)} = \frac{\dot{\text{mass}}_{\text{air}}}{\dot{\text{mass}}_{\text{fuel}}} \quad \text{or} \quad \text{Fuel/air ratio, (F/A)} = \frac{\dot{\text{mass}}_{\text{fuel}}}{\dot{\text{mass}}_{\text{air}}}$$

Common DI Diesel engines run with a low mean equivalence ratio with a strong gradient along the jet. The usual operating range is between 0.7 and 0.85.

Assuming that the mixture is oxygen insufficient to form CO_2 but produce CO , the stoichiometric equation can be written as:



$C_m H_n$ being the fuel and C_s the soot produced, the ratio of carbon to oxygen, C/O is equal to $m/2a$.

If $C/O = 1$, at stoichiometric condition, there is enough oxygen to produce only CO from the carbon available and then no soot is produced

If $C/O < 1$, the extra oxygen is used to produce CO_2 .

If $C/O > 1$, the excess of carbon form soot

While the mixture is too rich, soot is formed which is often the case locally especially upon diffusion flames.

The determination of the heat transfer is a way to be aware of what is happening in the combustion chamber. The most common way to analyse the rate of energy released by the fuel is to determine the heat release rate (HRR).

The in-cylinder pressure curve according to some assumptions (in Appendix D) allows for determining the HRR, via this expression (Heywood, 1988):

$$\frac{dQ}{dt} = \frac{\gamma}{\gamma-1} P \frac{dV}{dt} + \frac{1}{\gamma-1} V \frac{dp}{dt} \quad \text{Equation 10}$$

- Q heat released [J]
- γ ratio of heat capacities c_p/c_v .
- P in-cylinder pressure [$\text{N}\cdot\text{m}^{-2}$]
- V cylinder volume [m^3]
- θ crank angle [degree]

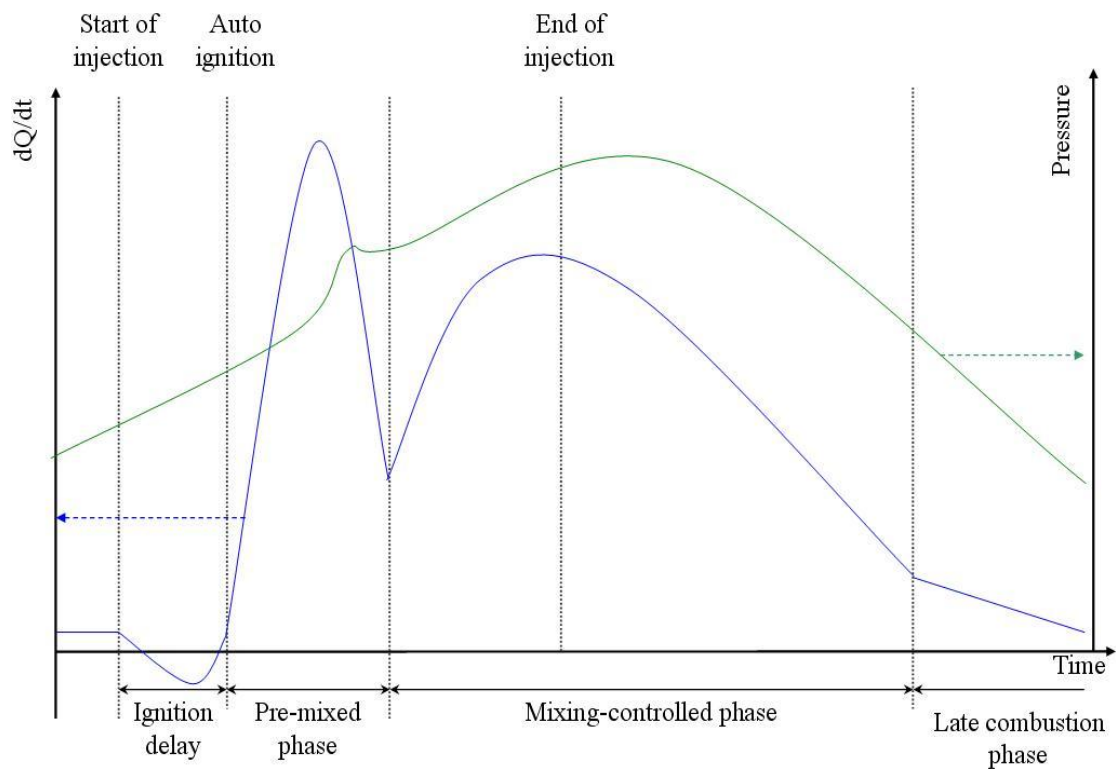


Figure 2-14 – Typical heat release rate and pressure diagram of a Diesel combustion engine

2.3.2 Soot formation model

The sharpest model existing is the one realised at the Sandia laboratory (Figure 2-15). The Sandia's conceptual model of diesel combustion (Dec, 1997) is the fruit of several researcher works. Sundry techniques have been used such as Mie scattering for the fuel spray, PLII and Rayleigh scattering for soot formation, LIF for the fuel vapour and PAH visualisations.



**Figure 2-15 – Sandia's conceptual model of Diesel combustion
(Dec, 1997, Siebers and Higgins, 2001)**

Two crank angles (CA) after injection, a small fraction of the fuel is vaporised and surrounds the liquid spray. The fuel/air ratio is estimated to be between 2 and 4 in the vapour phase. The vapour layer thickness increases until 4.5 CA after injection. After reaching the maximum penetration length, there is no liquid fuel, the fuel propagates downstream in a vapour state. At 5 CA after injection, PAH starts appearing in the area downstream the vapour fuel jet and till end of injection, the soot particles appears at 6 CA ASOI at the same location as the soot precursors (PAH).

The soot jet continues its propagation and particles are found in higher concentration in the downstream part. Particles are larger in the downstream part of the jet than in the upstream part due to particle growth process.

The OH radical appears where the HCHO has reduced, proof of a reaction at high temperature. A diffusion flame surrounds the jet periphery. This type of flame releases many OH radicals which are major factors for soot oxidation.

Oxygen oxidizes soot more at the jet periphery where oxygen is present in higher concentration.

There is a wide range of temperature variation across the jet. The jet envelope is the warmest area; the further the soot cloud is from the injector, the colder the temperature. Ambient temperature and injection pressure have a major impact on the total soot produced.

From ELS and LII images, Kosaka et al. (2005) have shown, in a rapid compression machine, larger particles are located downstream the flame head region (due to particle growth). Correlated with the particle number density, the authors found number of particles was reduced downstream due to agglomeration.



Figure 2-16 – Conceptual model of soot formation and oxidation processes in a Diesel spray flame (Kosaka et al., 2005).

In a Diesel engine, scattering and extinction techniques provides number density, diameter and soot volume fraction, Tree and Foster (1994) found a maximal diameter range between 30 and 50 nm, Soot volume fraction between 2.5 and 6.5×10^{-5} . The effect of different speeds was not conclusive, but the authors stated that peak soot diameter, soot volume fraction and soot temperature increase with the equivalence ratio. Picket and Siebers (2004) showed that in a pressurized vessel, the soot production increases and is located closer to the injector with higher ambient temperature. The results show a convergence of the soot volume fraction at the end of the jet. This was explained by the oxidation effect. In the late combustion phase, soot structures change and particles become more resistant to oxidation (Song et al., 2011).

Experimental researches (Figure 2-17) also demonstrated that a higher injection pressure reduces the soot production due to a better spraying of the fuel and a better

mixing between fuel and air. The relations between equivalent ratio, temperature and pollutant formation (soot and NO_x) are illustrated on Figure 2-17, the so-called ϕ -T map. The map shows that, with lower flame temperature, production of soot and NO_x can be avoided.

EGR strategy is nowadays largely spread in Diesel engines. The mixing of exhaust gas with fresh gas at the intake has for consequence to reduce oxygen ratio and therefore flame temperature. The dependence of the EGR, i.e. ambient oxygen concentration, on soot production is the purpose of many research (Gao and Schreiber, 2001, Idicheria and Pickett, 2007, Boiarciuc et al., 2006, Al-Qurashi et al., 2011). The EGR use allows a reduction of flame temperature at a level low enough to decrease significantly the NO_x emission level but it does not have such an effect on soot. Moreover, soot emissions initially increase while increasing EGR levels as the flame temperature and oxygen concentration decrease and so the oxidation process. For higher EGR levels, soot emissions start to decrease due to lower soot formation. This behaviour called soot bump is dependent on initial combustion temperature and combustion strategy. The effect of EGR is a trend between lower rates of formation and oxidation due to lower temperature and oxygen concentration.

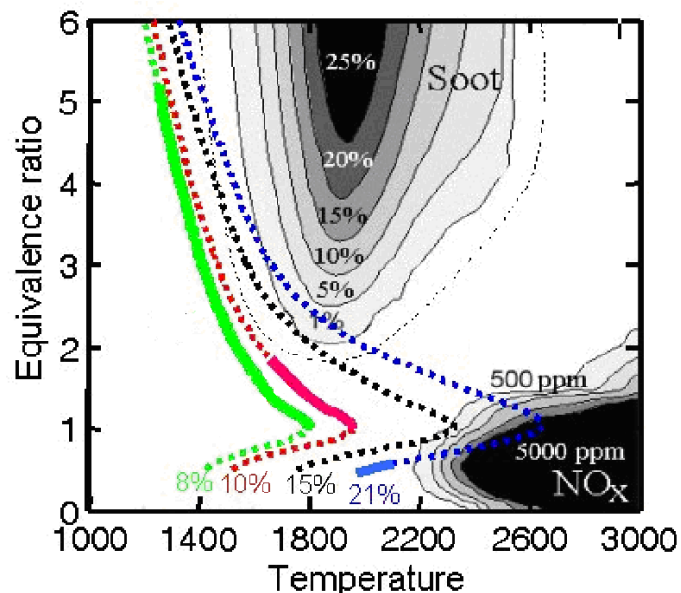


Figure 2-17 – ϕ -T map (Akihama et al., 2001, Idicheria and Pickett, 2005)

2.3.3 Physical parameters influencing the soot formation

Temperature

Temperature is the main factor in the soot formation (see Figure 2-17). This parameter increases all the reaction rates implied in the soot mechanism but the formation rate does not increase as fast as that of the oxidation. In a well-stirred reactor, the maximum rate of soot formation has been found to be around 1500-1700 K (Sato et al., 1990). Above this peak, the amount of soot produced decreases in premixed flames but in diffusion flame, this amount increases with the temperature. In a Diesel engine, high combustion temperature reduces the particulate emission (Kaminoto and Bae, 1989). Soot inception begins around 1400 K and burnout stops under 1300 K (Glassman, 1998a). Depending on gas temperature, the soot formation is a trade-off between higher oxidation rate and higher formation rate when temperature increases.

Pressure

Pressure is a difficult factor to isolate from the temperature, flow velocity, flame structure, density and thermal emissivity will vary. Pressure in diffusion flame alters flame structure and increases thermal diffusivity [combustion. San Diego academic press, 1996]. In premixed flame, mass burn rate increases with pressure. Soot formation increases with the pressure in premixed flames (Haynes and Wagner, 1981). Higher pressure also means larger particles, higher number of particles density and lower flame temperature peak.

An augmentation of the soot volume fraction at the P^2 dependence has been found in C_2H_4 and C_6H_6 premixed flames, (above 1650 K, C/O ratio between 0.65 and 0.75 and pressure 1 to 5 bar) (Böhm et al., 1988) and in diffusion ethylene flame (pressure 1 to 2.5 bar) . Other studies found a $P^{1.2}$ and $P^{1.4}$ dependence (respectively (Flower and Bowman, 1987, Flower, 1988)).

Density is proportional to pressure, so for a given sampled volume, the soot density will be higher at higher pressure. The dependence of the soot volume fraction is between P^1 and P^2 .

Stoichiometry

The stoichiometric condition can be changed through the oxygen content in the fuel composition or in the fuel/air premixing. Increasing the oxygen/fuel ratio leads in the majority of cases to a soot reduction, because more oxygen involves a higher combustion temperature, which as the major effect on the reaction rates involved in the soot processes. Therefore, it is difficult to isolate this factor from the temperature.

There is an equivalence ratio value (depending on the fuel) for which the soot formation is maximal. But if the equivalence ratio is slightly higher or lower compared to this value, the net soot production will be greatly reduced (Hura and Glassman, 1988).

Stoichiometric oxygen quantity is not needed to suppress soot production completely if there is enough oxygen to oxidise the carbon into CO. The carbon atom cannot be involved into soot formation process thereafter (Hura and Glassman, 1988).

Fuel structure and composition

The effects of the fuel structure (especially aromatic) on soot formation in Diesel engines have been largely investigated but there is no unanimity on the results. The main question was if the structure (straight chain, branched chain and aromatic) has an influence on the soot produced. In various fuel investigations (Table 2), comparisons are difficult because the composition of fuel changes the combustion conditions (temperature, pressure, local equivalence fuel ratio, lift-off length). Therefore it is difficult to isolate this factor.

On the one hand, the use in three different engines of T90 (containing aromatic and sulphur) has shown an increase in soot production (Ullman, 1989). On the other hand, using a more recent engine, it has been found that aromatic and cetane number do not increase the soot emission (Ullman et al., 1994). The conclusion is that fuel aromatic content will either increase the soot level or not depending on the engine technology. Aromatics and polyaromatics have no affect if the engine already emits a low soot level but will have a stronger effect if it is a heavy emitting engine (Lee et al., 1998). Nevertheless the C/H ratio is important, particulate emissions increase linearly with it (Exhaust measurement (Miyamoto et al., 1994) and in a diffusion flame (Olson et al., 1985)).

Fuel	Molecular formula	Reference
Toluene	C ₇ H ₈	(Ladommatos and Zhao, 1994)
n-Heptane	C ₇ H ₁₆	(Ladommatos et al, 1994; Hentschel and Richter, 1995)
Tetralin	C ₁₀ H ₁₂	(Miyamoto et al., 1994)
Dipentene	C ₁₀ H ₁₆	(Miyamoto et al., 1994)
Decalin	C ₁₀ H ₁₈	(Miyamoto et al., 1994)
α -Methyl naphthalene	C ₁₁ H ₁₀	(Ladommatos and Zhao, 1994, Miyamoto et al., 1994)
Alkyl benzene	C ₁₃ H ₂₀	(Miyamoto et al., 1994)
n-Tetradecane	C ₁₄ H ₃₀	(Miyamoto et al., 1994)
n-Hexadecane	C ₁₆ H ₃₄	(Dec et al, 1991; Dec and Espey, 1995; Dec, 1997 ; Musculus et al, 2002; Mueller and Martin, 2002)
Heptamethylnonane	C ₁₆ H ₃₄	(Espey and Dec, 1991; Dec and Espey, 1995; Dec, 1997 ; Musculus et al, 2002; Miyamoto et al., 1994 ; Mueller and Martin, 2002)
Diesel fuels	Various	(Hentschel and Richter, 1995)

Table 2 – Non-exhaustive list of fuel tested for their effects on soot

2.3.4 Diesel engine parameters influencing soot formation

The fuel injection is one of the main parameter that can be controlled and lead the combustion process (Crua et al., 2004). Many researches are carried out to characterize the fuel spray by optical techniques (Soid and Zainal, 2011).

Injector

Reducing the orifice diameter slightly reduces the lift-off length and the fresh air charge entering the jet. However, as it also reduces the fuel flow from the nozzle, the air/fuel stoichiometric is better at the lift-off length and in the premixed burn zone, thus reducing the soot formation.

The injection pressure increase improves the atomisation, the velocity of the fuel and the lift-off length, decreasing particulate formation as long as there is no contact between the jet with inner engine surface (impingement) or with another jet.

Injection timing

The injection timing plays an important role in pollutant emissions. An advanced timing will reduce the particulate emissions but increase the NO_x ones. However, retarded timing conducts to more particulate and less NO_x emissions (due to temperature and equivalence ratio in the combustion chamber, see Figure 2-17). The injection timing also affects the proportion of liquid fuel impingement on the engine surface.

Multiple injections

Multiple injection strategy is a modern technique to reduce particulate emissions by injecting several times during the same cycle (rendered possible via high-pressure common rail fuel systems and electronic control). A few researches have been carried out to understand the mechanism of particulate and NO_x reduction of this strategy (Tow et al., 1994, Pierpont et al., 1995, Chen, 2000, Montgomery and Reitz, 1996, Mellor and Chen, 2002, Yang et al., 2002, Park et al., 2004, Han et al., 1996, Mallamo et al., 2002). The multiple injections system is commonly composed of a pilot injection, main injection and post injection. The objective of the pilot is to increase the temperature before the main injection, therefore decreasing the ignition delay of the main injection (Park et al., 2004, Mallamo et al., 2002). This decrease reduces the fuel fraction which should be burnt in the premixed combustion, thus lowering the pressure rise and peak during the premixed burn. However, pilot injections generally increase the amount of particulate produced (Park et al., 2004) because of the higher temperature during the main injection, lift-off length and air (which also contains fuel from the pilot injection therefore containing an oxygen concentration at a lower level) mixing with fuel are reduced. However, the particulate benefit comes from the late injection (10% of the fuel injected after 10 to 40 °CA). A first explanation is that a small quantity of fuel which burns premixed and produces a small part of soot allows for having a higher temperature and better mixing late in the cycle, improving the soot oxidation when it usually starts to decline (Park et al., 2004, Mallamo et al., 2002). The second explanation is the delay between the two injections increases the fresh air charge which can be entrained with the jet, reducing the equivalence ratio. Soot can have a better mixing with incoming fresh air rather than carried downstream to evolve at the leading edge of the jet (Han et al., 1996).

Cylinder pressure and temperature

The effects of pressure and temperature have been discussed previously but commonly, if both temperature and pressure decrease, particulate emissions also decrease.

Combustion chamber design

The soot formation is dependent mainly on two key factors in the design of a combustion chamber: the internal air flow, especially the swirl, and the liquid fuel impingement. The fresh air going into the jet is not dependent on the swirl but on the jet velocity and the cone angle of the spray. The swirl increases the turbulence and improves the mixing and therefore the subsequent rate of combustion after the injection and after the end of injection. Soot burns out faster while the gas temperature remains high during early expansion and also has a higher oxidation rate. The swirl rate is limited by the interaction between two adjacent jets or the jet reaching the cylinder wall which must be avoided. When the liquid fuel impinges on the inner wall or piston, the impulsion of the jet and the mixing with fresh air are reduced. This can happen with early injection (piston is too close to the injectors), with late injection (in-cylinder temperature not high enough to evaporate the fuel), low cylinder pressure, over-fuelling or a variation in fuel enthalpy of vaporization (water-fuel emulsions). Liquid impingement on engine surface improves the atomisation leading to a better fuel/air mixing and consequently a decrease of soot level. The impingement of the leading edge of the jet was found to decrease the soot emissions but when jets were scattered back in the same direction they come from, produce the opposite effect - similar case if two adjacent jets cross each other (Musculus and Pickett, 2005).

Engine transient

The engine speed and load have an obvious effect on the emissions. A rapid change from idle or low load to high load and high speed (quick acceleration at low gears) is the moment when an important amount of soot is produced. This is due to a fuel rate too high compared to the air charge. The fuel/air ratio becomes too high and more impingement of the liquid fuel on the cylinder wall caused by a low charge air density (higher fuel penetration). The mixture in the cylinder is too rich in fuel and poorly mixed. This problem has been well-resolved with the implementation of electronic fuel injection regulated by computer and variable geometry turbochargers.

2.4 Soot formation modelling

Mainly three models are used, the two-step empirical soot model, the eight-step phenomenological model and the Complex-chemistry coupled phenomenological soot model. These three models have completely different approaches to simulate the soot formation. A brief review will be made, and further details can be found in the related articles.

At the first COMODIA conference in Tokyo in 1985, Hiroyasu (Hiroyasu, 1985) reviewed the soot models which had been published between 1962 and 1984 (Hiroyasu and Kadota, 1976). Among these, the two-step empirical model from Hiroyasu et al (Hiroyasu et al., 1983) is the most-well known and used due to its simplicity. In this model only two reactions are considered, the soot formation which is linked directly to the fuel vapour molecules and the soot oxidation by O_2 .

At the third COMODIA conference at Yokohama in 1994, Fusco et al, (Fusco et al., 1994) proposed the eight step phenomenological soot model for diesel studies. They suggested relaxing the strong tie between fuel vapour molecules and soot by introducing two intermediate species, the soot precursors and the growth species. This model also includes the particle inception, particle coagulation, surface growth, and surface oxidation.

At the fifth COMODIA conference at Nagoya in 2001, Tao et al, (Tao et al., 2001) presented the complex-chemistry coupled phenomenological soot model, a chemical mechanism which couples the phenomenological soot model with complex chemistry for gas-phase soot precursor formation and oxidation. This model involves 65 species in 268 reactions. As the chemical mechanisms are complex, they introduce many uncertainties and also computational time. Tao et al, (Tao et al., 2005), made the comparison between the Sandia's conceptual model and these three soot formation models. The two-step empirical soot model can be easily implemented in CFD codes and matches the experimental results via a correction on the coefficients but this does not agree with the Dec's model. To obtain more details and accuracy, the two other models are preferable.

The actual state-of-the art models can be resolved by Direct Numerical Simulation (DNS) or by Large Eddy Simulation (LES), PAH formation, soot aggregation (Bisetti et al., 2012, Mueller and Pitsch, 2012) and study soot formation under high pressures (Charest et al., 2011a, Charest et al., 2011b).

2.5 Conclusions

Soot, these carbon nanoparticles, which are the product of combustion too rich in fuel, can be found everywhere: flame, atmospheric pollution, engine exhausts. Soot particles have already been well characterized (properties, structure, formation). The formation paths from molecules to nuclei and the processes leading to agglomerates described. In the recent years, investigations have been carried out to understand the soot formation in Diesel engines. The study of the parameters influencing soot formation is a key to reduce the particulate emissions in internal combustion engines. The soot formation modelling has become a challenge. The CFD codes are more and more realistic but need accurate data to be validated.

3 CHAPTER III: SOOT MEASUREMENT TECHNIQUES

Several techniques exist for soot investigations. Measurements can be an in-situ or ex-situ, intrusive or non-intrusive. Industrials, especially in the automotive, commonly use ex-situ measurements beside researchers, in the aim to further understand the processes of soot formation, study in a non-intrusive way soot in situ the flame by mean of optical diagnostics. The different optical diagnostic applied in this work as long as the different existing optical technique and calibration methods related to soot measurement are reviewed in this chapter.

3.1 *Laser-induced incandescence*

As the name “Laser-Induced Incandescence” (LII) suggests this technique is based on the incandescence signal induced by a laser excitation. Soot particles are heated up by a short laser pulse of a few nanoseconds duration. The particle temperature increases significantly (~ 4000 K) above the initial gas and initial particle temperature (~ 1600 K). The strong incandescence signal radiated by the soot particles corresponds to the broadband radiation of a grey-body, emission governed by Planck’s radiation law (Figure 3-1).

In 1977, Eckbreth was the first scientist to recognise the interaction between laser and carbon particles (Eckbreth, 1977). However the real pioneer of the laser-induced incandescence technique was Melton (Melton, 1984a). Melton was the first to exploit its potentiality as a powerful diagnostic tool for soot concentration measurement and particle sizing. It is only recently that this method has been used for soot investigation (visualisation) in an optical diesel engine by Dec and co-workers (Dec et al., 1991). However, it was not until 1995 and 1996 that particle sizing was achieved by two different research groups (Roth and Filippov, 1996, Will et al., 1995b). Since, the technique has continually improved and plethorically applied for different conditions. Laser-Induced Incandescence (LII) has evolved over the last two decades, into a particularly attractive technique that offers the possibility of accurate and spatially resolved soot volume fraction and particle size measurements. This technique has been developed for in-situ spatially and temporally resolved measurements of soot concentration and had been applied into different conditions, from flame (Melton, 1984b) to engine (Dec et al., 1991, Bladh et al., 2006b).

The spectral radiance $E_{b,\lambda}$ for a black-body is given by the Planck's radiation law:

$$E_{b,\lambda}(T) = \frac{2hc^2}{\lambda^5} \times \frac{1}{\left[e^{\left(\frac{hc}{\lambda kT}\right)} - 1 \right]} \quad \text{Equation 11}$$

$E_{b,\lambda}$ spectral radiance [$\text{W}\cdot\text{m}^{-3}\cdot\text{Sr}^{-1}$]

The spectral radiance of a grey-body corresponds to the expression of a blackbody however multiplied by the soot emissivity.

$$E_{g,\lambda}(T) = \varepsilon_{\lambda_{em}} \times E_{b,\lambda}(T) \quad \text{Equation 12}$$

The emissivity is link to the refractive index function by the following expression:

$$\varepsilon_{\lambda_{em}} = \frac{\pi d_p E(m)}{\lambda_{em}} \quad \text{Equation 13}$$

At the temperature T , a particle of diameter d_p radiates in 4π steradian at the wavelength λ an incandescence signal equals to:

$$LII(\lambda) = \frac{8\pi c^2 h}{\lambda^6} \cdot \frac{1}{\left[e^{\left(\frac{hc}{\lambda kT}\right)} - 1 \right]} dp^3 E(m) \quad \text{Equation 14}$$

Depending on the black-body temperature, the radiance has a maximum at a specific wavelength determinable via the Wien's law:

$$\lambda_{\max}(T) = \frac{h \cdot c}{4.9561 \cdot K \cdot T} \quad \text{Equation 15}$$

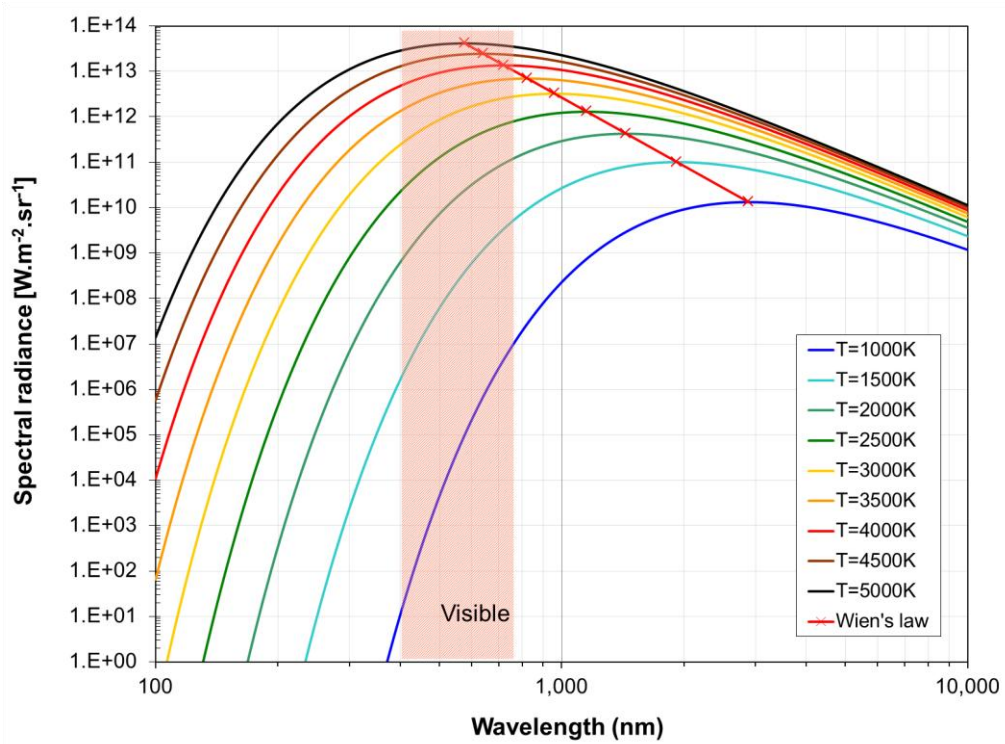


Figure 3-1 – Spectral radiance of a blackbody for different temperatures

The quantity of soot is often defined by the soot volume fraction f_v which is the unit of soot volume per unit of gas volume. It is related to the number density N and the volume-mean diameter of the soot particles by:

$$f_v = \frac{\pi}{6} N d_p^3 \quad \text{Equation 16}$$

As LII signal is proportional to the quantity of soot depending on their size, diameter distribution and number (Melton, 1984b, Smallwood et al., 2002, Snelling et al., 2005a), the LII signal at the peak can be expressed as:

$$LII = C_1 \int_0^{\infty} N_p f(d_p) \left(\frac{d_p}{2} \right)^x dd_p \quad \text{Equation 17}$$

C_1 Constant value

d_p soot particle diameter

N_d particle number density (number of particles by volume unit)

$f(d_p)$ function of particle size distribution

x $x=3+0.154 \times \lambda_{det}^{-1}$ with λ_{det} the detection wavelength (unit in μm)

Melton was the first to demonstrate the diameter dependence of the incandescence signal, assuming that laser fluence is high enough for the sublimation to be the mean heat transfer loss. In publications, the value of x has often been considered equal to 3 in order to simplify the equation and admit the incandescent signal proportional to the soot volume fraction.

The usefulness of the LII for 2D imaging of soot volume fraction was used first by Loye 1990 and Dec 1991 (Dec et al., 1991, zur Loye, 1990). In their works, they demonstrated the efficiency of the method when the background luminosity and the elastic scattering from liquid droplets are suppressed. They considered the LII signal as only proportional to soot volume fraction. Later experimental investigations (Quay et al., 1994b, Bengtsson and Alden, 1995) have confirmed this approximation between the LII signal and the soot volume fraction. Recent work shows (Crosland et al., 2011) the possible high spatial resolution and technique accuracy that can offer PLII to measure soot volume fraction.

Particle sizing using time-resolved LII technique is based on the energy balance and more especially on resolving the cooling rate of the particle. The mean cooling process after a low fluence laser pulse at atmospheric or high pressure is the conduction heat loss from particles to the surrounding gas. The overall cooling of a particle can be related to its size. Larger particles cool faster than the smaller ones due to a smaller surface area to volume ratio difference.

At high fluence, the particle cooling process is dominated by sublimation shortly after the laser pulse, for particle temperature sufficiently high (superior to 3800 K). Particles cool down and the heat conduction mechanism quickly becomes more important than sublimation. The LII signal comes from the radiation heat lost, and it is indeed a negligible mechanism in the cooling heat transfers compared to the others at atmospheric and higher pressures however not negligible at very low pressure conditions (Beyer and Greenhalgh, 2006).

Time-resolved LII has also been used as a powerful tool to characterize the primary particle diameter of soot, black carbon or ashes. However, the particle sizing can be applied to non-carboneous nano-particles, as long as the matter does not sublime at high temperatures and can radiates like a black or grey body. Studies had also been carried

out on iron, silver, manganese oxide and titanium particles (Kock et al., 2005, Filippov et al., 1999, Lehre et al., 2005, Cignoli et al., 2009) or on carbon nanotubes and nanofiber (Vander Wal et al., 2002).

The LII signal is dependent on gas temperature and pressure. The pressure effect on LII signal had been experimentally studied (Hofmann et al., 2003) as well as optimal excitation and detection conditions (Vander Wal, 1998, Vander Wal et al., 1996).

This technique have been applied for different types of flame, atmospheric laminar diffusion flame (Boiarciuc et al., 2006), in a pressurized vessel (Pickett and Siebers, 2004), in engine (Kock et al., 2006, Bladh et al., 2006a, Boiarciuc et al., 2006) or at exhaust conditions (Di Iorio et al., 2005). However in an internal combustion chamber, the conditions are less favourable than an atmospheric flame or a pressurized vessel. More attention must be given to the physical processes for laser-heated soot particles. The operating conditions in an internal combustion engine can vary over a large range of temperature and pressure during the engine cycle, the uncertainties in the relation between the LII signal strength and these different parameters may introduce uncertainties in measurements. Many research groups are working on it, to improve the LII in better quantitative and accurate diagnostic, especially in an internal combustion engine. (For example, investigations on the dependence between pressure, temperature and LII signal or model of soot temperature decrease). The interest in the model has increased with the fact that particle sizing can be estimated by time decay of time-resolved LII signal (Will et al., 1995a). Since this time, the comprehension of heat conduction has been improved. The heat conduction is the main cause of soot particle cooling after laser heating up. The treatment of the heat conduction in various environments including those encountered in engine, has been reviewed by Liu et al.(Liu et al., 2006b).

The theory of particle sizing is based on the energy balance and on the fact that the smallest particles cool down faster than the largest ones, after heating up by the laser pulse. The two-colour time resolved LII is used to determine the soot temperature by pyrometry.

3.1.1 Time-resolved LII

A recent technique is to measure temporally the soot incandescence signal during the heating-up by a laser pulse and cooling processes of the particles (Melton, 1984b, Will et al., 1995b, Castaldi et al., 1996). For this, a photomultiplier records the signal with a resolution near the nanosecond. Recording the LII decay signal allows particle sizing as the cooling rate is dependent on the particle's surface, the smaller the particle diameter, the higher is the cooling rate.

However the main difficulty is to determine the relation between particle size and heat transfers. Many models have been developed to compute the decay of the particle temperature. The mean diameter estimation is strongly dependent on the model and parameters used. All of the models are based on solving the energy balance. The soot internal energy must be equal to the different energies gained and lost, mainly heat conduction, vaporization, laser energy absorption and radiation. A later chapter is dedicated to the description of the different theoretical models used according to experimental conditions.

Each model is based on manifold hypothesis and more or less takes into consideration different physical processes. The comparison of these different models shows significant variation on the computed temperature decay i.e. LII signal (Michelsen, 2006). Therefore, some improvements are needed to go through an unique model.

Soot particle temperature rised up around of 4000 K, the sublimation of the particles will cause a heat and mass loss. This process is also temperature and pressure dependent. The most well-known model incorporating the pressure dependence was created by Kock et al (2002, 2003). This model was used recently for particle sizing in combustion engines by different research groups (Bougie et al., 2006, Boiarciuc et al., 2006).

To avoid the sublimation effect, the laser fluency must remain low. If the soot temperature does not exceed approximately 3800 K, the sublimation is supposed to not strongly reduce the particle's diameter. However if the soot particles reach higher temperature, the particle's diameter value obtain via the model will be skewed.

3.1.2 Two-colour time-resolved LII

The particular approach of the two-colour time resolved laser-induced incandescence (2C-TiRe-LII) consists to record simultaneously the incandescence signal at two different wavelengths in order to extract the soot temperature from two-wavelength pyrometry technique. The temperature is used thereafter as an initial input parameter for the heat transfer models and to compute soot volume fraction. The 2C-TiRe LII set-up is similar to the Time-resolved LII but with the addition of a second photomultiplier and a filter. The 2C-TiRe-LII signal can be recorded only for a small measurement volume due to the high frame rate needed to record the temporally signal. In this small measurement volume, the laser-heated particles temperature is considered constant and soot volume fraction and particle size (for particle sizing, see TiRe-LII and theoretical model) can be determined. The technique is used to calibrate the soot volume fraction and particle size and is further detailed in the calibration paragraph.

Temperature measurement by two-colour pyrometry

Soot particle temperature measurement is based on the broadband soot radiation. The radiation spectrum of soot is considered such as a grey body one. The intensity of black or grey body radiation depends on the temperature and the considered wavelength. The mathematical relation is described by Planck's equation:

$$E_{b,\lambda}(T) = \frac{C_1}{\lambda^5 \left[e^{\left(\frac{C_2}{\lambda T}\right)} - 1 \right]} \quad \text{Equation 18}$$

Where :

$E_{b,\lambda}$ spectral radiance of a black body at temperature T [$\text{W}\cdot\text{m}^{-3}$]

λ wavelength [m]

T temperature [K]

C_1 first Planck's constant equal to $3.7418 \cdot 10^{-16} \text{ W}\cdot\text{m}^2$

C_2 second Planck's constant equal to $1.4388 \cdot 10^{-2} \text{ m}\cdot\text{K}$

By acquiring the soot luminescence at two different wavelengths, the temperature of equivalent black body can be estimated:

$$T = \frac{\frac{hc}{k} \left(\frac{1}{\lambda_{R2}} - \frac{1}{\lambda_{R1}} \right)}{\log \left(\frac{LII_signal(\lambda_{R1}) \eta(\lambda_{R2}) \lambda_{R1}^6 E(m)_2}{LII_signal(\lambda_{R2}) \eta(\lambda_{R1}) \lambda_{R2}^6 E(m)_1} \right)} \quad \text{Equation 19}$$

Having the particle temperature and the LII signal, gives the possibility to calculate the soot volume fraction (Smallwood et al., 2002):

$$f_V = \int_{d_{p1}}^{d_{p2}} \frac{N_p \pi d_p^3}{6} f(d_p) dd_p \quad \text{Equation 20}$$

And can be expressed as:

$$f_V = \frac{LII_signal(\lambda)}{\eta(\lambda) W_b} \frac{\lambda^6 \left(e^{\frac{hc}{k\lambda T}} - 1 \right)}{12\pi C^2 h E(m)} \quad \text{Equation 21}$$

The main source of uncertainty to determine the temperature and F_v comes from the refractive index function.

3.2 Elastic light scattering

The scattering of the laser signal is due to the elastic collisions between photons and soot particles. The detected signal from the Rayleigh scattering is proportional to total density number. As the Rayleigh scattering arises from the electromagnetically induced dipole moment associated with individual molecules, the light is scattered instantaneously at the same wavelength of the laser. The scattered light is detected from the measurement volume within a particle cloud. The incident light and the scattered light are reduced via extinction on their paths. The scattered power detected can be expressed as:

$$P_{Scat} = V e^{-\int_{L_1} K_{ext} dx} e^{-\int_{L_2} K_{ext} dx} \int_A I_{scat} dA \quad \text{Equation 22}$$

L_1 and L_2 being the path lengths in and out and I_{scat} , the incident intensity.

Scattering for incident light perpendicularly polarised to the scattering plane by a small particle is:

$$I_{Scat} = \frac{\pi^4}{\lambda_{laser}^4} E(m) \times n_d \int_0^{\infty} P(d_p) d_p^6 dd_p \quad \text{Equation 23}$$

Calculations are based on isotropic spheres which are much smaller than the wavelength of the incident light to fall in the Rayleigh regime. The full theory can be found for example in Kerker ((Mie, 1908, Van de Hulst, 1957, Kerker, 1969) .

In the Rayleigh regime, the scattering light is given by (Kerker, 1969, Rayleigh, 1871):

$$I_{Ray} = CI_0 N \frac{d\sigma_{Ray}}{d\Omega} \Omega L \quad \text{Equation 24}$$

C Calibration constant, including the efficiency of the optical system and the quantum efficiency of the detector

I_0 Laser energy

N total particle number

W solid angle of the receiving optics

L length of the observed scattering volume

The power detected by the sensor is equal to:

$$P_{Scat} = C_{cal} E(m) \frac{n_d d_p^6}{\lambda_{laser}^6} \quad \text{Equation 25}$$

C_{cal} Calibration constant, including the efficiency of the optical system and the quantum efficiency of the detector

The soot particles are assumed to be ideally spherical, but it has been experimentally shown that they are indeed an agglomeration of primary particles. The scattered signal from agglomerate differs from a group of free primary particles.

Therefore the signal is not only dependent on the sphere diameter but also on the number of particle contained in the agglomerate and its shape. The intensity of the scattering signal is also dependent on the collection angle for agglomerates recently this relation has been used to obtain information on the number of particle s in agglomerates and soot aggregate information. The light scattering is described by the Rayleigh-Debye-Gans theory for fractal aggregates (RDG-FA) (Chakrabarty et al., 2007, Farias et al., 1996). Aggregate size, expressed as radius of gyration and fractal dimension were determined by ELS (Sorensen et al., 1992, Sorensen, 2001, Jones, 2006, Santoro et al.,

1983, Santoro and Miller, 1987, Gangopadhyay et al., 1991, Puri et al., 1993, Köylü et al., 1995, Oh and Sorensen, 1997, Moosmüller et al., 2009, Chakrabarty et al., 2007, Chakrabarty et al., 2008, Cai et al., 1993, Erickson et al., 1964, Pinson et al., 1993, Oltmann et al., 2010) and spatially resolved in two dimensions (Reimann et al., 2009).

In the present study due to limiting optical access, recording the signal under different angles positions was not possible. Soot particles are not the only matter that can scatter the light. The Mie scattering from liquid spray/droplets has a much higher signal than the Rayleigh scattering of the particles.

In a combusting Diesel spray, the decomposition of fuel by pyrolysis mechanism produces relatively simple molecules which are orders of magnitude smaller than the soot particles cross sections. Therefore, the scattering signal is only generated by particulates and not by PAH in the soot area (Vogel et al., 2005, Espey et al., 1997).

3.3 LII / ELS technique

It has been shown in the previous section that the LII signal is proportional to the soot volume fraction $f_v = n_d d_p^3$. Whereas the ELS signal is proportional to $n_d d_p^6$, for particles falling in the Rayleigh regime. Therefore for a single particle the incandescence signal is proportional to the volume whereas the scattering is proportional to the surface area at the power three. Consequently, it is possible to calculate the relative value of particle diameter, corresponding to the Sauter mean diameter d_{32} .

$$d_{32} = \left(\frac{d_p^6}{d_p^3} \right)^{\frac{1}{3}} \approx \left(\frac{I_{ELS}}{I_{LII}} \right)^{\frac{1}{3}} \quad \text{Equation 26}$$

The Sauter mean diameter represents the diameter of the sphere that has the same volume to surface ratio of the particle of interest. The Sauter mean diameter is defined as

$$d_{32} = \left(\frac{d_p^3}{d_p^2} \right) \quad \text{Equation 27}$$

And the density number of soot particles can also be calculated from:

$$n_d \approx \frac{I_{LII}^2}{I_{ELS}} \quad \text{Equation 28}$$

These d_{32} and n_d values need a calibration as the ELS signal is strongly dependent on the laser fluence compared to the LII signal (ELS is much stronger than the LII signal).

Extinction is one of the common techniques used to calibrate the relative LII and ELS signals.

The ELS signal can introduce errors in the relative size because the soot particles are not the only matter that can scatter the light. Scattering from liquid fuel droplets (Mie scattering) or PAH, ash, water, metal particles, (Lee et al., 2005) is also possible.

The simultaneous recording of the Rayleigh, LII and extinction signals (RAYLIX) was previously performed to obtain spatially resolved quantitative soot volume fraction, particle diameter distribution upon burner's flame and internal combustion chamber (Diesel and gasoline) conditions. (Geitlinger et al., 1998, Geitlinger et al., 1999, Axelsson et al., 2000, Axelsson et al., 2001, Lehre et al., 2003b, Bockhorn et al., 2002, Stumpf et al., 2005, Hentschel et al., 2005, Angrill et al., 2000, Velji et al., 2010)

In the previous researches, the data obtained by combining LII and ELS techniques were calibrated by laser light extinction. However the feasibility of calibrating spatially resolved soot volume fraction by 2C-TiRe-LII was performed by Boiarciuc et al. (2005). The use of the difference of cooling time according to the diameters to obtain spatially resolved size distribution has not been really exploited. An original approach to get the spatial size distribution was to take LII pictures at different times during the particle cooling process and use the energy balance to determine the soot particle size (Will et al., 1995b, Castaldi et al., 1996). However this technique is suitable to the combustion chambers as the cooling rate is too fast, and the acquisition frequency of the camera is not fast enough to take at least two pictures in this time range.

The approach in this thesis is similar to the RAYLIX technique but using 2C-TiRe-LII to calibrate the images instead of extinction.

Particle sizes determined by 2C-TiRe-LII correspond to the primary particle d_p (Mewes and Seitzman, 1997, Snelling et al., 2000) but in LII/ELS measurement for which the volume equivalent sphere diameter D_{32} or Sauter mean diameter is the measured quantity. In this work, particles are assumed to be spherical and not aggregated, the diameter determined by 2C-TiRe LII is used to calibrate the qualitative value obtained by LII/ELS measurements.

3.3.1 Aggregate effects

Aggregation of the particles is an issue for LII/ELS technique accuracy reliability. The scattering from agglomerated particles is not equal to the sum of the scattering of single primary particles. Therefore the signal intensity is dependent on the equivalent diameter of the agglomerate and then by the number of primary particles that count the agglomerate (Sorensen, 2001).

The incandescent signal is reformulated as:

$$I_{LII} \propto N_a n d_p^3 \quad \text{Equation 29}$$

If theoretically the incandescence intensity does not differ due to agglomeration however the shielding effect due to the reduced contact surface with ambient gas decrease the cooling effect.

Large agglomerates can reach the limit of the Rayleigh regime. The agglomeration has a major effect on the scattering:

$$I_{ELS} \propto N_a n^2 d_p^6 \quad \text{Equation 30}$$

The scattering is therefore function of the number of particles in the agglomerate at the second power and particle diameter at the sixth power.

$$\left(\frac{I_{ELS}}{I_{LII}}\right)^{\frac{1}{3}} = n^{\frac{1}{3}} d_p = d_{pe} \quad \text{Equation 31}$$

In the case of agglomeration, the equivalent diameter d_{pe} would differ by a coefficient $n^{\frac{1}{3}}$ compared to the case of considering only primary particles. This would introduce high variations across the flame as the agglomeration of the particles increases with time or path in the flame (Will et al., 1996) for example by a factor 2.15 from $n=1$ to $n=10$ or by 4.64 from $n=1$ to $n=10$.

The research community has shown an increasing interest for the last few years on the determination by optical diagnostics of soot aggregate parameters and fractal dimensions thanks to their scattering angle dependence (Charalampopoulos and Chang, 1991, Chakrabarty et al., 2007, Burr et al., 2010, Snelling et al., 2011, Oltmann et al., 2010) or coupling ELS with LII (Reimann et al., 2009, Snelling et al., 2011) As scattering signal is stronger than incandescence signal, lasers for the scattering techniques can be used at low power, avoiding sublimation of particles. In the approach used in this work, only one laser pulse is used for the scattering and the incandescence signal, the laser fluence being high in order to strongly heat-up the particle.

Agglomerates under high temperatures and at the temperatures reached, subject to high sublimation, annealing and carbon structure modifications. Assumption was made that van der Waals bonds linking the primary particles together cannot resist to the high impulsion/charge induced by the laser pulse and break up. The disaggregation prevails over the sublimation at intermediate fluence around $0.07 \text{ J}\times\text{cm}^{-2}$ at 532 nm wavelength (Filippov et al., 1999, Beyer and Greenhalgh, 2006). However the experimental results from Michelsen (Michelsen et al., 2007b) controverts the previous assumptions, suggesting that agglomerates do not disaggregate completely but depending on the laser fluence either break up into smaller aggregates or; primary particles change structures, become hollow and the bond considered covalent.

The soot aggregate shape has also an effect on the cooling transfer. The cooling rate of primary particles is not equal to the cooling rate of one agglomerate containing the same number of primary particles. The agglomerate surface being comparatively lower, the conduction rate is therefore reduced, this effect is commonly called shielding effect and has for effect to shift the results towards larger particles.

3.4 Soot analysis by TEM or SEM Images

The analysis of soot particles via microscope gives an image of the aggregates and primary particles therefore size and structure of the primary particles, shape of the agglomerate, numbers of particles per agglomerate and particle size distribution can be studied.

Soot particles are taken from the flame via thermophoresis and analyse afterwards by transmission electron microscopy i.e. TEM ((Dobbins and Megaridis, 1987, Cai et al., 1993, Köylü et al., 1995, Vander Wal, 1998, Vander Wal et al., 1996, di Stasio, 2001, Wentzel et al., 2003, Jung et al., 2004, Zhao et al., 2007) or scanning electron microscopy i.e. SEM (Dobbins and Megaridis, 1987, Van Gulijk et al., 2004, di Stasio, 2001, di Stasio et al., 2002). This technique is an ex-situ technique, even if soot is probed in the flame, the study is performed in different conditions and locations therefore cannot be considered identical to the original sampled soot.

3.5 Laser-induced fluorescence

Laser-induced fluorescence is an laser diagnostic used to detect and visualize a specific chemical specie such as for example in a flame: OH (Kosaka et al., 1996, Dec and Coy, 1996) or CO₂ (Bessler et al., 2003). Knowing where and when the soot oxidizing species are produced can help to understand the soot reduction. The fluorescence of C₂, from the soot sublimation induced by laser, can be used to visualise the presence of soot (Aldén et al., 1982, Bengtsson and Aldén, 1989, Bengtsson and Aldén, 1995, Hult et al., 2002, Bengtsson and Aldén, 1990, Westblom et al., 1991).

3.6 Calibration

Laser-induced incandescence is a technique which gives the relative value of soot volume fraction. To obtain an absolute value, a calibration is needed. Previous investigations commonly use light extinction calibration (Quay et al., 1994b, Axelsson et al., 2001). A recent method applied by the research of the NRC (Smallwood et al., 2002, Snelling et al., 2005a), show the possibility of using the LII at two detection wavelengths as a self-calibrated technique. The determination of the heated particle temperature by the ratio of the two LII signals provides information on the soot concentration. However, this technique also needs a calibration to be accurate. The optical efficiency of the detection device has to be well-know and it is usually carried out via a calibrated lamp.

Several techniques can be used for LII calibration but many are not well-adapted to engine conditions such as the Cavity-Ring-Down Spectroscopy (CRDS) technique which is suitable to laminar diffusion flame. The CRDS technique records the decay of the laser beam after several returns in the flame, used as cavity centre between two mirrors. The CRDS method is able to measure small soot volume concentration (Choi et al., 1995, Schoemaeker Moreau et al., 2004, Desgroux et al., 2008, Bouvier et al., 2007). Extinction and gravimetric technique are the most used ones to calibrate the LII signal (Choi et al., 1995).

3.6.1 Light extinction

Extinction is the main method to calibrate a LII signal. It is based on the fact that the absorption of the laser depends on the soot concentration. Beer's law (or Lambert-Beer's law) can be applied to determine the corresponding soot volume fraction (Vander Wal and Weiland, 1994, Axelsson et al., 2000, Axelsson et al., 2001, Geitlinger et al., 1998, Bryce et al., 2000, Zhao and Ladommatos, 1998, Choi et al., 1995).

The extinction coefficient K_{ext} is known from the Beer's law:

$$K_{ext} = \frac{1}{l} \ln \frac{I_0}{I} \quad \text{Equation 32}$$

I_0 incident light intensity [$\text{W}\cdot\text{m}^{-2}$]

I transmitted light intensity [$\text{W}\cdot\text{m}^{-2}$]

l optical path length [m]

K_{ext} extinction coefficient [m^{-1}]

Two negative points can be noticed. The first one is the soot volume fraction cannot be very high, that is why some researchers have been using a specific fuel called low-sooting fuel or too low otherwise the ratio of the two signals is close to one. In the case of low absorption, Cavity-ring down spectroscopy, technique based on increasing the optical length by reflecting the laser beam several times in the zone of interest. The second one is that the length of the light path must be determined experimentally. Then this technique needs to record the flame luminosity at 90° of the laser sheet (which can be a problem in some experiments).

Equation 32 can be expressed as:

$$\frac{I}{I_0} = e^{-\int_0^L k_{ext} dx} \quad \text{Equation 33}$$

The extinction coefficient is expressed as:

$$k_{ext} = \frac{\pi}{4} n_d \int_0^\infty Q_{ext} f(d_p) d_p^2 dd_p \quad \text{Equation 34}$$

n_d particle concentration [m^{-3}]

Q_{ext} efficiency of the particle extinction

d_p particle diameter [m]

$f(d_p)$ particle size distribution function

$f(dp)$ must fit this condition:

$$\int_0^{\infty} f(d_p) dd_p = 1 \quad \text{Equation 35}$$

According the Rayleigh regime, Q_{ext} can be expressed by:

$$Q_{ext} = 4x \operatorname{Im} \left(\frac{m^2 - 1}{m^2 + 2} \right) = 4xE(m) \quad \text{Equation 36}$$

m refractive index of soot

$$m = n + ik \quad \text{Equation 37}$$

n real component of the refractive index of soot

k imaginary component of the refractive index of soot

The refractive index is the main source of error and inaccuracy for the determination of the soot volume fraction.

The choice of this value is crucial; the variation can be up to 40%, depending on the used value. In the literature, many values are expressed (Dalzell and Sarofim, 1969) (Lee and Tien, 1981, Habib and Vervisch, 1988, Chang and Charalampopoulos, 1990).

$$E(m) = \operatorname{Im} \left(\frac{m^2 - 1}{m^2 + 2} \right) \quad \text{Equation 38}$$

And x equals to:

$$x = \frac{\pi d_p}{\lambda} \quad \text{Equation 39}$$

The soot volume fraction can be expressed as:

$$f_v = \frac{-k_{ext}}{\frac{6\pi}{\lambda} \operatorname{Im} \left(\frac{m^2 - 1}{m^2 + 2} \right)} \quad \text{Equation 40}$$

And can be simplified to:

$$f_v = \frac{\lambda}{6\pi l E(m)} \ln \left(\frac{I}{I_0} \right) \quad \text{Equation 41}$$

The setup for laser light extinction is relatively simple. A filter is used to prevent the recording of the flame luminosity which otherwise would cause interferences with the measurement. The filter is chosen to allow only the signal at the laser wavelength to go through; therefore a narrow band-pass centred at laser wavelength can be used.

The excitation wavelength usually used is 632.8 nm because of the cost of a Helium-neon laser compared to the other ones (Schoemaeker-Moreau, 2002, Choi et al., 1995). But other wavelengths can be used such as 674 nm (Konsur et al., 1999), 532 nm with a pulsed Nd:YAG laser (Axelsson et al., 2001). The Abel inversion can correct the mono-dimensionality of the measure to represent a bi-dimensional extinction in the flame and obtain a picture of soot concentration (De Iuliis et al., 1998, De Iuliis et al., 2005, Cignoli et al., 2001, Kent and Honnery, 1990, Dasch, 1992, Snelling et al., 1999).

Calibration by extinction has been performed in combustion chambers and technique has been reviewed (Zhao and Ladommatos, 1998). From extinction measurement, soot formation under different EGR conditions have been investigated (Hentschel and Schindler, 1996); and soot evolution in Diesel jet was quantitative studied (Pickett and Siebers, 2004).

The light extinction has four main defaults; the first one is the accuracy which is dependent of the uncertain value of the refractive index of soot. However this issue is recurrent in most of the soot laser diagnostics / optical calibration. The second default is the non-spatial resolution; the third is the calibration has to be performed separately from LII experiment which is an issue in hardly repeatable experiments. The last one is the extinction path must be known, that is an issue in an optical chamber as some volume of the chamber are out of field view.

But this technique has also many advantages, such as the cost and simplicity of the setup, the knowledge of the particle size distribution is not necessary and the possibility of combining it with other laser diagnostics.

The only approximation is on the value of the refractive index. Dalzell and Sarofin (Dalzell and Sarofin, 1969), Lee and Tien (Lee and Tien, 1981), Chang and Charalampopoulos (Chang and Charalampopoulos, 1990) and more recently (Van-Hulle et al., 2002, Krishnan et al., 2001) have worked on the determination of this value. It can be considered between $m = 1.48 - i \times 0.77$ and $1.90 - i \times 1.55$. The deriving $E(m)$

value will greatly affect the results. Soot volume fraction can decrease by a factor three if the second value is used instead of the first one.

The laser light can be attenuated by scattering and absorption by the different compounds in the combustion chamber such as air, dust and liquid droplets (fuel and, water coming from condensation of water vapour) or the soot particles. The optical set-up should minimize as much as possible the Schlieren and shadow graphic effect.

3.6.2 Self-calibration

The self-calibration or auto-compensating laser-induced incandescence (AC-LII) has been performed by Snelling (Snelling et al., 2005b) upon a laminar diffusion ethylene flame at atmospheric pressure, following by Thomson in 2006 (Thomson et al., 2006) at high pressures (up to 4.0 MPa) in a non-premixed methane/air flame and at an engine exhaust (Smallwood et al., 2002).

The idea of this LII technique is that the soot volume fraction can be estimated if the soot temperature and the absolute spectral intensity of the incandescence signal emitted from the laser heated soot particle are measured.

The temperature is needed to compute the theoretical spectral emission per unit volume of soot.

The calibration factor of the detectors is determined by:

$$\eta(\lambda) = \frac{V_{cal}(\lambda)}{R_s(\lambda, T)} \quad \text{Equation 42}$$

Where:

$\eta(\lambda)$ calibration factor, [$\text{m}^3 \cdot \text{Sr} \cdot \text{V} \cdot \text{W}^{-1}$]

$V_{cal}(\lambda)$ Voltage of signal recorded from the calibration lamp, [V]

$R_s(\lambda, T)$ spectral radiance of the lamp, [$\text{W} \cdot \text{m}^{-3} \cdot \text{Sr}^{-1}$]

The calibration factor η takes in account the collection efficiency of the system and the sensitivity at the detection wavelength λ .

The radiation by a single particle can be expressed as:

$$P_p(\lambda) = \frac{8\pi^3 c^2 h}{\lambda^6} \left(e^{\frac{hc}{\lambda T}} - 1 \right)^{-1} d_p^3 E(m_\lambda) \quad \text{Equation 43}$$

Where:

$P_p(\lambda)$ spectral radiant flux radiated by a single particle, [W]

c speed of light, [m.s⁻¹]

h Planck's constant, [J.s]

k Boltzmann's constant, [J.K⁻¹]

T particle temperature, [K]

$E(m_\lambda)$ refractive index

The particle number is defined as:

$$N_p = n_p (w_b A_p) \quad \text{Equation 44}$$

Where:

N_p particle number

n_p concentration of primary particles in the probed volume

w_b equivalent width of the laser sheet, [m]

A_p cross-sectional area of the probed volume and the viewed by the detection system

In the probed volume, the spectral radiance can be expressed as:

$$L_p(\lambda) = \frac{P_p(\lambda) n_p w_b}{4\pi} \quad \text{Equation 45}$$

$L_p(\lambda)$ equivalent spectral radiance for the particles in the probed volume, [W.m⁻³.Sr⁻¹]

The collecting system is calibrated via a calibration lamp of know radiance, temperature or irradiance.

The calibration factor can be expressed by:

$$\eta(\lambda) = \frac{V_{cal}}{L_{lamp}(\lambda)} \quad \text{Equation 46}$$

$V_{cal}(\lambda)$ recorded signal from the calibration lamp, [V]

$\eta(\lambda)$ calibration factor

$L_{lamp}(\lambda)$ Spectral radiance of the calibration lamp [$\text{W}\cdot\text{m}^{-3}\cdot\text{sr}^{-1}$]

The spectral radiance of the calibration lamp is obtained from calibration data. The spectral radiance can be obtained from tungsten emissivity (Pon and Hessler, 1984) and the lamp temperature when known.

The calibration factor defines difference between the signal recorded and the theoretical signal emitted. The calibration factor can therefore be expressed for the incandescent particles as:

$$\eta(\lambda) = \frac{LII_{\text{exp}}}{L_p(\lambda)} \quad \text{Equation 47}$$

This relation can be expressed for two wavelengths λ_1 and λ_2 :

$$\frac{LII_{\text{exp}}(\lambda_1)}{LII_{\text{exp}}(\lambda_2)} = \frac{L_p(\lambda_1)\eta(\lambda_2)}{L_p(\lambda_2)\eta(\lambda_1)} \quad \text{Equation 48}$$

$$\frac{LII_{\text{exp}}(\lambda_1)}{LII_{\text{exp}}(\lambda_2)} = \frac{\lambda_2^6 \left(e^{\frac{hc}{k\lambda_2 T}} - 1 \right) E(m_{\lambda_1})}{\lambda_1^6 \left(e^{\frac{hc}{k\lambda_1 T}} - 1 \right) E(m_{\lambda_2})} \quad \text{Equation 49}$$

$$\frac{LII_{\text{exp}}(\lambda_1)}{LII_{\text{exp}}(\lambda_2)} = \frac{\lambda_2^6 \left(e^{\frac{hc}{k\lambda_2 T}} - 1 \right) E(m_{\lambda_1}) \eta(\lambda_1)}{\lambda_1^6 \left(e^{\frac{hc}{k\lambda_1 T}} - 1 \right) E(m_{\lambda_2}) \eta(\lambda_2)} \quad \text{Equation 50}$$

Then, solving this equation is possible. T is the only one unknown, others values are known, estimated or approximated.

$$T = \frac{hc}{k} \left(\frac{1}{\lambda_2} - \frac{1}{\lambda_1} \right) \frac{1}{\log \left(\frac{LII_{\text{exp}}(\lambda_1)\eta(\lambda_1)\lambda_1^6 E(m_{\lambda_2})}{LII_{\text{exp}}(\lambda_2)\eta(\lambda_2)\lambda_2^6 E(m_{\lambda_1})} \right)} \quad \text{Equation 51}$$

Particle soot volume fraction is defined as:

$$f_v = n_p \frac{\pi d_p^3}{6} \quad \text{Equation 52}$$

And can be expressed as:

$$f_v = \frac{LI_{\text{exp}}(\lambda)}{\eta(\lambda)w_b} \frac{\lambda^6 \left(e^{\frac{hc}{k\lambda T}} - 1 \right)}{12\pi c^2 h E(m_\lambda)} \quad \text{Equation 53}$$

The main uncertainty of this method is the value of the soot volume index $E(m_\lambda)$ and even more with the use of two wavelengths. The soot refractive index increases around 20 % over the range 400 nm to 800 nm (Krishnan et al., 2001). However from Smallwood's work, the relative value of $E(m_\lambda)$ is constant over the range of the visible to the near-infrared. A sensitive analysis of the relation between the uncertainty of $E(m_\lambda)$ and the soot volume fraction gives a 1:1 correspondence, that means that 20 % of uncertainty in the magnitude of $E(m_\lambda)$ leads to 20 % of uncertainty in the computed value of the soot volume fraction.

Then, to have a good accuracy with this calibration, a correct value of $E(m_\lambda)$ is required but it still contains uncertainties.

$E(m_\lambda)$ can vary because of the temperature, the soot structure and the presence of SOF.

A minor uncertainty is the accuracy on the effective centre wavelength (for each of the two wavelengths) of the detection system (Smallwood et al., 2002). This systematic error is highest for low wavelengths, low temperatures, and large bandwidths. Smallwood et al. did not correct these values (which can be done by an iterative approach according to Smallwood et al.); error was estimated to be around 5%.

3.6.3 Gravimetric measurements

This technique is less widespread method for LII calibration but widely spread to control particle emissions in automotive. This method benefit from being independent of optical soot properties, source of major inaccuracy i.e. mainly the refractive index function (Greis et al., 2002, Vander Wal et al., 1996, Wainner et al., 1999). A sampling valve is needed to extract the soot from the combustion chamber, avoiding as much as possible any deposit on the wall. The sampled soot is in small quantity due to the short time of valve opening. This is why the sampling has to be performed on several cycles. The fast sampling valves can give average soot concentration at a given crank angle by

dumping the total cylinder volume. Soot can also be sampled from the exhaust. The sampling volume is filtered and deposited particles on are filter are weighted in order to determine the net soot mass. Then this mass can be linked to the LII signal for the calibration. The samples can be used thereafter for further analyses such as size and structure of soot particles via TEM.

3.7 *Technique assumptions*

Every optical technique comes with its assumptions and uncertainties. By coupling different techniques, this increases the number of possible errors. Errors can be related to:

- Temperature inaccuracy due to error on $E(m)$
- Particles not reaching the same temperature
- Different heat transfer models and initial input parameters
- Agglomerate effect: shielding effect (cooling reduced) and not in the Rayleigh regime
- Measurement error due to equipment
- Error on the calibration location
- Error on the spatial resolution (error on the overlaying of ELS/LII images)

Moreover, the ELS/LII technique is sensitive to the particle diameters (which can be agglomerated) while TiRe-LII is more sensitive to the primary particles. The techniques are based on different physical principles but used to determine the size of the particles.

3.8 *Conclusions*

Soot particles have always been source of interference for a various number of diagnostic. But in this work, LII and ELS techniques exploit the light scattering, absorption of the laser beam, the induced broadband radiation and the fact that the particles are small enough to fall in the Rayleigh regime. The LII and ELS techniques can provide information needed to quantify and visualize the soot formation (soot volume fraction, number density, particle size) in two-dimensions. The LII technique has recently involved into a quantitative technique for particle sizing by comparing the temporal LII decay signals obtained experimentally and theoretically. The theoretical LII signal is computed from solving the heat transfer equations. The advantage of the

two-colour time-resolved LII technique is the modelling of the LII signal during the pulse is not required, meaning that the laser fluence does not need to be known with accuracy. The disadvantage is the need to record the temporal LII signal (which decreases in a few hundred nanoseconds time or a dozen of nanoseconds for the worst extreme conditions). That requires recording the signal with good resolution with fast PMTs. However PMTs sample a small volume, so the representation in two-dimensions is not possible. The use of a conjoined technique as ELS and LII, allow getting the size distribution of the particles. A calibration, which can be performed by extinction (RayLiX) or 2C-TiRe LII, gives the possibility to obtain quantitative spatially resolved distributions of, soot volume fraction, particle size and density number (Figure 3-2).

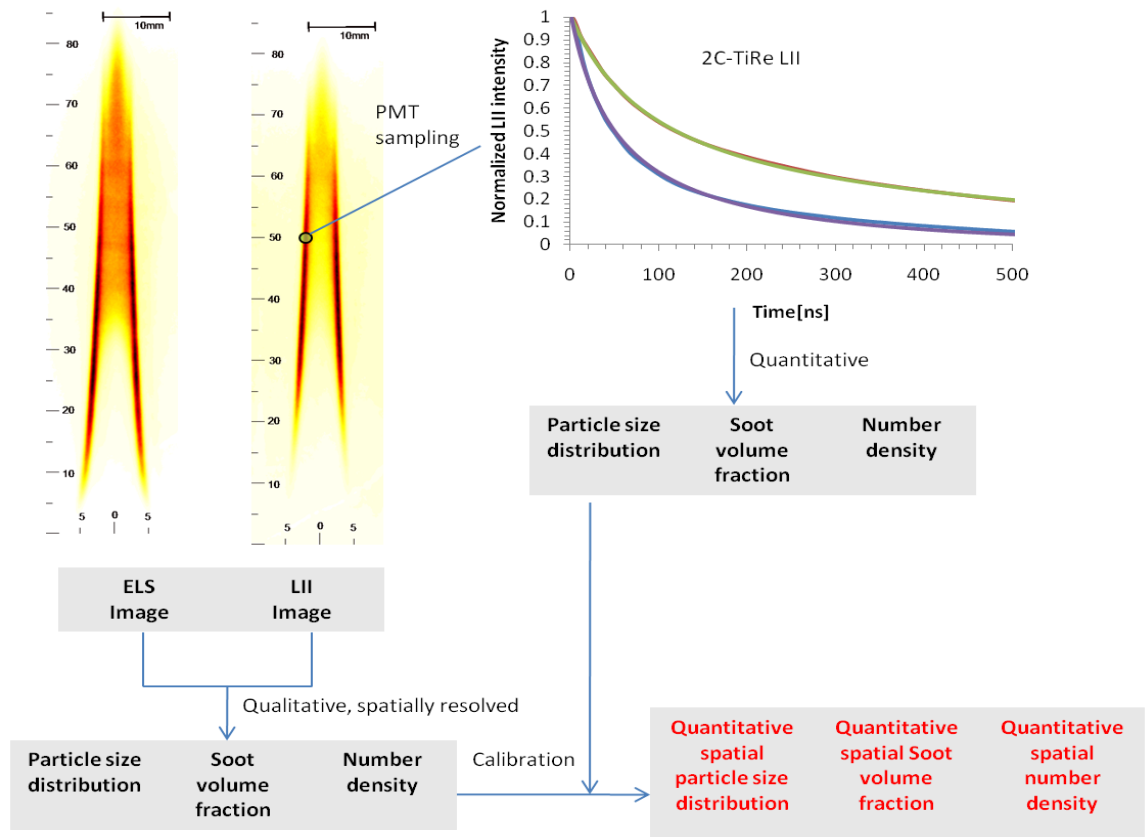


Figure 3-2 – Diagram of optical diagnostics

4 CHAPTER IV: THEORETICAL MODELS OF SOOT HEAT TRANSFER

Heat transfers are the basis of the particle sizing (Figure 4-1). The heating and the cooling processes of particles are modelled. From the theoretical temperatures obtained by solving the different heat transfers equations, the theoretical LII signal can be obtained. This signal is subsequently fitted to LII signal obtained experimentally. In this chapter the different models used are reviewed and resolved to theoretically study the effect of particle diameter on LII signal.

4.1 Theoretical models

Melton (Melton, 1984b) was the first to give a model to characterize the different heat transfers. They are four main heat transfers, absorption, sublimation, heat conduction and thermal radiation.

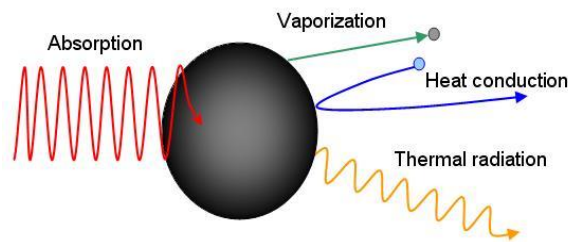


Figure 4-1 – Schematically representation of the energy balance of a laser heated particle (Will et al., 1998)

$$\dot{Q}_{abs} - \dot{Q}_{cond} - \dot{Q}_{sub} - \dot{Q}_{rad} = \dot{Q}_i \quad \text{Equation 54}$$

Q_{abs} energy absorbed by the particle

Q_{cond} energy released by conduction

Q_{sub} energy lost by sublimation

Q_{rad} energy released by radiation

Q_i internal energy of the particle

But since Melton's work, the different heat transfers have been discussed and reviewed (Schulz et al., 2006, Smallwood et al., 2001) and some new complementary processes have been added, such as oxidation and annealing of particles which were neglected in the past (Michelsen, 2003).

$$\dot{Q}_{abs} - \dot{Q}_{cond} - \dot{Q}_{sub} - \dot{Q}_{rad} - \dot{Q}_{ann} - \dot{Q}_{oxi} = \dot{Q}_i \quad \text{Equation 55}$$

Q_{ann} energy lost by annealing

Q_{oxi} energy lost by oxidation

To solve this equation, the mass balance equation is required to compute the temperature of the particle during the LII process. An example of the different energy transfer occurring for a 30 nm diameter particle in atmospheric conditions is represented in Figure 4-2. In this simulation, the particle is heated-up at more than 4000 K. Sublimation is the main cooling process at high temperatures (above 3400 K). As the temperature falls, the sublimation effect consequently decreases and for the second part of the cooling process, the heat conduction (which is a quasi-steady) overtakes the sublimation heat transfer and becomes predominant. The heat transfer from the radiation is weak compared to the other heat transfers (by at least a factor 10) and quickly decreases in time.

Several models exist to simulate the different processes (Michelsen et al., 2007a). One of them is more suitable for internal combustion purpose, by the fact that it takes into consideration the high pressure conditions. This model was presented by Kock (Kock et al., 2002, Kock and Roth, 2003) and applied in a combustion chamber of a Diesel engine to quantify the primary soot diameter.

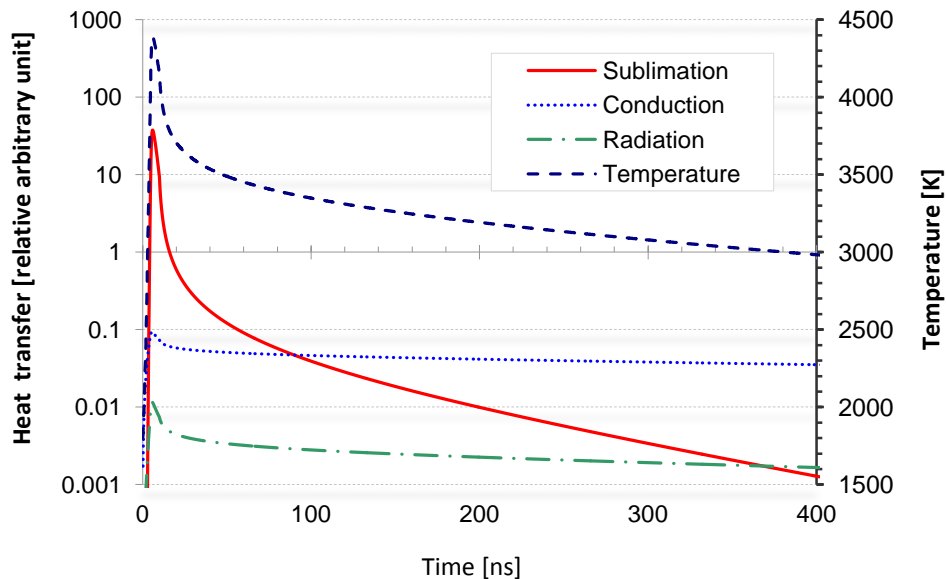


Figure 4-2 – Evolution of particle temperature and the different heat transfers during the LII process (Schraml et al., 2000)

4.1.1 Main theoretical assumptions

The main assumptions characterize the interactions between soot particles and surrounding gas. The particle is assumed to be spherical, any interaction effects between other particles or agglomerate effects are not considered (shielding effect). On agglomerates, primary particles are linked to each other. The shielding effect due to the reduced surface with surrounding gas, limits the conduction transfer.

Regime characterisation

To characterise the interaction between gas and particles, the Knudsen number Kn (dimensionless number) is used. This number is the ratio between the mean free path length of gas molecules and the particle diameter.

$$Kn = \frac{2\lambda_{MFP}}{d_p} \quad \text{Equation 56}$$

Kn Knudsen number [dimensionless]

λ_{MFP} mean free path length of the gas molecules [m]

$$\lambda_{MFP} = \frac{4}{5} \frac{\lambda_{cond} T_g}{P_g} \sqrt{\frac{m_g}{2\lambda_{cond} T_g}} \quad \text{Equation 57}$$

P_g gas pressure [$\text{N}\cdot\text{m}^{-2}$]

T_g gas temperature [K]

λ_{cond} gas thermal conductivity [$\text{W}\cdot\text{m}^{-1}\cdot\text{K}^{-1}$]

m_g mass of a single gas particle [kg]

Three regimes can be distinguished according to the value of the Knudsen number:

For $Kn \ll 1$, characterises the continuum regime.

For $Kn \approx 1$, the regime is called Knudsen regime or transient regime. It is the case for particles in the combustion chamber where the pressure is high.

For $Kn \gg 1$, characterises the free molecular regime, which corresponds to the atmospheric conditions.

4.1.2 Internal energy

The particle stocks energy, this energy is dependent on its mass and specific heat transfer. The heating of the particle increase the internal energy and decreasing during the cooling. The internal energy variation expressed by Melton (1984a) is:

$$\dot{Q}_i = \frac{d}{dt}(m_s c_s T_s) \quad \text{Equation 58}$$

And no variation of the diameter was assumed, the relation becomes:

$$\dot{Q}_i = \frac{1}{6} \pi d_p^3 \rho_s c_s \frac{dT_s}{dt} \quad \text{Equation 59}$$

ρ_s soot density [kg.m^{-3}]

c_s Soot specific heat capacity [J.K^{-1}]

But if the reduction of the particle size is taken into consideration, this decrease can be linked to the sublimation process (Kock et al., 2006):

$$\frac{dm_s}{dt} = -\dot{U}_{evap} \quad \text{Equation 60}$$

\dot{U}_{evap} Sublimation rate [kg.s^{-1}]

4.1.3 Absorption of laser light energy

The expression for the heat absorption for a single particle can be expressed as:

$$\dot{Q}_{abs} = C_a q = \frac{\pi^2 d_p^3 E(m)}{\lambda} q \quad \text{Equation 61}$$

C_a Cross section of the soot particle in the Rayleigh regime, [m^{-2}]

q laser flux, [W.m^{-2}]

$E(m)$ soot refractive index function, [-]

$$E(m) = \frac{m^2 - 1}{m^2 + 2} \quad \text{Equation 62}$$

Equation 61 is commonly used to compute the energy transferred to the particles (Melton, 1984b, Smallwood et al., 2001, Boiarciuc et al., 2006, Michelsen, 2003) and a rare accepted heat transfer equation to be unanimity accepted in the research community.

The recrystallization/annealing of the carbon atoms after the laser pulse can generate an empty space in the centre of the particle (Michelsen, 2003). The cross section must be re-expressed as:

$$C_a = (1 - X_{ann})C_a(\text{non-recrystallised}) + X_{ann}C_a(\text{recrystallised}) \quad \text{Equation 63}$$

X_{ann} recrystallised carbon mass ratio

Annealing occurs at fluence as low as 0.02 J.cm^{-2} and can strongly influence sublimation rate and emissivity. The signal decay rate is predicted to increase. Supersonic expansion of carbon clusters sublimed from the surface should occur for fluence above 0.12 J.cm^{-2} .

4.1.4 Heat conduction to the surrounding gas

As soot particles are hotter than the surrounding gas, they release heat to the surrounding gas particles. That occurs during their collisions with each other. Then heat conduction release will depend on the free-mean path of the particles. Due to partial sublimation of the particles, the particles are surrounded by carbon vapour.

Heat conduction is the main cooling process of soot particles after they have been heated up by the laser pulse. An accurate modelling of this mechanism is primary for the analysis (Particle sizing) of LII experimental data. The current models are imperfect. Liu (Liu et al., 2006a) reviewed the heat conduction modelling practice in the recent LII literature and an overview of the physics of heat conduction loss from a single spherical particle in the entire range of Knudsen number with emphasis on the transition regime, the heat conduction in engine condition are also discussed.

Heating the soot at too high temperature (more than 4000 K), will increase the sublimation process and increase the heat and mass loss. The sublimation is pressure dependent.

The best known model for taking into consideration the pressure dependence in the sublimation and heat conduction is the model by Kock (Kock et al., 2002, Kock and Roth, 2003). This model has been applied in internal combustion engine for particle sizing (Bougie et al., 2006, Boiarciuc et al., 2006).

The frequently used model (Melton, 1984b, Smallwood et al., 2001, Snelling et al., 2004, Boiarciuc et al., 2006) in free molecular regime, is the one based on McCoy and Cha (McCoy and Cha, 1974).

$$\dot{Q}_{cond, FMR} = \frac{2\pi d_p^2 \lambda_{cond} (T - T_g)}{(d_p + G \lambda_{MFP})} \quad \text{Equation 64}$$

G “geometric coefficient of heat transfer”

$$G = \frac{8f}{\alpha(\gamma + 1)} \quad \text{Equation 65}$$

With:

$f=5/2$ (Snelling et al., 2004)

α heat accommodation coefficient

γ isentropic coefficient

The isentropic coefficient is related to the specific heat of soot by:

$$\gamma = \frac{c_p}{c_v} \quad \text{Equation 66}$$

Snelling et al. use a fractal approach to take into consideration the agglomeration effect in the heat conduction. The equation 58 is rewritten as:

$$\dot{Q}_{cond, FMR} = \frac{2\pi D_A^2 \lambda_{cond} (T - T_g)}{(D_A + G \lambda_{MFP})} \quad \text{Equation 67}$$

D_A is the equivalent diameter of the sphere which has the same heat exchange surface of the corresponding aggregate.

$$D_A = \left(\frac{n}{k_{fr}} \right)^{\frac{1}{2} D_f} d_p \quad \text{Equation 68}$$

K_{fr} “Fractal constant” [dimensionless]

n number of particles per aggregate [dimensionless]

D_f fractal coefficient [dimensionless]

If there are expressions for the continuum and free molecular regime, there is not a unanimous one for the Knudsen regime.

Kock and Roth's model

This model uses the Knudsen number, to take into consideration the conditions of interaction gas/particle.

$$\dot{Q}_{\text{cond, tr}} = \dot{Q}_{\text{cond, c}} f_h(Kn_h) \quad \text{Equation 69}$$

$$\dot{Q}_{\text{cond, tr}} = 2\pi d_p \lambda_{\text{cond}} (T_p - T_g) f_h(Kn_h) \quad \text{Equation 70}$$

λ_{cond} thermal conductivity of the gas [$\text{W}\cdot\text{m}^{-1}\cdot\text{K}^{-1}$]

f_h empirical function correcting the continuum heat flux due to Knudsen effects

$$Kn_h = \frac{4\lambda_{\text{cond}}T_g}{5r_p p_g} \left(\frac{m_g}{2k_b T_g} \right)^{\frac{1}{2}} \quad \text{Equation 71}$$

According to Williams and Loyalka (Williams and Loyalka, 1991), f_h can be expressed as:

$$f_h(Kn_h) = \left[1 + Kn_h \frac{\frac{Q_{\text{cond, c}}}{Q_{\text{cond, fm}}} \xi_h + \zeta_h}{\xi_h Kn_h + 1} \right]^{-1} \quad \text{Equation 72}$$

$Q_{\text{cond, c}}$ released energy by conduction in continuum regime

$Q_{\text{cond, fm}}$ released energy by conduction in free molecular regime

ξ_h factor, $\xi_h = 1.9234$

ζ_h factor, $\zeta_h = 1.1759 * (5/8) * \pi^{1/2} = 1.3026$

$$\frac{\dot{Q}_{\text{cont}}}{\dot{Q}_{\text{fm}}} = 5 \frac{\sqrt{\pi}}{\alpha_T} \left(\frac{\gamma - 1}{\gamma + 1} \right) Kn_h \quad \text{Equation 73}$$

γ heat capacity ratio

α_T translational energy accommodation coefficient

α_T takes into consideration every collision between particles and gas molecules do not transfer the potential maximum energy. α_T represents the efficiency of the energy transfer during molecular collision (Filippov et al., 2000). Different values can be found in the literature, 0.07 (Lehre et al., 2003a) up to 1.00 (Starke et al., 2003). In transient Knudsen

conditions, the influence of α_T is much lower than in free molecular regime, then the assumption $\alpha_T=1$ can be made.

γ considers the energetic degrees of freedom of the gas molecules during the heat transfer.

This can be simplified into:

$$\frac{\dot{Q}_{cont}}{\dot{Q}_{fm}} = \frac{5\sqrt{\pi}}{4} Kn_h \quad \text{Equation 74}$$

4.1.5 Heat losses by carbon cluster sublimation

The high energy brought by the laser and therefore the high temperatures reached provokes the sublimation of some atoms or molecules from the particle surface. In this vapour produced, different carbon species exist but C_3 is the dominant one. (Dreyfus et al.; 1987).

$$\dot{Q}_{sub} = \frac{\Delta h_V}{M_v} J_{sub} \quad \text{Equation 75}$$

Q_{sub} sublimation energy of soot [$J.kg^{-1}$]

Δh_V Sublimation enthalpy [$kg.mol^{-1}$]

J_{sub} sublimation rate of soot [$kg.s^{-1}$]

J_{sub} can be determined from the mass balance equation:

$$J_{sub} = \frac{dM}{dt} \quad \text{Equation 76}$$

M mass of soot particle [kg]

$$\dot{Q}_{sub} = -\frac{\Delta h_V}{M_v} \pi d_p^2 \beta P_v(T) \sqrt{\frac{M_v}{2\pi RT}} \quad \text{Equation 77}$$

P_v Pressure of soot gas or vapour; [$N.m^2$]

β Sublimation coefficient

Coefficients Δh_V , M_v , P_v are considered temperature dependent, determined by data fit extrapolation (Leider et al., 1973), they are expressed as polynomial expressions:

$$\Delta h_v = \sum_{i=0}^5 h_i T_i \quad \text{Equation 78}$$

$$M_v = -\sum_{i=0}^4 m_i T_i \quad \text{Equation 79}$$

$$P_v = \exp\left(\sum_{i=0}^4 p_i T_i\right) \quad \text{Equation 80}$$

The polynomial coefficients are listed in Appendix B. The figures below show the evolutions of these different parameters with temperature.

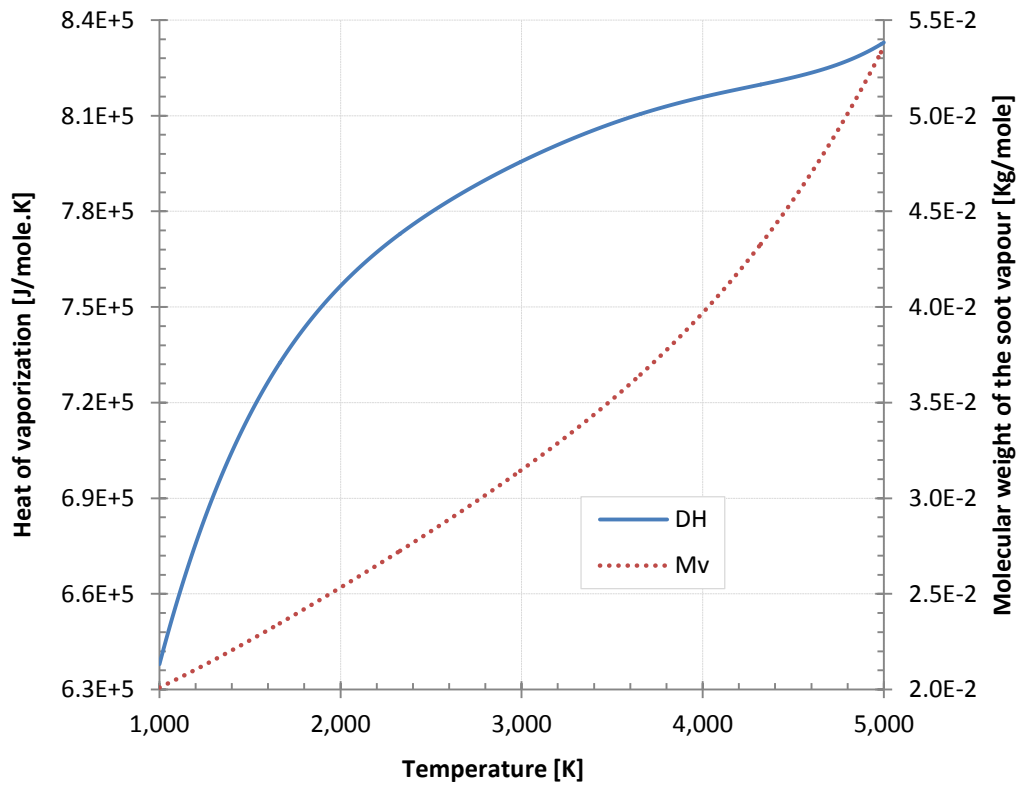


Figure 4-3 – Evolution of vaporization heat and molecular mass with temperature

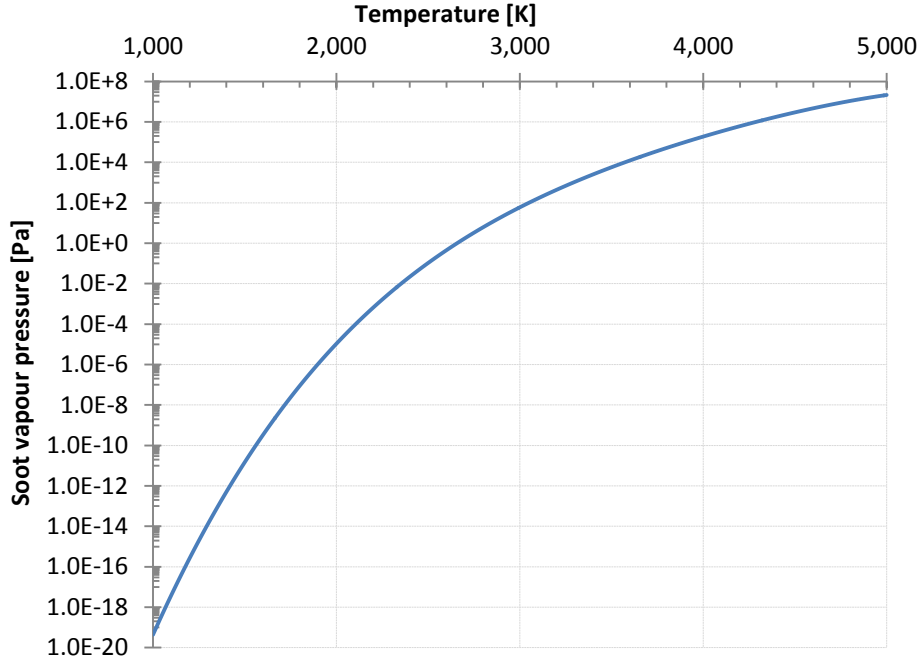


Figure 4-4 – Evolution of soot vapour pressure with temperature

Kock-Roth model

In the Kock-Roth model, the sublimation is expressed as:

$$\dot{Q}_{\text{sub}} = \dot{U}_{\text{sub}} \Delta h_v \quad \text{Equation 81}$$

Considering the transient regime, the sublimation heat transfer is expressed via the Knudsen number:

$$\dot{Q}_{\text{sub, tr}} = \dot{U}_{\text{sub, c}} f_c(Kn_c) \quad \text{Equation 82}$$

The heat loss by sublimation can be expressed as:

$$\dot{U}_{\text{sub, tr}} = 2\pi d_p D (\rho_s - \rho_\infty) f_c(Kn_c) \quad \text{Equation 83}$$

or

$$\dot{U}_{\text{sub, tr}} = 2\pi d_p D (\rho_s - \rho_\infty) f_c(Kn_c) \frac{\Delta h_v}{M_v} \quad \text{Equation 84}$$

With (Williams and Loyalka, 1991):

$$f_c(Kn_c) = \left[1 + Kn_c \left(\frac{1.3333B + 1.0161}{1.3333Kn_c + 1} \right) \right]^{-1} \quad \text{Equation 85}$$

$$B = \frac{\dot{U}_{\text{sub,c}}}{\dot{U}_{\text{sub,fm}}} = \frac{Kn_c \sqrt{\pi}}{\alpha_v} \quad \text{Equation 86}$$

α_v accommodation coefficient for sublimation (for nonequilibrium sublimation kinetics and real gas effects (Lehre et al., 2003a).

α_v can be assumed equal to 1.00, (Kock et al., 2006, Boiarciuc et al., 2006) which simplify the previous equation:

$$B = Kn_c \sqrt{\pi} \quad \text{Equation 87}$$

The Knudsen number of the vapour phase is given by:

$$Kn_c = \frac{2D}{r_p} \left(\frac{m_v}{2k_B T_v} \right)^{\frac{1}{2}} \quad \text{Equation 88}$$

Only the C₃ sublimates (hypothesis) from the solid carbon surface during the laser heating up (Leider et al., 1973).

$$Kn_c = \frac{2\lambda_{MFP-Vapour}}{d_p} \quad \text{Equation 89}$$

λ_{MFP} vapour mean free path of carbon gas molecules

ρ_s and ρ_∞ are the carbon vapour density respectively at the carbon surface and at infinity. ρ_∞ can be assumed to be negligible. With the thermodynamic equilibrium and ideal gas behaviour assumptions, ρ_s can be expressed by the carbon vapour pressure p_s .

4.1.6 Radiative heat transfer

The particle loses heat by emitting light. The heat flux due to radiation is lower than the two previous heat fluxes but it is on this one that the LII technique is based.

$$\dot{Q}_{rad} = \pi d_p^2 \int_0^\infty \varepsilon_\lambda \frac{2\pi hc^2}{\lambda^5 \left(e^{\left(\frac{hc}{k\lambda T} \right)} - 1 \right)} d\lambda \quad \text{Equation 90}$$

ε_λ spectral emissivity of the particle

ε_λ is dependent on the refractive index function of the soot:

$$\varepsilon_\lambda = \frac{4\pi d_p E(m)}{\lambda} \quad \text{Equation 91}$$

There are two ways to simplify this expression; the first one was used by Snelling (Snelling et al., 1997):

$$\dot{Q}_{rad} = 4\pi^2 d_p^3 \sigma_{SB} (T^4 - T_g^4) \left(\frac{E(m)}{\lambda} \right) \quad \text{Equation 92}$$

σ_{SB} Stefan-Boltzmann constant ($5.67040040 \times 10^{-8} \text{ W.m}^{-2}.\text{K}^{-4}$)

The λ value does not have a real importance due to the weakness of this heat transfer compares to the others; a value in the visible can be used (Snelling et al., 1997).

The second one by Knock et al., (Knock et al., 2006) :

$$\dot{Q}_{rad} = \pi d_p^2 \varepsilon_{pt} \sigma_{SB} (T_p^4 - T_g^4) \quad \text{Equation 93}$$

ε_{pt} total emissivity of the particle

The maximal value of ε_{pt} (i.e. $\varepsilon_{pt} = 1$) is assumed, since the influence of the radiation is not the major heat transfer in the cooling process and is almost negligible.

4.1.7 Oxidation

The oxidation term is commonly not taken into consideration in the literature and so in this work. The part of the oxidation on the cooling process is negligible due to the short time scale considered and therefore others transfers are prevailing. Its influence is dependent on the location in the flame and the free mean path of the oxidizing molecules. The only model considering oxidation (Michelsen, 2003) expresses the oxidation contribution, including heating and mass loss; assuming the CO production from the surface reaction of C+O₂, as:

$$\dot{Q}_{oxidation} = \left(-\Delta H_{ox} - 2\alpha_T C_P^{CO} T \right) \frac{\pi D^2 k_{ox}}{N_A} \quad \text{Equation 94}$$

The rate of mass loss caused by oxidation is estimated equal to:

$$\left(\frac{dM}{dt} \right)_{ox} = - \frac{2\pi d_p^2 W_1 k_{ox}}{N_A} \quad \text{Equation 95}$$

4.1.8 Particle size distribution

The heat transfers previously expressed were for a single particle. Average LII signal being the addition of all the particles in the measurement volume. The heat transfers have to be considered for a number of particles N_p . However, all the particles do not obviously have the same dimension. There is no theory that could predict the particle size distribution. But from experimental results based on the analysis via microscope (Douce et al., 2001, Kronholm and Howard, 2000, Manzello et al., 2007, Mathis et al., 2005) of soot sampled in flame, choc tube or at the engine exhaust, the distribution can be considered as lognormal (Equation 96) or even multi-lognormal.

$$f(d_p) = \frac{1}{d_p \ln \sigma \sqrt{2\pi}} \exp \left[-\frac{(\ln d_p - \ln \bar{d}_p)^2}{2 \ln(\sigma)^2} \right] \quad \text{Equation 96}$$

$f(d_p)$ probability density function

σ standard deviation

\bar{d}_p mean particle diameter

Particle size distributions from only one source are always considered to be lognormal (Hinds, 1982). In a lognormal distribution, there are as many values under as above the mean value, point that must be considered in the discretisation. This distribution involves a major difference in the global decay rate of LII signal and also in the determination of the temperature due to the fact that the bigger particles cool slower than the smaller ones.

For an increase of σ , there is a widening of the particle distribution, involving the presence of larger particles. Even if there are also smaller particles, the effect of the largest particles will predominate the global cooling. For a low standard deviation value, the influence of the distribution is similar to the mono-disperse one. Distribution function has clearly an effect on the model for predicting size and temperature of the soot particles.

The maximal computed temperatures determined upon different cases of distribution, are relatively similar. The effect of the distribution will not influence the determination of the soot volume fraction if the measure is taken around the maximal temperature that reaches the soot.

4.2 Modelling examples of LII signals

The outlined models describe mathematically the different processes involved during the LII. The differential equations were solved numerically by a fourth order Runge-Kutta routine. (RK4) and a time step of 0.1 ns. The programming was done with Matlab®. As example, the model was applied with the conditions of the experimental work to represents the difference of temporal decay of temperature and LII signal:

Laser fluence	0.10 J.cm ⁻²
Pulse duration	7 ns
Excitation wavelength	532 nm
Detection wavelength	700 nm
Surrounding gas temperature	1,800 K
Surrounding gas pressure	101,325 N.m ⁻²
Surrounding gas thermal conductivity	0.12 W.m ⁻¹ .K ⁻¹
Soot particle diameter	30 nm
Specific heat capacity of soot	2,100 J.kg ⁻¹ .K ⁻¹
Soot density	2,000 kg.m ⁻³
Soot absorption function	0.299

Table 3 – Main theoretical parameter for LII signal computation

4.2.1 Laser fluence

The temporal laser profile was considered as Gaussian with a 7 ns FWHM. The laser profile distribution was discretised into 280 points with a time step of 0.1 ns and normalized to the laser fluence (Figure 4-5).

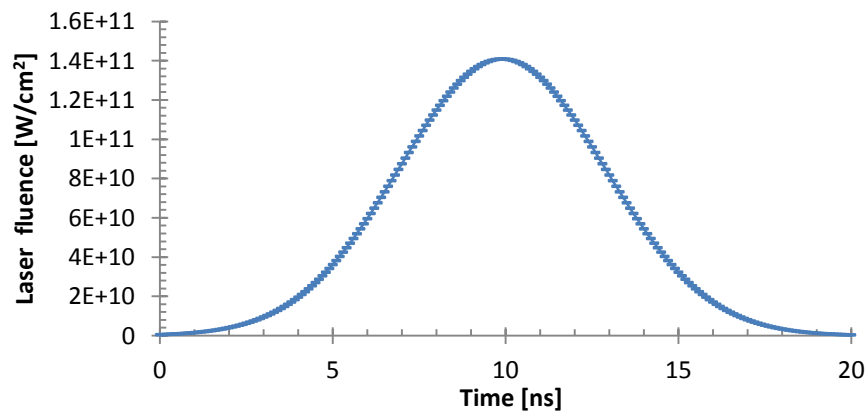


Figure 4-5 – Temporal laser profile distribution

4.2.2 Particle diameter distribution

The particle distribution affects the LII signals due to unequal contribution in the LII signal between small and large particle. The distribution of soot particles is mainly considered to be log-normal (Maricq, 2004) or in some cases multi-lognormal (He et al., 2010).

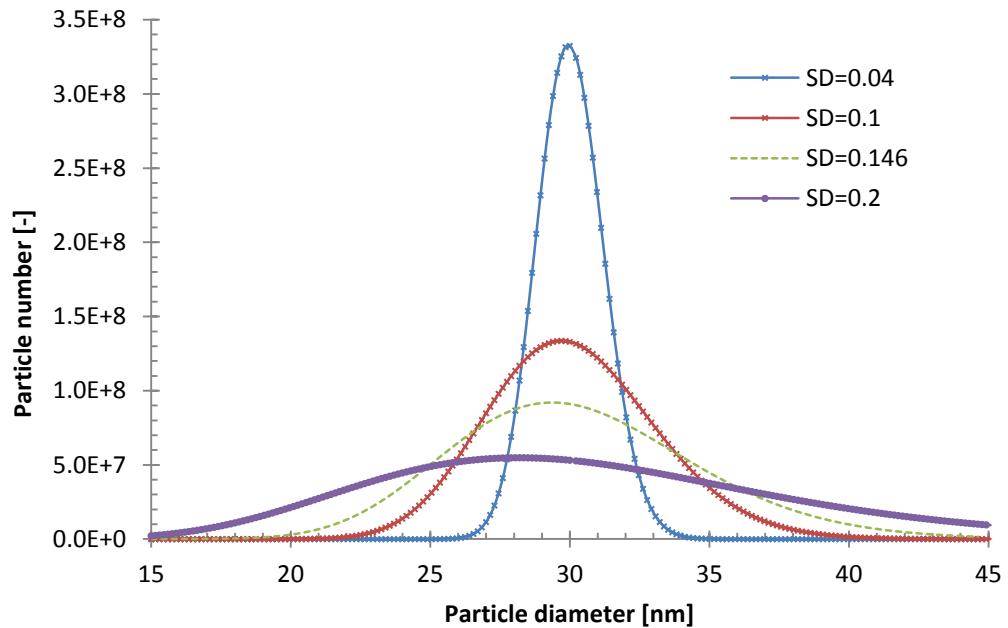


Figure 4-6 – Particle lognormal size distribution for different standard deviations

4.2.3 Particle diameter

The influence of particle diameter on the LII decay signal was investigated. The signal was computed from the model formulated in the previous chapter. The curves of normalised LII signal were plotted for different particle diameters from 5 to 150 nm.

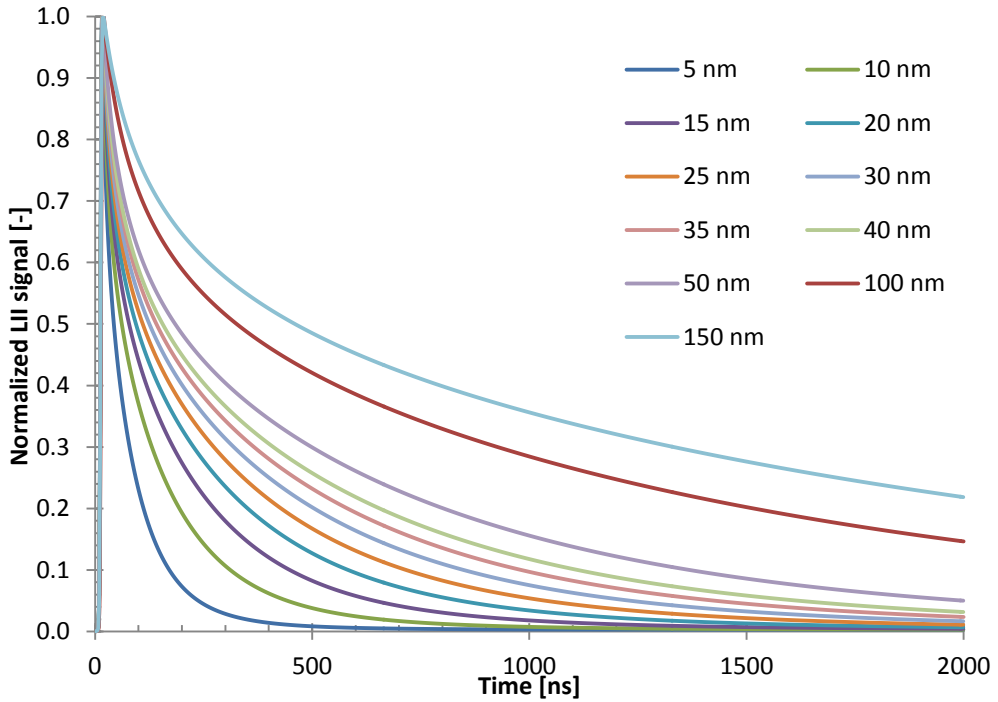


Figure 4-7 – Normalised LII signals for various particle diameters.

The difference of signal decay is significant between the different diameters. Higher is the difference, better the particle sizing accuracy is.

The LII signal decreases faster for smaller particle diameters rather than the larger ones.

The temperature cooling of the particles is represented in Figure 4-8.

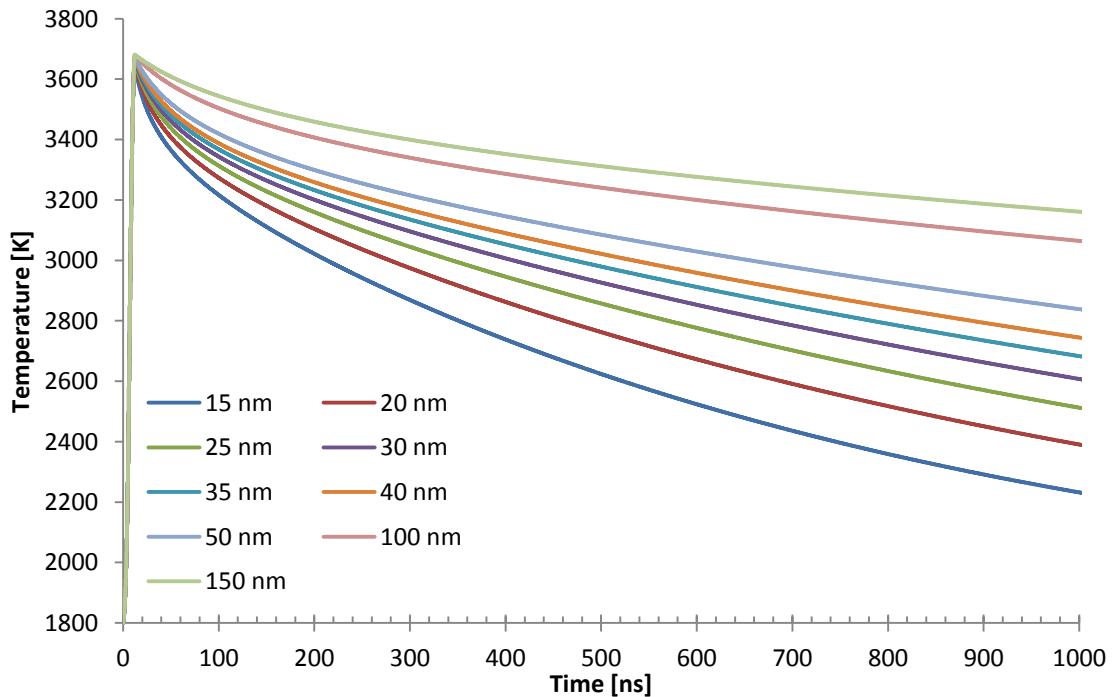


Figure 4-8 – Particle's temperature profiles during LII process for various particle diameters.

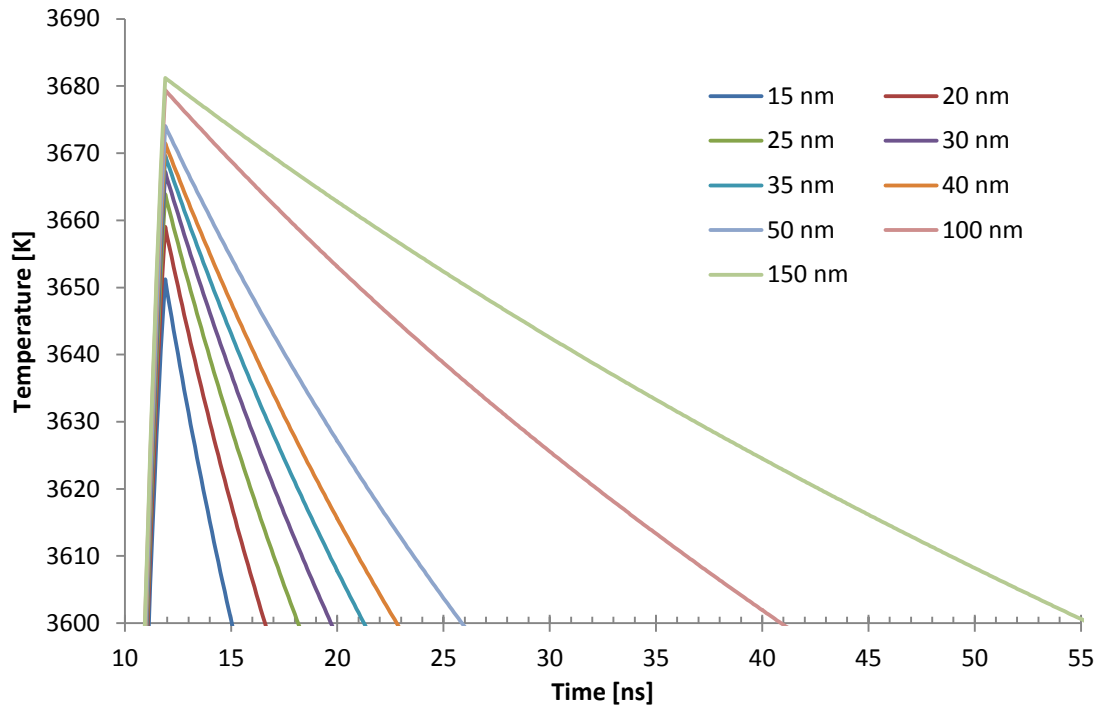


Figure 4-9 – Particle’s maximal temperature profiles during LII process for various particle diameters.

Temperature peaks reach almost the same value (difference less than 1%). Temperature peak is slightly dependent on the particle size. This agrees well with the literature and the assumption (Rayleigh conditions), that the temperature peak is quasi-independent of the particle size. The absorption is the main heat transfer and according to the equations used and if the cooling processes were neglected, it could be simplified as:

$$\frac{dT}{dt} = \frac{6\pi E(m)}{\lambda \rho_s C_s} q_{laser} \quad \text{Equation 97}$$

The cooling process is mainly due to the sublimation at the signal peak. Diameter dependent, the sublimation process makes a slight difference in the maximal temperatures reached.

The cooling rate depends on the temperature but as the temperature peak of the particles is almost the same for all the particles. The particle size can be considered as the main parameter of the cooling process variations.

Plotting these LII decay curves allows a comparison with the curves published in the literature. The curves have matched the ones found in the literature, proving that no error have been made during the model programming

4.2.4 Pressure effect

The pressure has a major effect on the LII signal. By increasing the interaction between the particle and its surrounding, the conduction heat transfer dramatically increases. This physical process is modelled via the Knudsen number. A signal lasting a few hundred nanoseconds at atmospheric pressure will last a dozens of nanoseconds at high pressure.

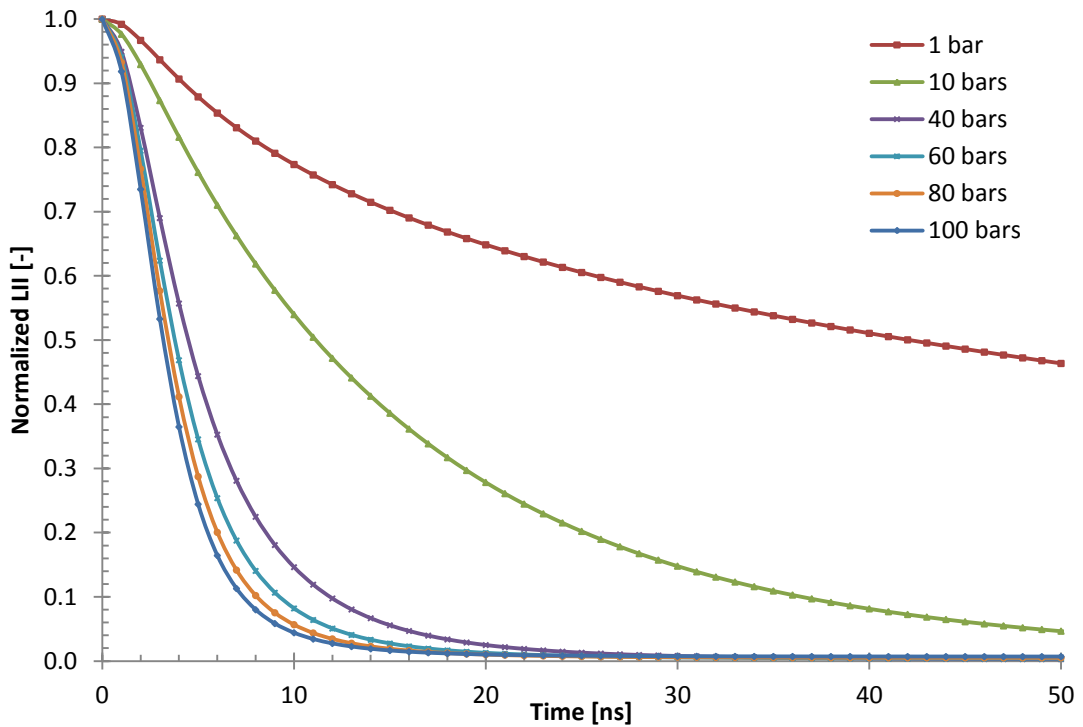


Figure 4-10 – Normalized LII signal for various pressures

The high energy lost by conduction also affects the maximum temperature reached by the particles. The fast cooling rate at high pressure involves lower temperature peak. Lower peak temperature and short duration signal explain the challenge to perform LII signal acquisition in an optical combustion chamber compared to an atmospheric flame. The LII signal difference between 60 to 100 bars is relatively small. An error on the pressure value will not cause major error on the results.

4.3 Conclusions

Different expressions are possible to describe the different heat transfers of soot particles. Depending on the pressure conditions, an appropriate model is applied to compute the temperature and the temporally decreasing LII signal that derives. At atmospheric pressure, sublimation is the main cooling process after the laser pulse, once a 3400 K temperature threshold is reached; the conduction becomes dominant. However at higher pressure, conduction heat transfer dramatically increases and prevails over sublimation, reducing the LII signal to a few dozens of nanoseconds. Extreme care on the model selection is crucial as different models exist. A comparison study of all the existing models demonstrated large difference between the resulting cooling temperatures and LII signals. Choosing a different model results in finding different particle sizes. Sublimation modelling is the main error source. Some physical phenomena (annealing, multiple cluster sublimation, shielding effect, oxidation, thermionic emission) and assumptions remain open to many questions. In this work, the four main heat transfers i.e. absorption, conduction, sublimation, radiation have been considered, the other physical phenomena have been excluded for the interpretation of the decreasing LII signal. The models used in this work (Table 4) are common but have proven to give results in good agreement with the reality. Results obtained from solving the model equations have matched those found in the literature, discarding the possibility of a programming error.

Heat flux	Atmospheric conditions	Engine conditions
Absorption	$\dot{Q}_{abs} = C_a q = \frac{\pi^2 d_p^3 E(m)}{\lambda} q$	
Conduction	$\dot{Q}_{cond, FMR} = \frac{2\pi d_p^2 \lambda_{cond} (T - T_g)}{(d_p + G\lambda_{MFP})}$ (McCoy and Cha, 1974)	$\dot{Q}_{cond, tr} = 2\pi d_p \lambda_{cond} (T_p - T_g) f_h (Kn_h)$ (Kock and Roth, 2003) (Williams and Loyalka, 1991)
Sublimation	$\dot{Q}_{Sub} = -\frac{\Delta h_v}{M_v} \pi d_p^2 \beta P_v (T) \sqrt{\frac{M_v}{2\pi RT}}$ (Melton, 1984b) (Smallwood et al., 2001)	$\dot{Q}_{evap, tr} = 2\pi d_p D (\rho_s - \rho_\infty) f_c (Kn_c) \frac{\Delta h_v}{M_v}$ (Kock and Roth, 2003) (Williams and Loyalka, 1991)
Radiation	$\dot{Q}_{rad} = 4\pi^2 d_p^3 \sigma_{SB} (T^4 - T_g^4) \left(\frac{E(m)}{\lambda} \right)$ (Snelling et al., 1997)	
Crystallisation	Not taken in consideration/neglected (Michelsen, 2003)	
Oxidation	Not taken in consideration/neglected (Michelsen, 2003)	
Internal energy	$\dot{Q}_i = \frac{1}{6} \pi d_p^3 \rho_s c_s \frac{dT_s}{dt}$ (Melton, 1984b, Michelsen, 2003)	
Mass balance	$\frac{dM}{dt} = -\pi d_p^2 \beta P_v (T) \sqrt{\frac{M_v}{2\pi RT}}$	$\frac{dM}{dt} = 2\pi d_p D (\rho_s - \rho_\infty) f_c (Kn_c)$
Mass variation	$\frac{dM}{dt} = \frac{1}{2} \pi d_p^2 \rho_s \frac{dd_p}{dt}$	

Table 4 – Table summarizing the different heat transfers used in the condition of atmospheric flame and high pressure condition (Diesel combustion chamber).

5 CHAPTER V: EXPERIMENTAL CONSIDERATIONS AND APPARATUS

State of the art optical diagnostics are subject to special requirements to be correctly performed. Depending on the objectives and issues of a given experiment, different approaches are often possible. The selection of excitation and detection wavelengths, laser fluence, spatial beam profile, temporal detection and calibration methods have a major impact on the result accuracy. In this chapter, the reasoning behind the choices made for the optical experimental settings are discussed and presented.

5.1 *Experimental parameters*

5.1.1 Excitation wavelength

Soot absorbs broadly, in a large spectral band from the ultraviolet to the infrared, therefore any laser wavelength can be used to heat-up the particles. However not the same fluence is needed according to the laser wavelength as the lower the wavelength, the higher the absorption cross section. The choice of the wavelength must also take into consideration some specific excitation wavelengths that generate parasitic fluorescence emissions. UV excitation wavelengths have demonstrated to generate LII (Rohlfing, 1988) but also generate more fluorescence from PAH (Bengtsson and Aldén, 1995) and more photodissociation than particle heating (Stipe et al., 2004). A wavelength falling in the resonance wavelength of the Swan band of C₂ radicals (resulting from the vaporization) must be avoided. However the C₂ radicals fluorescence signal can and has been used for diagnostic purposes (Bengtsson and Aldén, 1990, Bengtsson and Aldén, 1995, Mercier et al., 2005)

The excitation wavelength used is often dependent on the equipment available due to the cost of high energy lasers. Nd:YAG lasers are commonly used, this type of laser produces reliable and high-power pulses of duration ~8 ns FWHM, and can be set at 1064 nm, 532 nm or 355 nm (fundamental and harmonics) excitation wavelengths. The first two wavelengths, 1064 nm (Vander Wal et al., 1996, Dec, 1997, Vander Wal, 1998, Schoemaeker-Moreau, 2002, Smallwood et al., 2002, Kock and Roth, 2003, Boiarciuc et al., 2006) and 532 nm (Espey et al., 1997, Dec, 1997, Schraml et al., 2000,

Hofmann et al., 2003) are predominantly used, but any other wavelengths can be employed such as 560 nm (Shaddix and Smyth, 1996) or 355 nm (Rohlfing, 1988).

While using a Nd:YAG laser, the 1064 nm excitation wavelength is preferred in order to avoid any PAH fluorescence that could involve an overestimation of the LII signal, especially at the peak as fluorescence signal is prompt and lasts a few dozen of nanoseconds. The PAH fluorescence perturbation was highlighted by the signal comparison resulting from 532 and 1064 nm excitation wavelength and use to visualize the PAH presence in atmospheric flame (Vander Wal and Weiland, 1994, Schoemaeker-Moreau, 2002, Schoemaeker-Moreau et al., 2004) or in combustion chambers (Bobba and Musculus, 2012).

The electronic detection equipments (intensified camera, PMTs) are not sensitive to the infrared wavelength range i.e. 1064 nm, therefore no laser scattering can be recorded simultaneously with the LII signal, which could disturb the LII measurement accuracy. But as the scattering signal is needed to determine the particle size distribution, the 532 nm wavelength was selected in this study.

The laser wavelength and particle diameter must fulfil the condition of the following equation to be considered in the Rayleigh regime:

$$\frac{\pi d_p}{\lambda_{laser}} \leq 1 \quad \text{Equation 98}$$

In this experiment, to respect the Rayleigh criterion, particle diameters must be less than 170 nm to be in the Rayleigh regime. This condition seems satisfied as primary particles are assumed to be in the range of 30 nm. However that becomes critical when considering aggregates as their size can be larger than this criterion.

5.1.2 Laser fluence, spatial energy distribution and pulse duration

The intensity, pulse duration and energy distribution are interlinked (Tait and Greenhalgh, 1993a). The difference between a 1D and 2D Gaussian energy distribution is not negligible. The fluorescence of C₂ for a 2D Gaussian energy distribution starts around 50 MW.cm⁻² (Schraml et al., 2000) while an energy around 100 MW.cm⁻² (Hofmann et al., 2003) for the other distribution does not reveal the presence of the C₂ fluorescence.

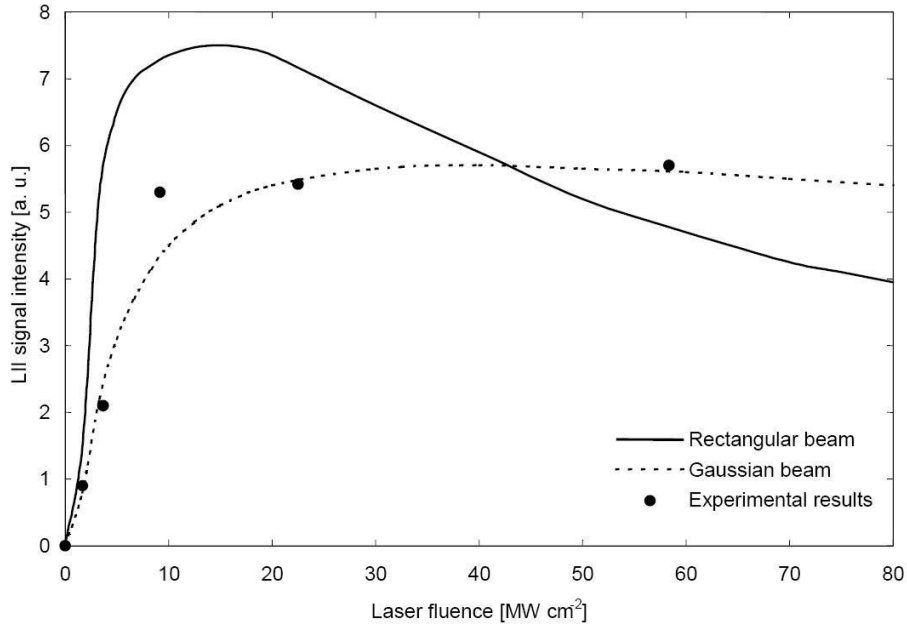


Figure 5-1 – Dependence of laser profile and fluence on LII signal for 100 nm particles radius (Tait and Greenhalgh, 1993b).

The laser pulse characteristics have a major impact on the LII signal. Laser fluence and beam profile (temporal and spatial) are parameters that must be well-characterised.

The LII signal strongly rises with the increase of the laser fluence. The soot temperature increases and so the LII signal with the laser fluence (Quay et al., 1994a).

The laser excitation fluence effect is obtained by plotting the integrated LII signal versus the laser fluence (Figure 5-1). The integrated LII is almost constant for laser fluence between 0.09 and 0.15 J.cm⁻² (Vander Wal and Jensen, 1998). From the results of Ni et al. (1995b) if the laser excitation is too high, the LII signal decreases due to the energy dissipated by sublimation. The particles are vaporised instead of being heated up over 4000 K.

For Gaussian beam profile condition, after reaching a fluence of ~0.15 J.cm⁻², the LII intensity seems to reach a plateau while increasing the laser excitation does not increase the incandescence signal. This is an artefact of the experimentation, by increasing the fluence, the volume excited also increases, the particles excited at the centre of the Gaussian beam tend to vaporize, reducing the signal while the ones at the edges of the laser beam, under the vaporization threshold see their temperatures rising as the fluence increases. These two phenomena tend to compensate and explain the shape of the LII curve function of fluence. Whereas this artefact does not occur for homogeneous spatial

laser energy distribution, after reaching a maximum the LII signal decreases due to the sublimation of the particles (Figure 5-2).

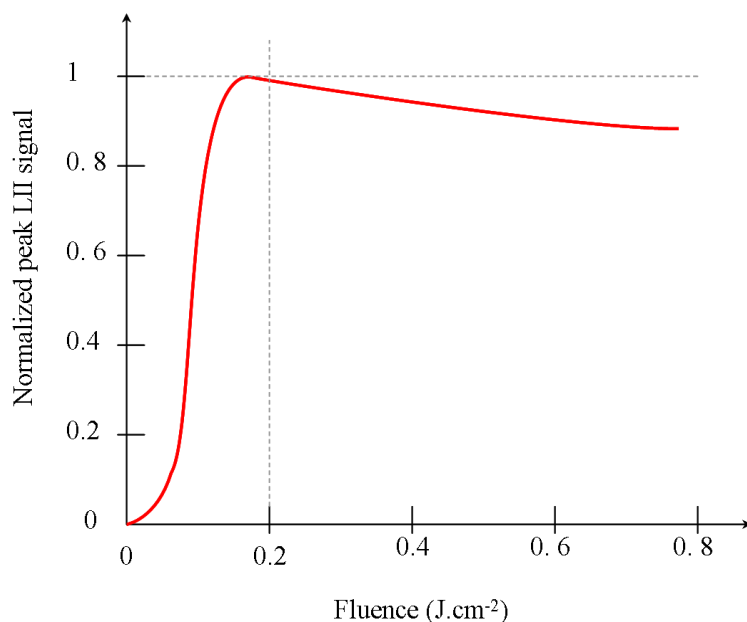


Figure 5-2 – Dependence of LII signal peak on laser fluence. Measurements were carried out at 532 nm excitation wavelength with a top-hat beam profile on Santoro burner flame conditions (Michelsen, 2003, Michelsen et al., 2003).

5.1.3 Detection wavelength

The selection of the detection wavelength is a critical issue because of advantages or disadvantages of using shorter or higher wavelengths. It has been previously shown that the radiance from the soot considered as grey-body and therefore LII signal intensities are higher for wavelengths between the end of visible and the near infrared range at temperature considered.

It has been shown the higher the detection wavelength, the higher the LII signal intensity. Choosing higher collection wavelength results in higher signal but also in higher noises from the natural flame incandescence. The spectral sensitivity of the equipment has to be considered to maximize the recorded signal intensity.

For 2C-TiRe-LII, the apparent soot temperature can be estimated by measuring the luminescence signal at two different wavelengths. The choice of these two wavelengths is crucial for a good accuracy of the 2C-TiRe-LII. The wavelength has to be in the range of the spectral radiance of a blackbody radiator at a temperature between 3000 K and

4000 K. The maximum radiance at these temperatures falls in the visible wavelength area.

Electronic devices have higher yield in the visible range and even more for the low wavelengths in the visible range. So even if the LII signal is weaker for at wavelength ~ 400 nm, the signal recorded will be higher than the one acquired at ~ 700 nm.

A larger separation between the two collection wavelengths improves the sensitivity of the temperature measurement.

During the combustion, many different chemical radicals can produce a non-negligible emission such as the CH radical (435 nm) or C_2 radical (438.3, 473.7, 516.5 and 563.6 nm). The filters used must prevent from recording any parasite emissions.

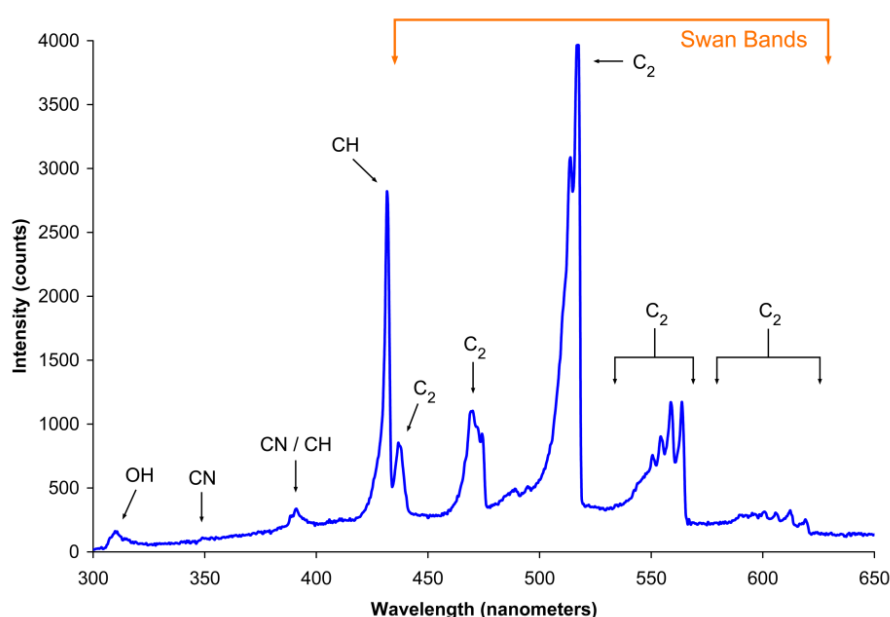


Figure 5-3 – Spectrum of a laminar blue flame showing Swan bands

Choosing wavelengths centred on 400 or 450 nm, and 650-700 nm was considered to be the best option. 400 and 700 nm wavelengths were selected for 2-colour pyrometry. The 300 nm difference admits a good temperature resolution.

For the PLII image recording, a filter centred on 416 nm of 64.4 nm FWHM and for the scattering signal, a filter centred at the 532 nm wavelength, wavelength of the laser excitation, with a 9.4 nm FWHM were used.

5.1.4 Temporal detection strategy

The detection gate must be prompt and short ~ 25 to 100 ns (Vander Wal et al., 1996) to record the LII peak signal. Different strategies are possible and four of them are exemplified in Figure 5-4. The start of recording can start at, after, or few dozens of nanoseconds after the laser pulse. Delayed detection gate biases the results toward the largest particles (Melton, 1984b, Ni et al., 1995a, Vander Wal et al., 1996) and the same statement applies for long integration gate (Tait and Greenhalgh, 1993a). A longer integration time has the advantage of increasing the overall signal recorded but in return can also integrate signal noises (natural luminescence of the flame or Fluorescence).

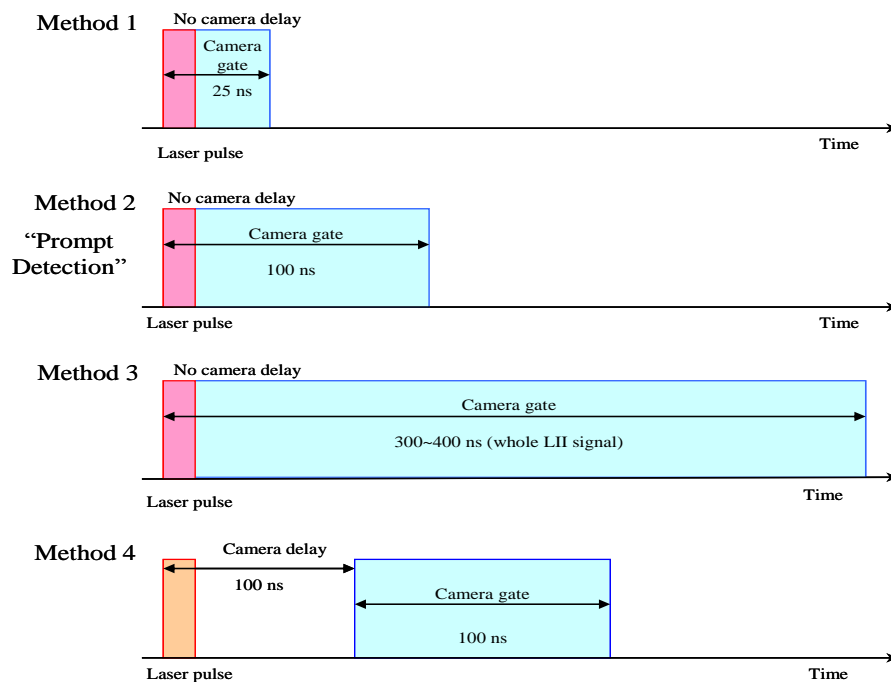


Figure 5-4 – Different temporal detection strategies for camera acquisition

A prompt detection (method 1) was preferred due to the need of recording the scattering signal and LII on the same camera, and a short camera opening gate of 50 ns in order to record the complete scattering signal ~ 15 ns and ~ 40 ns for LII signal. The 40 ns were selected from the estimated LII duration at high pressure conditions. This strategy avoids the shift of the results towards the largest particles and to not record the natural luminescence background but has the disadvantage to be sensible to possible fluorescence signal noise. The integration time lasting only 50 ns, the recorded signal is obviously lower than for a longer integration time. The signal intensity is not an issue at atmospheric conditions as after 50 ns the LII signal is still high but at pressures representative of Diesel conditions, the signal is almost nil after 50 ns.

5.1.5 Calibration method

The calibration of the soot volume fraction is commonly performed by extinction measurement. This calibration technique does not involve major issues in open configuration such as flame from burners but can in in-cylinder measurements. The extinction is usually carried out on steady flames and performed separately from the LII measurement by another laser beam of lower energy. Acquiring simultaneously extinction and LII measurement is more problematic. One of the solutions is to quantify the extinction of the laser, used for LII by measuring the fluorescence produced.

The extinction of the Nd-YAG laser beam was preliminary performed upon a flame. The turbulent conditions in the rapid compression machine (RCM) required to record simultaneously the LII and extinction. However due to some difficulties in recording the transmitted signal (high fluence density), this technique was rejected. The extinction measurement by estimation of the fluorescence was also considered as an option but the absorption by the optical windows, the spatial resolution and underestimation of the soot cloud due to some part not visualised, were considered as factors introducing large inaccuracies. The self-calibration method was preferred to calibrate the data. The LII auto-calibration has proven to be a reliable technique, even at high pressures, by different research groups. However the fact that extinction could not be achieved meant that the RAYLIX technique could not be used to compare with the 2C-TiRe-LII measurements.

5.2 *Set-up configurations*

Figure 5-5 presents the global lay out of the experiment set-ups. The set-up can be divided into three parts, the excitation, the two-dimensional acquisition and the temporal acquisition (2C-TiRe-LII). Two different configurations were set depending on the volume probed by the photomultipliers. The two setups are identical apart from the light collection system for the photomultipliers.

For the excitation, the high-power laser beam was spatially selected and restrained by an adjustable iris and transformed to a sheet using a lens kit composed of 4 optics. The laser sheet was spatially selected and clipped by a vertical slit. A large beamsplitter was used to split the signal between the 2D acquisition and 2C-TiRe LII acquisition. The spatially resolved measurement was performed with a single camera coupled to an image doubler. The scattering and incandescence signals were differentiated by two

spectral filters. Neutral density filters were used to reduce the strong scattering signal, and to obtain similar amplitudes on the ELS and LII images. A 50 mm diameter lens was used to improve light collection.

On the first approach, the flame was focused and magnified by a second lens onto a 1 mm pinhole to select the part of the flame to be probed. The light was split by a beamsplitter plate and filtered by specific filters before reaching the PMTs.

The second approach had a different light collection configuration for the 2C-TiRe-LII technique. By a 500 mm focal length lens, the flame was focused straight on the PMTs. A diaphragm was set to spatially limit the light collected.

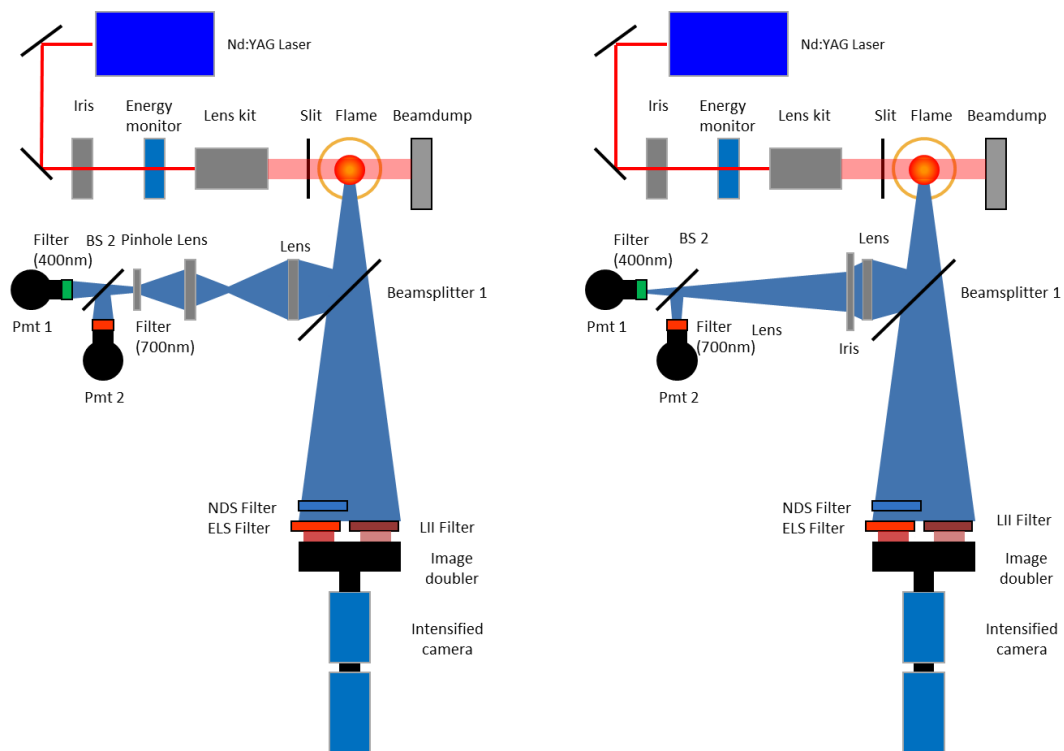


Figure 5-5 – Optical set-ups

LEFT: local measurement 2C-TiRe-LII

RIGHT: Global measurements 2C-TiRe-LII

The acquisition chain was set up on a single optical table, and designed to fit the RCM environment. Initial tests were conducted on a laminar flame and the whole acquisition chain was then transferred to the RCM without modifying its layout.

5.3 Laser

5.3.1 Description

A Nd:YAG (Neodymium Yttrium Aluminium Garnet) laser was used for the ELS and LII experiments. This laser, a Quanta-Ray® GCR 150 by Spectra-Physics can deliver pulses of 300 mJ at 532 nm with a 10 Hz frequency. The laser pulses were spatially and temporally Gaussian with a beam diameter of 8.7 mm and a pulse length of 7 ns at FWHM. The pulse-to-pulse energy fluctuation is quoted by the manufacturer to be less than 3 % and a long term power drift less than 5 % over 8 hours. The light was vertically polarized.

5.3.2 Synchronisation

The laser power output is dependent on its frequency. The Nd:YAG laser allowed a frequency range from 9.30 to 10.90 Hz with an optimal frequency at 10 Hz. The laser pulse was triggered by the injection pulse. The Proteus RCM ran at a constant speed of 500 rpm (i.e. 8.33 rotations per second), therefore the maximal injection frequency is 8.33 Hz. A skip-cycle strategy was applied to lower the injection frequency and adapt to suit the camera and laser firing frequency. The skip-cycle strategy has two purposes; the first one is to ensure that burnt gases are fully scavenged and the second is to reduce window fouling. The best setting was previously determined by Demory (2007), the laser and injection frequencies can perfectly match if 9 (or 14) cycles are skipped. The skipping cycle reduces the possible acquisition frequency to 0.83 Hz (or 0.56 Hz) which falls in the frequency acquisition range of the camera (10 Hz).

The laser and camera settings were kept the same for the burner and RCM experiments, including the image acquisition rate of 0.83 Hz.

5.3.3 Beam profile

As described previously, care must be taken with the beam profile and energy. The Gaussian beam laser profile was shaped into a vertical sheet. To transform the spatial distribution of the beam, a set of 4 lenses was used to reduce the thickness in one direction and extend its height in the other direction. An iris was positioned before the laser sheet-forming optics, and an adjustable vertical slit was set after. Their purpose was to spatially restrain the laser beam and avoid incandescence wing effect on the

sampled volume. The laser energy was recorded via the energy monitor before the lens kit (Figure 5-6). The energy was controlled to be in the moderate energy fluence regime, i.e. between 0.11 to 0.12 J.cm².

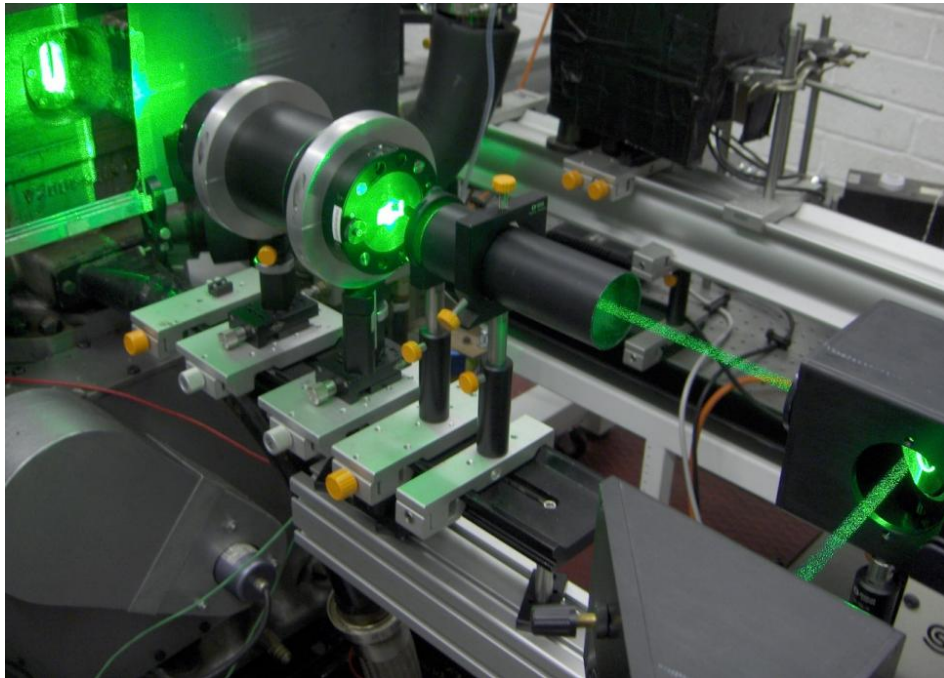


Figure 5-6 – Laser excitation optical equipment layout

The dimensions of the laser sheet were deduced from the analysis of photographic paper (Figure 5-7) and the profile acquired by the scattering of the laser sheet on a plate set at the measurement position and recorded by the CCD camera (Figure 5-8). The laser sheet dimensions were measured to be 87.1 mm by 0.4 mm i.e. 0.348 cm².

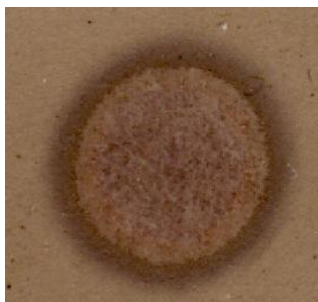


Figure 5-7 – Laser beam print before the sheet-forming optics on photographic paper (single shot)

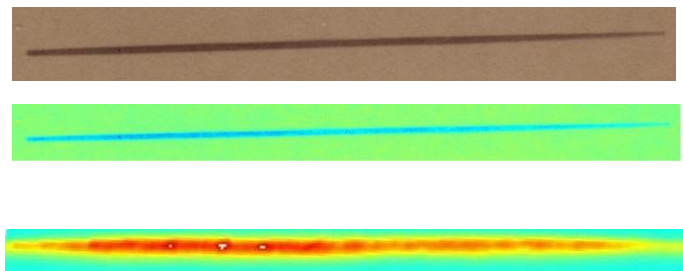


Figure 5-8 – Laser beam profile (single shot) after the sheet-forming optics on photographic paper (true and false colour) (top) and from the camera fitted with the LII and ND filters (bottom)

The energy profile of the laser sheet seemed uniformly distributed on the photographic paper but not on the laser profile taken via the camera. Moreover a further investigation

via the 3D representation of the laser profile shows an expanded Gaussian shape which is coherent with the different optics used and its original Gaussian round beam shape.

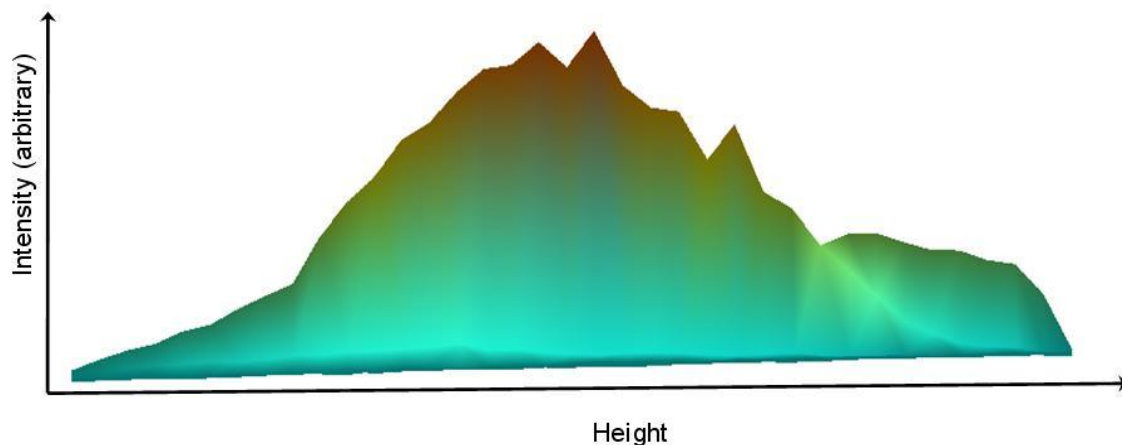


Figure 5-9 – Laser beam profile in three dimensions recorded by the camera

5.4 *Light collection system*

The light collection chain consisted of two different beamsplitters, one or two lenses (according to the measurement volume), one pinhole, different filters, two PMTs and one intensified CCD camera as illustrated in Figure 5-5 and Figure 5-10.



Figure 5-10 – Optical detection equipment layout

To split the light, two beamsplitter plates were used. These plates have an average reflectance and transmittance of 50/50 in the visible wavelength range.

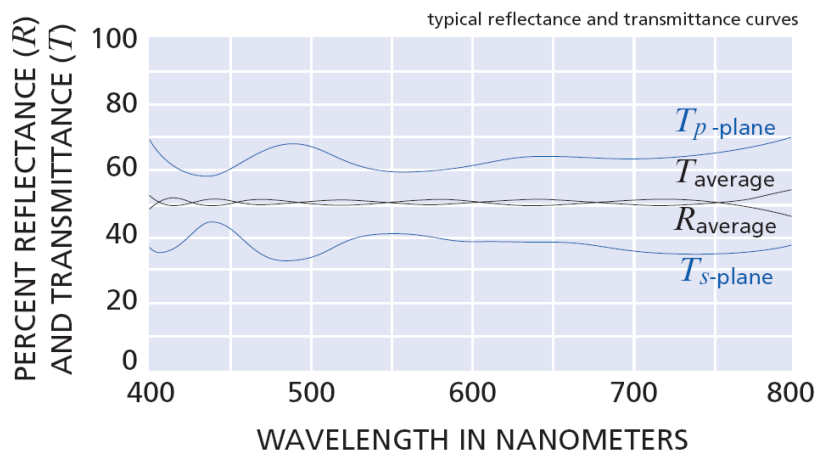


Figure 5-11 – Transmittance and reflectance ratio of the beamsplitters (Melles-Griot)

Due to beamsplitters, the light intensity reaching the detectors was reduced from the original signal by 50 % at the camera and by 75 % at the PMTs.

The filters used for the 2C-TiRe-LII are narrow-band interference filters centred at 400 and 700 nm wavelengths with 10 nm FWHM.

A 1 mm diameter pinhole was used to select the desired flame region with sufficient accuracy and sufficiently large enough to avoid dramatically dropping the signal level.

5.5 Spatial signal acquisition

The images of the flame were acquired via a camera coupled to an image intensifier, and characterised by a natural spectral sensitivity response between the range 340 to 700 nm. The intensifier was monitored by a control box able to configure the sensitivity and integrating time/gate. This improves the set-up by a higher sensitivity and by faster gating capabilities (a minimal time exposure of 5 ns to compared to the 100 ns for the camera). A lens was used to focus the camera on the desired area. To focus the camera, a calibration pattern was positioned where the centre of the flame was normally located.

Two other filters were used for the ELS and LII images. A 532 nm narrow interference filter (FWHM 9.4 nm) was selected for ELS to discriminate the background luminosity and record only the signal coming from the scattered laser beam light. Soot emits broadband and as long as the wavelength does not fall in the range where light is emitted by fluorescence, elastic scattering or flame natural luminosity, any wavelength can be used. Thus, a wide-band pass filter with a maximum transmittance peak at

400 nm and 80 nm FWHM was filling the LII selection conditions and was set in front of the camera.

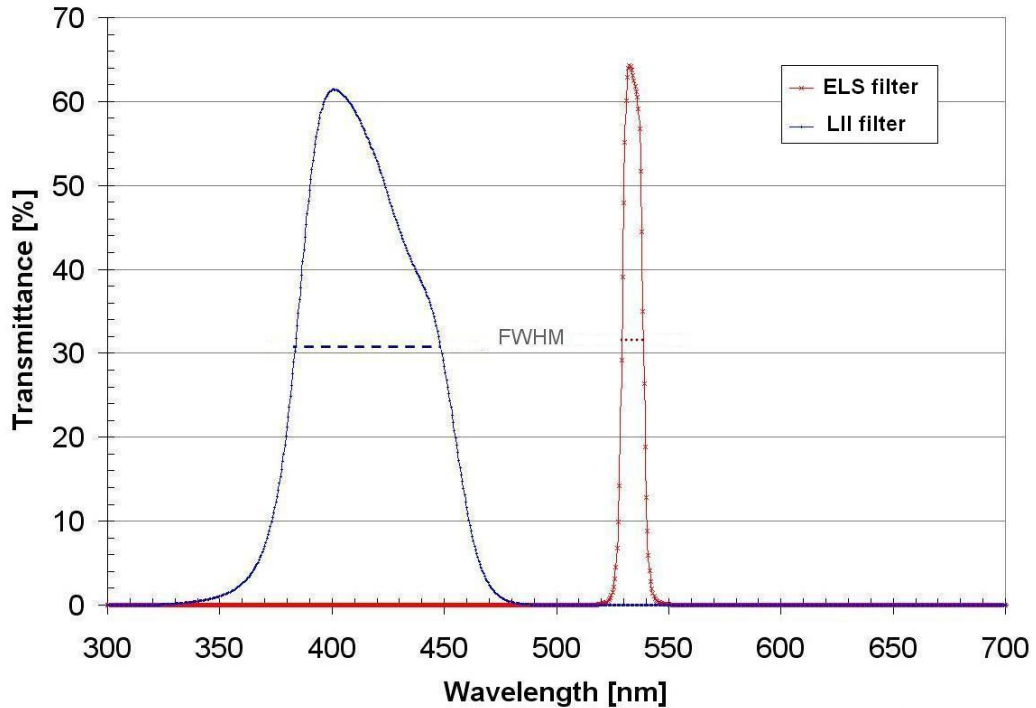


Figure 5-12 – ELS and PLII transmittance filter profiles

The ELS and PLII images were simultaneously taken by the same camera via an image doubler introduced between the filters and the camera lens.

5.5.1 CCD Camera

The camera used in this experiment is a LaVision FlowMaster 2 coupled to an intensifier. The camera was piloted by DaVis 7.2. The acquisition of the two images was performed by an image doubler in front of the camera lens. A special feature of the acquisition software splits into two the signals received on the CCD sensor and recognizes the setting as two different cameras. The characteristics of the camera are summarised in Table 5.

Camera type	Intensified camera
Sensor type	CCD
Sensor size	8.6×6.9 mm
Sensitivity	160 counts/photoelectron
Bit depth	12 bits
Exposure time	5 to 999,999 ns
Resolution	Up to 1280×1024 pixels
Frame speed	1 per fired cycle i.e. 0.83 Hz

Table 5 – Intensified camera's characteristics

5.6 Temporal detection system

From the previous chapter, the technique reviewed allowing soot particle sizing and soot volume fraction estimation is based on recording the LII signal with a good temporal resolution and at two different wavelengths. The current cameras are not fast enough to sample this signal. However, photomultipliers, with their fast rising time, allow recording the fast temporal decay of the LII signal but at the cost of a punctual sampling.

5.6.1 Photomultipliers

The two photomultipliers used were RCA 4526 from Dantec Dynamics LTD. Their characteristics (sensitivity, rising time) depend on the voltage applied to them (Figure 5-13). They have a noticeably good sensitivity in the visible range i.e. 300 up to 700 nm.

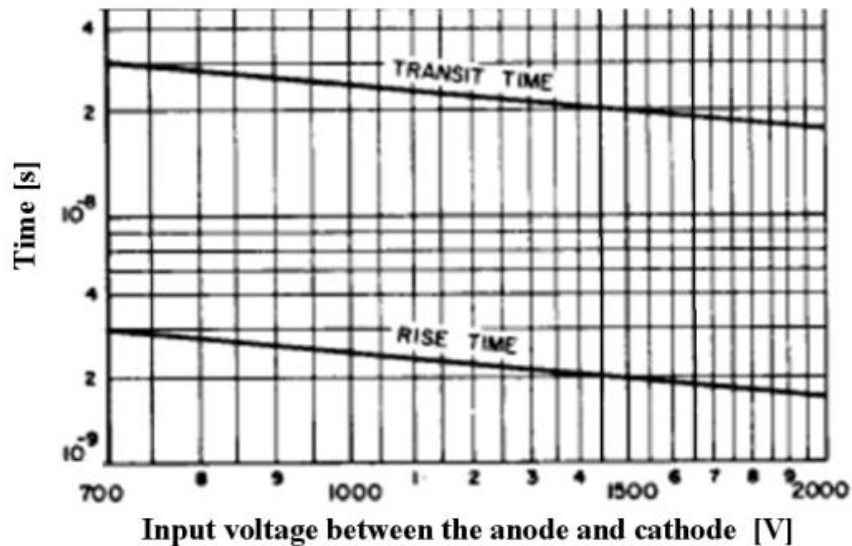


Figure 5-13 – PMTS temporal characteristics

The rising time and sensitivity of the photomultipliers depends of the input voltage between the anode and cathode (Figure 5-14). In the experiments different voltages were used, between 1000 up to 1800 V i.e. a rising time between 2.3 and 1.9 ns.

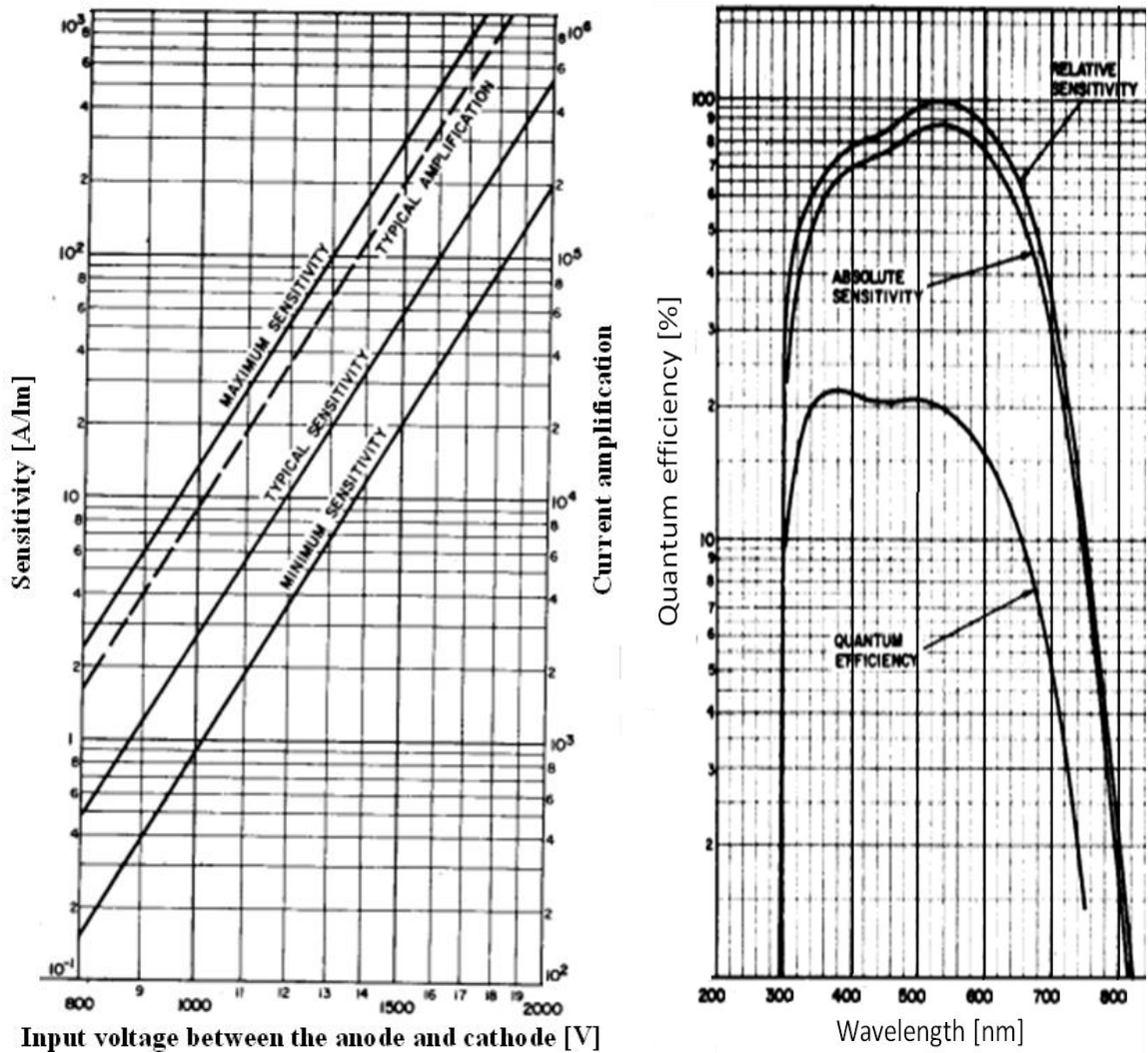


Figure 5-14 – Sensitivity and efficiency of the PMTs

PMT efficiency decreases for the upper visible wavelengths. The sensitivities of interest for the wavelengths used are 80 % for 400 nm and 30 % at 700 nm (from the relative sensitivity curve). These photomultipliers are characterised by a relatively good spectral response at 700 nm, even if the sensitivity ratio is in favour of the 400 nm wavelength.

5.6.2 Oscilloscope

The signals from the PMTs were acquired via a Wavesurfer 422 from LeCroy™, a digital oscilloscope capable of recording at 2 GS/s and with a 8 bits vertical resolution. This type of oscilloscope is fast enough to sample the signal coming from the PMTs. PMTs being the “slowest” component, limiting the sampling rate of the acquisition chain. The acquisition was triggered on one of the temporal LII signals and stored automatically in, and by, the digital oscilloscope.

5.7 Calibration method

The calibration of the PMTs is one of the most crucial parts of the experiment, which allows quantitative results to be obtained after data processing.

5.7.1 Absolute light calibration

The estimation of equivalent particle temperature and soot volume fraction according to the NRC group method (Snelling et al., 2005a, Smallwood et al., 2002) need the yield of the optical equipment which is defined as the relation between emitted light from a calibrated lamp expressed by the spectral irradiance in $[\text{W}\cdot\text{m}^{-2}\cdot\text{nm}^{-1}]$ or spectral radiance $[\text{W}\cdot\text{sr}^{-1}\cdot\text{m}^{-2}\cdot\text{nm}^{-1}]$ and the output signals from the PMTs [V].

To determine the coefficient of this relation, a quartz tungsten halogen calibrated lamp from Oriel was used as a calibration source. According to the manufacturer's data, the lamp has an equivalent blackbody radiation temperature of 3221 K and a filament size of 6.0×16.0 mm, which is wide enough to cover the volume sampled by the pinhole/PMTs. This type of lamp has only one operating point, the voltage of the lamp cannot be modified and was supply by a high quality dedicated power supply.

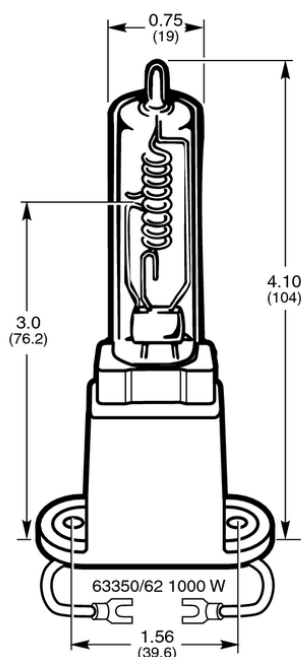
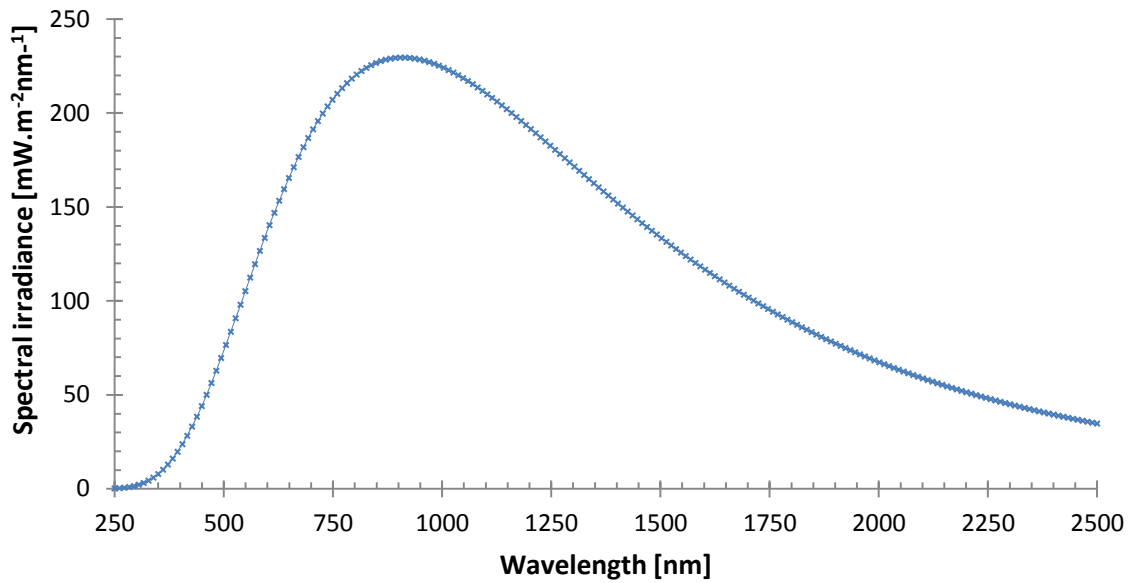


Figure 5-15 – Drawing of the calibration lamp (source: Oriel™)



**Figure 5-16 – Calibrated spectral irradiance of the Oriel lamp
(full spectrum equivalent to a blackbody radiating at 3221 K)**

In this experiment, only values at 400 and 700 nm wavelengths are necessary, i.e. 21.7197 and 188.996 $\text{mW}\cdot\text{m}^{-2}\cdot\text{nm}^{-1}$. Therefore signal intensity at 700 nm is 8.7 times higher than at 400 nm.

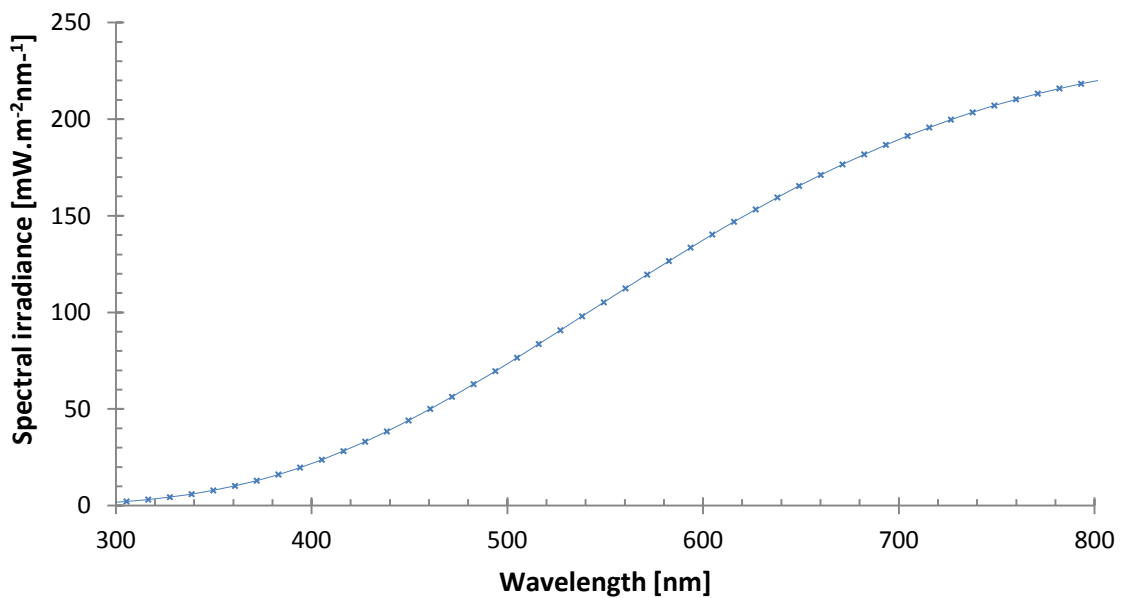


Figure 5-17 – Calibrated spectral irradiance of the Oriel lamp

The calibration of the optical system was carried out with the same layout and settings as the experiment. The lamp was set at the flame position, the lamp strip positioned at the sampling area. The influence of all the optics was taken into consideration such as beamsplitters, pinhole, lenses, filters, optical windows (for the RCM) and PMTs.

Photomultipliers have a better response to pulsed signals as they can saturate for continuous signal. Hence a 1 kHz chopper was used to pulse the steady flux emitted by the calibration lamp.

The figure below (Figure 5-18) shows the typical calibration curves of the PMTs for the different filters used. Each point is an average of 100 consecutive measurements.

The calibration for local 2C-TiRe LII was performed by imaging the incandescent tungsten strip at the pinhole plan. The methodology described by Snelling et al. (2005a) was applied using the tungsten emissivity and knowing the equivalent temperature of the filament. The calibration was repeated for each measurement location.

However the calibration of the PMTs output for global 2C-TiRe LII was performed differently as the Snelling's calibration method is no longer valid if the complete probed volume is not fully covered by the strip of the calibration lamp. An iris was set at 500 mm away from the lamp and a 500 mm focal length lens was set next to it. The spectral irradiance of the flame was calibrated and measured at 500 mm from it. Knowing the surface area at 50 cm of the lamp defined by the iris, the theoretical irradiance received by the PMT can be computed. The surface area at 50 cm being $5.024 \times 10^{-3} \text{ m}^2$, the photomultipliers received theoretically, if no energy (light) was lost, 0.109 mW.nm^{-1} at 400 nm wavelength and 0.949 W.nm^{-1} for 700 nm wavelength. Due to the relatively large collection angle covered by the lens/PMTs, the configuration was slightly more sensitive to the central position than on the edges of the sampled area. Usually in the Snelling's calibration method, the calibration factor includes the collection angle and sampled cross section area. In the case of global 2C-TiRe-LII, surface of sampled measurement and collection angle are measured. PLII images give accurate measurements of the flame cross section, which is required for the correction of the soot volume fraction data.

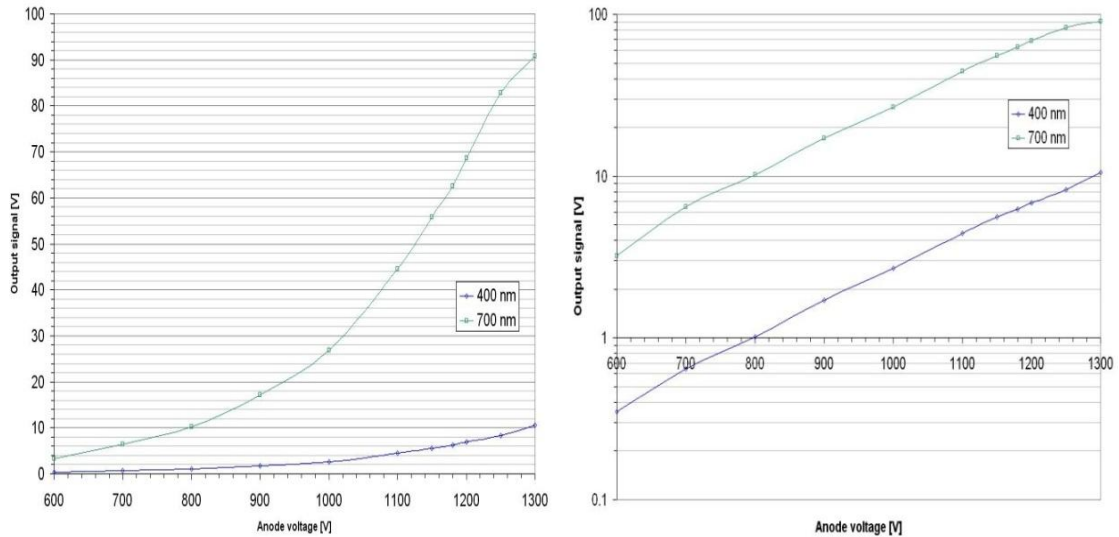


**Figure 5-18 – Calibration curves of the Photomultipliers
(from Santoro burner and global 2C-TiRe-LII conditions)**

Figure 5-18 represents the output voltages from the PMTs (source was the calibration lamp) for different anode voltages. According to the PMT manufacturer the sensibility is exponentially proportional to the voltage applied; the experimental calibration curves verify this trend. The signal filtered at 400 nm wavelength is weaker than the one at 700 nm. As stated before, the radiance at 700 nm wavelength is almost eight times greater than at 400 nm (Figure 5-19). But this difference is partially compensated by variations in the PMTs' spectral efficiency (almost 3 times more efficient at 400 nm). Above 1250 V, at 700 nm, the signal is too high and the PMT starts to saturate. While a PMT is in a saturated mode, the output signal is not linear i.e. the output voltage signals are not proportional to the light received by the detector. The linearity response of the PMT is primordial in order to obtain valid results. The calibration curve also defined for which output voltage the PMTs start to be in the saturated mode (~80V). The LII signal intensities were lower than the intensity from the calibration lamp, confirming that the temporal LII signals were recorded within the linear response of the PMTs.

The PMT voltages were set differently according to the sampling region and surface. In order to give a range of the voltage used for global 2C-TiRe LII measurements, on the 700 nm wavelength channel, 1000 V was apply to the PMT, and 1200 V for the channel at 400 nm wavelength. However higher amplifications were necessary for local 2C-TiRe LII measurements as signal intensities were lower, 1700 V at 700 nm and 1800 V at 400 nm wavelength.

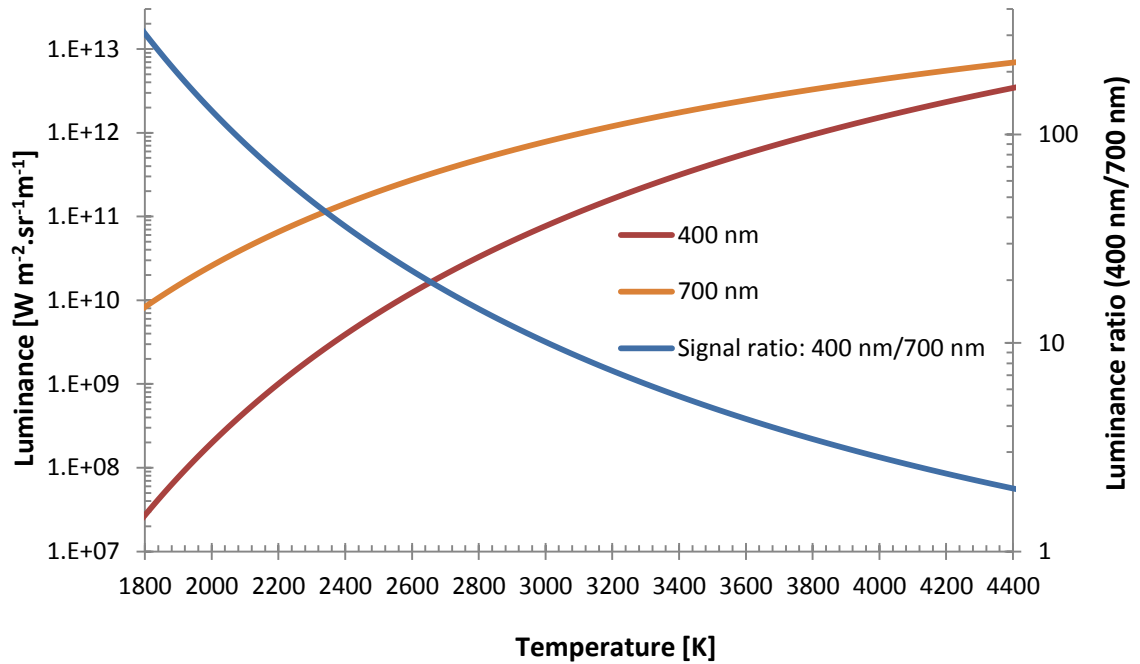


Figure 5-19 – Blackbody radiation at 400 nm and 700 nm wavelengths as function of the temperature and the corresponding signal ratio

5.8 Camera spatial calibration

A test pattern was acquired via the camera to estimate its field of view, to spatially calibrate and to correct the two images to each other. The acquisition of the target pattern presented in Figure 5-20 was recorded by the intensified camera with the spectral filters on. The target was illuminated by an extra spotlight. Due to low and different intensities on the two acquisitions; to compensate images were recorded separately with different integration times.

The spatial calibration and corrections for a perfect juxtaposition of the two images were processed by a DaVis script. The images acquired thereafter were automatically pre-processed by the software. The equivalent positions of the simulated two cameras are represented in Figure 5-21.

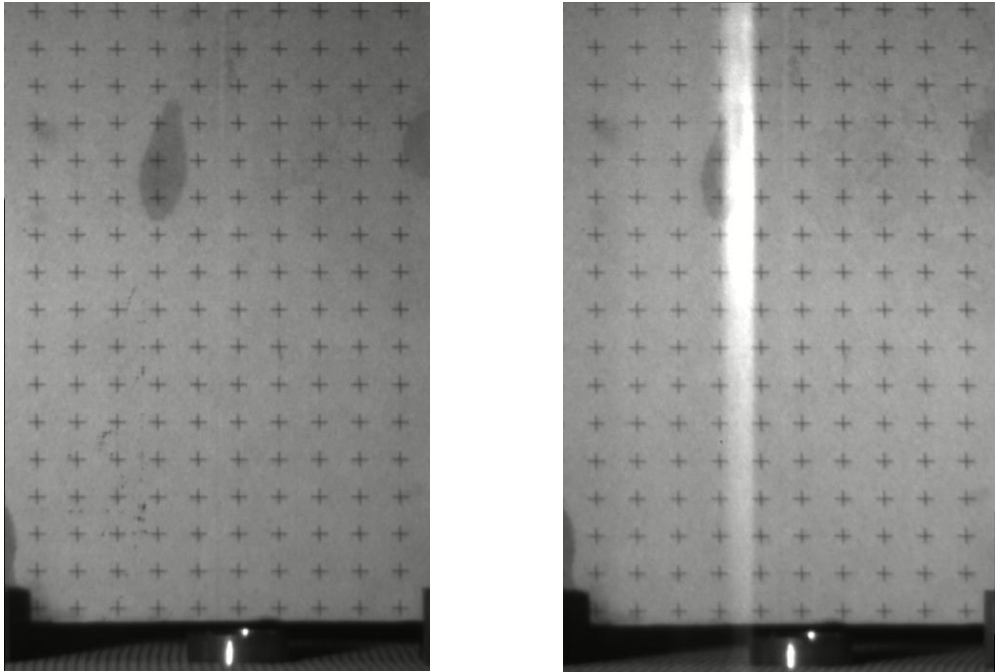


Figure 5-20 – Camera calibration patterns for the ELS (left) and PLII images (right).

A field of view of 25 mm wide and 110 mm high was large enough to cover the region of interest, which consisted of the entire height of the flame and optical access of the RCM. Images were spatially resolved to 8 pixels per millimetre.

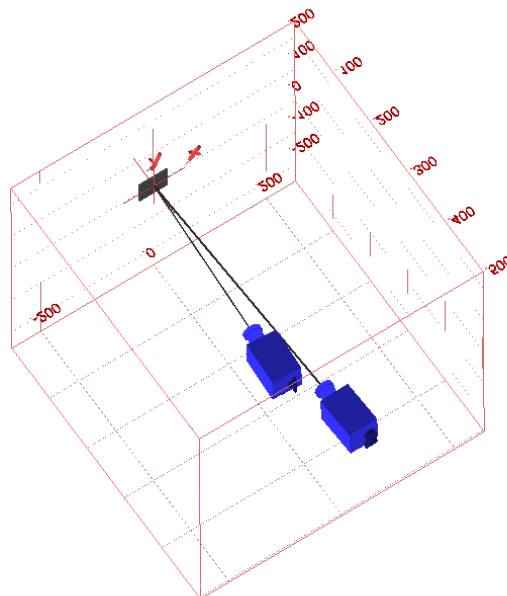


Figure 5-21 – Camera image correction (DaVis processing)

A slight difference could be noticed on the intensities between the two images while the target was observed without any filters, and also a difference in the field of view boundaries due to the use of the image doubler and beamsplitter that introduced a

difference in visualisation angles. To avoid this effect, the camera was set as far as possible from the beamsplitters and the beamsplitter was set to the minimal distance possible from the flame according to the RCM machine surrounding. The extended distance between the camera and the flame was slightly detrimental to the spatial resolution and signal collection efficiency.

The angle difference in the recorded images is not significant when the flame is in an open area, such as in the burner condition, however this can be critical for optical combustion chambers conditions. With a restricted optical access, the angle difference generates ‘blind spots’ which are different for each camera. Images were cropped to select only the field of views that overlapped, thus only considering regions that could yield particle diameters and soot density values.

However, no correction was made for the sensitivity fluctuations across the CCD sensor as they are negligible. The difference is due to a non-uniform illumination of the pattern. The intensity is the main factor in determining the soot particle size as it is the ratio of the intensity of each image. A difference in intensity would not introduce a systematic error in the 2D mapping of the particle size, as the error would be integrated in the calibration factor.

5.9 *Spatial calibration of the local measurement 2C-TiRe-LII*

One of the main challenges of the technique is to determine accurately which region within the flame is sampled by the PMTs, and to link it to the image recorded by the camera. To solve this problem a pinhole of 1 mm diameter was set on the laser beam path. A plate was set at the position of the flame and at 45 degrees to the collection optics. The position of the spot was recorded via the spatially-calibrated camera. The position of the laser spot was adjusted to the desired location by either moving the plate for lateral shift or by moving the pinhole up or down for vertical shift. A second pinhole was set at the plane where the image of the flame was imaged. The pinhole position was adjusted to coincide with the laser spot location.

The estimated uncertainty on the position error of the sampled volume in the flame is better vertically than horizontally, as an error on the 45 degree angle can introduce an error on the lateral position.

5.10 Conclusions

The various experimental parameters influencing the LII signal or affecting the accuracy of the experiment have been outlined and reviewed. The different parameters used in the experiment have been defined with regards to the benefits or restrictions due to the setup. The devices and optical components have been listed and their main properties described. The calibration of the photomultipliers was achieved and presented for the case of the diffusion flame. Experimental settings being chosen and calibration being done, the application of the optical diagnostic to investigate soot formation can be carried out.

6 CHAPTER VI: QUANTITATIVE STUDY OF SOOT FORMATION UPON A LAMINAR DIFFUSION FLAME

The fundamental investigation of soot formation to further understand soot growth and oxidation was preliminary performed and achieved by applying the new laser diagnostic upon a laminar diffusion flame. A diffusion flame has the advantages of being relatively steady (no major variations between shots) and simpler to operate than an optical engine. Another major advantage is the possibility of comparing measurements against published results for similar burner designs (e.g. Santoro, Gülder or McKenna burners). A diffusion flame was preferred to a premixed flame for higher soot volume fraction, larger particle size and nearest conditions to the type of combustion present in Diesel combustion chambers. Therefore a Santoro burner was selected to first validate the technique before applying it to an optical Diesel engine. However a diffusion flame is a complex flame to investigate, with spatial temperature variations, different concentrations of several chemical species, variations in soot volume fraction and particle diameters. Soot properties and degrees of agglomeration may also vary throughout the flame. Therefore the laminar diffusion flame produced by this type of burner is a useful investigation place to study soot formation by determining particle size, soot volume fraction and number density across the flame.

6.1 *Santoro Burner*

The Santoro burner along with the McKenna and Gülder designs, is a reference burner utilised in the LII community. Flames from these burners are used for soot studies and LII measurement comparisons. They have been investigated by several research groups, they are well characterized and data are available in the literature (Glassman, 1998b, Pinson et al., 1993, Quay et al., 1994a, Santoro and Miller, 1987, Santoro et al., 1983, Santoro et al., 1987, Lee et al., 2005) – (Table 6 and appendix E). CFD results on soot formation for a laminar diffusion flame are also available (Liu et al., 2002, Liu et al., 2008) - (results in appendix E). The CFD computation results can be compared to the experimental results. Temperature is relatively steady across the flame (Santoro and Miller, 1987). Soot volume fraction of the flame produced by this burner was investigated in parallel by extinction measurement (appendix E).

Soot volume fraction [ppm]		Soot primary particle diameter		Gas phase temperature [K]		Particle carbon to hydrogen-atom ratio	
3	LII; Yale (Schulz et al. 2006)	74 nm $\sigma=1.5$	LII; IVG (Schulz et al. 2006)	1600	TC; Santoro and Miller 1987	5.94	Dobbins et al. 1998
3.7	LII; IVG (Schulz et al. 2006)	29.3nm $\sigma=1.18$	TEM; IVG (Schulz et al. 2006)	1600	TC; Vander Wal et al. 1999		
4.3	Santoro et al. 1983	35 nm ± 3 nm	TEM; Dobbins and Megeridis, 1997	1600	TC; Koylu et al. 1997		
3.8	TSPD; Koylu et al. 1997	31 nm	TEM; Koylu et al. 1997	1584	TC; Dobbins et al. 1998		
5.5	TPD; McEnally et al. 1997	33.3nm ± 3.2 nm 32 nm	TEM; Vander Wal et al. 1999 TEM; Puri et al. 1993				

Table 6 – Published results for the Santoro burner at 50mm HAB

Research group: IVG: Duisburg-Essen University (B. Tribalet, B. Kock, C. Schultz)

Yale: Yale University (B. Connelly, M. Long)

6.1.1 Set-up

The Santoro burner was first designed and described in Santoro et al. (1983). The burner was made at the University of Brighton according to the drawings (appendix C) published in the literature (Quay et al., 1994a) in order to replicate the burner and experimental conditions as accurately as possible. The burner is composed of an 11 mm brass tube for the ethylene flow, surrounded by a ceramic honeycomb of 102 mm outer diameter for the air co-flow. Air goes through a copper mesh grid, a 52.4 mm high layer of 3 mm diameter glass marbles and ceramic honeycomb for straightening the flow into a laminar co-flow. The Santoro burner produces an axisymmetrical laminar diffusion flame (Figure 6-1), standard conditions being an ethylene (C_2H_4) flow of 0.231 slm and an annular air co-flow of 43 slm (Dobbins and Megeridis, 1987, Koylu et al., 1997, Smyth et al., 1997). However, due to the flame being particularly sensitive to small ambient drafts, the air co-flow was slightly increased to 64 slm (Ni et al., 1995b, Santoro et al., 1983, Santoro et al., 1987, Michelsen, 2006) and the flame was confined by a solid wall cylinder of 108 mm diameter by 195 mm high with optical accesses. An air extractor was positioned at 100 mm above the chimney to extract the burnt gases and soot produced by the flame. Increasing the air co-flow from 43 slm to 64 slm did not

have a noticeable effect on the flame height and flame irradiance but greatly improved the flame stability. However, a higher co-flow contributes to increasing the oxygen to ethylene ratio and increases chemical reaction rates, especially the soot oxidation rate. Therefore soot volume fraction and particle diameter can be expected to be slightly reduced as compared with an experiment performed for a 43 slm air co-flow. A laminar diffusion flame is mainly characterised by its visible height; in this experiment, a 98 mm visible flame height was measured. The diffusion coefficients of the different chemical species present in the flame are the principal factors influencing the combustion.



Figure 6-1 –Laminar diffusion flame produced by the Santoro burner

The purity of the ethylene was stated to be 99.5% from the supplier and the air was supplied from the compressed air grid. The ethylene flow was measured and controlled accurately with an ethylene-calibrated electronic mass flow controller (model: Omega FMA 3104) and the air flow with an inline flow meter.

In order to repeat the experiment on the RCM, the layout of the optical set-up was designed to fit around the Proteus RCM rig. The two different optical layouts are detailed in the previous chapter.

6.2 Soot quantification by Auto-calibrated-2C-TiRe-LII

6.2.1 Measurement volume

Two different 2C-TiRe-LII sampling approaches were used in the experiment, the first one was to sample a small location within the flame while in the second, sampling volume was extended to an entire vertical slice of the flame.

The flame was sampled at different heights, from 30 to 60 mm above burner, and at different lateral positions (on centreline and at the edges of the flame) for two different laser planes (on centreline and 3 mm forward from the central axis). Figure 6-2 illustrates the different sampled points by the PMTs. The standard measurement height location for this burner defined by the LII research consortium is located on the flame's centreline, at 50 mm above burner measured from the tip of the 11 mm diameter fuel pipe outlet. A $\times 1.5$ magnified image of the flame was focalised on a 1 mm diameter pinhole in order to select the flame location, thus creating a probe flame volume of 0.785 mm^2 times the laser sheet thickness.

However a different set-up was considered in the possible case of low LII signal in the RCM. The LII signal coming from the flame was focused on the PMTs and was not spatially filtered by a pinhole. By increasing the probed volume to a vertical slice of the flame, the signal was stronger and steadier. However this is an unusual way to operate. TiRe-LII technique is usually used for sampling a few cubic millimetres volumes and therefore, with some compromise on the accuracy, the sampling volume was extended to an entire vertical slice of the flame.

The effect of laser fluence on the LII signal was first studied to validate the moderate fluence regime. Particle temperature, soot volume fraction, particle diameter, number density were investigated at different sampling locations. Higher fluences generated slightly higher LII signal amplitudes. However when signals were normalized, their decreasing rates were very similar. Particle temperatures were therefore very close and the high sublimation regime was not reached.

The PMT control voltages were adjusted according to the LII peak intensities. However due to low intensity levels of the LII signal at some locations, higher amplifications

were set by increasing to their maximum PMT voltages (1800 V), causing the disadvantage of higher noise to signal ratio on the recorded signal.

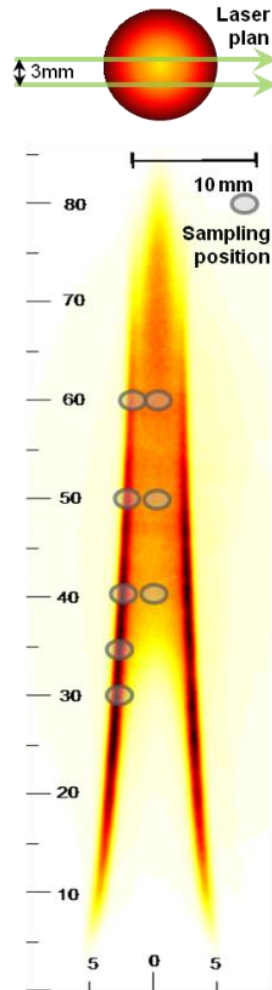


Figure 6-2 – Illustration of the different 2c-TiRe-LII sampling locations within the flame and the two laser planes

The complex data processing requires different operations in order to obtain the quantitative spatial distributions of soot volume fraction, number density and particle size. The different tasks are summarized in the diagram (Figure 6-3).

For all the images presented, the laser excitation comes from the left side as presented in Figure 6-2.

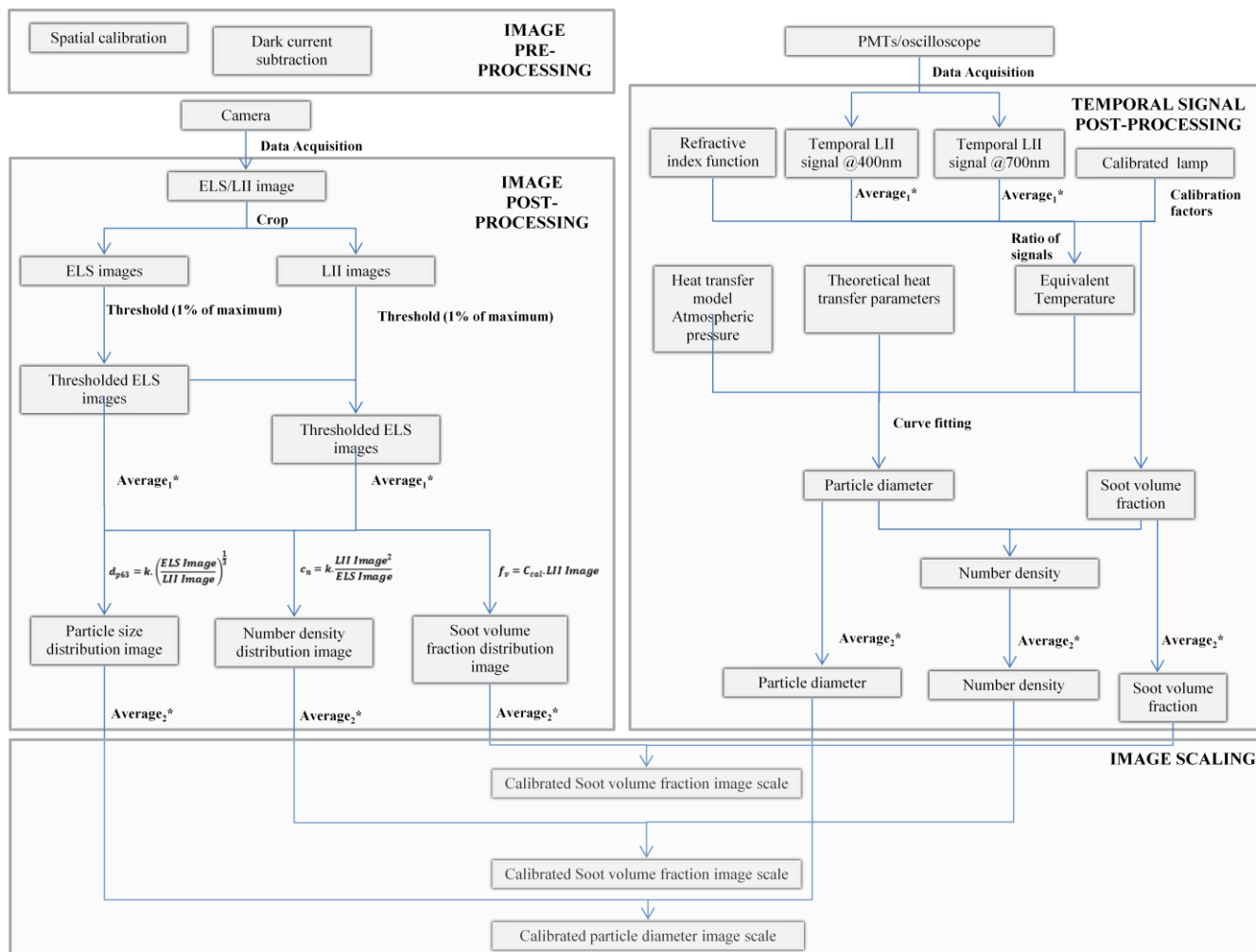


Figure 6-3 – Post-processing diagram for the Santoro burner

6.3 Global 2C-TiRe-LII measurements

6.3.1 Time-resolved LII signals

The raw LII signals recorded at 400 and 700 nm for a probing volume of a vertical slice of the flame are presented in Figure 6-4. The global TiRe LII signals were averaged over 1000 signals in order to reduce the noise, to smooth the signals and to obtain sensible mean results. Theoretically, the maximum amplitude is not temporally dependent on the wavelength and the peaks must occur simultaneously. However a few nanoseconds' delay is noticeable on the experimental signals recorded at different collection wavelengths, thus peaks were not perfectly synchronised. The PMTs have a different response time mainly due to different PMTS voltage settings. The problem was corrected through signal post-processing to synchronise the LII peaks in time.

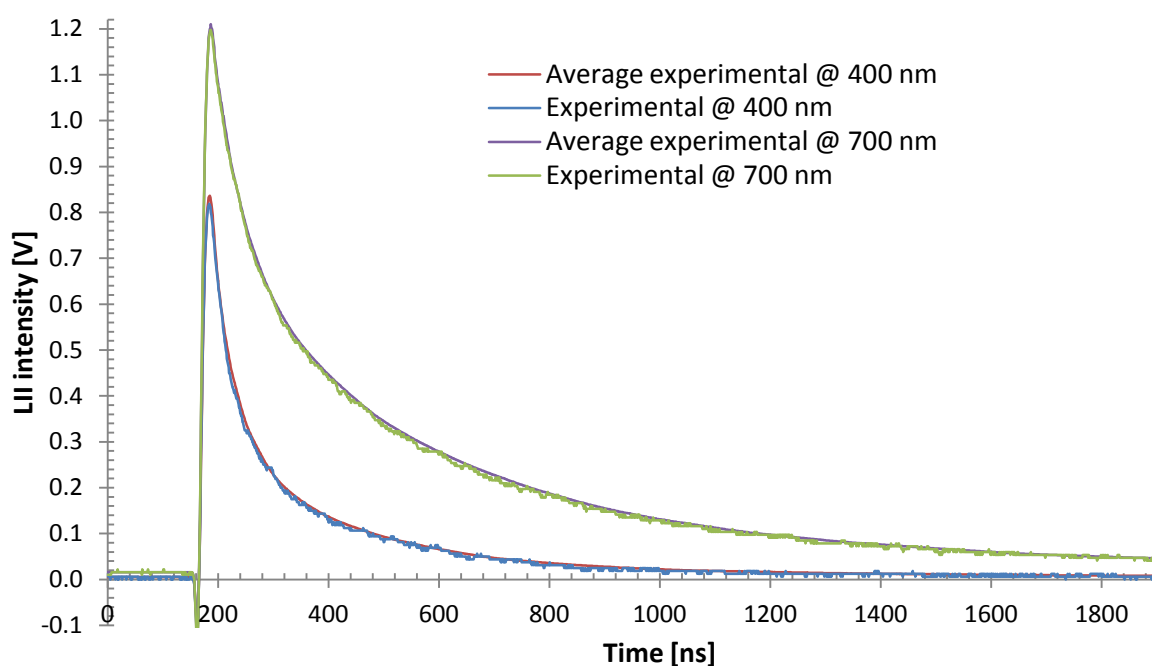


Figure 6-4 – Raw and averaged temporal LII signals recorded at 400 nm and 700 nm (vertical slice of the flame sampled)

The standard deviation between shot to shot measurements and averaged signals is low (Figure 6-4), 4.86×10^{-5} V for the signal recorded at 400 nm and 3.29×10^{-5} V for the one recorded at 700 nm. Therefore the repeatability and stability of the experiment was considered excellent. A pre-selection of the signals was operated by the oscilloscope as the trigger threshold was set to 1 V on the 700 nm LII temporal signal.

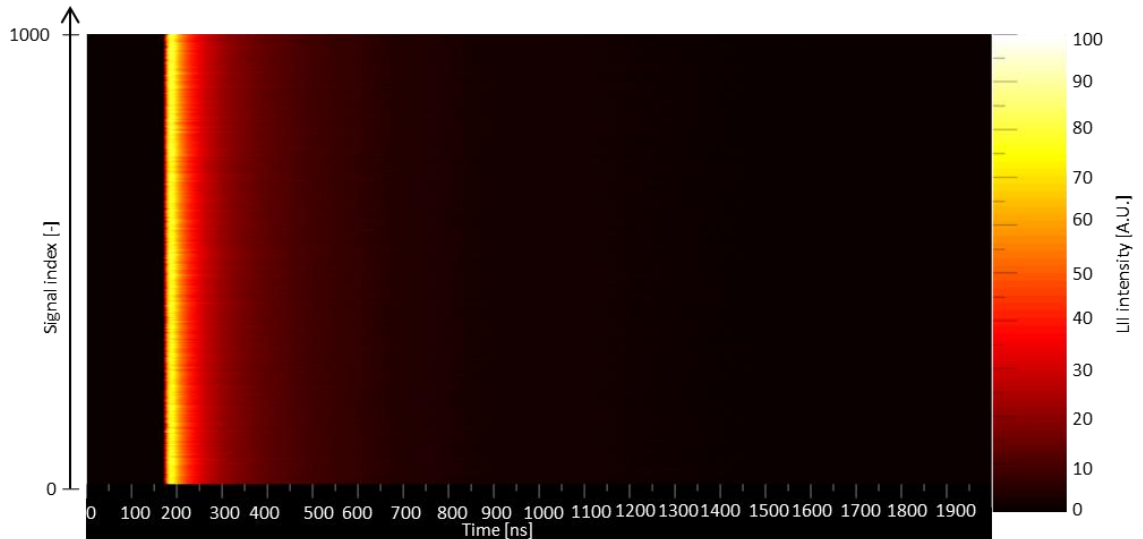


Figure 6-5 –Image representing 1000 LII temporal signals

The figure above is the illustration of 1000 temporal LII signals, representing it this way allows the global visualization of a large data set of temporal LII signal decay.

To discard any possible unwanted signals, a selection criterion was based from the maximum LII peak intensity of the data set. Signal peaks inferior to 5 % of the maximum LII peak intensity of the dataset were discarded from the averaging. The repeatability of the measurements was excellent, with less than 0.5 % discarded samples. An example of dataset (Figure 6-5) shows the good repeatability of the data, although as the selection is based on the highest signals value this processing biased the results towards higher averaged soot volume fractions. Figure 6-5 also shows a maximum variation of ± 2 ns on the temporal shift of the LII peaks.

Laser fluence

In the previous chapter the influence of laser fluence on incandescence signal was reviewed. The sublimation being the predominant heat transfer above ~ 3400 K, a sublimation threshold involving major sublimation of the soot particles is usually assumed to be around 3800 K corresponding to a laser fluence above 0.15 J.cm^{-2} at 1064 nm, and 0.12 J.cm^{-2} at 532 nm.

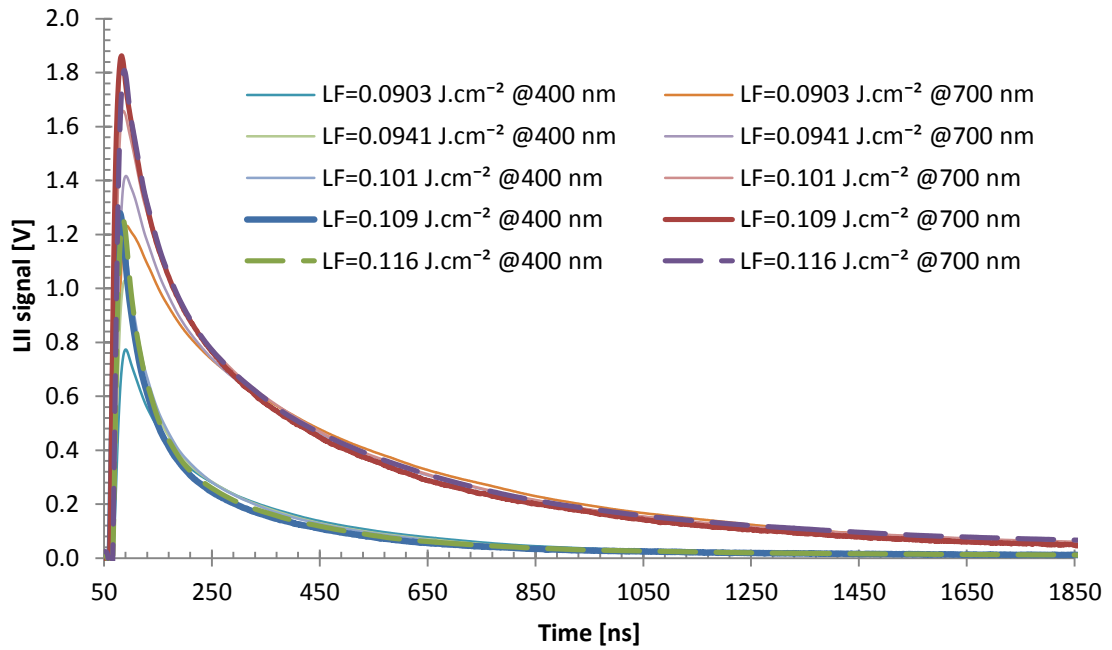


Figure 6-6 – Laser fluence effect on LII signal (experimental)

From the two LII signals recorded at two different wavelengths, the mean equivalent temperature of the particles can be determined using Equation 10. The peak temperature is used to determine the laser fluence by solving the different heat transfer equations. The fluence effect on LII signal was experimentally studied for fluences between 0.09 and 0.116 J.cm⁻². The laser energy was measured with a power meter and the laser sheet dimensions were considered constant over the different fluences.

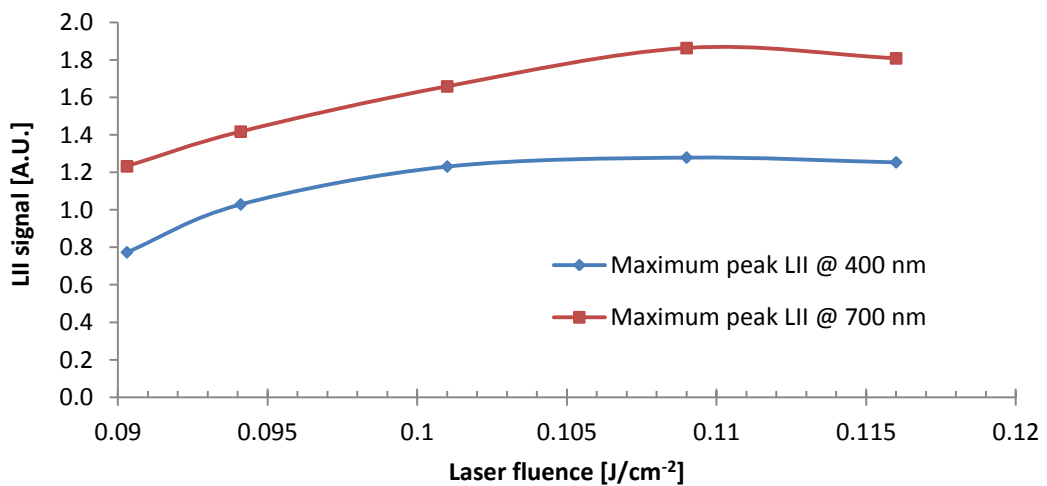


Figure 6-7 – Laser fluence effect on LII signal peak (experimental)

From Figure 6-6 and especially on Figure 6-7, the threshold is noticeable and measured to be between ~0.110 and 0.116 J.cm⁻². A slight increase of the fluence does reduce the incandescence peak signal. A sharper peak due to sublimation effect is not noticeable

when increasing the fluence above 0.11 J.cm^{-2} . The temperature sensibly reaches the same value and therefore the cooling rate is in the same range. The results from Figure 6-8 validate the assumption on the fluence, i.e. the chosen fluence is at the limit of the moderate regime and avoids high sublimation of soot particles.

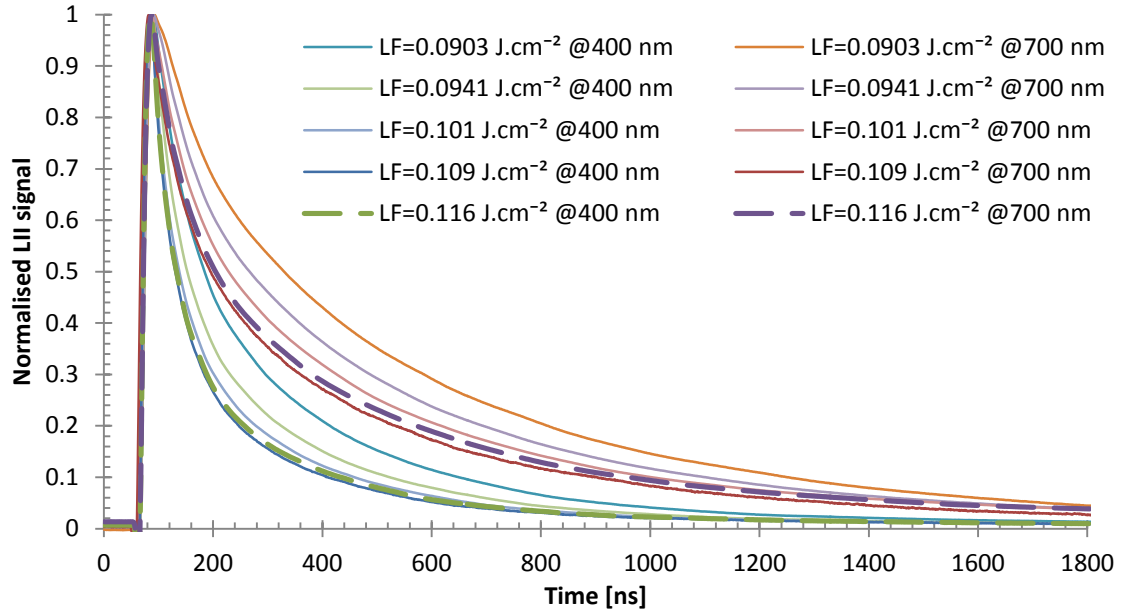


Figure 6-8 – Laser fluence effect on normalized LII signal (experimental)

For the maximum laser excitation (0.116 J.cm^{-2}), the fluence estimation by solving the heat transfer equations and from the equivalent peak temperature as initial parameter give a fluence of 0.1145 and 0.1221 J.cm^{-2} depending on $E(m)$. There are several explanations about finding a different fluence from the one recorded experimentally. The energy was measured before the slit (due to the laser sheet being wider than the head of the power meter after the slit); therefore the fluence at the sampled position was slightly overestimated. Absorption and scattering reduce the fluence along the laser path. The theoretical model uses an initial temperature of 1600 K which can be considered low, an initial temperature of 1800 K gives a fluence of 0.1027 or 0.1113 J.cm^{-2} (depending on $E(m)$) which does not give a better agreement with values in the literature and fluences recorded experimentally. In the processing, $E(m)$ was supposed to be wavelength independent in order to match the recorded experimental laser fluence (0.116 J.cm^{-2}). In the theoretical parameter comparative study, $E(m)$ was considered to be constant and wavelength dependent in section 6.3.2, but the difficulty to fit properly the experimental curve for a λ -dependent $E(m)$ value confirmed the choice of using a constant value for the refractive index function.

6.3.2 Particle sizing

As reviewed in chapter 2, particle sizes can be estimated from the decrease of the incandescence signal due to the cooling rate depending on the particle diameter. The heat transfer equations governing the cooling rate were solved using a Runge-Kutta method (RK4) with a 10^{-10} s time step. The resulting theoretical LII signals were used to fit the experimental LII signals. A least mean square method was used as a criterion to determine the quality of the fitting, and using this criterion the optimal diameter was adjusted by dichotomy.

The PMTs have a fast rising time, in the order of the nanosecond, however they are not fast enough to record accurately the initial rise of the LII signal. Therefore the fitting of the experimental LII signal is not possible from the start of the heating up; the rising part of the signal is never considered in the fitting even if the modelling is possible by using the laser fluence as the main input parameter.

Therefore the theoretical fitting always starts from the decreasing part of the LII signals. The initial inputs values for the LII signal computation are crucial; two approaches are possible for the fitting of the curves. The first one considers that all the particles reach the same temperature, using this temperature as initial parameter and the modelling starts at the LII peak or after the laser pulse considering that particle temperature is known by determining it by 2-colour pyrometry (Kock et al., 2002, Boiarciuc et al., 2006). This approach involves some inconvenience such as not considering the slight difference between temperature peaks depending on particle diameter, neglecting sublimation effects during the heating up and moreover does not consider the effect of the absorption at the end of laser excitation if modelling starts from the LII peak. There have been attempts to fit the LII decay curves with this approach. However, due to the maximum gradient happening a dozen of nanoseconds after the peak, not considering absorption would create an important error between the experimental and theoretical LII signal straight from the beginning. Starting the comparison a few dozens of nanoseconds after the peak was considered to be too late due to large temperature difference between the particles.

The second approach uses the peak temperature to determine the exact laser fluence, and then compute the complete LII signal. This approach does not have disadvantages of the previous approach; however, it does increase the sensitivity dependence to the absorption modelling and input parameters.

The first approach was first opted; different time-zeros for the start of the fitting were considered, at the peak, 15 ns and 60 ns after the peak. After taking into consideration all possible variable combinations in order to best fit the curves, the deviation between theoretical and experimental was still high. Therefore the second approach was considered.

A time step of 0.1 ns in the Runge-Kutta method was defined for the modelling in order to avoid any computation artefact due to the high gradients during absorption heat transfer. A time step equivalent to the experimental one (1 ns) was demonstrated to be too long and did introduce some computational errors in the modelling.

LII curve fitting was carried out on the two LII signals collected at 400 nm and 700 nm. A slight difference was found between the optimal diameters. An average was not considered as the final particle diameter, the fit quality of the signal at 700 nm being better, the diameter resulting from this fit was considered as the final optimal diameter. From the fit of the signal at 700 nm, a 27.1 nm equivalent particle diameter is obtained with a standard deviation of 7.6×10^{-2} and from the fit of the signal at 400 nm, an equivalent particle diameter of 25.4 nm with $\chi^2=0.13$, producing a final result of 26.25 nm. Using the first approach to determine the particle diameter, the fits give an equivalent diameter of 33.6 nm at 700 nm and 30.2 nm at 400 nm wavelength, with a respective standard deviation of 0.36 and 0.82, for an average of 31.9 nm.

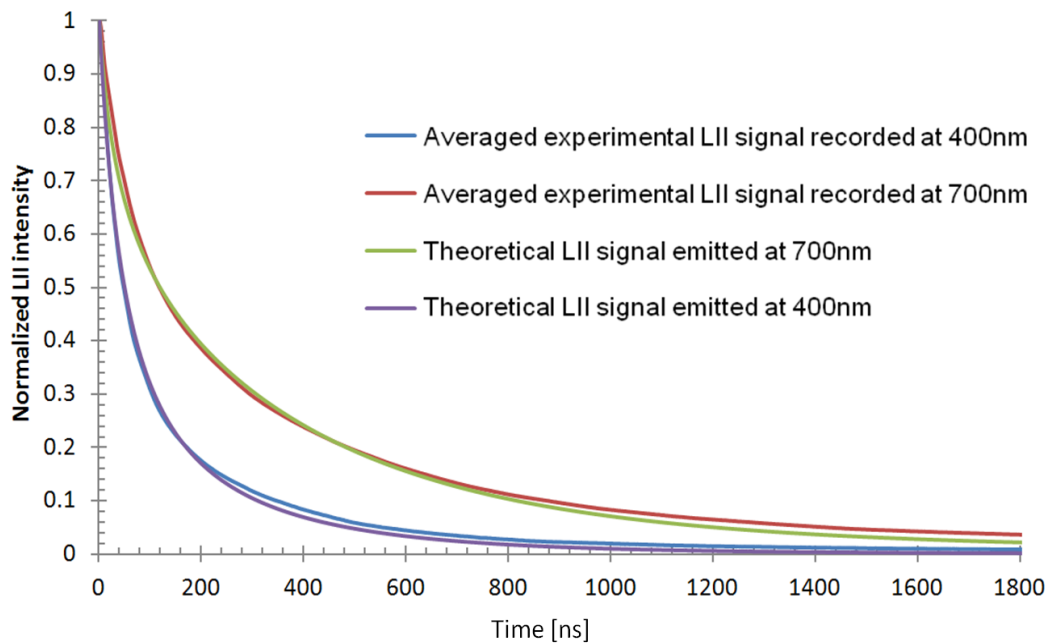


Figure 6-9 –Averaged experimental temporal LII signals with their best fitting by theoretical curves (entire flame sampled)

The lower the collection wavelength, so the shorter the LII signal recorded. The quality of the curve fitting depends on the number of measurement points, therefore on the signal intensity and on the decay rate. A LII signal lasting longer can be compared with more relevant points and the initial point is less crucial as the decay rate is lowered therefore the estimation error decreases. The figure below shows the fit quality for the two different wavelengths and for different diameters (± 2 nm and 5 nm from the optimal fit diameter).

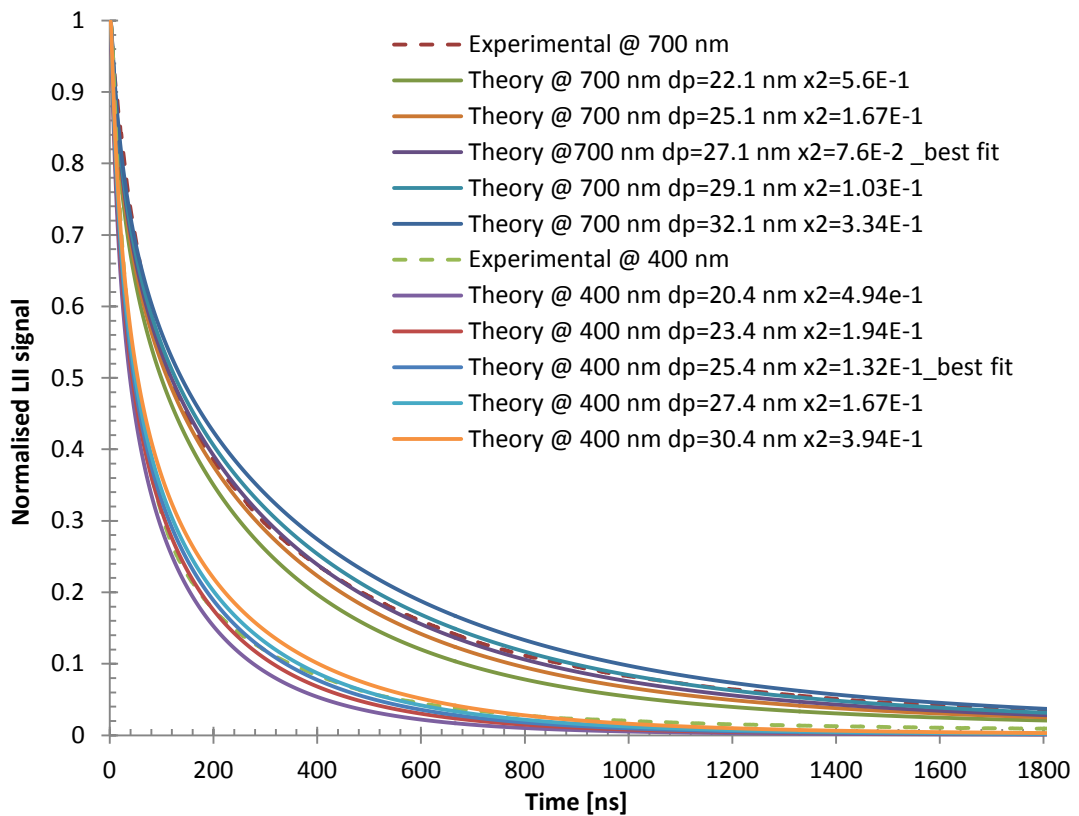


Figure 6-10 – Fit quality between experimental and theoretical signals

The fitting quality of the experimental data by the computed temporal LII decay curves is better at 700 nm than 400 nm. At 700 nm, the difference between experimental and theoretical signal is obvious at ± 2 nm of the best diameter fit, but not at 400 nm. Therefore the final equivalent diameter was considered to be the one resulting from the 700 nm fits. The fit accuracy is relevant up to one decimal. It is possible to obtain diameters at two decimals, or even three, but there is not a significant change in χ^2 and becomes mainly dependent on the first part of the curve (~ 100 ns) due to the normalisation and not to the global shape of the LII temporal decay curve.

The temperature decay of a single 27.1 nm diameter particle radiating at a wavelength of 700 nm was calculated. The comparison of temperature decays obtained by pyrometry measurement and by computed signal is illustrated on Figure 6-10.

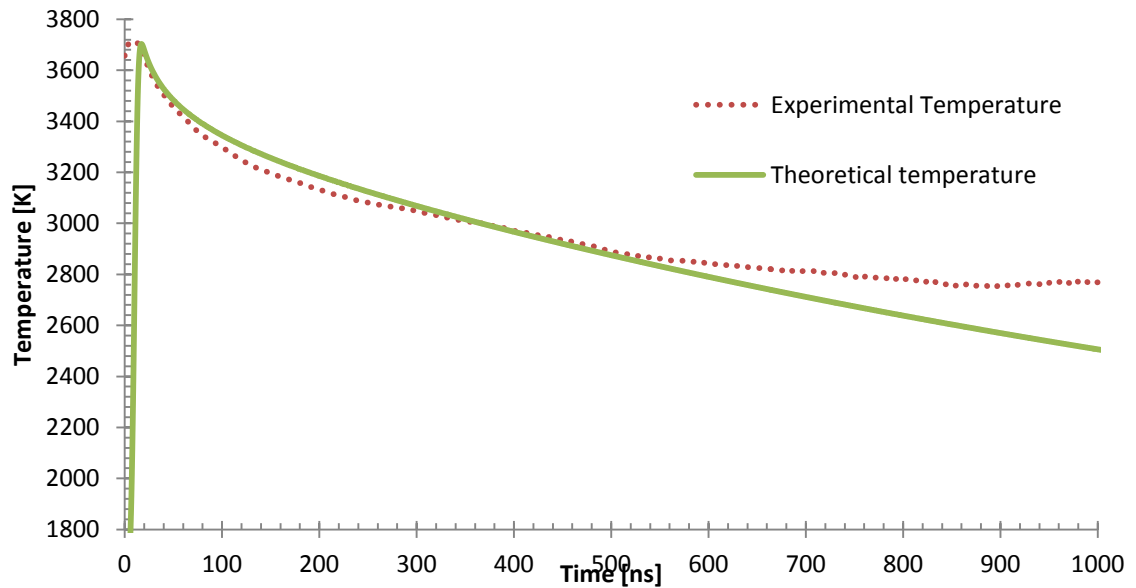


Figure 6-11 – Temperature decay curves, comparison between experimental and simulated

The temperature decay curve obtained by solving the different heat transfer equations and the temperature decay curve obtained by pyrometry are in reasonably good agreement. The temperature difference between the two approaches increases after 600 ns due to the limited temperature range of the pyrometry technique and the log-normal size distribution not considered.

Parameter optimisation

There is no unanimous agreement among the research community on the different parameter values used for modelling the theoretical temperature decay rate/LII signal. The refractive index function $E(m)$, temperature of the surrounding gas, thermal accommodation coefficient α , sublimation coefficient β and standard deviation σ of the size distribution - all these values can be optimized in order to obtain an optimal fitting of the LII signal using the least square method as an optimization criterion.

$$\chi^2 = \sum_{i=1}^{N_m} (S_{LII_exp} - S_{LII_theo})^2 \quad \text{Equation 99}$$

χ^2 Sum of the squared residuals

The optimisation of the coefficients was performed only for the global-TiRe-LII.

Refractive index function

The refractive index function is the main source of uncertainty. Its value varies from 0.193 to 0.4 (Lee and Tien, 1981; Koylu and Faeth, 1995; Krishnan, 2001) and can be considered constant, wavelength dependent or temperature dependent. Reducing the error introduced by the wavelength dependence uncertainty is crucial as the temperature determined by pyrometry is strongly dependent on $E(m)$.

A 3715 K peak temperature is obtained when considering $E(m)$ constant and 3831 K when considering its wavelength dependency. Therefore the temperature difference between taking a refractive index function constant and wavelength dependent introduces a difference of up to 3.1 % at peak temperature, i.e. around 116 K (the higher the particle temperature, so the higher the percentage error), which has a significant effect when modelling the particle cooling, especially on the sublimation heat transfer.

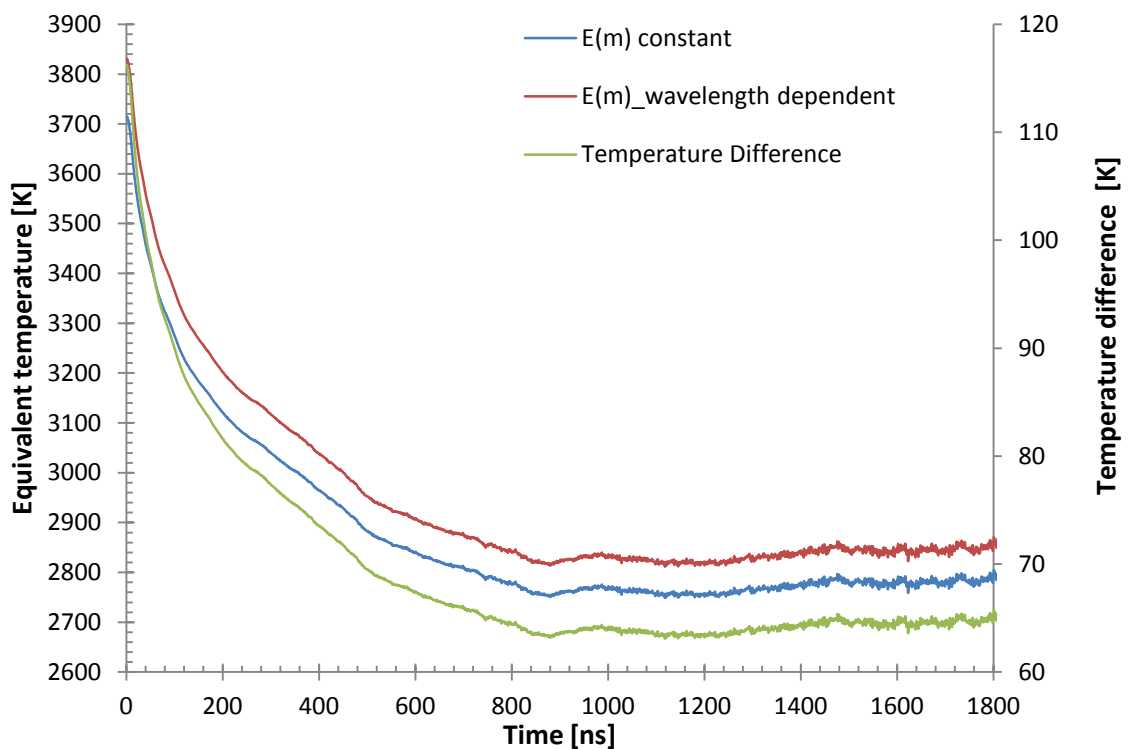


Figure 6-12 – Temperature curves corresponding to data of Figure 6-9

After 800 ns, the ratio between the two LII signals becomes noticeably noisy (Figure 6-12) due to the incandescence signal recorded at 400 nm becoming very weak (3% of the peak value). The dynamic range of the equipment shows its limitation and therefore the pyrometry technique has a minimal temperature estimation limit of 2800 K.

The best quality fits are obtained for $E(m)$ constant. The increase on the heat transfer rate due to a higher equivalent temperature cannot be compensated by an increase of the particle size. The cooling effect due to sublimation increases strongly in the first dozens of nanoseconds, therefore the LII signal computed highly decreased after the laser pulse. The first dozens of nanoseconds are crucial in the modelling. Figure 6-13 highlights the influence of the peak temperature on the processed LII signal and the importance of input parameters on the results. Overestimating the temperature makes the fitting of the curve difficult (i.e. with very high deviation error). Therefore $E(m)$ was considered constant in this study thereafter.

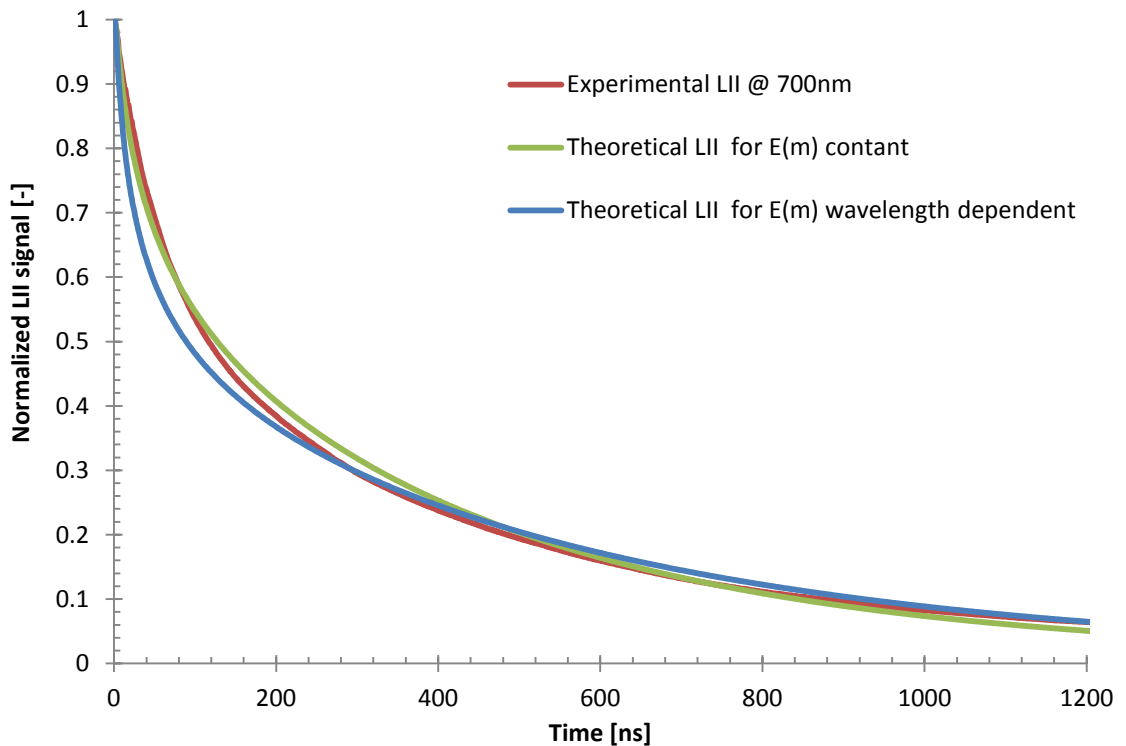


Figure 6-13 – Effect of λ -dependency of $E(m)$ on the quality fit of the temporal LII

6.3.2.1.1 Surrounding gas temperature

In the condition previously cited, the optimal surrounding gas temperature is estimated to be close to 1600 K, corresponding to the best fit (Table 7). An error of $\pm 3.125\%$ generates a maximum error of $\pm 7.0\%$ on the diameter. Increasing the ambient gas temperature contributes to reduce the heat transfer by conduction and so the equivalent surface of the particle. Therefore increasing the ambient gas temperature value, results in finding smaller equivalent particle diameters.

E(m)	Constant					
Laser fluence [$\text{J}\cdot\text{cm}^{-2}$]	0.1142					
β	0.3					
α	1					
Gas Temperature (K)	1400	1500	1550	1600	1650	1700
Δ Temperature [%]	12.5	6.25	3.125	0	-3.125	-6.25
Diameter @700nm	33.6	28.9	27.5	27.1	25.2	23.9
χ^2	0.4213	0.1752	0.1338	0.0760	0.0895	0.0954
Δ Diameter [%]	-23.99	-6.64	-1.48	0.0	7.01	11.81

Table 7 – Gas temperature optimization

An optimal temperature of 1600 K compares favourably with the values published in the literature, which are 1600 K (Santoro and Miller, 1987; Vander Wall et al, 1999; Koylu et al, 1997) and 1584 K (Dobbins et al, 1998).

Laser fluence

In the case of a hypothetical error on the equivalent temperature obtained by pyrometry, the input laser fluence was studied to observe the effect on the diameters and fitting errors (Table 8). The laser fluence has a major effect on the particle sizing since it determines the peak temperature, so that slightly increasing the fluence strongly increases the particle temperature peak. Heat loss rates increase with the fluence, and so do the equivalent particle diameters. At ± 5 and 10 % of the initial laser fluence, the equivalent diameters differ by approximately ± 13 and ± 25 % respectively.

Signal averaging reduces the signal to noise ratio, which is relatively high, especially after 800 ns. The quality of the results (temperature, soot volume fraction, diameter, and particle density number) is highly dependent on the signal to noise ratio. An error in the estimated temperature generates major error on the soot volume fraction and density number.

E(m)	Constant					
Laser fluence [J.cm⁻²]	0.10278	0.105635	0.10849	0.1142	0.11991	0.12562
Δ Fluence [%]	-10.00	-7.50	-5.00	0.00	5.00	10.00
β	0.3					
α	1					
Gas Temperature [K]	1600					
Size distribution	0.2					
Diameter [nm] @700nm	20.8	22	23.6	27.1	29.6	33.1
χ^2	0.1140	0.1036	0.0984	0.0760	0.0945	0.1286
Δ Diameter [%]	-23.25	-18.82	-12.92	0.00	9.23	22.14
Peak temperature [K]	3579	3617	3649	3715	3765	3821

Table 8 – Laser fluence optimization

Size distribution

The particle size distribution was primarily determined by the histogram of the image ratio between incandescence and scattering (Figure 6-26). The 0.2 standard deviation was estimated. This value is related to the diameter proportionality between incandescence and scattering signal; this proportionality can be controverted due to agglomerated particles and non-uniformity of the laser sheet causing non-uniformity of the temperatures reached by the particles.

When varying the log-normal distribution's standard deviation from 0.1 to 0.5, the fitting error decreases as the distribution widens (Table 9). This effect was considered due to all the particles not reaching the exact same temperature. By widening the size distribution, the cooling rates are spread over more different values, allowing a better fit with the experimental signals.

$E(m)$	Constant						
Laser fluence	0.1142						
β	0.3						
α	1						
Gas temperature (K)	1600						
Distribution	0.1	0.15	0.2	0.25	0.3	0.4	0.5
Δ Distribution [%]	-50	-25	0	25	50	100	150
Diameter @700nm	27.5	27.3	27.1	25.5	24.7	24.1	23.8
χ^2	0.1019	0.0927	0.0760	0.0915	0.0986	0.0943	0.0891
Δ Diameter [%]	7.8	7.1	6.3	0.0	-3.1	-5.5	-6.7

Table 9 – Size distribution optimization

Sublimation and conduction accommodation coefficients

Effects of the sublimation and thermal accommodation coefficient were also investigated. The best fitting coefficients are highlighted in red in the table below.

$E(m)$	Constant						λ -dependent					
Laser fluence [J.cm ⁻²]	0.1142						0.1225					
β	0.23		0.3		0.37		0.23		0.3		0.37	
α	0.8	1	0.8	1	0.8	1	0.8	1	0.8	1	0.8	1
Diameter [nm] @700nm	22.9	23.9	26	27.1	31.2	32.4	26.7	28	31.3	32.6	36	37.5
χ^2	0.11	0.18	0.082	0.076	0.11	0.094	0.11	0.18	0.082	0.113	0.11	0.094
Diameter [nm] @400nm	21.8	22.7	24.6	25.4	27	27.9	25.7	26.5	27.2	27.9	32.3	33.7
χ^2	0.197	0.32	0.147	0.13	0.198	0.159	0.197	0.32	0.147	0.20	0.198	0.166

Table 10 – Equivalent diameters and error fits depending on $E(m)$, α and β

Increasing accommodation factors has the effect of increase the heat transfers and therefore the resulting particle diameter. The resulting diameters are dispersed from 21.8 nm up to 37.5 nm. The spread over a large range of diameters illustrates the

influence of the different parameters on the results and the importance to better characterise them. The optimization of the parameters minimises the errors of the fitting and renders the diagnostic more accurate. However the process is time-consuming.

6.3.3 Soot volume fraction

The incandescence signal is proportional to the quantity of soot and their temperature (Equation 13). Therefore from the LII signal intensity and temperature obtained by pyrometry, the soot volume fraction can be computed quantitatively by following the auto-calibrated LII technique of Snelling et al. (2002).

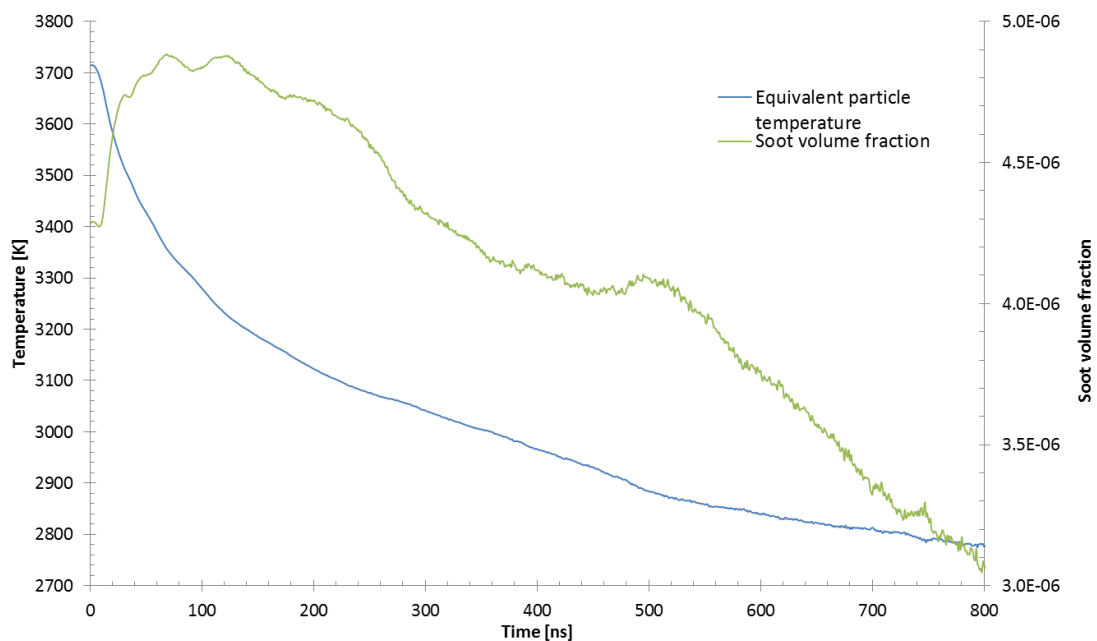


Figure 6-14 – Temperature and soot volume fraction from the averaged LII signals from the entire flame

A 0.6 % difference between the soot volume fraction computed from the LII signal at 400 nm and 700 nm was computed.

Depending on the part of the f_v curve selected, the mean soot volume fraction can vary between 4.74 ppm (averaged over the first 200 ns) and 4.14 ppm (averaged over the first 800 ns).

When the average soot temperature is over 3800 K, the sublimation rate is high and therefore the soot volume fraction should decrease. However there is no decrease of the

soot volume fraction in the first 100 ns, meaning that the sublimation is minimal and not detectable. Due to the high influence of the temperature on the soot volume fraction (inversely exponential), a slight temperature overestimation generates lower values of soot volume fraction. Therefore the soot fraction profile can be explained by an overestimation of the temperature due to the small particles reaching a higher peak temperature, shifting the soot volume fraction towards lower values. The small particles cool down faster; therefore the average temperature is controlled increasingly by the largest particles or agglomerates.

On the second part of the soot volume profile, f_v decreases due to this same phenomenon. After 200 ns, the apparent temperature is becomes less biased towards the smaller particles, whose LII signal reduces strongly, and therefore the apparent global soot volume fraction reduces with time.

The averaged f_v is taken at the transition between these two phases (30-120 ns) and considered to be equal to 4.79×10^{-6} i.e. 4.79 ppm.

This variation of f_v with time has also been observed by Snelling et al. (2005a) and Beyer (2006). The decrease of the soot volume fraction in time was explained by the difference in heat conduction rate (due to size the distribution and shielding effect of agglomerates). Beyer explained the soot volume fraction rise after the laser excitation by the annealing of primary particles.

6.3.4 Particle number density

The particle number density represents the concentration of particles by volume of gas while the soot volume fraction represents the volume of soot by volume of air. Particles are considered strictly spherical with a log-normal size distribution. Their volumes can be computed and, from the soot volume fraction, the estimation of the number of particles by volume of gas is possible.

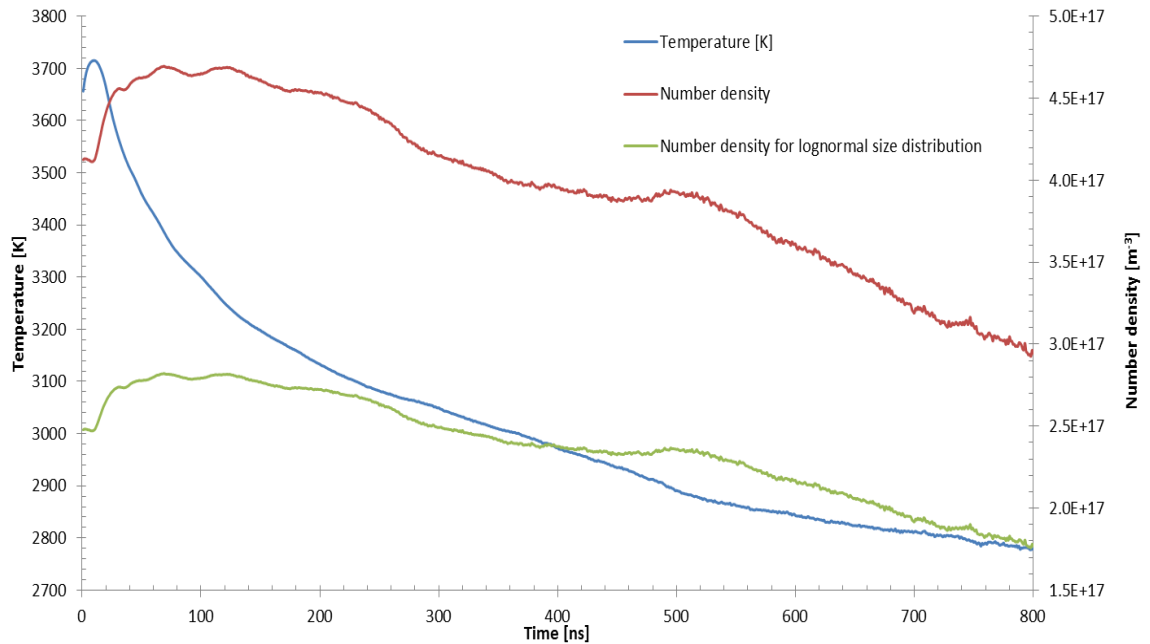


Figure 6-15 – Particle number densities and temperature from 2C-Tire LII measurements

Number density curves obviously follow the profile trend of soot volume fraction (average particle diameter considered to be equal to the one obtained by TiRe LII and considered constant during the LII process). The average particle number density found in the flame is $2.6 \times 10^{17} \text{ m}^{-3}$ when considering a log-normal particle size distribution and $4.4 \times 10^{17} \text{ m}^{-3}$ for a mono-disperse distribution. Not considering the log-normal distribution of the particles would result in an overestimation of their number by 69%.

6.4 Local 2C-TiRe-LII measurements

2C-TiRe LII technique was performed to determine soot particle temperature diameter and soot volume fraction at different “strategic” locations in the flame. Spatial distribution of the laser excitation was unmodified to estimate the effect of the laser fluence non-homogeneity on the results. Particles do not reach the same temperature due to the disparate energy fluence across the laser sheet. Therefore the cooling rate for each position depends not only on the particle size but also on the temperature reached and local gas temperature.

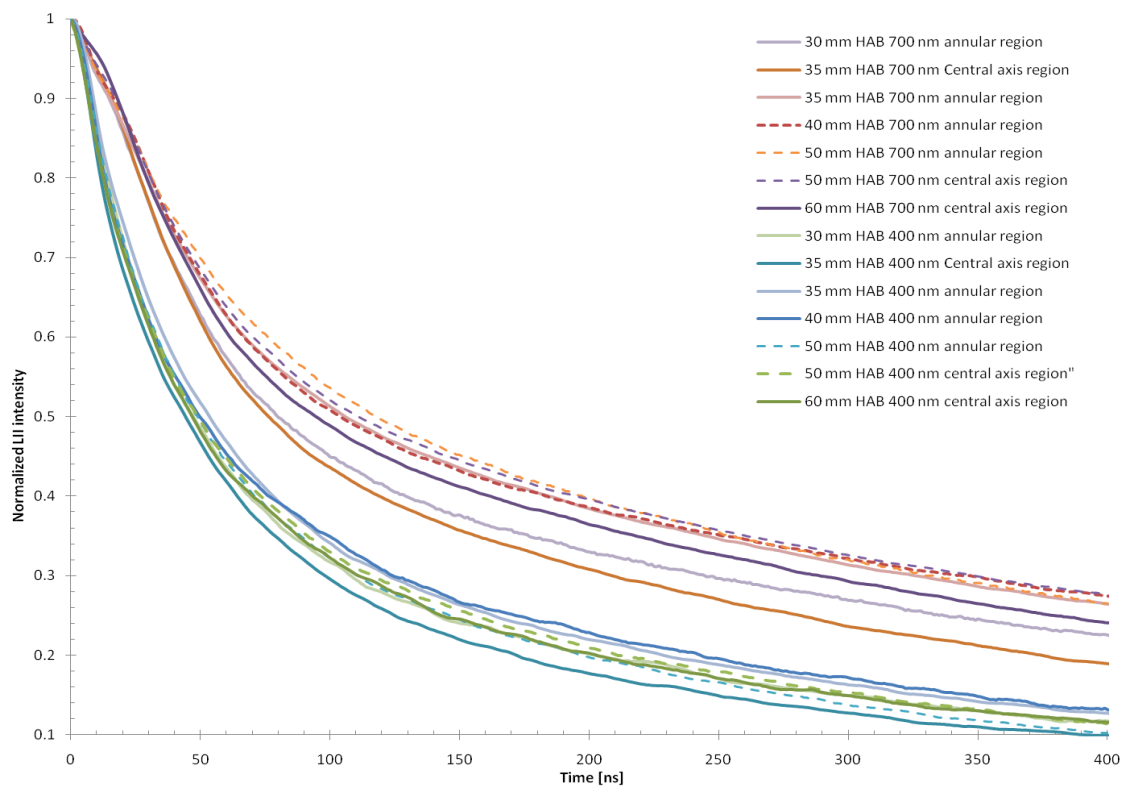


Figure 6-16 – Averaged temporal LII decay signals for different flame locations

During the first 30 nanoseconds, signals for a same collection wavelength cannot be differentiated. The different temporal LII signals are presented on a logarithmic scale for a better visualisation.

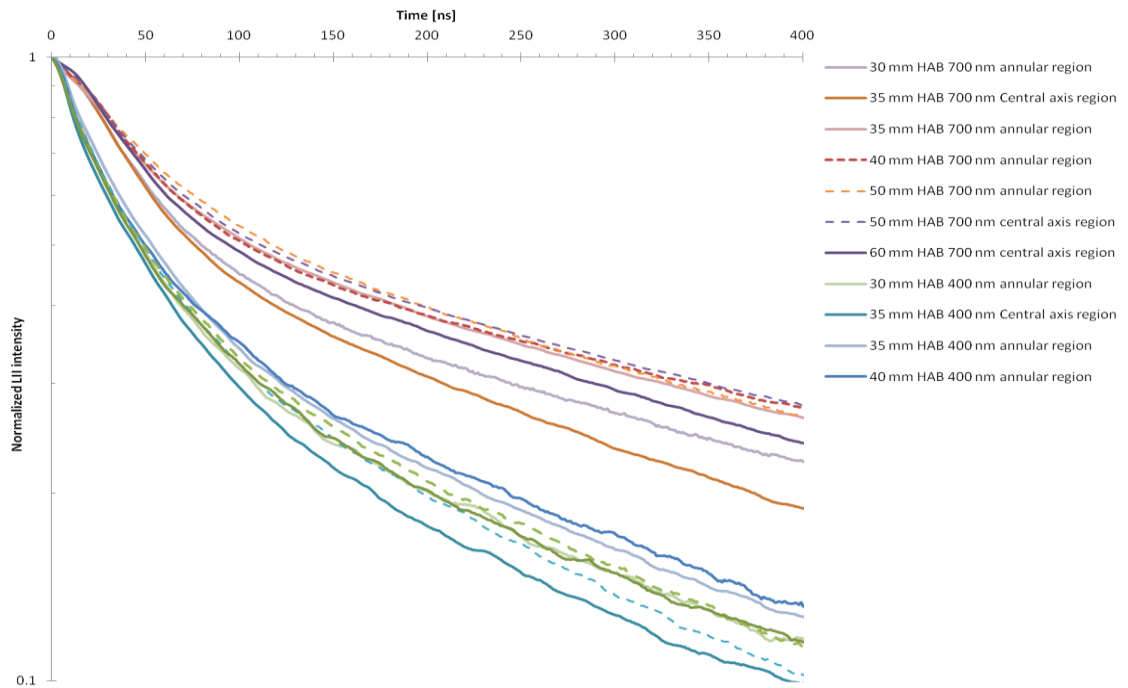


Figure 6-17 – Temporal LII decay signals for different flame locations

Temperatures for each point location were determined by two-colour pyrometry. The temperature variation of 134°C between 30 mm HAB and 40 mm HAB is due to laser fluence variations and initial soot temperature differences.

HAB [mm]		30	35	40	50	60
Peak	Annular region	3744	3768	3878	3866	3783
	Central region		3721	3814	3765	

Table 11 – Peak temperatures from 30 to 60 mm HAB

The temperatures obtained by point measurement are higher than the average temperature measured by global 2C-TiRe-LII. The difference is due to three distinct causes: the positions of the point measurements are located where the laser fluence was at its maximum, the particle peak temperature reduced as the laser crossed the flame (laser extinction) and the accuracy of the calibration technique.

6.4.1 Result summary

The results of point and global 2C TiRe-LII measurements are summarized on Table 12. The temperatures reached by the particles vary from 3697 to 3878 K depending on the location. The maximum 181 K difference measured was mainly due to the inhomogeneity of the fluence across the laser sheet and to the initial soot temperature varying slightly across the flame. The 90 mm high laser sheet was centred at 50 mm HAB, the energy being higher on its central axis than on its edges, the consequence being that the soot reached higher temperatures at the centre. The difference in temperature for a same height is due to the absorption of either the laser beam through the flame (when sampling position is on the central axis of the flame) either the absorption from the incandescent particle to the detection device. The particles absorbing more of the signal at lower wavelengths; the equivalent peak temperature is therefore biased towards higher temperatures. A part of the temperature fluctuation can also be imputed to the accuracy on the measurement of the LII signal peaks. The temperature can be considered relatively homogeneous among the flame, validating the assumption that all particles reached sensibly the same temperature. The global LII signal is biased towards the largest particles in the centre of the flame and their higher temperature due to the difference of laser fluence excitation.

Sampling height [mm]	Sampling region	Laser plan	Energy fluence [J.cm ⁻²]	Peak temperature [K]	Particle diameter [nm] @400/700 nm	Soot volume fraction [PPM]	Particle number density [m ⁻³]
30	annular	centre	0.1151	3744	27.4/22.7	5.4	8.8×10 ¹⁷
35	annular	centre	0.1188	3768	33.6/27.3	5.6	5.3×10 ¹⁷
40	annular	centre	0.1281	3878	49.1/32.6	4.7	4.4×10 ¹⁷
	centre	centre	0.1213	3814	26.4/20.3	2.9	6.6×10 ¹⁷
50	annular	centre	0.1268	3866	45.3/32.3	3.9	2.2×10 ¹⁷
	centre	centre	0.1179	3765	28.8/21.2	2.6	5.2×10 ¹⁷
60	annular		0.1197	3783	31.5/26.4	3.1	3.2×10 ¹⁷
	centre		0.1137	3697	29.4/23.8	2.4	3.4×10 ¹⁷
Entire flame		centre	0.1142	3715	22.4 nm @ 400 nm	4.74	2.43×10 ¹⁷
			0.1142	3715	27.1 nm @ 700 nm		3.94×10 ¹⁷

Table 12 – Results from 2C-TiRe-LII

The difference in size distribution between the annular and central-axis regions was noticeable at 35 mm HAB with larger diameters in the annular region. However at 50 mm HAB, the difference in particle mean diameter between annular and central region was less distinguishable and less than the one recorded by the other method. The flattening of the distribution from annular to central region was mainly due to the combination of the sampling volume being relatively large compared to the annular region thickness (1.1 mm) and to the flame flickering effect increasing with height above burner.

Sampling a large volume by two-colour TiRe-LII is valid only if all the particles in the measurement volume reach the same peak temperature. This is hardly achievable in a flame of this height due to temperature gradients and laser sheet inhomogeneities. The choice of the energy fluence was critical; in this study an average medium laser fluence across the sheet was selected in order to minimise the effect of ambient temperature gradients and laser energy inhomogeneity. The particles reach high temperature in order to compensate these conditions.

6.5 Quantitative spatial soot distribution study

The previous part has shown the possibility of obtaining quantitative data from the 2C-TiRe-LII technique. These results are used in this section to calibrate the images or qualitative spatial distributions in order to obtain quantitative two-dimensional spatial distribution of soot volume fraction, particle size and particle number density from laser-induced incandescence and elastic laser scattering image acquisitions.

The visible height of the flame was 94 mm; however a flame height of 87 mm was measured by PLII images and 83 mm by ELS (Figure 6-18). The height difference is due to the limited dynamic range of the camera's image intensifier. The camera amplification is limited by the strongest intensity; the threshold determined by the maximum does not allow for a higher amplification in order to visualize the tip of the flame where soot is at lower concentration, and therefore where the signal is the lowest. The addition of the chimney to stabilize the flow had the disadvantage of introducing higher background intensity on both LII and ELS images due to the scattering by the back wall.

The natural luminescence of the flame shows high soot concentration between 25 and 50 mm HAB. The higher soot concentration on the edges is due to the annular

distribution and thicker signal integration depth on the edges compared to the central axis. No natural flame incandescence was detected without laser excitation for identical settings. Therefore no correction was applied for the natural incandescence for the ELS and LII images.

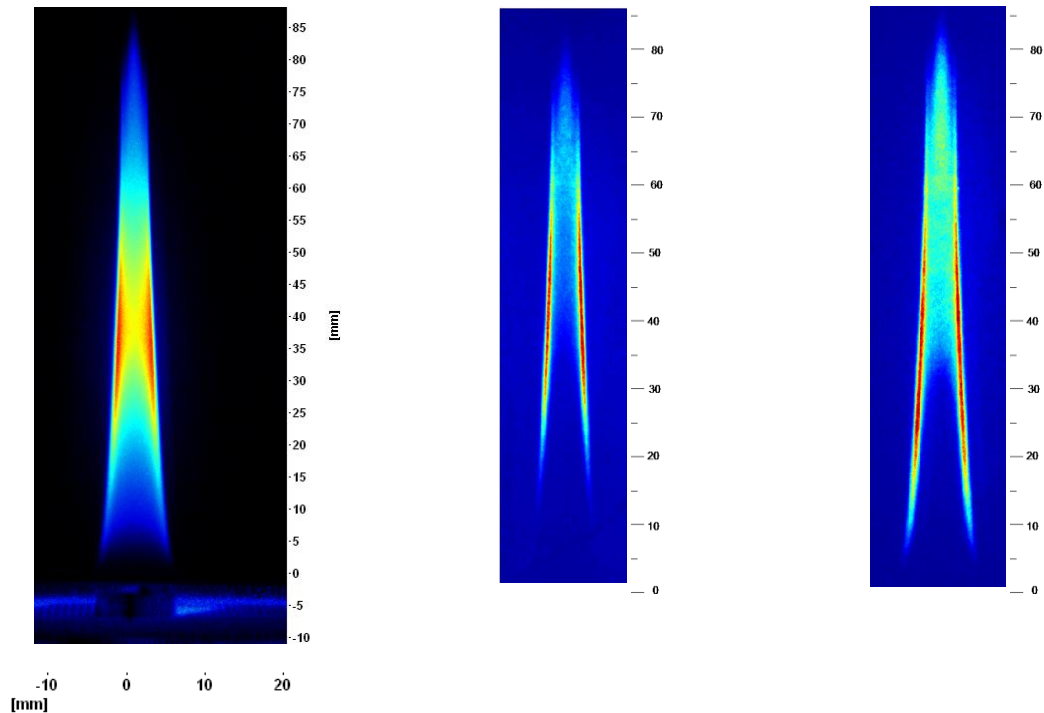


Figure 6-18 – Typical image acquisitions

LEFT: Natural flame luminescence

CENTER: Raw scattering image (ELS)

RIGHT: Raw incandescence image (PLII)

The soot volume fraction is considered proportional to the incandescence whereas particle diameter and number density are considered to be proportional to ratio between scattering and incandescence signal (c.f. chapter 3).

From the PLII and ELS images of two data sets, the results of individual calibrated distributions of soot volume fraction, particle diameter and density number are presented in Figure 6-19.

From either the ELS or PLII images, no major disparate continuity can be noticed, demonstrating a homogeneous and satisfactory laser fluence distribution.

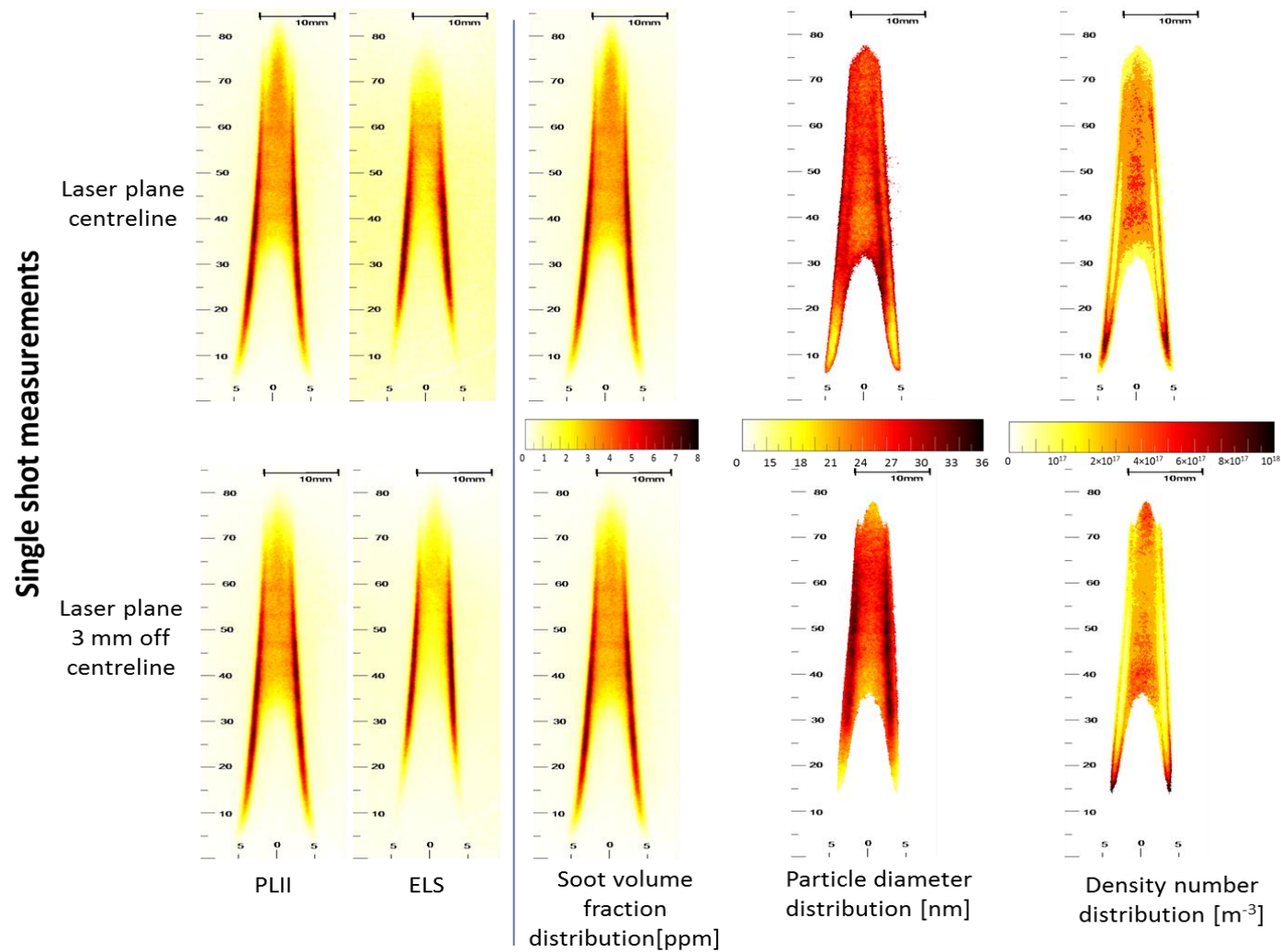


Figure 6-19 – Flame soot mapping for single shot measurement and two laser plans - ELS and LII images, soot volume fraction, particle size and density are calibrated by 2C-TiRe-LII

The dynamic range of the camera is limited to 12 bits (4096 grey levels) and the intensity range of the scattering and incandescence signal depends respectively on d_p^6 and d_p^3 .

The dynamic range of the ELS images is limited to 4 times the maximal particle size ($4^6=4096$) instead of 16 for the incandescence images ($16^3=4096$). For a given particle size distribution, the ELS signal range is spread over a larger range of value than the LII signal. Therefore if the larger particles can be recorded on both ELS and LII images, some of the smallest particles will be recorded by the LII techniques but not by ELS due to the limited dynamic range. This effect is discernible more on the ELS than LII images. The particles can be detected lower in the flame, where they are very small, by incandescence but not by scattering.

Some artefact effects on the particle size and density number spatial distribution appear on the border of the flame. This effect is due to the ratio of low intensity pixels.

The low turbulence of the experimental conditions and the excellent repeatability of the measurement allow the averaging of the data in order to obtain sensible mean results.

The results are presented in Figure 6-20, averaged ELS and PLII images and calibrated distributions are represented.

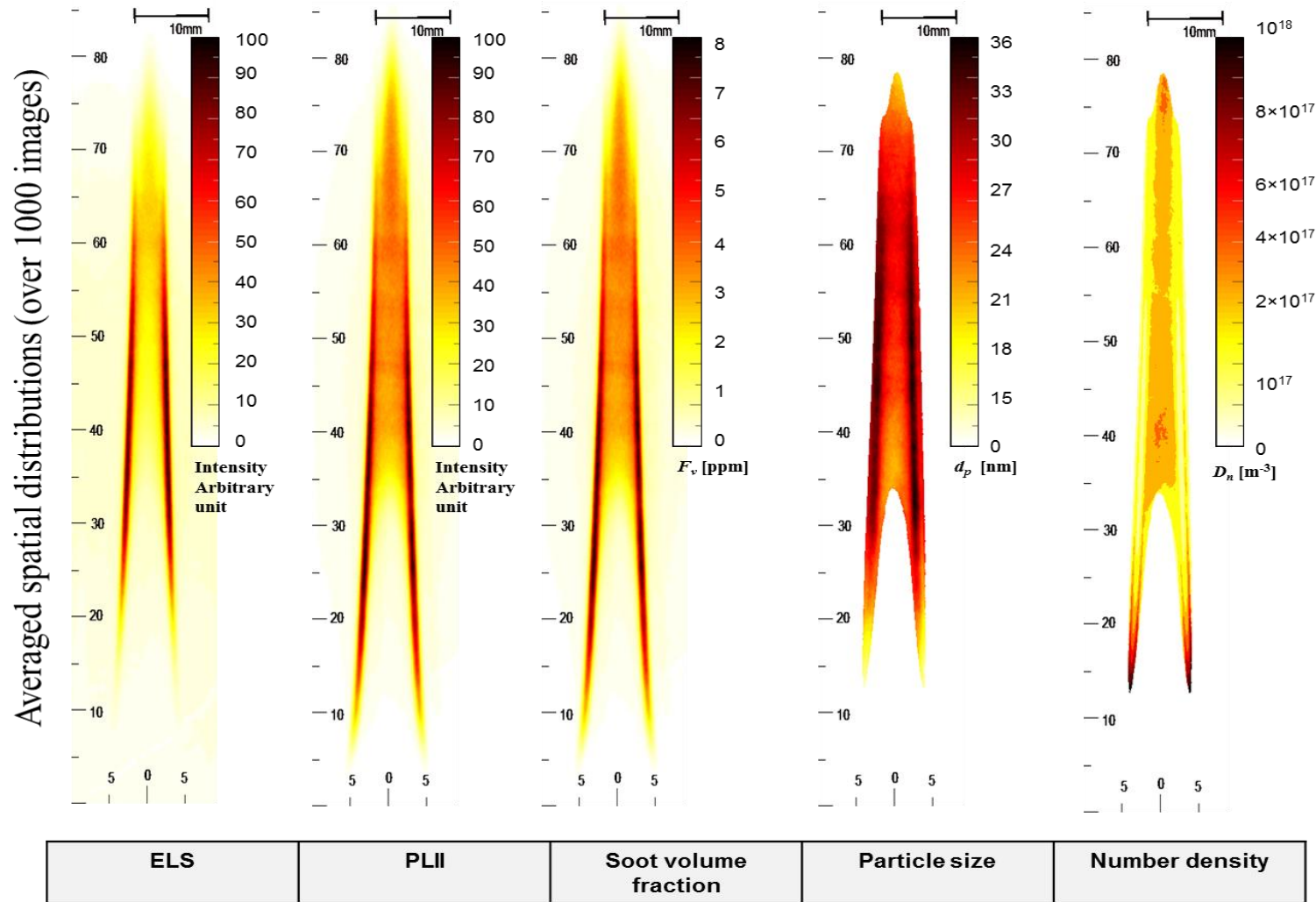


Figure 6-20 – Flame soot mapping - Averaged ELS and LII images over 1000 images, the average soot volume fraction, particle size and density are calibrated by 2C TiRe-LII

6.5.1 Comparison between sampling approaches

The point location measurement is an approach more accurate than global 2C-TiRe-LII. Therefore results from this technique were used as reference points and quality criteria on the results obtained by global 2C-TiRe LII. Data from point location measurements are compared with data from the quantitative spatial distribution (calibration by global 2C-TiRe-LII) to characterize the accuracy of the diagnostic. Intensities of each spatial distribution are averaged over a small surface at the same location performed by point measurement 2C-TiRe-LII.

The comparison between the results from the two different approaches is presented in Table 13

Bearing in mind the point measurement results have also their uncertainties. The maximum errors between the two techniques are almost 30% for the particle diameters, 37.5% for soot volume fraction and 56% for number density. These uncertainties are relatively high but considering the assumptions and diagnostic accuracy, the results from global and point measurement can be considered in good agreement. The results from two different approaches follow the same trends which supports the validity of ELS/LII approach. The point measurement results have slightly more amplitudes compared to the other technique. Global measurements results tend to overestimate the mean particle diameters while they underestimate the soot volume fraction. As the number density is highly dependent on the mean particle diameter, overestimating the size of the particles has the effect of underestimating the number density.

HAB [mm]	Sampling region	Point measurement 2C-TiRe-LII			Global 2C-TiRe-LII + ELS/PLII			Error on particle diameter [%]	Error on soot volume fraction [%]	Error on particle number density [%]
		Particle diameter [nm] @400/700 nm	Soot volume fraction [ppm]	Particle number density [m ⁻³]	Particle diameter [nm]	Soot volume fraction [ppm]	Particle number density [m ⁻³]			
30	annular	27.4/22.7	5.4	8.8×10 ¹⁷	29.1	5.7	4.3×10 ¹⁷	28.2	-5.6	-51.1
35	annular	33.6/27.3	5.6	5.3×10 ¹⁷	31.4	5.9	3.6×10 ¹⁷	15.0	-5.4	-32.1
40	annular	49.1/32.6	4.7	4.4×10 ¹⁷	32.12	5.38	3.1×10 ¹⁷	-1.5	-14.5	-29.5
	centre	26.4/20.3	2.9	6.6×10 ¹⁷	25.1	3.3	2.9×10 ¹⁷	23.6	-13.8	-56.1
50	annular	45.3/32.3	3.9	2.2×10 ¹⁷	33	4.82	2.7×10 ¹⁷	2.2	-23.6	22.7
	centre	28.8/21.2	2.6	5.2×10 ¹⁷	27.5	3.2	3.1×10 ¹⁷	29.7	-23.1	-40.4
60	annular	31.5/26.4	3.1	3.2×10 ¹⁷	32.6	3.56	2×10 ¹⁷	23.5	-14.8	-37.5
	centre	29.4/23.8	2.4	3.4×10 ¹⁷	29.1	3.3	2.6×10 ¹⁷	22.3	-37.5	-23.5

Table 13 – Comparison of the different results from two measurement approaches

6.5.2 Results and discussion

Table 13 regroups the results obtained for the Santoro burner. Averaged PLII and ELS images as well as calibrated two-dimension profiles of soot volume fraction and particle diameter and particle number density are presented in Figure 6-20.

The results demonstrate a good agreement with the expected behaviour of a laminar diffusion flame, with the results obtained from extinction measurements and the published results available in the literature.

First soot particles are detected from 4.9 mm HAB in the annular region and from 32 mm at the central axis of the flame. The concentration and particle size in the annular region increase till 20 mm where they reach their maxima, and soot volume fraction stays high until 50 mm HAB and 62 mm HAB for the particle size.

The particles from the annular regions diffuse with ethylene; the region has a temperature above 1600 K, but the lack of oxygen inhibits oxidation in the centre of the flame.

In this setting, the diagnostic was not sensitive enough to measure the smallest diameters. The inception zone under 15 mm HAB could not be characterized, mainly due to the low ELS signal levels and the dynamic range of the camera.

The soot volume fraction in the centre of the flame is relatively constant (~ 4 ppm). f_v starts decreasing after 78 mm HAB where the thickness of the flame has decreased, increasing the air mixing process and so the oxidation as the temperature still high. The effect of oxidation can be seen with the reduction of particle size at the tip of the flame but also at the edges of the flame.

The flame can be divided in two parts, the lower part dominated by soot production on the annular region and the upper part dominated by the oxidation process on the annular region and central region.

The oxidation process increases with height above burner due to higher air to fuel ratio caused by the progressive depletion of fuel along the height of the flame.

A model of soot formation in a laminar diffusion flame is represented in Figure 6-21. In the present case, the dimensions of the flame are a visible length of 94 mm; a lift-off length of 5 mm, a soot formation zone up to 50 mm (45 mm height) and an oxidation zone from 50 mm to 94 mm (44 mm height). The flame structure could be simplified as a cone of 1 mm constant thickness wall and 60 mm height where soot is produced. The particles can either be oxidized if they leave the flame zone, grow if they stay in this volume or be diffused to the central region of the fuel. The particles in the central region are mainly due to the diffusion of the smallest particles from the annular region rather than be the resulting products of a combustion in the central axis of the flame.

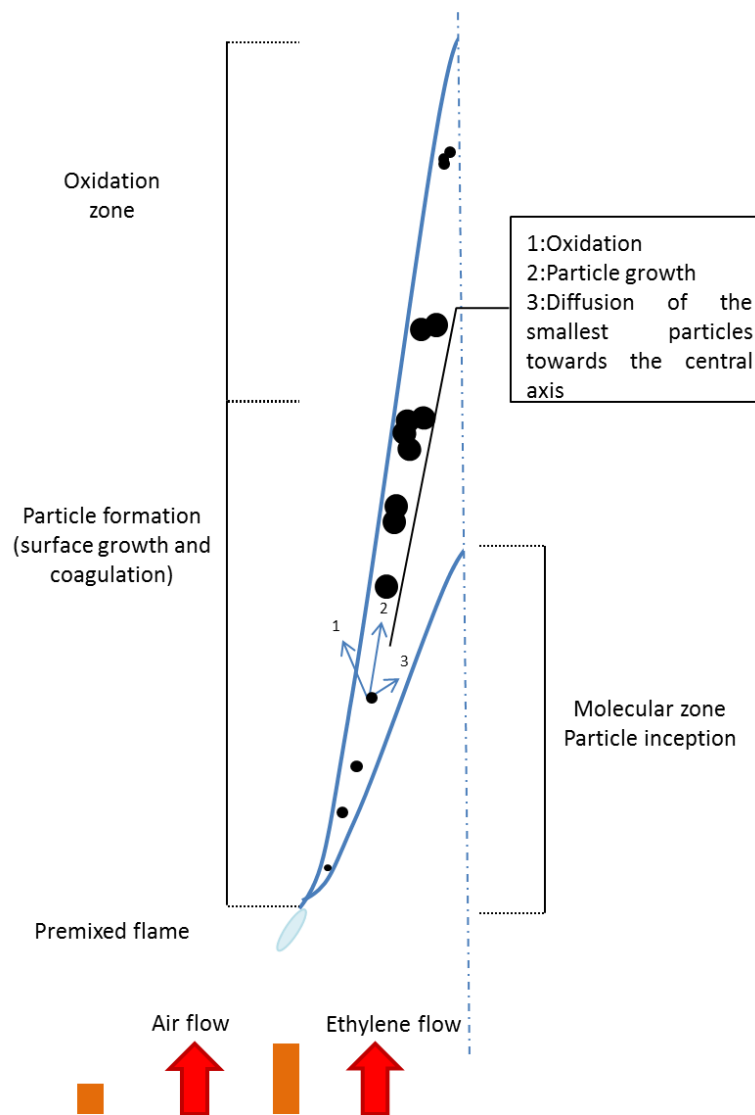


Figure 6-21 – Soot formation model in a laminar diffusion flame

6.5.3 Profiles

The spatial distribution from the images gives a good picture of the soot formation behaviour however to refine the description the radial and longitudinal soot volume fraction profiles are plotted below.

The different profiles of soot volume fraction, particle diameter, and particle number density at different heights (10 mm interval, from 10 to 80 mm HAB) of the flame, provided by the horizontal sections of the calibrated images, shows the different stages of the soot formation in a diffusion flame.

The radial soot volume fraction profiles extracted from the calibrated images are presented on Figure 6-22.

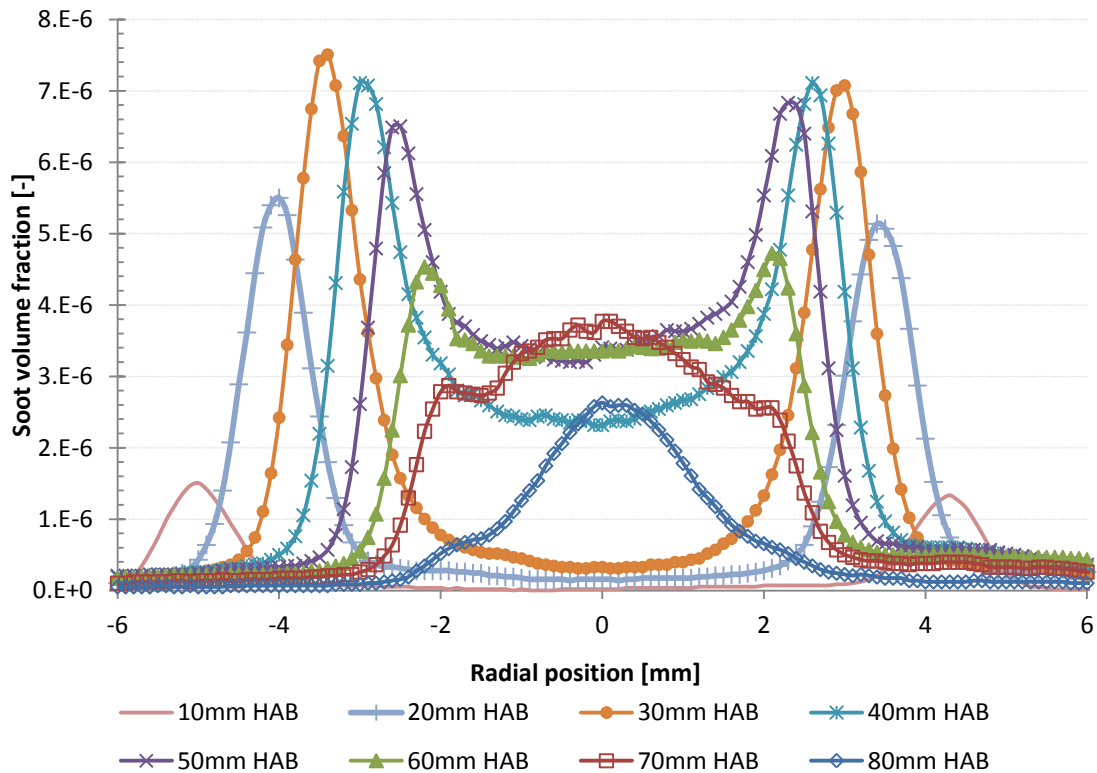


Figure 6-22 – Soot volume fraction profiles across the flame for different heights above burner (averaged measurement)

The longitudinal profiles were extracted for a single measurement and are shown on Figure 6-23. Non-averaged measurements were preferred to illustrate the possible fluence variation over the measurement volume which could have been smoothed by averaged measurements and by flame flickering. The profiles do not show high disproportionality which could have been the consequence of local laser fluence (minima or maxima) peaks.

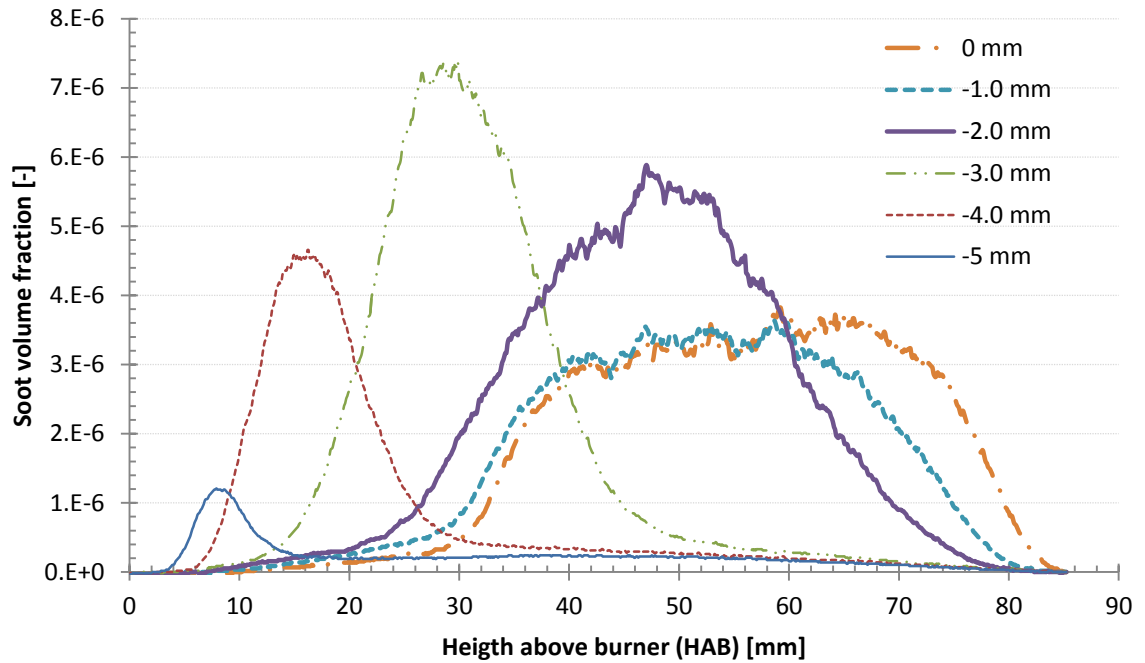


Figure 6-23 – Longitudinal soot volume fraction profiles across the flame for different radial positions (single measurement)

Soot volume fraction profiles show soot presence at the periphery of the flame from 10 to 50 mm HAB with an increase up to 30 mm HAB and reduction downstream the flame afterwards. In the centreline of the flame, soot concentration increase strongly after 40 mm HAB and stay high up to 80 mm HAB.

The height of f_v peak in the annular region coincides with the first apparition of soot in the centreline of the flame. A fraction of oxygen penetrates in the ethylene central flow and supposed not to be in so large quantity to produce a combustion zone at the centre of the flame. The presence of soot in the central region of the flame is considered to be mainly due to the diffusion of the soot particles from the annular region to the centre of the flame, especially the smallest particles due to their lower inertia.

The soot volume fraction profiles have the same shape as the ones published by NIST and the one obtained by Lebourgeois (2010) (Appendix E). However, the profiles found are slightly wider on the radial axis (from 0.1 to 0.4 mm), soot volume fraction amplitudes on the annular regions differ by a coefficient of 2 and ratio between the peak of the annular and central regions varies by a coefficient 2.3 in the present result while the Santoro's result, a coefficient of 3.1 is recorded. The spatial variations on the radial axis can be explained by the slightly higher co-flow and reduced perturbation due to the

chimney. Noticeable differences on f_v values are obtained according to the calibration technique. The f_v values obtained by extinction are more sensitive to soot agglomerate while the auto-calibration technique is more sensitive to the primary particle sizes.

Signal intensities are negligible in the centreline of the flame for height under 40 mm HAB. Therefore fluorescence of PAH is considered negligible. The risk of recording LIF of PAH by exciting at 532 nm has been reduced by heating-up the particles with moderate laser fluence. Consequently errors that could have been introduced by integrating the PAH fluorescence into the incandescence signal were minimised.

The f_v profiles are slightly asymmetric; LII signal is stronger on the right side of the flame from 45 to 60 mm HAB where the flame optical thickness is higher due to the presence of soot in the central region. The asymmetry is caused by laser fluence variation across the sheet, initial soot temperature fluctuation and laser absorption. The fluence fluctuation across the sheet induces that some regions are excited by fluence above or below the sublimation threshold. For fluence below the sublimation threshold, LII signal increased with the laser fluence. However, for fluences above the sublimation threshold, a noticeable quantity of soot is sublimated thus reducing the soot volume fraction and LII signal emitted.

The laser beam, coming from the left side, is absorbed along the flame path; hence the left part of the flame is excited by higher laser fluence than the right part. The fluence is high enough to sublimate the soot. This has for effect to reduce the LII signal on the left but increasing the signal on the right due to the decrease of the laser fluence by absorption and so the sublimation. This case occurs from 45 to 60 mm HAB, at the other heights, the sublimation phenomena is not high enough (due to energy fluence difference across the laser sheet) to be observed and therefore provokes higher incandescence signal on the left side and due to laser attenuation, lower incandescence signal on the right side.

The consequence is an underestimation of soot volume fraction either by the sublimation of particles or by an underestimation of the laser fluence.

The radial profiles for 10 mm height interval are presented in Figure 6-24

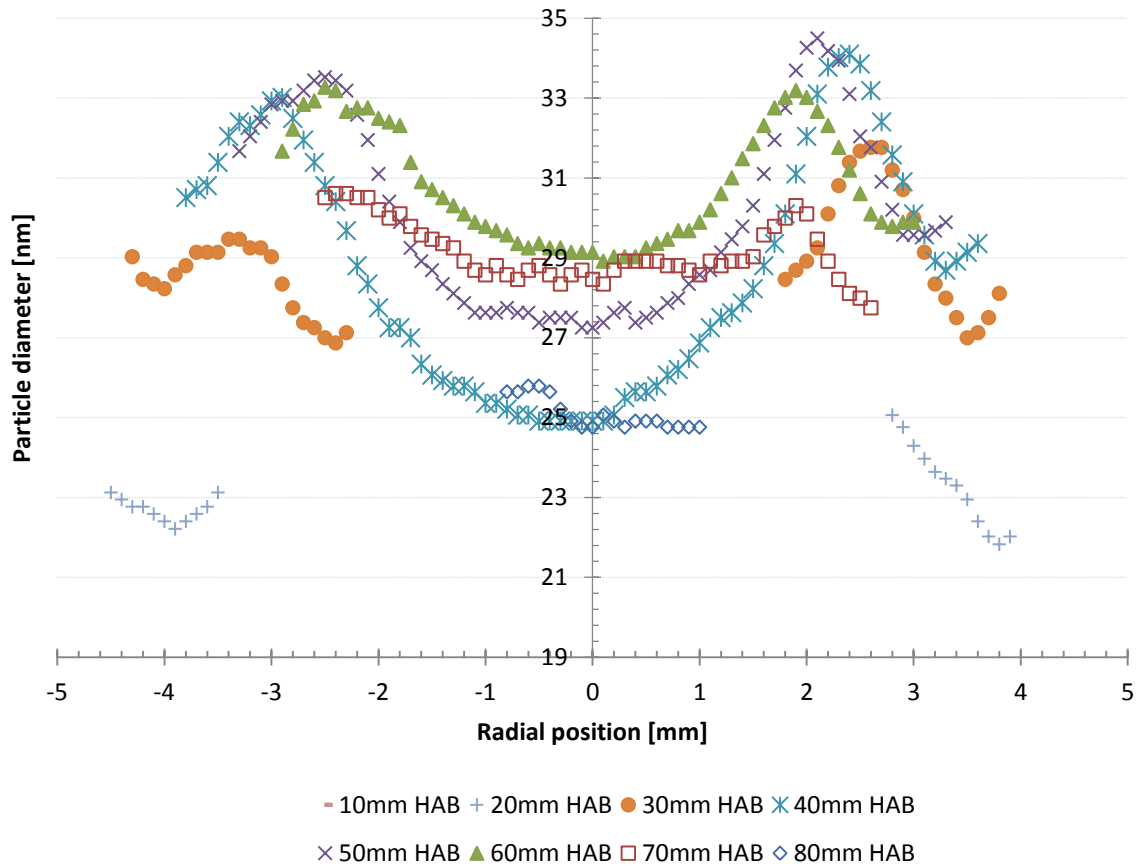


Figure 6-24 – Particle diameter profiles at different heights above burner across the flame

The growth of the particle is noticeable from 10 to 60 mm HAB. While a decrease of the particle diameter due to oxidation occurs after 60 mm HAB. The trend is valid for the annular and central region of the flame. An increase of 50 % in diameter, from 20 to 33.5 nm is measured in the annular region.

The Gaussian profiles on the edges of the flame characterize the oxidation phenomena. The particles going outward from flame are oxidized due to high temperature and high oxygen concentration conditions.

The asymmetry on the diameter radial distribution is more pronounced than the soot volume fraction profiles. The diameter difference between left and right side can reach up to 7 %. This phenomenon occurs at any height of the flame but is stronger between 30 to 50 mm HAB. The scattering over LII ratio is biased to lower ratios on the left from the decrease of the LII signal due to soot sublimation.

On the outer border of the flame, computation artefacts are noticeable due to low incandescence signal. This highlights the limit of the technique.

From the particle diameters and soot volume fraction profiles, the number density are computed (Figure 6-25). The assumption of mono-dispersed size distribution was made for this calculation.

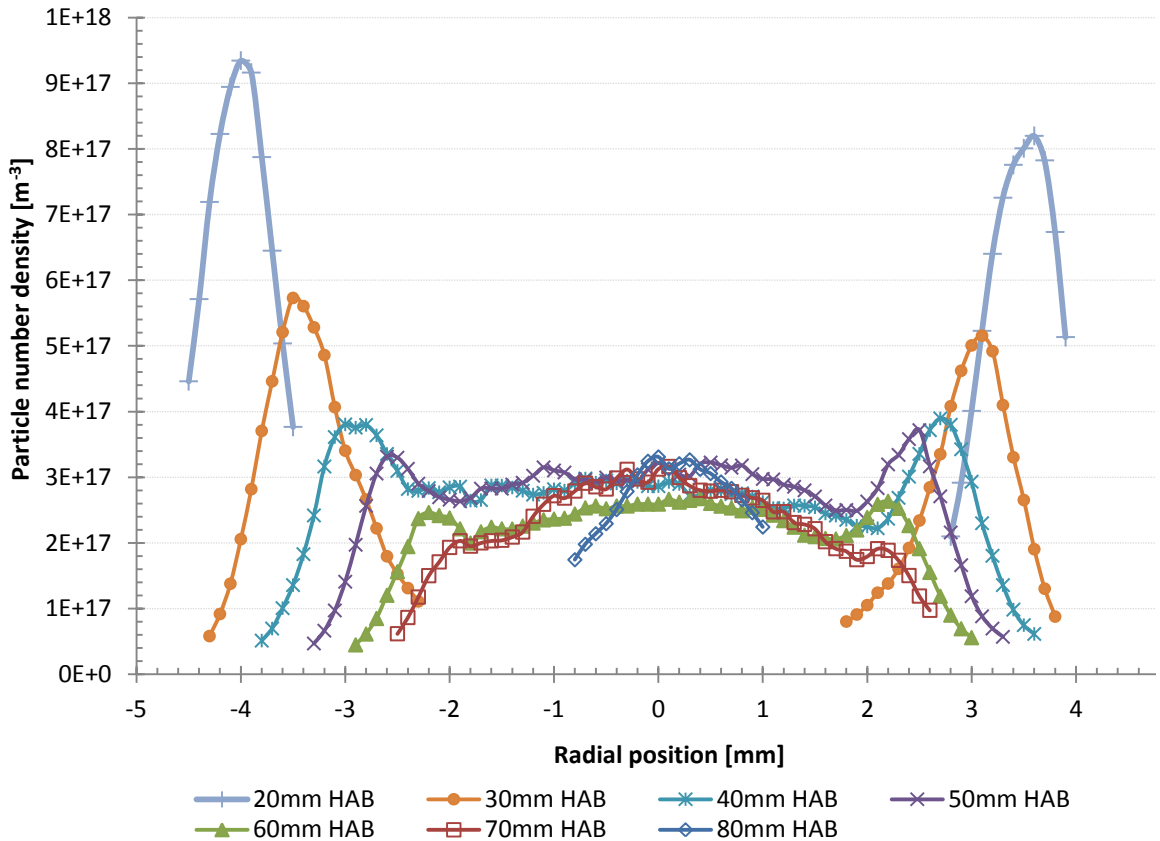


Figure 6-25 – Number density profiles for different heights above burner across the flame

The numbers of particles is clearly higher with peaks reaching up to 1.15×10^{17} particles per cubic meter on the lowest part of the flame, at the inception zone. The density of particles becomes relatively constant after 40 mm HAB with density between 3.2 and 4×10^{17} particles per cubic meter.

6.5.4 Particle size distribution

The histogram of the size distribution image gives the particle size distribution within the entire flame (Figure 6-26). However, this distribution is qualitative and a correction is applied from the average diameter obtained by TiRe-LII. The size distribution can be divided into three groups. The first one for particle size range from 19 to 24.5 nm mainly located at both ends of the flame, where inception occurs, smallest particle

growth at the lower part of the flame and at the tip where larger particles are oxidized. The second group, sizes vary from 24.5 to 31 nm. This part represents more than 70 % of the particles and they are predominantly located on the centreline of the flame. The third part represents the largest particles, above 31 nm. They are present in large quantity up to 34 nm. These large particles are located on the peripheral edges of the flame between 28 and 65 mm HAB. They are the result of particle grows from smaller particles and the fact of an oxygen deficiency in this part of the flame.

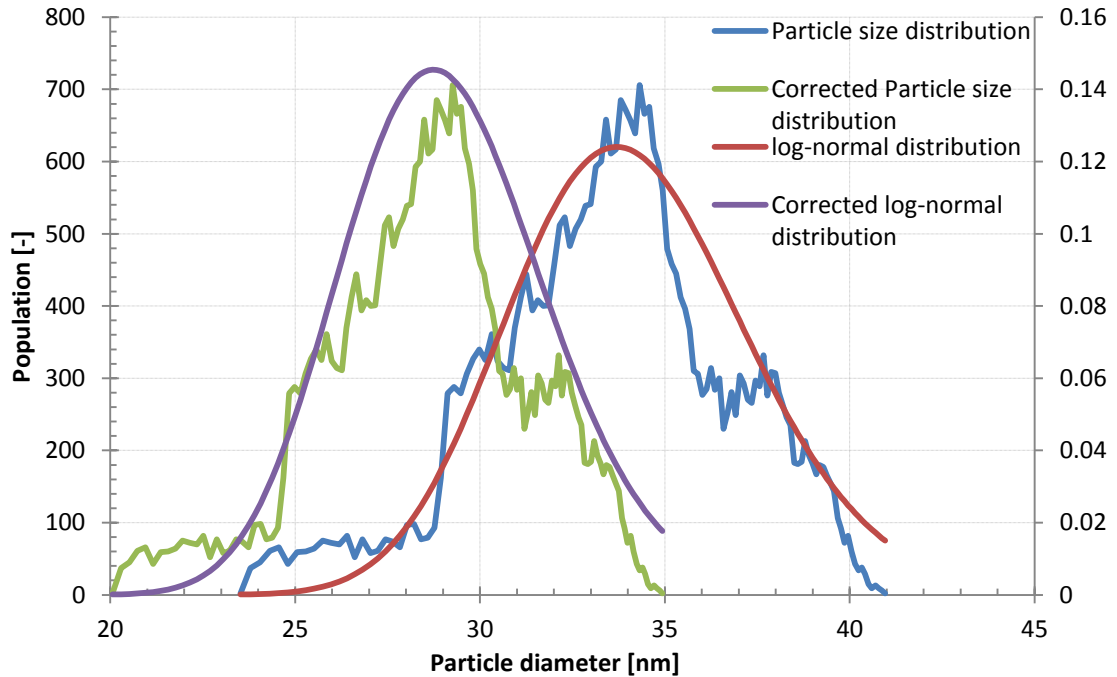


Figure 6-26 – Histograms of the spatial particle size distribution

In the literature, size distributions are usually considered log-normal or multi-log-normal. In the present case, the theoretical size distribution was simulated by a log-normal distribution with a standard deviation of 0.2. The size dispersion is in the range of the published values (for a small sample volume between 0.1 and 0.59). The relatively low value is due to background noise correction, limited dynamic range on the ELS signal and a non-linearity of the ratio between scattering and incandescence due to the presence of agglomerates. Because of all these factors particle diameters under 20 nm cannot be measured. The narrow distribution confirms the fact that the optical diagnostic detection is biased towards the larger particles. Particle diameter distribution determined by the study of the LII decay signal is coherent with the distribution obtained from the ELS/LII image ratio.

6.5.5 Errors due to the technique

The LII technique is often presented as a quantitative technique, even though its accuracy is relatively questionable. It is difficult to find publications reporting rigorous error analysis for measurements based on the LII technique. This is mainly due to unknown parameters in the theoretical heat transfer and uncertainties with $E(m)$. Moreover, error on the calibration factor and error introduced by the noise of the temporal signal, especially at the peak, add to the accuracy problem. Nonetheless the sensitivity of the 2C-TiRe-LII is below a nanometre, as illustrated in Figure 6-10.

In the incandescence and scattering theory, soot particles are considered perfectly spherical. In reality, soot particles are agglomerates of hundreds of primary particles. The assumptions of only considering the soot as primary particles neglecting any agglomeration effect was made. The agglomeration was considered to be low and the agglomerates to fragment during the laser pulse.

The scattering signal is considered independent on the laser fluence in the Rayleigh regime. However the scattering can be slightly dependent on the fluence and this dependency differs from the incandescence one. The laser energy not being perfectly spread across the sheet can lead to an overestimation of the diameter in the spatial distribution. The difference of energy distribution also leads to a difference of temperature reached by the particles, and biased the results obtained by global 2C-TiRe LII. The difference of conditions and soot properties across the flame and height above burner also influence accuracy results from 2C-TiRe-LII (Bladh et al., 2011).

In the post-processing, the effects of the filters' spectral bandwidths and laser extinction were neglected. The background noise was suppressed by thresholding. Additional signal added to LII or ELS signal was integrated, such as potential laser-induced fluorescence, scattering from the back wall and natural luminescence signal.

6.6 Conclusions

This chapter presents the application of a new laser diagnostic approach in a laminar ethylene/air diffusion flame. The experiment was set on a standard Santoro burner in order to first validate the new technique and compare against data from the literature. The different techniques used in this approach: auto-calibration, 2C-TiRe-LII and ELS/LII technique were successfully carried out. The soot formation regions, soot growth and oxidation, were located and characterised by the technique. Equivalent particle temperature, soot volume fraction and particle diameter were quantified. Moreover, soot volume fraction and particle sizes were obtained with good spatial resolution. The spatiality of the diagnostic lead to a compromise on the accuracy and measurement range, although the results are in relatively good agreement with point measurements and published data.

Particle size results are highly dependent on the input parameters. Increasing heat loss parameters gives higher particle diameters. According to these parameters, particle diameters can vary significantly. An extensive study of the parameters allowed the determination of the most suitable values for our experiment. The best parameters are dependent on the equivalent peak temperature. The temperature inaccuracy due to the uncertainty of the refractive index is the major source of error on the results. The fitting of the experimental signals were particularly sensitive to the first theoretical values as the signal was normalised and a fit quality criteria based on the square of the relative difference between the two signals was used to optimize the curve fitting. The averaged particle diameter obtained for the flame was 27.1 nm (with $E(m)=\text{constant}$) with a standard deviation of 0.2 and for an averaged peak temperature of 3715 K. The temperature was lower than expected (3800 K) due to non-uniform laser excitation and laser absorption. The 2C-TiRe-LII was applied at different point locations of the flame to determine the difference in temperature and diameter with the previous technique. The comparison showed slight differences between diameters found by 2C-TiRe-LII and by the calibrated ELS/LII technique. The validity of the technique depends on the temperatures reached by the different particles in the sampled volume, therefore on the energy distribution of the laser sheet and also the initial particle temperature across the flame. To obtain spatially resolved soot volume fraction and particle size distributions, compromises were made on the accuracy of the technique.

Two different experimental setup approaches were investigated. Firstly, local 2C-TiRe-LII measurements were used to sample a small volume of the flame using PMTs and secondly, global 2C-TiRe-LII, to sample the entire flame in order to avoid the dependency of soot location and low signal intensity when applied to a combustion chamber. Point measurements induced fewer errors than global measurements, therefore the effect and validity of spreading over a larger volume was discussed by the comparison of the two approaches.

Two different ways of fitting temporal LII signals were investigated. The first one, based on getting the value of the fluence and modelling the complete LII signal and the second one by using the equivalent particle temperature at the end of the laser pulse as main input for computing the theoretical LII signal. The difference of signal processing approach had an important impact on the results. The first approach was selected within the framework of applying the technique in an optical engine.

A temperature overestimation resulted in overestimating the particle diameter to compensate for the higher heat loss by sublimation and conduction.

Questions on the accuracy limits of this technique were described in depth. Some uncertainties came from unreliable properties, such as the refractive index. Other errors were introduced by the combination of different spatially-resolved techniques; increasing the sampling volume increased the error due to the spatially inhomogeneous particle temperature, surrounding gas temperatures are not uniform across the flame.

The study of the different parameters from the heat transfer model and soot properties highlighted the wide range of diameters that can results from the fittings according to these theoretical assumptions. The optimal parameters for the present study are summarised in the table below.

$E(m)$	Laser fluence	β	α	Gas temperature (K)	Standard deviation
0.3	0.1142	1	0.3	1600	0.2

Table 14 – Optimal fitting parameters

However the existence of different sets of parameters is possible, there is not an unique solution to optimally fit the experimental data.

The results from global and local measurements concur relatively well considering the experimental and theoretical assumptions inherent to the technique. The temperature reached by the particles varied throughout the flame by less than 85K difference. The technique is time-efficient compared to point location techniques, and the ability to conduct spatially-resolved soot measurements is crucial to further understand soot formation especially in turbulent flames.

The experiment on the laminar diffusion flame was conducted to investigate the feasibility of the technique to spatially and quantitatively measure particle size, soot volume fraction, and number density, with the intention of applying it to an optical Diesel combustion chamber.

7 CHAPTER VII SOOT FORMATION IN A DIESEL ENGINE

The main objective of this work was to investigate the soot formation processes in a Diesel engine combustion chamber. Particle emissions are commonly measured at the exhaust. The sample is the final emission of one full cycle and several techniques based on different physical principles exist. It is ideal for emissions calibrations when engine parameters are adjusted and the effect on the overall produced emissions analysed. However, measuring the size of particles and soot volume fraction inside the combustion chamber at different timing can only be performed by laser diagnostic techniques. Two optical Diesel rigs, “Vertigo” and “Proteus”, were available at University of Brighton to carry out the experiments. The LII/ELS experiments were first set on the Vertigo, a more advanced optical engine with glass bowl piston. Unfortunately the design of the optical accesses was not optimised for soot visualisation, due to the optical accesses located too high in the combustion chamber, and therefore no satisfactory laser-induced incandescence signals could be recorded. The same experiment as the one carried out on the Santoro burner was conducted on the “Proteus”, a reciprocating rapid compression machine (RCM) able to replicate the in-cylinder pressures and temperatures of a modern Diesel engine and designed to have quiescent air flow in the combustion chamber. The effects of the main parameters - injection and in-cylinder pressures, intake air temperature and cetane number - influencing the combustion in an internal combustion chamber were investigated. The soot formation study was temporally restricted by the presence of the fuel spray to avoid the strong Mie scattering from the liquid. Therefore soot quantification and particle size measurement were conducted slightly after the end of fuel injection, and during the late combustion phase.

7.1 Experimental set-up

Proteus rig

The Proteus reciprocating rapid compression machine, was designed and commercialised by Ricardo. This optical engine has been developed to further our understanding of the Diesel combustion processes. In particular, by means of optical accesses, the spray and flame development can be investigated, auto-ignition, liquid and vapour fuel penetration (Karimi, 2007, Shoba, 2011), soot formation (Crua, 2002), OH and NO formation (Demory, 2007) were previously investigated in this RCM.

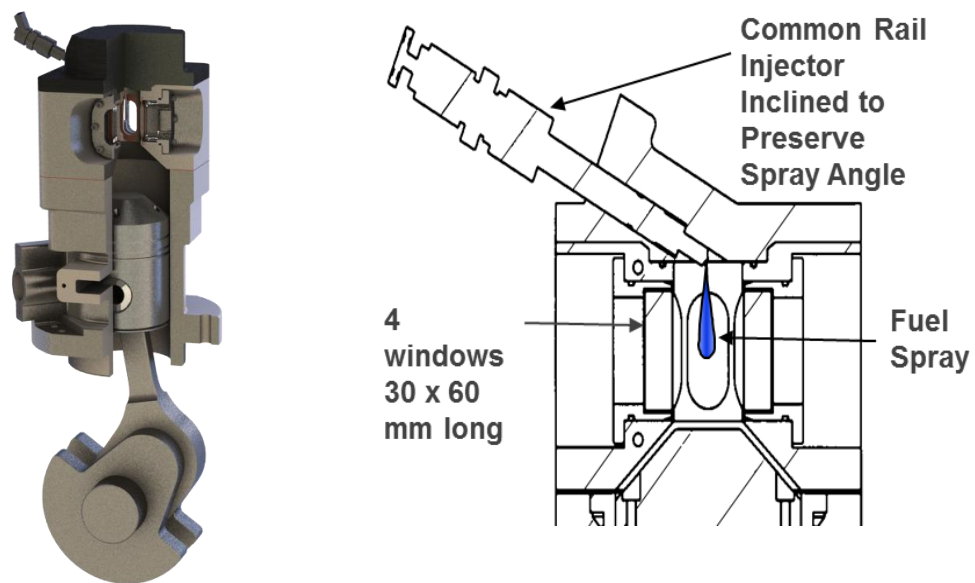


Figure 7-1 – CAD drawings of the Proteus design

The Proteus is a modified single-cylinder engine converted for two-stroke cycle operations and implemented with four optical accesses. This RCM was designed for quiescent air motion inside the combustion chamber. It was first described and tested by Kennaird et al (2000) and thereafter presented by Crua (2002) and Demory (2007). The main engine characteristic and running conditions are summarized in Table 15. The principal characteristics of this engine are a bore of 135 mm, a stroke of 150 mm and a displacement volume of 2.2 litres. The operating conditions were kept the same as in previous studies (Crua, 2002; Demory 2007) in order to further improve the combustion model. The engine was set to 500 rpm and a single hole injector was used to deliver 30 mm³ of fuel in a single injection starting at 15 crank angle (CA) degrees before top-dead centre (TDC). The injector was inclined in order to inject vertically in the combustion chamber and to visualise a unique spray through the optical accesses. The RCM running

at a constant speed of 500 rpm, the correspondence between crank angle degree and time is 1 ms for 3 °CA (Figure 7-3), the injection being used as reference time, the timings are expressed as millisecond After Start Of Injection trigger (ASOI).

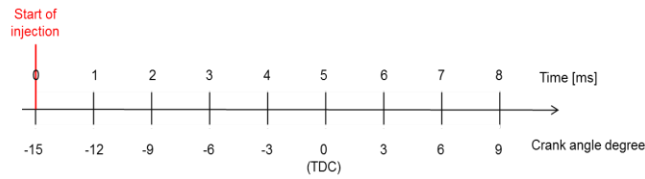


Figure 7-2 – Crank angle degree and time ASOI correspondence

Engine model	Ricardo Proteus
Type	Optical, Diesel common-rail, two-stroke, single-cylinder
Air motion	Quiescent
Injection system	Bosh, VCO single guided injector, 0.2 mm diameter single straight hole
Injected fuel quantity	30 mm ³ of fuel
Injection duration	1.95 to 3.42 ms, depending on pressure
Injection firing rate	Once in 10 revolutions (9 are skipped)
Start of injection	-15 °CA after TDC
Spray cone angle	135°
Inlet port opening	95 °CA
Exhaust port opening	85 °CA
Speed	500 rpm
Bore / stroke	135 / 150 mm
Displacement	2.2 litres
Compression ratio	9:1
Injection pressure	60 to 160 MPa
In-cylinder pressure (TDC not firing)	6 to 10 MPa (designed for up to 12MPa)
EGR	none
Water jacket temperature	363 K
Intake air temperature	393 and 493 K
Intake air pressure	0.2-0.3 MPa absolute

Table 15 – Main engine characteristic and operating conditions

The fuel injected was a BP ultra-low sulphur reference Diesel fuel with no additive (ref: G09/066). The volume of fuel injected was kept the same for the different injection pressures. The fuel injection was calibrated and injection durations defined in order to inject 30 mm³ of fuel at any test point.

The choice of maintaining a fixed fuel volume delivery was made in order to facilitate the investigation of the effect of injection pressure on soot formation. This choice was also made to keep the same conditions as previous studies (Crua, 2002; Demory 2007) for a comprehensive Diesel combustion model development.

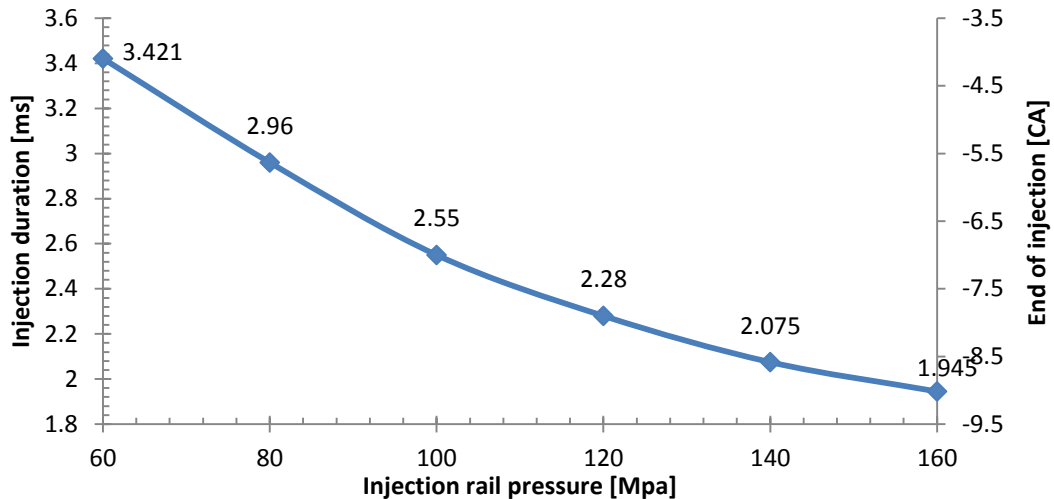


Figure 7-3 – Injection duration and end of injection for the different injection rail pressure

However, because injection durations were longer for lower injection pressure and the start of injection angle was fixed, the in-cylinder pressure and temperature at the end of injection varied with injection pressure.

Windows were available in three different materials (BK7, sapphire and fused-silica); sapphire was preferred for its better transmittance, especially in the UV, and durability. The windows were designed to be easily removable and interchangeable due to frequent cleaning and replacements. Windows of 60 mm high and 30 mm wide give optical accesses to the combustion chamber. A zone between injector tip and the top of the window was out of field of view, although this was not an issue for soot investigations as the soot formed downstream of the liquid spray. The investigation field of this experiment was located at 23 mm to 83 mm from the tip of injector. Images were acquired with a resolution of 625×341 pixels, thus one pixel corresponded to $9.06 \times 10^{-3} \text{ mm}^2$.

The optical set-up was kept identical to the previous experiment. However, the laser sheet was reduced in height by adjusting a lens of the laser sheet-forming optics in order to increase the fluence and to compensate for the increase of the conduction. Furthermore, a sheet height larger the optical windows was not necessary and would have increased background scattering. Two different laser sheet positions were set: the

first one in the centreline of the injector axis and a second position offset by 7 mm towards the camera. The second plane was favoured to avoid the high signal absorption – signal trapping - by the soot cloud. An example of this effect is illustrated in Figure 7-4.

7.2 *Optical engine transposition challenges*

Performing LII in a combustion chamber introduces new challenges. The high pressure condition provokes a faster temporal decay of the LII signals, lasting a few dozens of nanoseconds (compared to more than a millisecond at atmospheric pressure condition). The widening of the soot cloud volume highly attenuated the laser beam and LII signal to the limit where the signal is below measurable level, and in these conditions only a few millimetres on the left part were observable (Figure 7-4). Obtaining exploitable LII images in a combustion chamber constitutes a real challenge.

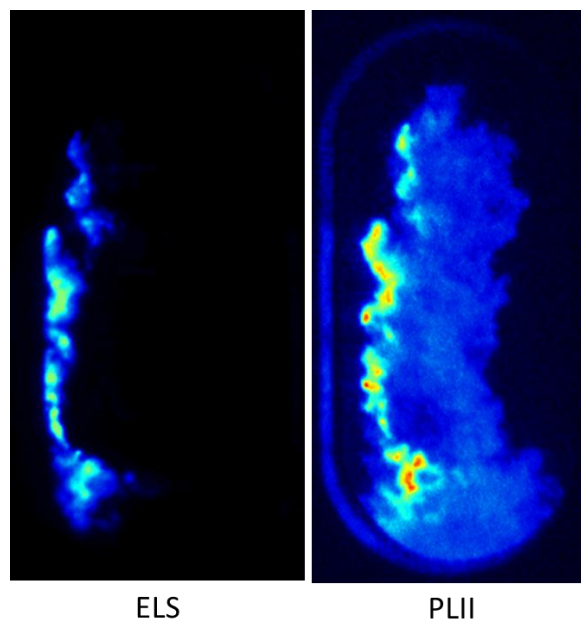


Figure 7-4 –Soot cloud absorption

Therefore for high soot concentration, the flame was optically too dense; the optical technique reached its limit of use and validity. For these conditions, high soot concentrations are produced, 2-ethylhexyl nitrate was added as an additive to the fuel in order to reduce the soot production by promoting OH production (Higgins et al., 1998). The higher flame temperature and soot cloud width, plus the shortened LII signal duration, introduced a higher background noise from the natural flame luminescence. The measurement recordings being after the end of injection, the contribution of the

fluorescence from PAH to the recorded signals was minimised (Bobba and Musculus, 2012).

The optical accesses were subject to deposition of soot and oil on their surfaces exposed to the combustion chamber. The soot deposit occurred when the soot cloud impinged directly on the cylinder walls. Due to the injector nozzle angle and soot cloud propagation, the jet impinged more on the lower part of the optical accesses. The extinction due to the deposit of soot on the window was therefore non-homogeneous along the vertical axis of the windows. The window fouling was a major issue for an optical technique recording at different wavelengths, due to soot absorption being inversely proportional to the wavelength (Equation 61). Therefore the signal recorded at the lowest wavelength (400 nm) was more attenuated than the one recorded at higher wavelength (700 nm), introducing errors in the pyrometry technique. In order to avoid high wall soot absorption, the optical accesses were cleaned up before recording each data set point, the injection skip cycle strategy was adopted and a limit of 30 fired cycles was defined. However the laser energy absorption was minimised by vaporization by the laser of the deposits on the window; minimizing the possible laser fluence decrease by fouled windows (Ranner et al., 2007). The laser was firing continuously between injections to improve the window cleaning.

Cycle to cycle variations lead to significant differences in the quantity of soot produced and measured. Depending on the engine running conditions, the soot cloud could be located lower than the field of view, the optical access being limited in height and width. The spatially limited optical access and angle difference between the two optical paths for LII and ELS generated areas that are not covered by both acquisitions.

To prevent any damage to the intensifier by the strong Mie scattering from the fuel, the recording was started at 0.1 ms after the end of fuel injection. This timing was not the most favourable as the soot concentration was at its peak (Crua et al., 2004), resulting in high absorption of the laser sheet and LII signal trapping by the soot cloud.

Test conditions

Table 16 lists the operating conditions carried out in the Proteus when additive was added or not to the fuel for various in-cylinder and injection pressures. The additive, Ethyl Hitec 4103 or giving its chemical name 2-ethylhexyl nitrate ($C_8H_{17}NO_3$) was added to the fuel with a dosage of 0.375 cm^3 per litre for a cetane number increment of 2. The in-cylinder pressure refers to the pressure at TDC for a motored cycle.

		Injection Pressure (MPa)											
		60		80		100		120		140		160	
Cetane number	55.3	Excessive absorption						6	8	8	10	8	10
	59.3	6	8	6	8	6	8	6	8	6	8	6	8
	61.3	6	8	6	8	6	8	Low soot					
In-cylinder pressure (MPa)		Correct Signal											
In-cylinder pressure (MPa)		Weak signal											

Table 16 – Suitable operating conditions

From the qualitative results of the table above, initial deductions can be drawn. With no fuel additive and injection pressures less than 120 MPa, the soot cloud absorption is too high to obtain exploitable signals. By increasing the injection pressure or the additive concentration, the soot concentration is reduced. However, for even higher cetane number and injection pressures, the quantity of soot produced was not sufficient to be detectable by LII measurement. This approach gave a wide range of operating conditions and sooting levels.

Two different set-up approaches were investigated. Different areas of the combustion chamber were sampled with the PMTs, but due to erratic conditions and low signal intensity, the point measurement was discarded in favour of a global measurement approach. Data acquisition becomes extremely random for turbulent flames if a small volume of the combustion chamber is sampled. Moreover, in order to be in the optimal conditions, the RCM had a limited running time when sampling could be done without being affected by optical access fouling. In order to optimize this running time, the second approach was considered to be the best option and more representative of the global soot presence at a given timing.

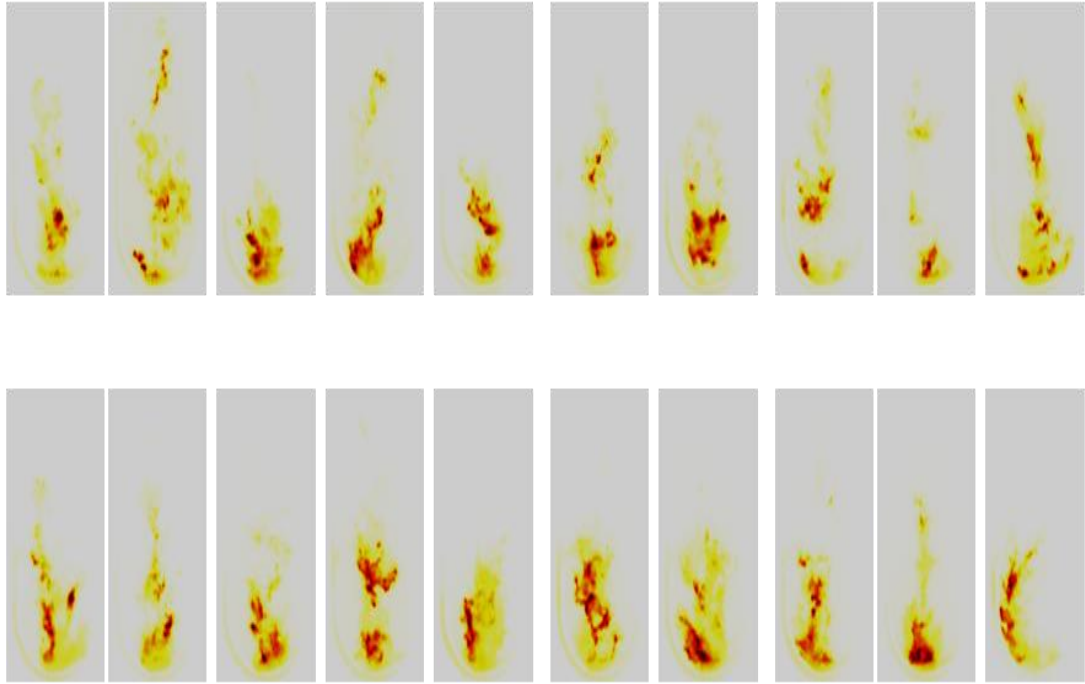


Figure 7-5 – Illustration of cycle to cycle variations of soot clouds by PLII measurements in a combustion chamber

Information obtained by globally sampling the flame by LII diagnostic are more representative of the particle size distribution for a given timing than sampling the flame locally. In a combustion chamber, results from locally resolved LII are too dependent on the sampling position and flame structure. The variations of flame structure are relatively different from one shot to another (Figure 7-5). The soot clouds are distributed in definite clusters, due to non linear fuel distribution caused by injector needle oscillations (Crua et al., 2003).

The field of view inside the combustion chamber prevented the soot cloud to be visualized after 83 mm from the tip of injector. To put things in perspective, this is twice the length of a flame plume in a light duty engine (~86 mm bore).

7.3 Post-processing

The post-processing approach was explained in the previous chapter. The temporal LII decay signal was fitted by a theoretical model more suitable for internal combustion conditions. The model was switched for a more realistic, already tested and approved model for high pressure conditions (Table 4). The input pressures of the model were obtained from the in-cylinder pressure at the laser firing moment.

The image processing was different from the Santoro burner experiment. The flame being wider and hotter, the natural flame luminescence was not negligible on the recorded LII images. The overall soot cloud position could be inferred from the LII images. A background noise from the in-cylinder wall was also recorded on the ELS images due to multiple laser scattering. The optical thickness due to the soot cloud reduced this background noise at the soot cloud location. Therefore from the ELS image, the flame luminescence recorded on the LII images could theoretically be removed. However, the background subtraction being not constant due to cycle to cycle flame variation would have biased the results and therefore was not processed. An empirical intensity threshold system was applied. The background noise induced by the laser was subtracted with a threshold of 3% of the ELS signal peak amplitude and a threshold condition on the LII signal was set to subtract the flame luminescence. The threshold condition on the LII images was defined as: if the intensity of the ELS image pixel was 0, the LII image pixel was set to 0. The threshold on the ELS images limits the resolution of the technique, if the signal was under the threshold value, the pixel was considered as background i.e. = 0.

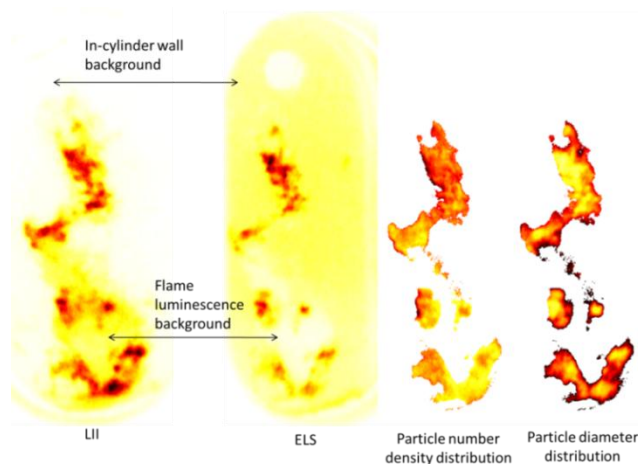


Figure 7-6 – Background noise from flame luminescence and cylinder-wall

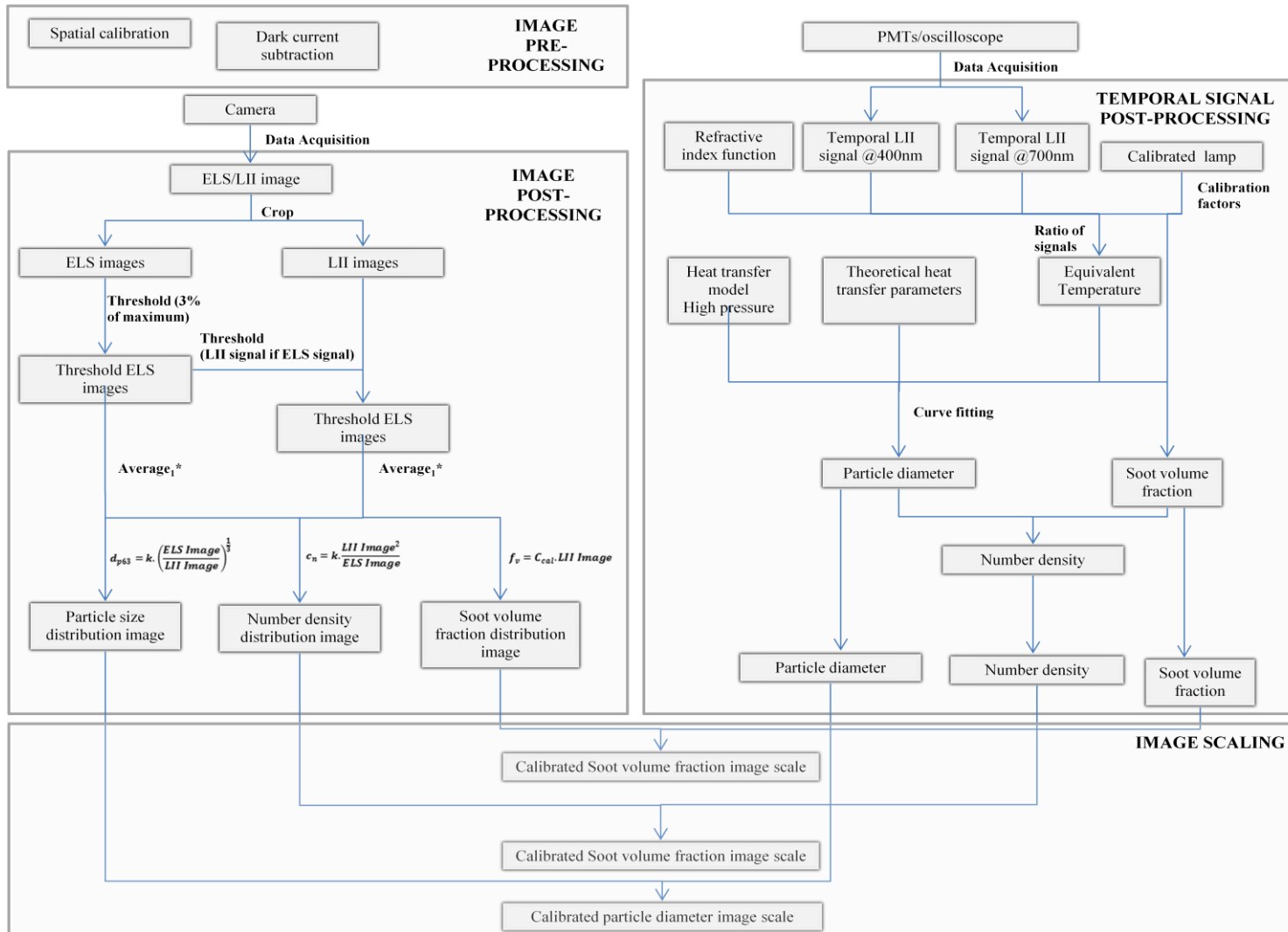


Figure 7-7 – Post-processing diagram

The natural luminescence is an inconvenience in LII measurement but it can be used to estimate the overall position of the soot cloud by averaging the non-post-processed LII images. The estimation of the sampled flame volume needed to compute the soot volume fraction measured by LII depends on this threshold. The number densities were computed from these values, but the uncertainty introduced by the thresholding means that they should be used for indication only.

In all the images presented for the RCM conditions, the laser excitation was coming from the left side and the fuel spray was going downward as shown on Figure 7-8.

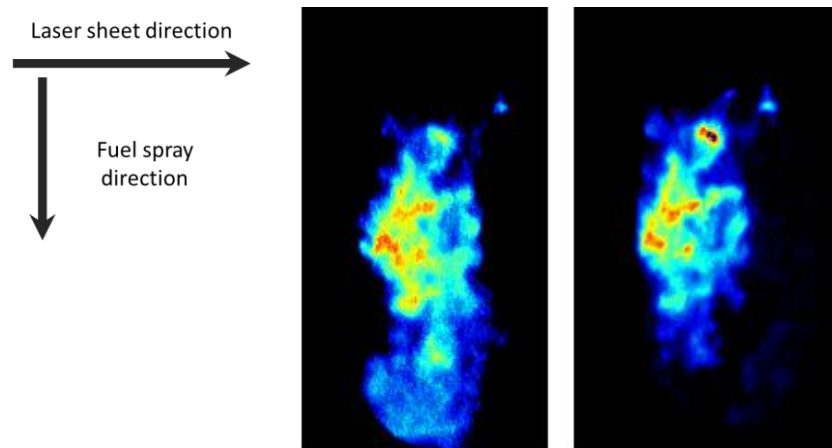


Figure 7-8 – RCM acquisition image example

LEFT: PLII image – RIGHT: ELS image

Figure 7-9 illustrates the image post-processing; the third image shows the effect of the background noise on the post-processed spatial distributions, in this case the size distribution. The advanced post-processing allows reducing these artefacts that result from the division by small values. This example shows the comprehensive results that the technique can provide with the location of the zone where particles are small but in high quantities (zone where they are produced) and the zone where they grow and agglomerate.

The particle sizing was performed from the LII signal recorded at 700 nm wavelength. This choice was made by the higher signal to noise ratio and the duration of the signal lasting longer. The modelling was computed using the parameters of Table 17 for all the RCM running conditions.

$E(m)$	Laser fluence [$J.cm^{-2}$]	Gas temperature (K)	Standard deviation of size distribution
0.3	0.1142	1900	0.3

Table 17 – Fitting parameters for RCM conditions

The particle size dispersion varies in the combustion chamber and distribution law can be considered as multi-lognormal. The particle size distribution in the RCM was considered log-normal, with a wider standard deviation of 0.3 compared to the Santoro flame condition, to improve time processing.

7.3.1 Heat release rate analysis

The combustion inside a non-optical or optical engine is commonly characterized from the rate of energy released by the fuel, the so-called heat release (HRR). The heat release rate is computed from the in-cylinder pressure recorded by a water-cooled pressure transducer (Kistler) and the crank angle by a 3600 pulse crank shaft encoder. The net heat release rate under specified assumption (in appendix D) can be computed using Equation 10.

Pressure traces (single measurement and a set of 50 cycles) representing the pressure inside the combustion chamber resolved by crank angle are illustrated in Figure 7-11.

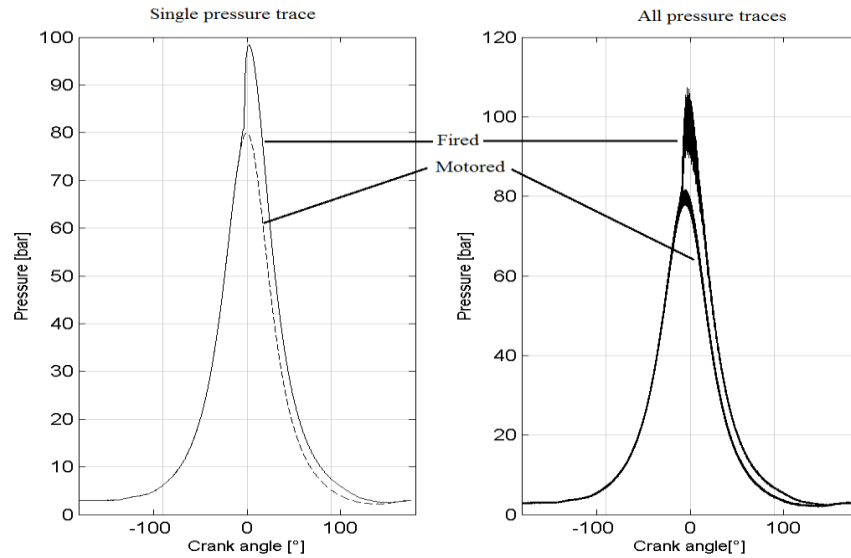


Figure 7-11 – In-cylinder pressure traces for 8 MPa in-cylinder pressure and 160 MPa injection pressure for motored or fired condition

(RIGHT: Single measurement; LEFT: all measurements).

The combustion can increase the peak in-cylinder pressure by between 1 and 2.5 MPa. The spread in these combustion pressures is indicative of the cycle to cycle variability. Heat release rates were computed for all pressure traces and an example of HRR for different injection pressures is presented on Figure 7-12 and for different in-cylinder pressures on Figure 7-13.

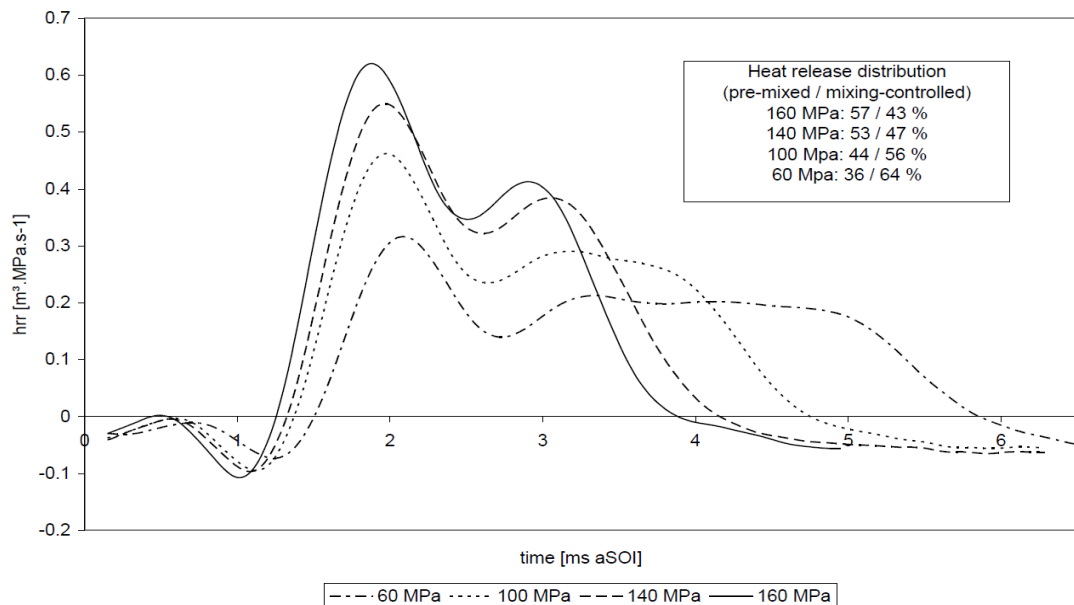
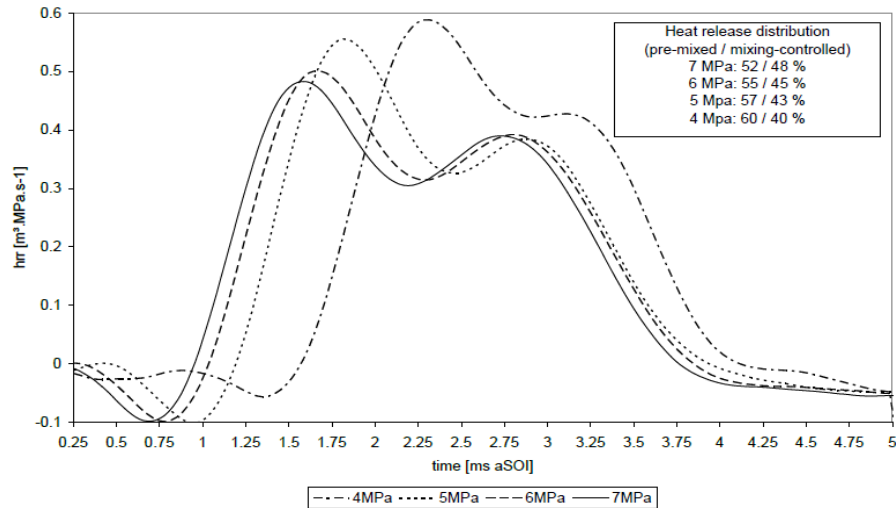


Figure 7-12 – Heat release rates for different injection pressures (for 6 MPa in-cylinder pressure)

Increasing the injection pressure, in-cylinder pressure, air temperature and cetane number has for effect to reduce the ignition time. For lower injection pressures, the combustion event lasted longer due to the longer injection duration. That favours a mixing controlled combustion and the HRR peak amplitudes were reduced for both, pre-mixed and mixing-controlled combustion.



**Figure 7-13 – Heat release rates for different in-cylinder pressures
(for 160 MPa in-cylinder pressure)**

7.4 Experimental results and discussion

The influence of engine parameters were investigated from 60 MPa to 160 MPa injection pressures, 6 to 10 MPa in-cylinder pressures, different heated air intake temperatures (100 and 150 °C) and different fuel cetane numbers (55.3, 59.3, 61.3). The experimental set-up was unchanged (same fuel system, laser excitation and data acquisition system) during all the data set acquisitions, only fuel was changed.

The soot formation study starts slightly after the end of injection due to image acquisition requirements. At this timing the flame position was well established, with the soot cloud being 13 mm and 27 mm in diameter at its upper and lower extremities, respectively. The study of the soot formation was based on the spatially and temporally resolved distributions of the soot volume fraction, particle size and number density.

7.4.1 Influence of injection pressure

In the past decades, increasing the injection pressure has been one of the promoted technologies to improve combustion engine fuel efficiency and to reduce pollutant emissions. Nowadays, modern fuel system prototypes rise up to 250 MPa injection pressure (Thirouard, 2009). Increasing the injection pressure has the direct effect of increasing the fuel delivery rate. Higher injection pressures are known to reduce droplet sizes, to improve mixture formation and therefore to improve the combustion efficiency, to reduce soot production but also to affect soot particle size distribution. Further understanding of the soot formation mechanisms - especially on the link between injection pressure and size distribution - was one of the main objectives of this work.

From the heat release rate curves, the start of the fuel vaporization and start of combustion could be determined. For higher injection pressure, the auto-ignition started slightly earlier due to higher fuel interaction with surrounding gas and a better air/fuel mixing condition.

The spatially resolved distributions of soot volume fraction, particle size and number density for different times after injections are illustrated for two different injection pressures (120 and 160 MPa) for in-cylinder pressures of 10 MPa (Figure 7-14 and Figure 7-15) and 8 MPa (Figure 7-16 and Figure 7-17). The comparison for fixed in-cylinder pressures highlights the effect of injection pressure on soot formation. The calibration values resulting from global 2C-TiRe LII are presented in Figure 7-18 and Figure 7-19.

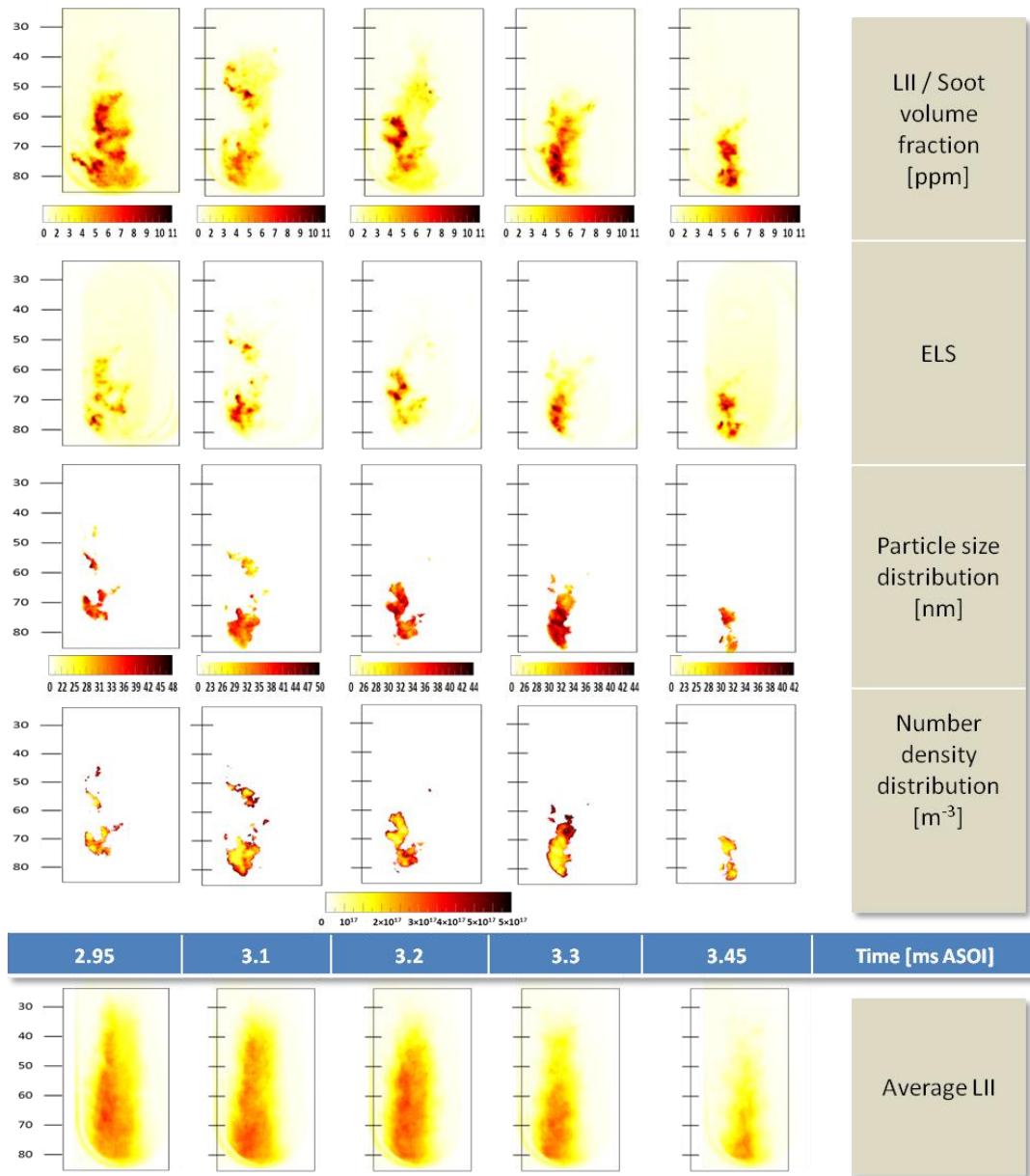


Figure 7-14 – Results for 160 MPa IP/10 MPa ICP/55.3 CN

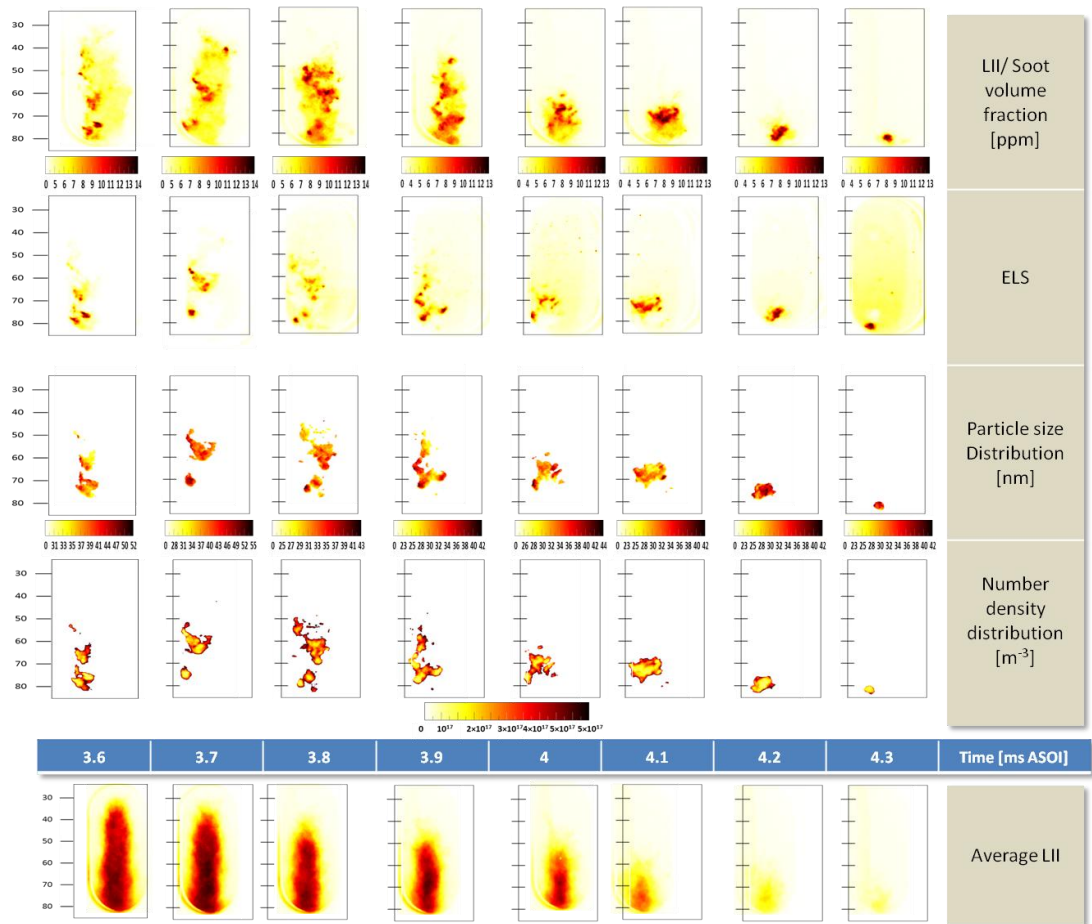


Figure 7-15 – Results for 120 MPa IP/10 MPa ICP/55.3 CN

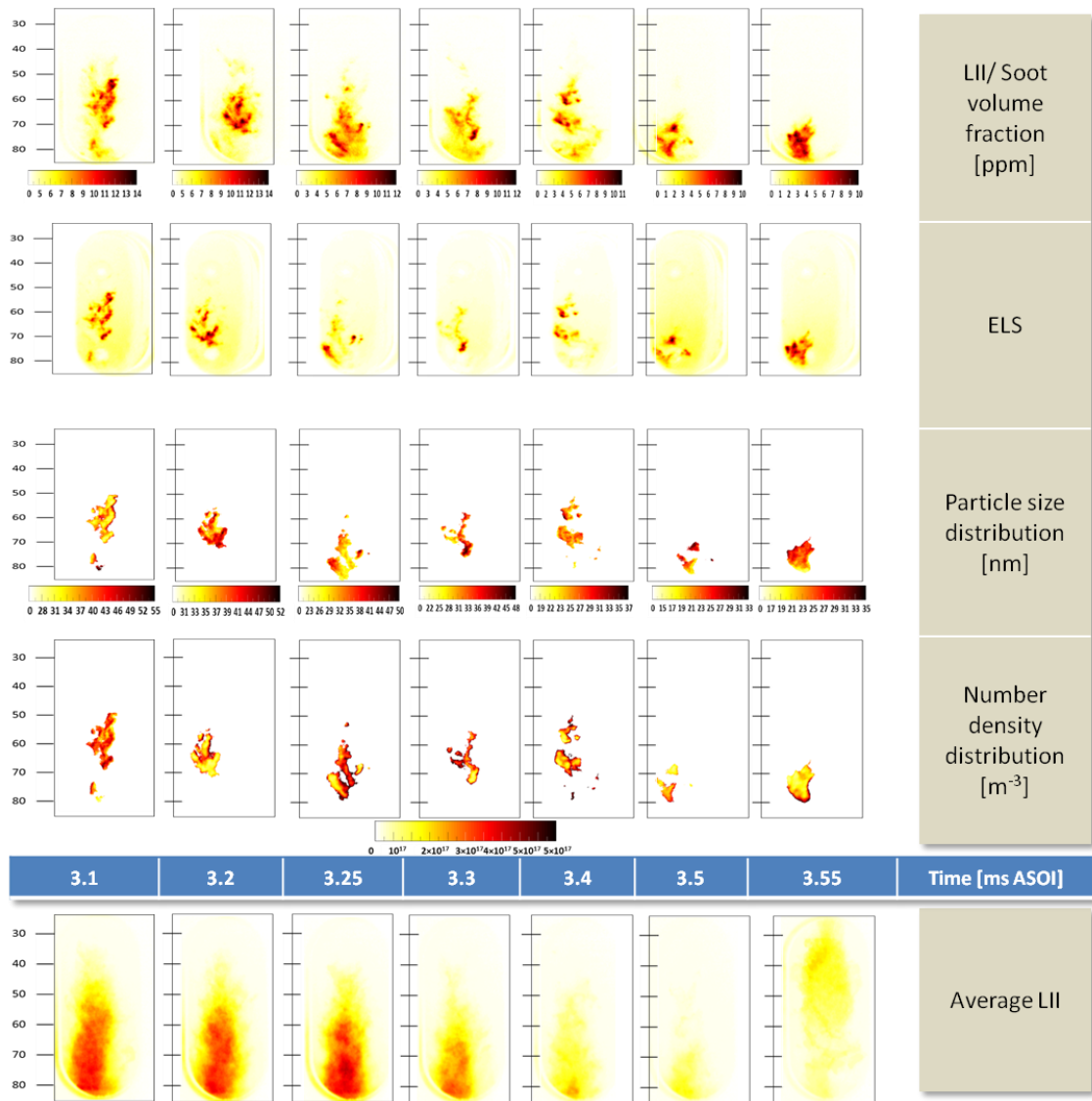


Figure 7-16 – Results for 160 MPa IP/8 MPa ICP/55.3 CN

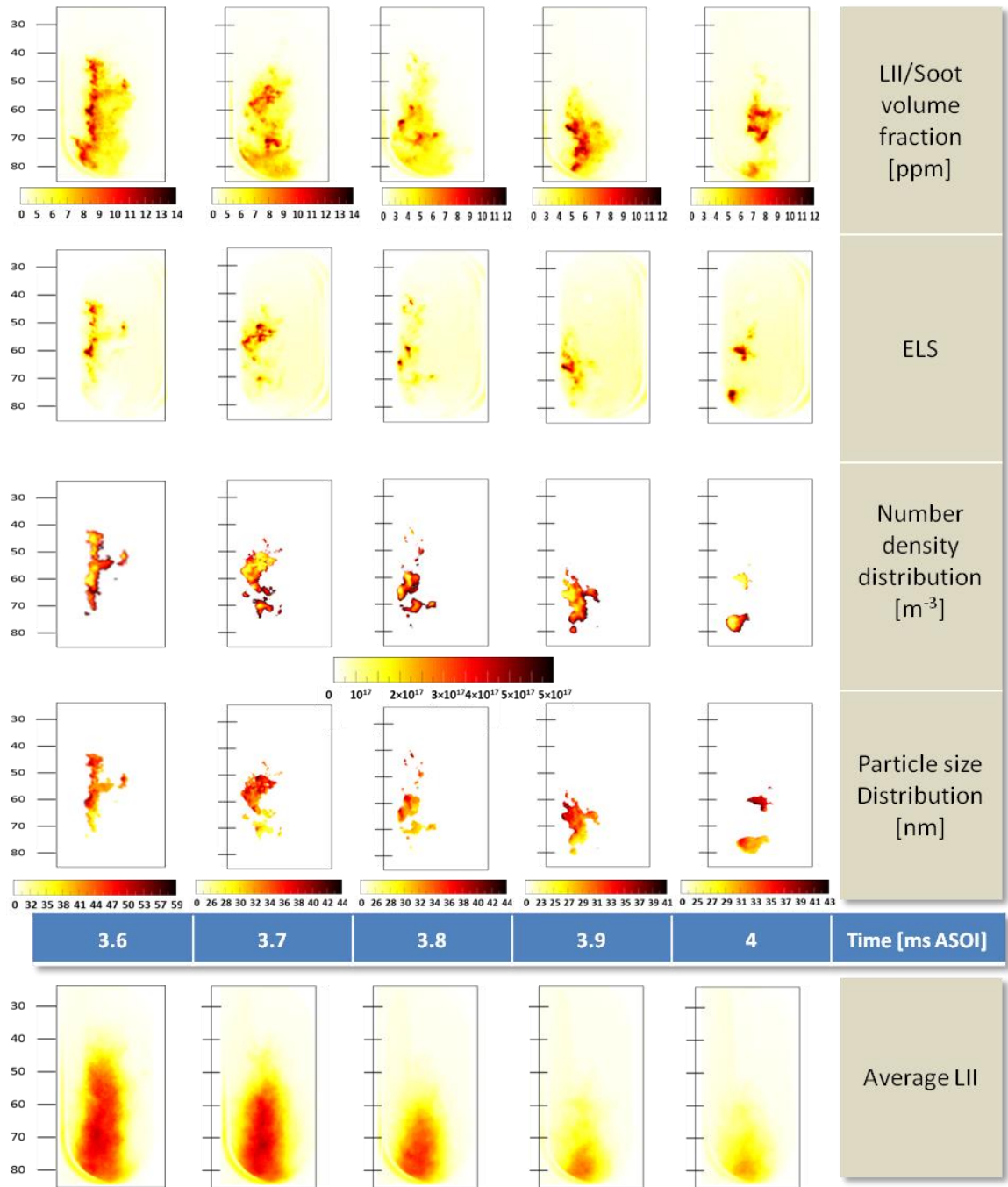


Figure 7-17 – Results for 120 MPa IP/8 MPA ICP/55.3 CN

The soot clouds appear approximately 33 mm from the tip of injector. The injection pressure can be seen to have little effect on the location of the upper edged of the soot cloud. A slight difference is noticeable for lower injection pressure, with the soot cloud being located higher up in the combustion chamber. The amount of soot is higher at lower pressure. The fact that the soot is located at the same position helps for the comparison of the quantity of soot produced. The soot cloud is vertically more stretched and radially less diffused at higher injection pressure. The larger soot cloud and higher soot volume fraction at lower injection pressure leads to higher laser absorption and signal trapping.

These phenomena can be explained by improved fuel atomisation/vaporization and better air entrainment at high injection pressure. Better air/fuel mixing is known to improve the fuel pyrolysis (Bruneaux, 2002) but momentum of the liquid and vapour fuel is higher. The fuel droplets at lower injection pressure are larger, have lower velocities and mix slower than the ones at higher injection pressure. Nevertheless the better atomisation and higher spray velocity seem to compensate to obtain first soot particles at almost the same distance from the nozzle, independent of the injection pressure.

The soot clouds tend to move downstream at similar velocity. The inertia given to the nanoparticles by the fuel vapour/droplets is negligible compared to the contribution of the turbulent flow inside the combustion chamber.

The soot cloud decreased in volume faster for higher injection pressure, from 3.2 to 3.4 ms ASOI for 160 MPa compared to 2.6 to 4 ms ASOI at 120 MPa, at 8 MPa in-cylinder pressure, with a similar behaviour for 10 MPa ICP.

The particle size was relatively well distributed in the cloud, with larger particles downstream at 160 MPa compare to 120 MPa where the peak concentration were further upstream. For the number density, the trend is the opposite. The soot volume fraction was relatively compact for 160 MPa IP/8 MPa ICP until 3.25 ms ASOI when soot was spread into several points but in high concentrations. At lower injection pressure (120 MPa), soot was found in more varied different small clouds, broken away from the main soot spray.

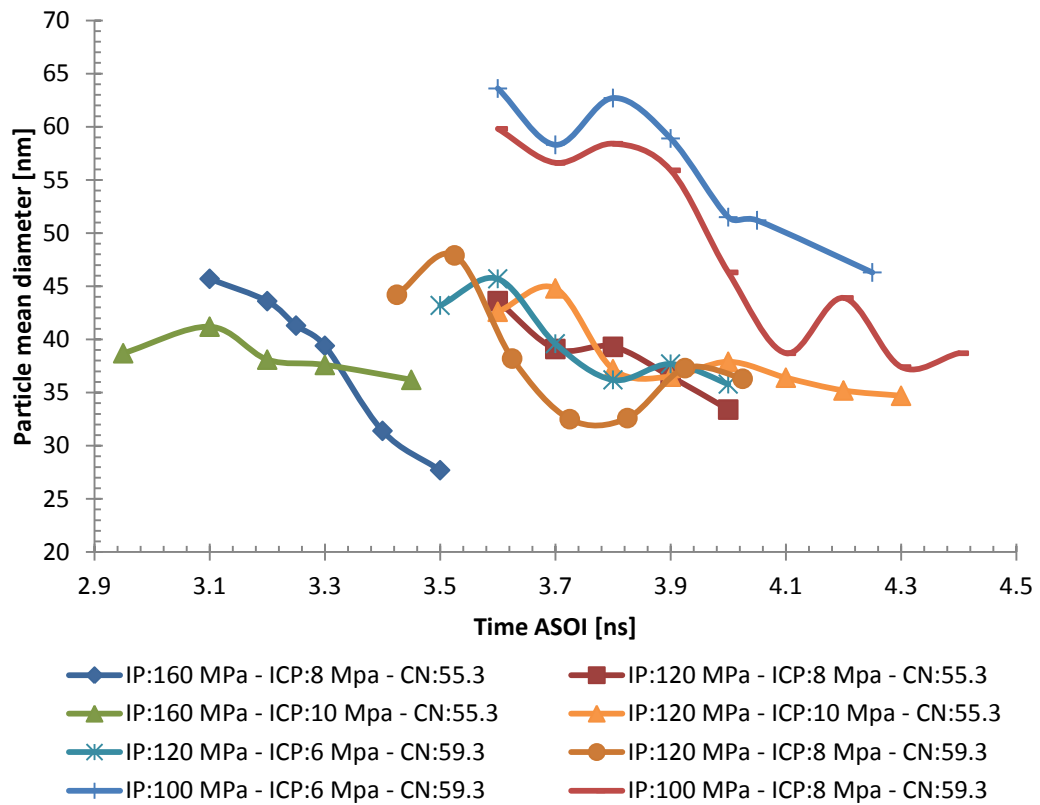


Figure 7-18 – Mean particle diameters obtained from 2C-TiRe LII measurements for different injection pressures

With all other parameters kept constant, a reduction of particle size with an increase of the injection pressure was noticeable. From the heat released rate curves, the combustion event was shortened with higher injection pressure. The image sequence acquisition was also shortened due to the soot cloud being lower down in the combustion chamber. The reduction rate of particle size tends to increase with higher injection pressure. Higher injection pressures improve the atomization of the fuel, resulting in smaller droplets, which evaporate faster due to their higher surface to volume ratio, pyrolyse less thus releasing fewer soot precursors. The improved mixing increases the temperature in the chamber and can be noticed on the different heat released rates. Temperature was the main factor influencing the soot formation: higher temperatures mean high rate of soot formation and oxidation. The trend for particle size to decrease can be thus explained by a higher temperature in the combustion chamber increasing the oxidation rate and by the fact that smaller, or less agglomerated, particles are likely to oxidise more readily.

Time resolved soot volume fractions obtained by global 2C TiRe LII are presented in Figure 7-19. An increase in injection pressure can be seen to reduce soot volume fraction.

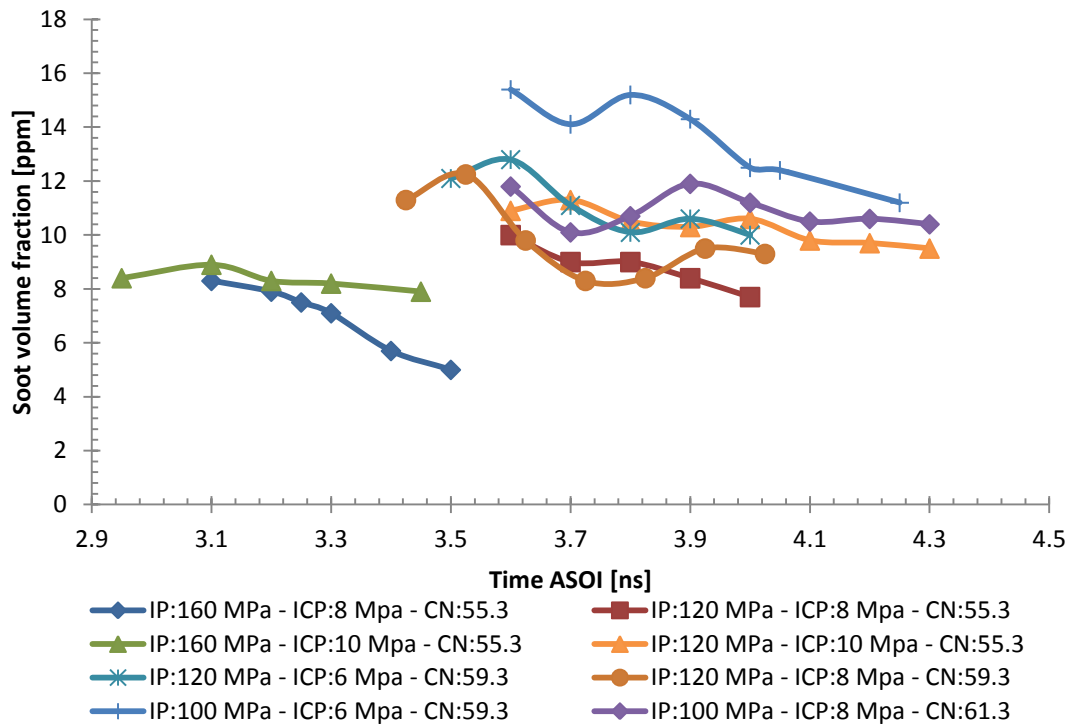


Figure 7-19 – Soot volume fractions obtained from 2C-TiRe LII measurements for different injection pressures

Higher injection pressures involve higher fuel flow rate and therefore higher fuel droplets or fuel vapour density for the same given time. The consequence would be higher soot concentration due to higher fuel/air density. However, the higher inertia of the fuel and higher gas turbulence counteract this process thus lowering the fuel and soot local concentrations. The soot volume fraction followed the same trends as the particle size evolution. f_v tended to decrease after the end of liquid fuel injection due to high temperature and oxygen concentration. At lower injection pressure, the soot volume fraction reduced slower due to slightly lower inertia, temperature, higher particle/agglomerate size and lower oxygen concentration due to larger and denser soot cloud.

When comparing the particle size for the conditions 160MPa IP/10 MPa ICP with 120MPa IP/10MPa ICP, the particle size distributions tend to be similar. However, the soot volume fraction is lower for the higher injection pressure, corresponding to a higher number of soot particles.

7.4.2 Influence of in-cylinder pressure

The in-cylinder pressure is, with the injection pressure, the main optimization parameters. In the new era of downsized engines - especially for gasoline engines, significant developments have occurred. These include variable compression ratio to improve fuel efficiency and pollutant emission of internal combustion engines by increasing the air mass in the combustion chamber by turbocharging, resulting in an increase in in-cylinder pressures. Modern Diesel engines have direct injection, thus changes in in-cylinder pressures modify a number of parameters such as injection phasing, air charge and air motion, local fuel air mixture. All these parameters will influence the power output and pollutant emissions of the engine.

The spatial distributions of soot formation are further illustrated with additional spatially resolved results at 100 MPa injection pressure for 8 and 6 MPa (Figure 7-20 and Figure 7-21) and, 120 MPa in-cylinder pressure for 6 MPa injection pressure (Figure 7-22); complementing the four previous spatially-resolved distributions (Injection pressure: 120/160 MPa and ICP: 6/8 MPa).

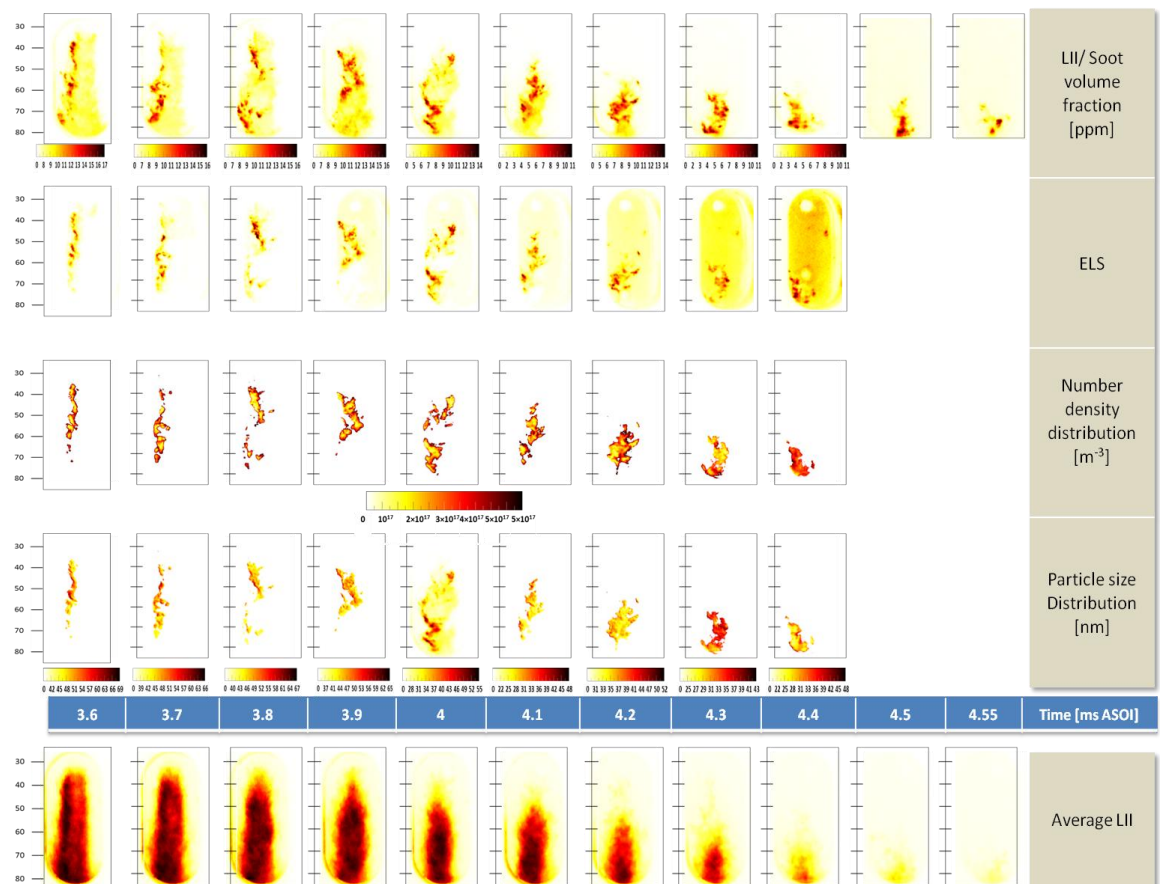


Figure 7-20 – Results for 100 MPa IP/8 MPa ICP/59.3 CN

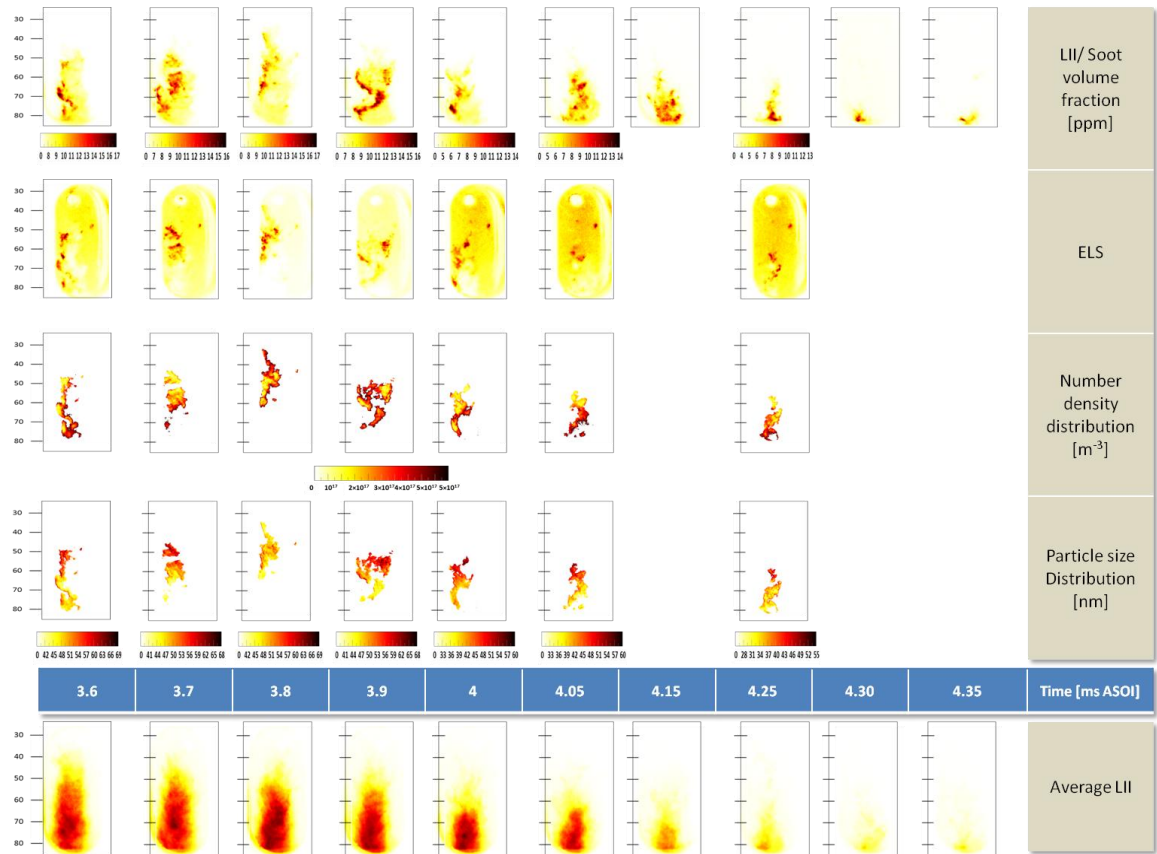


Figure 7-21 – Results for 100 MPa IP/6 MPa ICP/59.3 CN

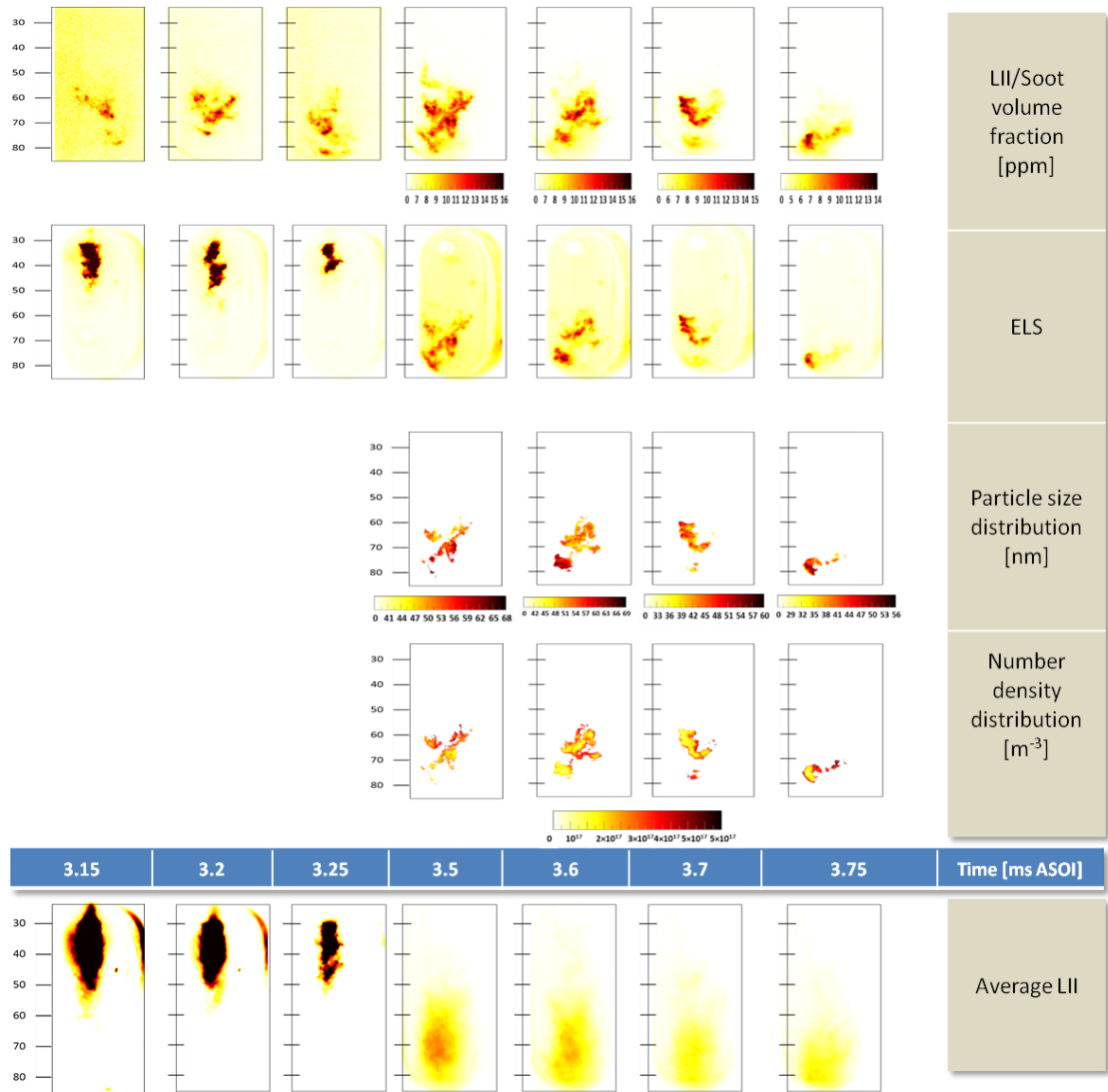


Figure 7-22 – Results for 120 MPa IP/6 MPa ICP/55.3 CN

Figure 7-22 illustrates the high scattering of the fuel when the acquisition was set slightly too early before the end of injection. Between 3.15 and 3.25 ms ASOI the fuel liquid core length was sensibly constant (~ 45 mm) and the soot cloud appeared to be located at the same position (~ 55 mm) between 3.25 and 3.5 ms ASOI. Between the two locations, in a 10 mm space, the vapour phase fuel was not detectable but certainly present. This is in agreement with the previous experiment by Crua (2002) where a full sequence from the start of injection until the end of combustion was recorded. The position of the soot cloud once it reached a stable condition was fairly constant during injection, until 0.5 ms ASOI (160 MPa IP – 6 MPa ICP).

The increase of the air density had the distinctive effect of reducing the spray penetration length and the soot cloud appeared further upstream in the combustion chamber.

The soot density was higher for higher air density. It therefore should appear a higher soot volume fraction for higher in-cylinder pressure. Instead of following this statement, a reduction of the soot volume fraction was noticed when increasing the in-cylinder pressure for identical injection pressure. The soot cloud appeared rather tall, and could occupy almost all the field of view. The soot cloud tended to disappear faster for lower in-cylinder pressure. The better oxidation of the particles at lower in-cylinder pressure can be due to higher gas temperature, higher oxygen concentration surrounding the soot, smaller particles/agglomerates. The temperatures and particles size remained sensibly the same. The longer spray penetration length and the lower soot and air density seem to lead the soot production and oxidation.

The results from global 2C-TiRe LII are presented in Figure 7-23 for particles sizes and Figure 7-24 for soot volume fraction. The comparison of the particle sizing results is dependent on the theoretical model used for heat conduction and its pressure dependency. However, lower in-cylinder pressures appeared to generate slightly larger particle sizes. The higher gas density improved the local air/fuel ratio and therefore the combustion and oxidation of the particles.

Similar soot volume fractions were noticed for 160 MPa injection pressure but particles were slightly larger for lower in-cylinder pressure. It can be deduced that higher number of particles were produced at higher in-cylinder pressure.

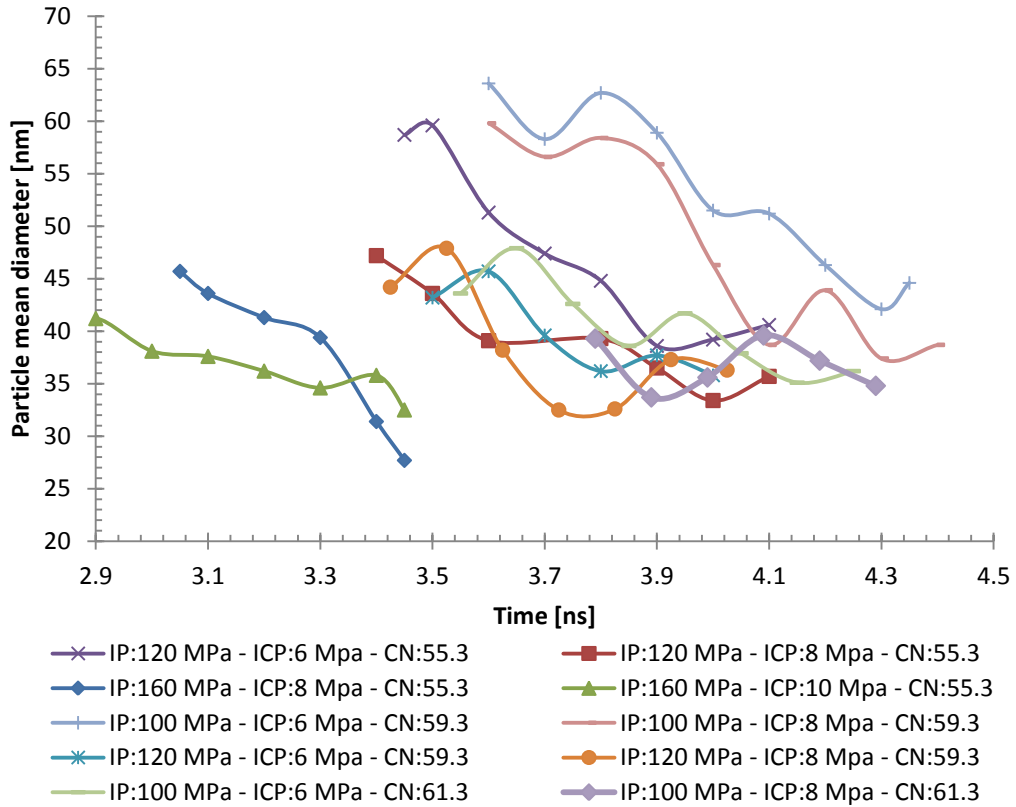


Figure 7-23 – Mean particle diameters by 2C-TiRe LII for different in-cylinder pressures

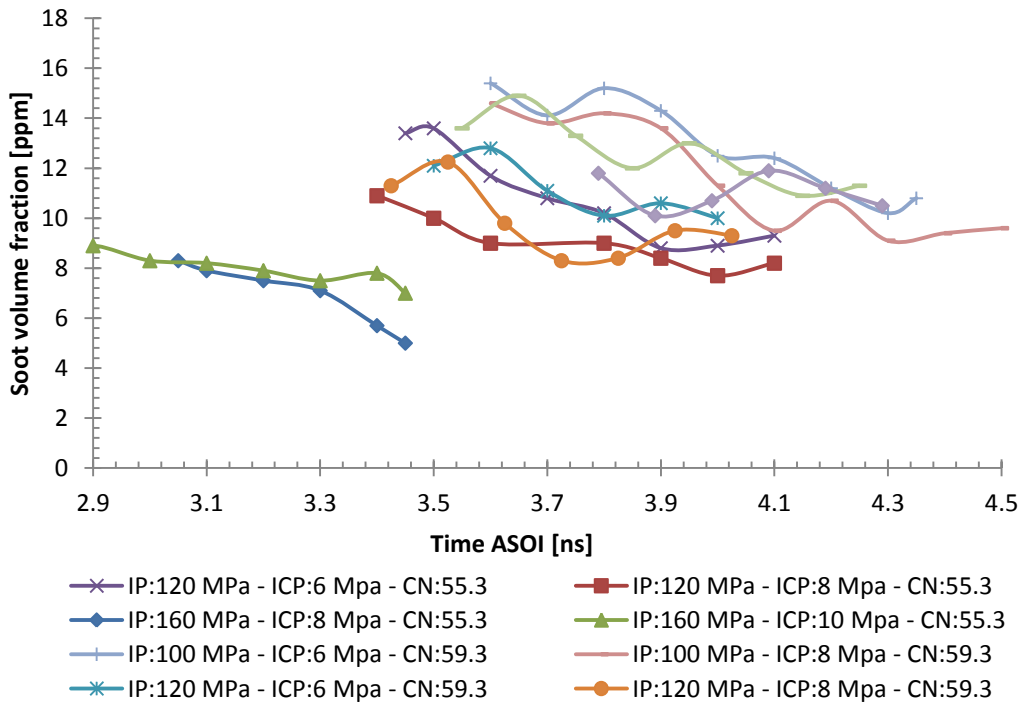


Figure 7-24 – Soot volume fractions obtained from 2C-TiRe LII measurements for different injection pressures

7.4.3 Influence of cetane number

Combustion research studies are often conducted using different commercial Diesel fuels with varying properties. To reduce soot, fuels with higher cetane number or different constituents are used. However, these are different fuels and the combustion will differ and comparison of injection pressures or in-cylinder pressures effects cannot be performed if the fuel used was different. The effects of the cetane number on the soot formation were investigated for three different values at several injection and in-cylinder pressures. The auto-ignition occurred earlier for higher cetane number, as expected, and the flame moved upward, closer to the injector. This change in combustion phasing has the effect of improving combustion and reduces the formation of soot.

The additional spatially-resolved results for 120 MPa IP / 8 MPa ICP / 59.3 CN (Figure 7-25) and 100 MPa IP / 8 MPa ICP / 61.3 CN (Figure 7-26) conditions are compared respectively with results for CN= 55.3 from Figure 7-17 and CN=59.3 from Figure 7-20.

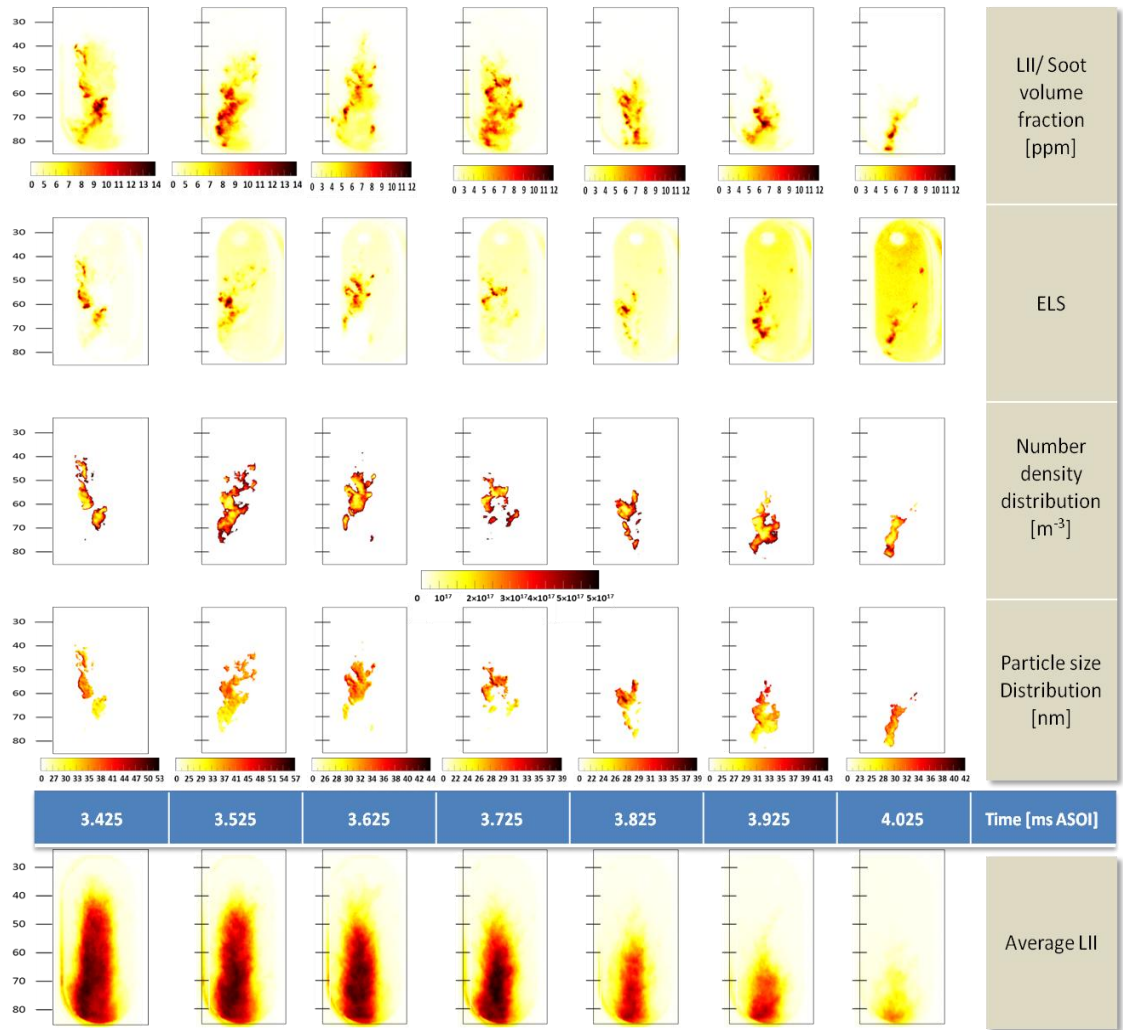


Figure 7-25 – Results for 120 MPa IP/8 MPa ICP/59.3 CN

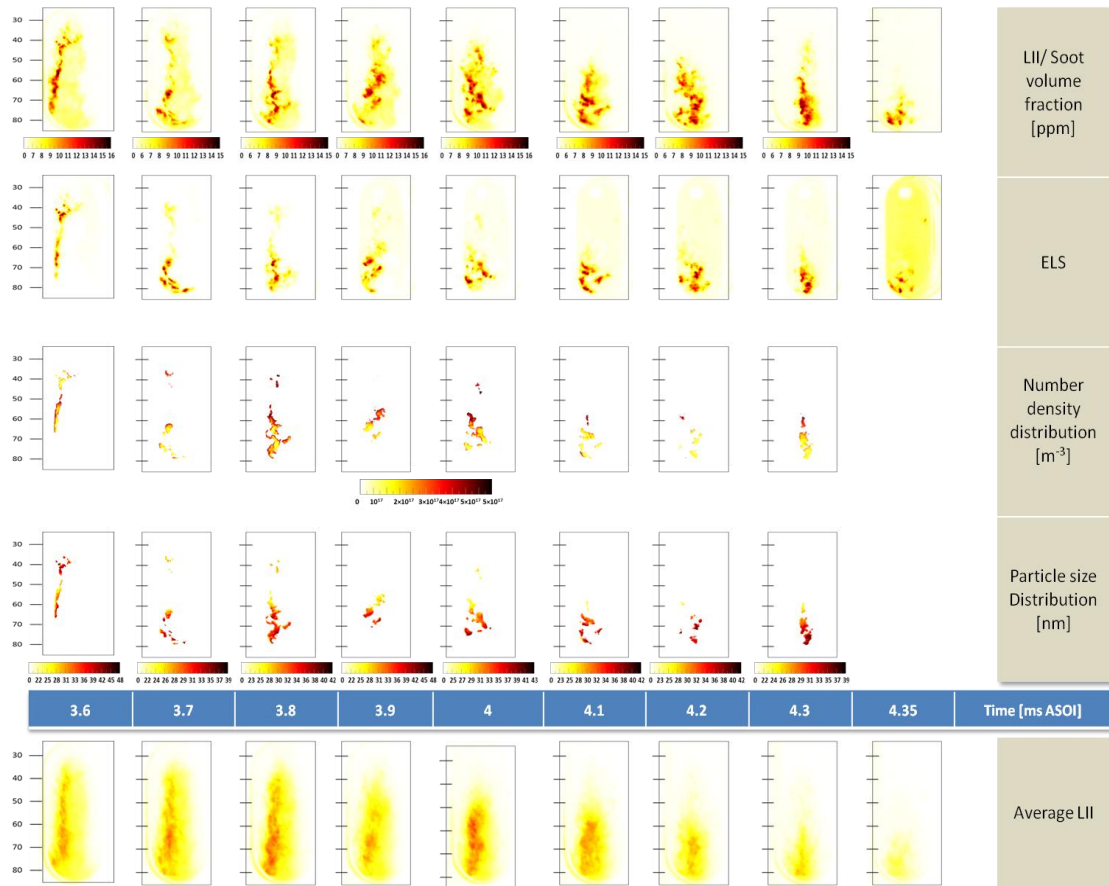


Figure 7-26 – Results for 100 MPa IP/8 MPa ICP/61.3 CN

The cetane number influenced the combustion timing: the higher the cetane number, the shorter the auto-ignition delay and the presence of soot. Smaller particles were produced by using a fuel with higher cetane number, as illustrated in Figure 7-27. Overall, less soot was produced with a higher cetane number, due to smaller particles oxidising more readily.

A higher number of smaller soot clouds, breaking off from the main soot spray were noticed for a lower cetane number. Diameters tended to be smaller upstream the soot cloud.

The soot volume fraction function of time ASOI and conditions are shown in Figure 7-28.

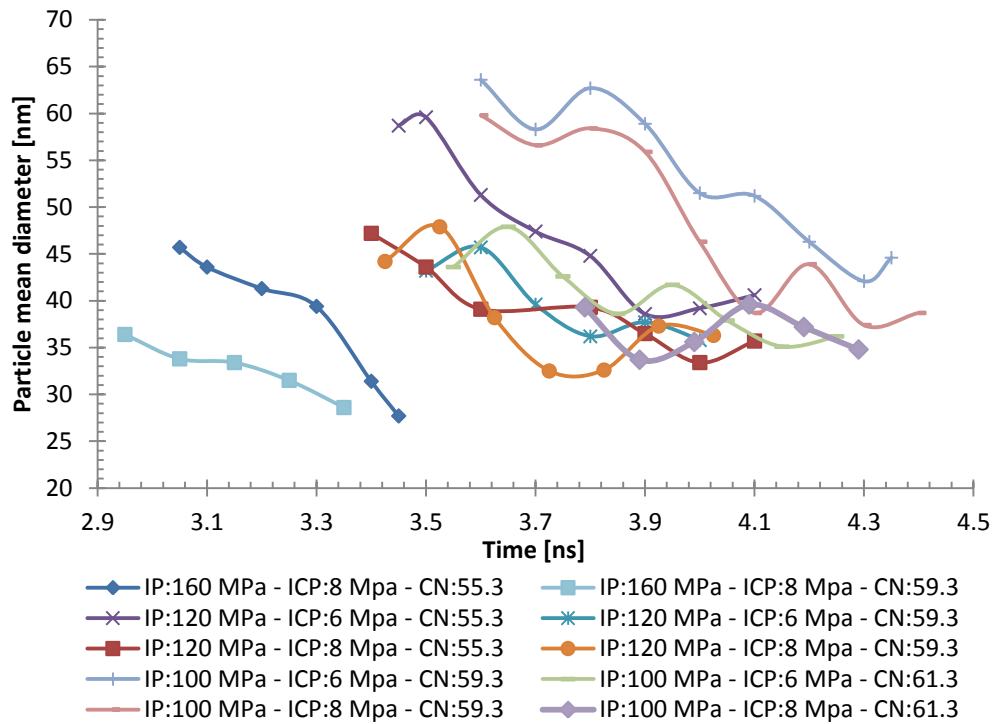


Figure 7-27 – Mean particle diameters obtained by 2C-TiRe LII for different cetane numbers

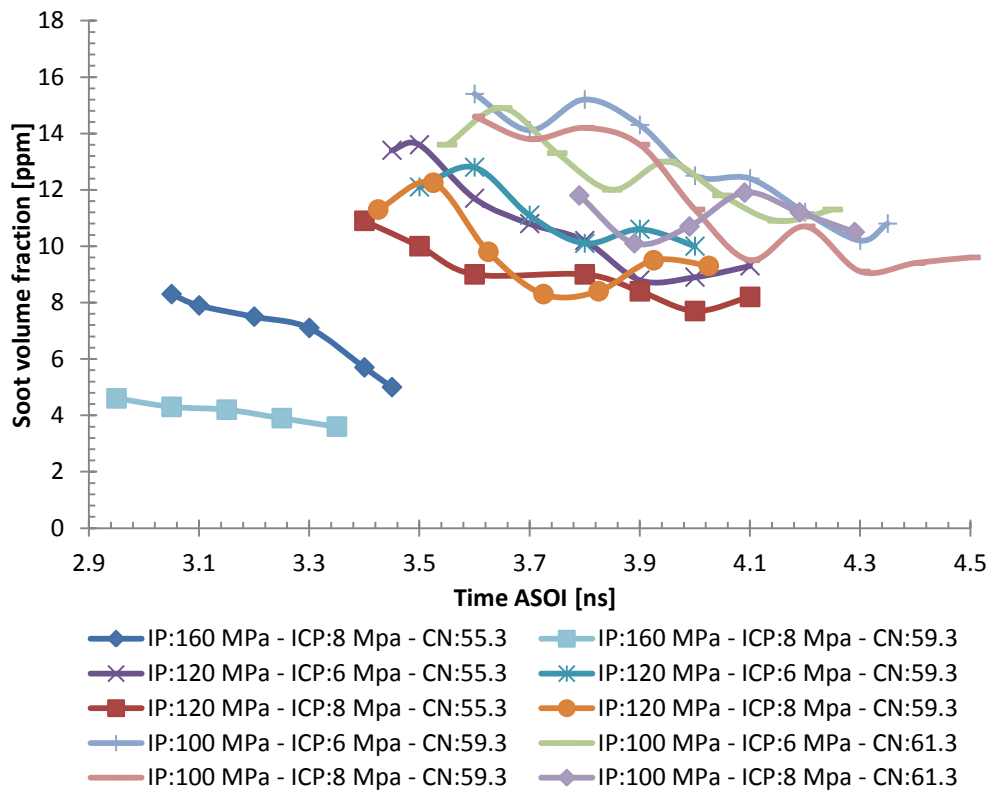


Figure 7-28 – Soot volume fractions obtained by 2C-TiRe LII for different cetane numbers

The cetane number had a visible effect on the measured soot volume fraction. For higher cetane numbers, a reduction of the soot volume fraction was noticeable from the start of recording. The decrease rate of the soot volume fraction trends tended to be similar. The additive was more effective for low level of soot. A net reduction occurs at the 160 MPa injection pressure conditions.

7.5 Conclusions

The work presented has shown the possibility of quantitatively measuring soot volume fraction, particle diameter and number density spatially and temporally-resolved for different times after injection inside an optical combustion chamber for an extensive range of operating parameters as well as different fuel cetane numbers, representative of modern Diesel engines. Experimental investigation using state-of-the-art laser diagnostics on a rapid compression machine has shown its application, validity limits and possibilities for further improvements. Experimental investigations using optical techniques do not guarantee being able to obtain comprehensive results as demonstrated with the experiments carried out in Vertigo RCM and for some of the conditions in the Proteus RCM. High pressure in the combustion chamber meant very short duration of the incandescence signal (~30 ns) and therefore very low signal intensity. Beyond that, a realistic Diesel combustion chamber is a place where the environment is highly absorbent (fuel especially when injecting commercial fuel, soot, oil, etc...) which affects both the laser pulse propagation and the incandescence signal. The soot cloud thickness was a real problem for optical diagnostic due to its optical thickness and natural incandescence. In a combustion chamber, interpretations of the results are possible although the accuracy is lower compared to atmospheric pressure conditions. Soot particles eventually moved out of field of view, meaning that the full oxidation process could not be visualised. The end of image sequence acquisition was due to the soot cloud being too low, and the last images acquired are the upper part of the cloud previously visualised. This part has lower soot volume fraction and particle size.

The technique was able to measure soot volume fraction from a range of 2 ppm for the lower limit up to 17 ppm. 17 ppm being the maximum soot volume fraction measured. At level above 12 ppm, the diagnostic could not probe the soot cloud correctly due to high absorption. Particle sizes from 28 up to 70 nm were recorded. The large particles

can be considered due to higher agglomeration. Agglomerates cooling down slower, the TiRe-LII measurements tend to be biased towards larger particles results. The large variation of sizes obtained by TiRe-LII is also due to the fast decay of the LII signal, the fitting is therefore as not as sensitive as atmospheric conditions.

The global spatially-resolved 2C-TiRe-LII gave valuable information on the mean particle size and soot volume fraction in the combustion chamber. In the late combustion phase considered, the particle size and soot volume fraction were at their highest just after the end of injection and sensibly reducing afterwards. A better air entrainment in the fuel spray and better atomization due to higher injection pressure or in-cylinder pressure led to a better mixing of the fuel upstream of the soot cloud, thus increasing the oxidation rate of the soot particles formed. Larger soot clouds tended to reduce slower due to lower air entrainment and presence of larger particles/agglomerates being slower to oxidize.

For all the conditions, the soot volume fraction and particle size tend to decrease slowly in time.

The use of additive to reduce soot signal absorption has been widely disseminated in the research community. However, in order to avoid major combustion variations due to fuel difference; soot formation was investigated with fuel containing no additive first. The additive had the effect of changing the combustion phasing and reduced the overall soot production. For higher cetane numbers, a more complete combustion occurred from the beginning of the soot cloud; even if the penetration length was reduced, the in-cylinder temperature increased, soot was produced in smaller quantities straight from the beginning, reducing the number of particles and their diameter. This also has the direct effect of improving the oxidation efficiency.

Soot volume fraction, number density and particle diameter, all tend to reduce a few tenths of milliseconds after end of injection, showing that soot oxidation was the main process and that soot production became negligible. Previous investigation based on OH LIF (Demory, 2007) has shown the diffusion flame sheath surrounding the soot cloud and the diffusion flame was the place of high soot oxidation.

Particle sizes tended to reduce later on in the combustion. However; for some conditions, particle sizes were increasing; this indicates the competing oxidation and agglomeration processes, and is consistent with the evolution of the number density.

The soot volume fraction was not evenly distributed across the flame. Clustered soot distributions were observed and were more noticeable for lower injection pressures. This was consistent with fuel injection and air motion varying with time and location; leading to heterogeneous fuel concentrations and therefore soots distribution. These differences in fuel distribution are likely to be due to needle lift oscillations (Crua, 2002) and cavitation inside the injector orifices.

8 CHAPTER VIII: CONCLUSION

Soot is the focus of a large number of research projects worldwide, mostly initiated by the need to reduce automotive emissions. The recent progresses in LII technique make this diagnostic self-evident as an important topic of study for in-situ soot formation. Out of the vast number of publications on soot formation, only a few deal with conditions close to those found in modern Diesel engines. Most of the published results are focused on determining theoretical soot/carbon properties or quantifying soot in standard laboratory burner flames and exhaust pipes. For similar experimental conditions, the results vary widely from one research group to another, revealing the difficulties in obtaining highly reproducible results. Soot parameters can vary from one experiment to another and can leave accuracy open to question.

Nevertheless, optical diagnostics based on incandescence are currently the most suitable for in-situ investigations of soot formation. Techniques based on Elastic Light Scattering (ELS) were recently used for investigating soot aggregates (Chartwarth, 2007; Velji, 2010), and coupled with LII and extinction (RAYLIX technique) to spatially determine particle size distribution, number density and soot volume fraction.

8.1 *Research outcomes*

This research uses the recent progress undertaken in these state-of-the-art techniques to make a step forward into two-dimensional soot measurements in order to obtain spatially and quantitatively resolved distributions for soot volume fraction, particle diameter and number density. The aim was to gain further understanding of soot formation upon a standard laminar diffusion flame and more importantly, in an optical combustion chamber representative of those found in a passenger Diesel vehicle. The technique is based on the different diameter dependency of the incandescence and scattered signals induced by laser. The qualitative spatial distribution recorded by the camera was calibrated by two-colour time-resolved laser-induced incandescence.

Different sampling approaches were experimented, and the 2C-TiRe LII technique was used to sample small volumes at different locations throughout the flame, and the possibility of a full flame sampling approach was investigated to further simplify the experimental configuration. If there is no real benefit with the Santoro burner

experiment, the benefits were consequent in the combustion chamber as the soot location was erratic. The possibility of sampling a larger volume was a real advantage in the case of a turbulent flame. The global 2C-TiRe-LII was compared to calibrated diameter and soot volume fraction distribution obtained by ELS/LII technique in order to conduct a critical appraisal of the validity of this approach.

However moving from point to spatial measurement generated higher uncertainties and, in this work a compromise between accuracy and spatiality was accepted.

Assumptions were made about the relation between scattering and agglomerate size, neglecting agglomerates in considering only primary particles. Such working hypothesis was set due to the fact that agglomerates are exposed to high energy and the bonds between the primary particles would break up during the excitation process. The second major hypothesis is that all the particles in the excited volume reach the same peak temperature. This assumption was the main challenge in order to obtain quantitative spatially results. To minimize the peak temperature difference, moderate fluence was opted ($\sim 0.12 \text{ J/cm}^2$) corresponding to a particle temperature of $\sim 3700 \text{ K}$. Participation of particles reaching much higher temperatures on LII signal was reduced due to their sublimation.

The optical diagnostic was performed initially in a laminar diffusion flame in order to validate the technique. Soot volume fraction, particle size and concentration were spatially-resolved by laser diagnostics in an air/ethylene laminar diffusion flame (Santoro burner like). The results gave good agreement between the global LII technique used with the point location measurements and results from literature. However the advantages of the spatial results to the comprehension of the soot formation were offset by a poorer accuracy. Questions on the limitations of the accuracy due to the spatiality of the technique have been raised.

The mapping of different characteristic values of soot formation helps for further understand the formation and to develop a comprehensive model. The spatial distribution obtained in this work make a step forwards compared to the published results by a better spatial resolution, laser energy distribution and calibration based on 2C-TiRe-LII. The spatially resolved results can be used as data reference for validation of soot formation models in CFD codes.

The accuracy of the 2C-TiRe-LII technique is highly dependent on the parameters chosen. An extensive study of the influence of these different parameters on the resulting particle diameter, and recommendations for the values of parameters that best fit the experimental LII curves, were carried out. The results are also dependent on the approach chosen to fit the curves, if the theoretical LII decay is computed based on the laser fluence or temperature and when the initial point is considered, at the peak or at a time delayed after the peak. These are crucial points as they can greatly change the output and quality of the curve fitting processing.

The refractive index function was concluded to be wavelength independent. The measured energy fluence and the temperature derived from two-colour pyrometry were matching for a constant value of $E(m)$. Moreover, the fitting quality of the LII curve by theoretical curves for λ -dependent $E(m)$ was lower due to a higher estimated peak temperature ($\sim +120$ K) and overestimation of the sublimation.

Experiments in combustion chamber were first performed in an optical single cylinder Diesel engine (Vertigo). The presence of soot and incandescence signal was not as high as anticipated. Designs of optical chambers are often structured for fuel spray formation study. Hence, windows are set too high up to allow for the complete study of soot formation, especially at the tip of the flame. Unfortunately, no exploitable data could be recorded. Incandescence signals were too low and the background scattering signal too high to apply the newly developed technique. However, experiments in the Proteus engine were more successful. Soot volume fraction, particle size and concentration were spatially and temporally-resolved in the RCM. The presented data represents the different range of Diesel conditions helpful to further understand the soot formation processes in the late combustion phase. Conventional Diesel fuel and injector geometry were used. However, the large soot cloud and technique requirement made the data acquisition only possible after the end of fuel injection, corresponding to a late timing in the combustion phase, and for low soot absorption. Averaged images were discarded in favour of single shot measurements due to the high cycle to cycle variability typical of Diesel combustion. However, averaging the PLII images has shown the integrated incandescence of the flame. The resulting images are quite similar to the conceptual model of Sandia (Dec, 1997). The post-processed images of single shot measurements show a heterogeneous soot cloud.

Better atomization and air mixing were beneficial to minimise soot formation as the soot particles were smaller and produced in smaller quantity. The large soot clouds generated by low injection pressures were found to be more difficult to oxidise and conducive to particle agglomeration.

The soot cloud position remained steady for a few tenths of milliseconds after the end of injection due to the continuous contribution of vaporized fuel. The soot concentration remained sensibly constant. The soot cloud moved downstream as the soot formation rate collapsed. Oxidation became the dominant process and a decrease of the soot volume fraction was noticed.

The inhomogeneous soot distributions across the flame were shown by the single-shot measurements. Particle size and number density distributions showed the soot evolution throughout the jet. Clusters of soot, breaking off from the main spray, were noticeable and found in larger quantities with lower injection pressure.

The influence of injection pressure, in-cylinder pressure, cetane index of the fuel on soot formation were decoupled and investigated from the end of injection until the end of visible combustion. The conclusions drawn for each parameter are summarized below. Nevertheless it is not possible to isolate only one parameter in a combustion chamber, changing one of them as for direct effect to change other parameters such as the gas temperature, auto-ignition and air density/peak pressure.

Injection pressure

The soot volume fraction and particle size decreased with increase of injection. The higher velocity and atomisation of the fuel spray by increasing the injection pressure resulted in enhanced air/fuel mixing with a better air entrainment from the tip of injector to the first appearance of the soot. The location of the first soot particles appeared to be nearly independent of injection pressure, the increased spray penetration being compensated by a faster pyrolysis. However the soot cloud disappearing sooner at high injection pressure was explained by a better air mixing and the smaller particle size distribution which both increased the oxidation rate.

In-cylinder pressure

Increasing the in-cylinder pressure had different effects. Soot volume fraction was expected to increase locally due to higher gas density. However, lower soot concentration and particle size were obtained. The higher ambient gas densities increased the air entrainment, gas temperature and improved the air/fuel mixing. Higher oxygen density meant more contacts between carbon particles and oxygen. All these factors are believed to have contributed to improving the oxidation rate.

Cetane number

Increasing the cetane number had for direct effect to advance auto-ignition, thus increasing the ambient gas temperature and peak pressure, and reducing soot production from the start of the process, and therefore leading to the overall mass being produced.

8.2 Recommendations for future work

As stated previously, another technique (RAYLIX) could confirm the results obtained on soot volume fraction and particle diameter. Soot particles could be visualized via TEM. The image from TEM would give an idea of the agglomeration of the particles and could confirm the diameters and size distribution determined by our technique.

The technique could be improved with the use of an intensified PIV camera which is able to take a second image in a short delay after the laser pulse in order to subtract the flame luminosity.

The image sequences in this work were acquired for different cycles. A study based on sequence recorded during a single injection using a high repetition rate laser and acquisition camera would give comprehensive details on the evolution of the soot cloud.

A global visualisation of the flames was preferred in order to visualize the entire flame structures and processes of the soot formation. However, the investigation could be performed at a micro-scale to visualise more accurately the soot formation and oxidations zones.

The technique could be extended to gasoline engines, especially to HCCI engines. New gasoline combustion strategies are in need of more information on the soot formation inside the combustion chamber. The recording could start from ignition and not end of injection as done in this work. Recent work from Velji et al. (2010) augurs the possibility to apply the technique to optical spark ignition direct injection engines.

Understanding the effect of the equivalence ratio on the soot formation could be investigated on the Santoro burner by increasing the ethylene flow.

Further work to obtain spatially resolved soot formation could be done by taking a couple of pictures during the cooling process and at two different wavelengths for pyrometry, similar to the approach of Axelsson et al. (2001). With the recent progress done with CCD sensors this technique would be possible at atmospheric pressures but would be hardly applicable at high pressure due to the short life of the LII signal. The signal lasting 40 ns, taking a few shots with a sufficiently short integrating time will be challenging. The main advantage would be the consideration of the temperature difference of the particles inside the large sampling volume.

In addition, scattering is developing as an optical technique to investigate agglomeration of the particles and could be used to investigate agglomerate formation and agglomeration effect on LII measurement.

The experimental data gives the opportunity to compare with data resulting from CFD. A comparison with soot distributions obtained by CFD simulations could validate the models for the prediction of soot formation.

9 REFERENCES

- AKIHAMA, K., TAKATORI, Y., INAGAKI, K., SASAKI, S. & DEAN, A. M. 2001. Mechanism of the smokeless rich Diesel combustion by reducing temperature. *SAE Paper 2001-01-0655*.
- AL-QURASHI, K., LUEKING, A. D. & BOEHMAN, A. L. 2011. The deconvolution of the thermal, dilution, and chemical effects of exhaust gas recirculation (EGR) on the reactivity of engine and flame soot. *Combustion and Flame*, 158, 1696-1704.
- ALDÉN, M., EDNER, H. & SVANBERG, S. 1982. Simultaneous, spatially resolved monitoring of C₂ and OH in a C₂H₂/O₂ flame using a diode array detector. *Applied Physics B: Lasers and Optics*, 29, 93-97.
- AMANN, C. A. & SIEGLA, D. C. 1981. Diesel particulates—What they are and why. *Aerosol Science and Technology*, 1, 73 - 101.
- ANGRILL, O., GEITLINGER, H., STREIBEL, T., SUNTZ, R. & BOCKHORN, H. 2000. Influence of exhaust gas recirculation on soot formation in diffusion flames. *Proceedings of the Combustion Institute*, 28, 2643-2649.
- ARRHENIUS, S. 1896. On the influence of carbonic acid in the Air upon the temperature of the ground. *Philosophical Magazine and Journal of Science*, (fifth series), 237–275.
- AXELSSON, B., COLLIN, R. & BENGTSSON, P.-E. 2000. Laser-Induced Incandescence for Soot Particle Size Measurements in Premixed Flat Flames. *Applied Optics*, 39, 3683-3690.
- AXELSSON, B., COLLIN, R. & BENGTSSON, P.-E. 2001. Laser-induced incandescence for soot particle size and volume fraction measurements using on-line extinction calibration *Applied Physics B: Lasers and Optics*, 72, 367-372.

- BARTOK, W. & SAROFIM, A. F. 1991. Fossil fuel combustion. *New York, NY (USA)* ;*John Wiley and Sons Inc.*
- BENGTSSON, P.-E. & ALDEN, M. 1995. Soot-visualization strategies using laser techniques
Laser-induced fluorescence in C₂ from laser-vaporized soot and laser-induced soot incandescence *Applied Physics B: Lasers and Optics*, 60, 51-59.
- BENGTSSON, P.-E. & ALDÉN, M. 1990. Optical investigation of laser-produced C₂ in premixed sooty ethylene flames. *Combustion and Flame*, 80, 322-328.
- BENGTSSON, P. E. & ALDÉN, M. 1989. Application of a pulsed laser for soot measurements in premixed flames. *Applied Physics B: Lasers and Optics*, 48, 155-164.
- BENGTSSON, P. E. & ALDÉN, M. 1995. Soot-visualization strategies using laser techniques. *Applied Physics B: Lasers and Optics*, 60, 51-59.
- BESSLER, W. G., SCHULZ, C., LEE, T., JEFFRIES, J. B. & HANSON, R. K. 2003. Carbon dioxide UV laser-induced fluorescence in high-pressure flames. *Chemical Physics Letters*, 375, 344-349.
- BEYER, V. 2006. *A study of laser-induced incandescence under high vacuum conditions*. PhD, University of Cranfield.
- BEYER, V. & GREENHALGH, D. A. 2006. Laser induced incandescence under high vacuum conditions *Applied Physics B: Lasers and Optics*, 83, 455-467.
- BISETTI, F., BLANQUART, G., MUELLER, M. E. & PITSCH, H. 2012. On the formation and early evolution of soot in turbulent nonpremixed flames. *Combustion and Flame*, 159, 317-335.
- BLADH, H., BENGTSSON, P.-E., DELHAY, J., BOUVIER, Y., THERSSEN, E. & DESGROUX, P. 2006a. Experimental and theoretical comparison of spatially resolved laser-induced incandescence (LII) signals of soot in backward and right-angle configuration *Applied Physics B: Lasers and Optics*, 83, 423-433.

- BLADH, H., HILDINGSSON, L., GROSS, V., HULTQVIST, A. & BENGTSSON, P.-E. 2006b. Quantitative soot measurements in an HSDI Diesel engine. *13th Int. Symp on Appl. Laser Techniques to Fluid Mechanics, Lisbon, Portugal*.
- BLADH, H., JOHNSON, J., OLOFSSON, N. E., BOHLIN, A. & BENGTSSON, P. E. 2011. Optical soot characterization using two-color laser-induced incandescence (2C-LII) in the soot growth region of a premixed flat flame. *Proceedings of the Combustion Institute*, 33, 641-648.
- BOBBA, M. K. & MUSCULUS, M. P. B. 2012. Laser diagnostics of soot precursors in a heavy-duty diesel engine at low-temperature combustion conditions. *Combustion and Flame*, 159, 832-843.
- BOCKHORN, H., GEITLINGER, H., JUNGFLEISCH, B., LEHRE, T., SCHON, A., STREIBEL, T. & SUNTZ, R. 2002. Progress in characterization of soot formation by optical methods. *Physical Chemistry Chemical Physics*, 4, 3780-3793.
- BÖHM, H., HESSE, D., JANDER, H., LÜERS, B., PIETSCHER, J., WAGNER, H. G. & WEISS, M. 1988. In: *Twenty-Second Symposium (International) on Combustion The Combustion Institute, Pittsburgh*, 403.
- BOIARCIUC, A., FOUCHER, F. & MOUNAIM-ROUSSELLE, C. 2006. Soot volume fractions and primary particle size estimate by means of the simultaneous two-color-time-resolved and 2D laser-induced incandescence. *Applied Physics B: Lasers and Optics*, 83, 413-421.
- BOIARCIUC, A., FOUCHER, F., PAJOT, O. & MOUNAÏM-ROUSSELLE, C. 2005. Laser-Induced Incandescence to study the soot formation inside the combustion chamber of a Diesel engine. *Proceedings of the European Combustion Meeting*.
- BOUGIE, B., GANIPPA, L. C., VAN VLIET, A. P., MEERTS, W. L., DAM, N. J. & TER MEULEN, J. J. 2006. Laser-induced incandescence particle size measurements in a heavy-duty diesel engine. *Combustion and Flame*, 145, 635-637.

- BOUVIER, Y., MIHESAN, C., ZISKIND, M., THERSSEN, E., FOCSA, C., PAUWELS, J. F. & DESGROUX, P. 2007. Molecular species adsorbed on soot particles issued from low sooting methane and acetylene laminar flames: A laser-based experiment. *Proceedings of the Combustion Institute*, 31, 841-849.
- BRUCE, C. W., STROMBERG, T. F., GURTON, K. P. & MOZER, J. B. 1991. Trans-spectral absorption and scattering of electromagnetic radiation by diesel soot. *Applied Optics*, 30, 1537-1546.
- BRUNEAUX, G. 2002. A study of mixture formation in direct injection Diesel like conditions using quantitative fuel concentration visualizations in a gaseous fuel Jet. *SAE Technical Papers*, 2002-01-1632.
- BRYCE, D. J., LADOMMATOS, N. & ZHAO, H. 2000. Quantitative Investigation of Soot Distribution by Laser-Induced Incandescence. *Applied Optics*, 39, 5012-5022.
- BURR, D. W., DAUN, K. J., LINK, O., THOMSON, K. A. & SMALLWOOD, G. J. Year. Soot particle sizing by inverse analysis of multiangle elastic light scattering. *In: Proceedings of the 6th International Symposium on Radiative Transfer*, June 13-19, 2010 2010 Antalya, Turkey.
- CAI, J., LU, N. & SORENSEN, C. M. 1993. Comparison of size and morphology of soot aggregates as determined by light scattering and electron microscope analysis. *Langmuir*, 9, 2861-2867.
- CASTALDI, M. J., MARINOV, N. M., MELIUS, C. F., HUANG, J., SENKAN, S. M., PIT, W. J. & WESTBROOK, C. K. 1996. Experimental and modeling investigation of aromatic and polycyclic aromatic hydrocarbon formation in a premixed ethylene flame. *Symposium (International) on Combustion*, 26, 693-702.
- CHAKRABARTY, R. K., MOOSMÜLLER, H., ARNOTT, W. P., GARRO, M. A., SLOWIK, J. G., CROSS, E. S., HAN, J.-H., DAVIDOVITS, P., ONASCH, T. B. & WORSNOP, D. R. 2007. Light scattering and absorption by fractal-like carbonaceous chain aggregates: comparison of theories and experiment. *Appl. Opt.*, 46, 6990-7006.

- CHAKRABARTY, R. K., MOOSMÜLLER, H., GARRO, M. A., PATRICK ARNOTT, W., SLOWIK, J. G., CROSS, E. S., HAN, J.-H., DAVIDOVITS, P., ONASCH, T. B. & WORSNOP, D. R. 2008. Morphology based particle segregation by electrostatic charge. *Journal of Aerosol Science*, 39, 785-792.
- CHANG, H. & CHARALAMPOPOULOS, T. T. 1990. *Proceedings Royal Society London A* 430, 577-591.
- CHARALAMPOPOULOS, T. T. & CHANG, H. 1991. Agglomerate parameters and fractal dimension of soot using light scattering--effects on surface growth. *Combustion and Flame*, 87, 89-99.
- CHAREST, M. R. J., GROTH, C. P. T. & GÜLDER, Ö. L. 2011a. Effects of gravity and pressure on laminar coflow methane-air diffusion flames at pressures from 1 to 60 atmospheres. *Combustion and Flame*, 158, 860-875.
- CHAREST, M. R. J., JOO, H. I., GÜLDER, Ö. L. & GROTH, C. P. T. 2011b. Experimental and numerical study of soot formation in laminar ethylene diffusion flames at elevated pressures from 10 to 35 atm. *Proceedings of the Combustion Institute*, 33, 549-557.
- CHEN, S. K. 2000. Simultaneous reduction of NO_x and particulate emissions by using multiple injections in a small diesel engine. *SAE Paper 2000-01-3084*.
- CHOI, M. Y., MULHOLLAND, G. W., HAMINS, A. & KASHIWAGI, T. 1995. Comparisons of the soot volume fraction using gravimetric and light extinction techniques. *Combustion and Flame*, 102, 161-169.
- CIGNOLI, F., BELLOMUNNO, C., MAFFI, S. & ZIZAK, G. 2009. Laser-induced incandescence of titania nanoparticles synthesized in a flame. *Applied Physics B: Lasers and Optics*, 96, 593-599.
- CIGNOLI, F., DE IULIIS, S., MANTA, V. & ZIZAK, G. 2001. Two-Dimensional Two-Wavelength Emission Technique for Soot Diagnostics. *Appl. Opt.*, 40, 5370-5378.

- COLKET, M. B. & SEERY, D. J. 1994. Reaction mechanisms for toluene pyrolysis. *Symposium (International) on Combustion*, 25, 883-891.
- CROSLAND, B., JOHNSON, M. & THOMSON, K. 2011. Analysis of uncertainties in instantaneous soot volume fraction measurements using two-dimensional, auto-compensating, laser-induced incandescence (2D-AC-LII). *Applied Physics B: Lasers and Optics*, 102, 173-183.
- CRUA, C. 2002. Combustion Processes in a Diesel Engine. *PhD Thesis, University of Brighton*.
- CRUA, C., HEIKAL, M. R. & GOLD, M. R. Year. Diesel Spray Formation, Autoignition and Soot Production at Elevated In-Cylinder Pressures. *In: 12th International Symposium on Applications of Laser Techniques to Fluid Mechanics*, 12-15 July 2004 2004 Lisbon, Portugal. paper_17_5.pdf.
- CRUA, C., KENNAIRD, D. A. & HEIKAL, M. R. 2003. Laser-induced incandescence study of diesel soot formation in a rapid compression machine at elevated pressures. *Combustion and Flame*, 135, 475-488.
- DALZELL, W. H. & SAROFIM, A. F. 1969. Optical Constants of Soot and Their Application to Heat-Flux Calculations. *Journal of Heat Transfer*, 91, 100-104.
- DASCH, C. J. 1992. One-dimensional tomography: a comparison of Abel, onion-peeling, and filtered backprojection methods. *Appl. Opt.*, 31, 1146-1152.
- DE IULIIS, S., BARBINI, M., BENECCHI, S., CIGNOLI, F. & ZIZAK, G. 1998. Determination of the soot volume fraction in an ethylene diffusion flame by multiwavelength analysis of soot radiation. *Combustion and Flame*, 115, 253-261.
- DE IULIIS, S., CIGNOLI, F. & ZIZAK, G. 2005. Two-color laser-induced incandescence (2C-LII) technique for absolute soot volume fraction measurements in flames. *Appl. Opt.*, 44, 7414-7423.

- DEC, J. E. 1997. A conceptual model of DI Diesel combustion based on laser-sheet imaging. *SAE Paper 970873*.
- DEC, J. E. & COY, E. B. 1996. OH radical imaging in a DI Diesel engine and the structure of the early diffusion flame. *SAE Transactions, paper no. 960831*, 105, 1127-1148.
- DEC, J. E., ZUR LOYE, A. O. & SIEBERS, D. L. 1991. Soot distribution in a DI Diesel engine using 2-D Laser-Induced Incandescence imaging. *SAE Technical Papers*, 910224.
- DEMORY, R. 2007. *Optical measurement of nitric oxide and hydroxyl radicals distributions in combusting Diesel sprays*. PhD, University of Brighton.
- DESANTES, J. M., BERMÚDEZ, V., GARCÍA, J. M. & FUENTES, E. 2005. Effects of current engine strategies on the exhaust aerosol particle size distribution from a Heavy-Duty Diesel Engine *Journal of Aerosol Science* 36, 1251-1276.
- DESGROUX, P., MERCIER, X., LEFORT, B., LEMAIRE, R., THERSSEN, E. & PAUWELS, J. F. 2008. Soot volume fraction measurement in low-pressure methane flames by combining laser-induced incandescence and cavity ring-down spectroscopy: Effect of pressure on soot formation. *Combustion and Flame*, 155, 289-301.
- DI IORIO, S., MEROLA, S. S., VAGLIECO, B. M. & TORNATORE, C. 2005. Nanoparticles Characterization at Spark Ignition Engine Exhaust. *SAE Paper 2005-24-010*.
- DI STASIO, S. 2001. Electron microscopy evidence of aggregation under three different size scales for soot nanoparticles in flame. *Carbon*, 39, 109-118.
- DI STASIO, S., KONSTANDOPOULOS, A. G. & KOSTOGLU, M. 2002. Cluster-Cluster Aggregation Kinetics and Primary Particle Growth of Soot Nanoparticles in Flame by Light Scattering and Numerical Simulations. *Journal of Colloid and Interface Science*, 247, 33-46.

- DOBBINS, R. A. & MEGARIDIS, C. M. 1987. Morphology of flame-generated soot as determined by thermophoretic sampling. *Langmuir*, 3, 254-259.
- DOUCE, F., DJEBA\AKLI-CHAUMEIX, N. & PAILLARD, C.-E. 2001. Soot formation from heavy hydrocarbons representatives of diesel fuel. *SAE Paper 2001-24-0026*.
- ECKBRETH, A. C. 1977. Effects of laser-modulated particulate incandescence on Raman scattering diagnostics. *Journal of Applied Physics*, 48, 4473-4479.
- ERICKSON, W. D., WILLIAMS, G. C. & HOTTEL, H. C. 1964. Light scattering measurements on soot in a benzene-air flame. *Combustion and Flame*, 8, 127-132.
- ESPEY, C., DEC, J. E., LITZINGER, T. A. & SANTAVICCA, D. A. 1997. Planar laser rayleigh scattering for quantitative vapor-fuel imaging in a diesel jet. *Combustion and Flame*, 109, 65-78.
- FARIAS, T. L., KÖYLÜ, Ü. Ö. & CARVALHO, M. G. 1996. Range of validity of the Rayleigh-Debye-Gans theory for optics of fractal aggregates. *Appl. Opt.*, 35, 6560-6567.
- FILIPPOV, A. V., MARKUS, M. W. & ROTH, P. 1999. In-situ characterization of ultrafine particles by laser-induced incandescence: sizing and particle structure determination. *Journal of Aerosol Science*, 30, 71-87.
- FILIPPOV, A. V., ZURITA, M. & ROSNER, D. E. 2000. Fractal-like Aggregates: Relation between Morphology and Physical Properties. *Journal of Colloid and Interface Science*, 229, 261-273.
- FLOWER, W. L. 1988. An investigation of soot formation in axisymmetric turbulent diffusion flames at elevated pressure. In: *Proceedings of the 22nd international symposium on combustion*. The Combustion Institute, 425-435.

- FLOWER, W. L. & BOWMAN, C. T. 1987. Soot production in axisymmetric laminar diffusion flames at pressures from one to ten atmospheres. The Combustion Institute. 1115–1124.
- FUSCO, A., KNOX-KELECY, A. L. & FOSTER, D. E. 1994. Application of a Phenomenological Soot Model for Diesel Engine Combustion. *COMODIA 94*, 571-576.
- GANGOPADHYAY, S., ELMINYAWI, I. & SORENSEN, C. M. 1991. Optical structure factor measurements of soot particles in a premixed flame. *Appl. Opt.*, 30, 4859-4864.
- GAO, Z. & SCHREIBER, W. 2001. The effects of EGR and split fuel injection on diesel engine emission. *International Journal of Automotive Technology*, 2, 123-133.
- GEITLINGER, H., STREIBEL, T., SUNTZ, R. & BOCKHORN, H. 1998. Two-Dimensional Imaging of Soot Volume Fraction, Particle Number Densities, and Particle Radii in Laminar and Turbulent Diffusion Flames. *Twenty-Seventh Symposium (International) on Combustion*, 1613-1621.
- GEITLINGER, H., STREIBEL, T., SUNTZ, R. & BOCKHORN, H. 1999. Statistical Analysis of Soot Volume Fractions, Particle Number Densities and Particle Radii in a Turbulent Diffusion Flame. *Combustion Science and Technology*, 149, 115-134.
- GLASSMAN, I. 1989. Soot formation in combustion processes. *Symposium (International) on Combustion*, 22, 295-311.
- GLASSMAN, I. 1998a. Soot formation in combustion processes. *Symposium (International) on Combustion, 22nd, Seattle, WA; UNITED STATES*, 295-311.
- GLASSMAN, I. 1998b. Sooting laminar diffusion flames: Effect of dilution, additives, pressure, and microgravity. *Symposium (International) on Combustion*, 27, 1589-1596.
- GREIS, A. E., GRUNEFELD, G., BECKER M. & S., P. 2002. Quantitative measurements of the soot distribution in a realistic common rail D.I. Diesel engine. *11th*

International Symposium on Application of Laser Techniques to Fluid Mechanics, Lisbon.

HABIB, Z. G. & VERVISCH, P. 1988. On The Refractive Index of Soot at Flame Temperature. *Combustion Science and Technology*, 59, 261-274

HAN, Z., ULUDOGAN, A., HAMPSON, G. J. & REITZ, R. D. 1996. Mechanism of soot and NO_x emission reduction using multiple-injection in a diesel engine. *SAE Paper 960633*.

HAUPAIS, A. 1993. Combustion dans les moteurs Diesel. *Techniques de l'Ingénieur Edition*, B2700, 1-32.

HAYNES, B. & WAGNER, H. 1981. Soot formation. *Progress in Energy and Combustion Science*, 7, 229-273.

HE, C., GE, Y., TAN, J., YOU, K., HAN, X. & WANG, J. 2010. Characteristics of polycyclic aromatic hydrocarbons emissions of diesel engine fueled with biodiesel and diesel. *Fuel*, 89, 2040-2046.

HENTSCHEL, J., SUNTZ, R. & BOCKHORN, H. 2005. Soot formation and oxidation in oscillating methane/air diffusion flames at elevated pressure. *Appl. Opt.*, 44, 6673-6681.

HENTSCHEL, W. & SCHINDLER, K. P. 1996. Flow, spray and combustion analysis by laser techniques in the combustion chamber of a direct-injection diesel engine. *Optics and Lasers in Engineering*, 25, 401-413.

HEYWOOD, J. B. 1988. *Internal Combustion Engine Fundamentals*, New York.

HIGGINS, B., SIEBERS, D., MUELLER, C. & ARADI, A. 1998. Effects of an ignition-enhancing, diesel-fuel additive on diesel-spray evaporation, mixing, ignition, and combustion. *Symposium (International) on Combustion*, 27, 1873-1880.

- HINDS, W. C. 1982. *Aerosol Technology: Properties, Behavior, and Measurement of Airborne Particles*. Wiley-Interscience, New York, NY.
- HIROYASU, H. 1985. Diesel Engine Combustion and its Modeling. *International Symposium on Diagnostics and Modeling of Combustion in Reciprocating Engines (COMODIA)*. 53-75.
- HIROYASU, H. & KADOTA, T. 1976. Models for combustion and formation of nitric oxide and soot in DI diesel engines.. *SAE Paper 760129*.
- HIROYASU, H., KADOTA, T. & ARAI, M. 1983. Development and use of a spray combustion modeling to predict diesel engine efficiency and pollutant emissions (Part 1 Combustion Modeling). *Bulletin of the JSME*, 26, 569–575.
- HOFMANN, M., BESSLER, W. G., SCHULZ, C. & JANDER, H. 2003. Laser-induced incandescence for soot diagnostics at high pressures. *Applied Optics*, 42.
- HULT, OMRANE, NYGREN, KAMINSKI, AXELSSON, COLLIN, BENGTSSON & ALDÉN 2002. Quantitative three-dimensional imaging of soot volume fraction in turbulent non-premixed flames. *Experiments in Fluids*, 33, 265-269.
- HURA, H. S. & GLASSMAN, I. 1988. Soot formation in diffusion flames of fuel/oxygen mixtures. *In: Proceedings of the 22nd international symposium on combustion*. The Combustion Institute.
- ICRP 1994. Human Respiratory Tract Model for Radiological Protection. *Publication 66 (Oxford, Pergamon Press)*, 24.
- IDICHERIA, C. & PICKETT, L. M. 2005. Soot Formation in Diesel Combustion Under High-Egr Conditions. *SAE Paper 2005-01-3834*.
- IDICHERIA, C. A. & PICKETT, L. M. 2007. Effect of EGR on diesel premixed-burn equivalence ratio. *Proceedings of the Combustion Institute*, 31, 2931-2938.

- IVLEVA, N. P., MESSERER, A., YANG, X., NIESSNER, R. & PÖSCHL, U. 2007. Raman Microspectroscopic Analysis of Changes in the Chemical Structure and Reactivity of Soot in a Diesel Exhaust Aftertreatment Model System. *Environmental Science & Technology*, 41, 3702-3707.
- JACOBSON, M. Z. 2002. Control of fossil-fuel particulate black carbon and organic matter, possibly the most effective method of slowing global warming. *Journal of Geophysical Research*, 107, 4410.
- JONES, A. 2006. Light scattering in combustion. In: KOKHANOVSKY, A. A. (ed.) *Light Scattering Reviews*. Springer Berlin Heidelberg.
- JUNG, H., KITTELSON, D. B. & ZACHARIAH, M. R. 2004. Kinetics and visualization of soot oxidation using transmission electron microscopy. *Combustion and Flame*, 136, 445-456.
- KAMINOTO, T. & BAE, M. 1989. High combustion temperature for the reduction of particulate in diesel engines. *SAE transactions*, 97, 692-701.
- KARIMI, K. 2007. *Characterisation of Multiple-Injection Diesel Sprays at Elevated Pressures and Temperatures*. PhD thesis, Brighton.
- KASTING, J. & ACKERMAN, T. 1986. Climatic consequences of very high carbon dioxide levels in the earth's early atmosphere. *Science*, 234, 1383-1385.
- KENNAIRD, D. A., CRUA, C., HEIKAL, M. R., MORGAN, R., BAR, F. & SAPSFORD, S. 2000. A new high-pressure Diesel spray research facility. *IMEchE International Conference on Computational and Experimental Methods in Reciprocating Engines*. London, UK.
- KENT, J. H. & HONNERY, D. R. 1990. A soot formation rate map for a laminar ethylene diffusion flame. *Combustion and Flame*, 79, 287-298.
- KERKER, M. 1969. The scattering of light, and other electromagnetic radiation. *Academic Press, New York*.

- KOCK, B. F., ECKHARDT, T. & ROTH, P. 2002. In-cylinder sizing of diesel particles by time-resolved laser-induced incandescence (TR-LII). *Proceedings of the Combustion Institute*, 29, 2775-2782.
- KOCK, B. F., KAYAN, C., KNIPPING, J., ORTHNER, H. R. & ROTH, P. 2005. Comparison of LII and TEM sizing during synthesis of iron particle chains. *Proceedings of the Combustion Institute*, 30, 1689-1697.
- KOCK, B. F. & ROTH, P. 2003. Two-Color TR-LII Applied to In-Cylinder Diesel Particle Sizing. *Proceedings of the European Combustion Meeting*, 2003.
- KOCK, B. F., TRIBALET, B., SCHULZ, C. & ROTH, P. 2006. Two-color time-resolved LII applied to soot particle sizing in the cylinder of a Diesel engine. *Combustion and Flame*, 147, 79-92.
- KONSUR, B., MEGARIDIS, C. M. & GRIFFIN, D. W. 1999. Soot aerosol properties in laminar soot-emitting microgravity nonpremixed flames. *Combustion and Flame*, 118, 509-520.
- KOSAKA, H., AIZAWA, T. & KAMIMOTO, T. 2005. Two-dimensional imaging of ignition and soot formation processes in a diesel flame. *International Journal of Engine Research*, 6, 21-42.
- KOSAKA, H., NISHIGAKI, T., KAMIMOTO, T., SANO, T., MATSUTANI, A. & HARADA, S. 1996. Simultaneous 2-D Imaging of OH Radicals and Soot in a Diesel Flame by Laser Sheet Techniques. *SAE Transactions*, 105, 960834.
- KOYLU, U. O., FAETH, G. M., FARIAS, T. L. & CARVALHO, M. G. 1995. Fractal and projected structure properties of soot aggregates. *Combustion and Flame*, 100, 621-633.
- KÖYLÜ, Ü. Ö., FAETH, G. M., FARIAS, T. L. & CARVALHO, M. G. 1995. Fractal and projected structure properties of soot aggregates. *Combustion and Flame*, 100, 621-633.

- KOYLU, U. O., MCENALLY, C. S., ROSNER, D. E. & PFEFFERLE, L. D. 1997. Simultaneous measurements of soot volume fraction and particle size / microstructure in flames using a thermophoretic sampling technique. *Combustion and Flame*, 110, 494-507.
- KREYLING, W. G., SEMMLER, M. & MÖLLER, W. 2005. Ultrafeine Partikel und ihre Wirkungen auf die menschliche Gesundheit. *Experten-Workshop*.
- KRISHNAN, S. S., LIN, K.-C. & FAETH, G. M. 2001. Extinction and Scattering Properties of Soot Emitted From Buoyant Turbulent Diffusion Flames. *Journal of Heat Transfer*, 23, 331-339.
- KRONHOLM, D. F. & HOWARD, J. B. 2000. Analysis of soot surface growth pathways using published plug-flow reactor data with new particle size distribution measurements and published premixed flame data. *Symposium (International) on Combustion*, 28, 2555-2561.
- LADOMMATOS, N. & ZHAO, H. 1994. A Guide to Measurement of Flame Temperature and Soot Concentration in Diesel Engines Using Two-Color Method - Part 1: Principles. *SAE Paper 941956*.
- LEBOURGEOIS, V. 2010. Studies of Soot Measurement. University of Brighton.
- LEE, K.-O., MEGARIDIS, C. M., ZELEPOUGA, S., SAVELIEV, A. V., KENNEDY, L. A., CHARON, O. & AMMOURI, F. 2000. Soot formation effects of oxygen concentration in the oxidizer stream of laminar coannular nonpremixed methane/air flames. *Combustion and Flame*, 121, 323-333.
- LEE, K., HAN, Y., LEE, W., CHUNG, J. & LEE, C. 2005. Quantitative measurements of soot particles in a laminar diffusion flame using a LII/LIS technique. *Meas. Sci. Technol*, 16, 519-528.
- LEE, K. O., COLE, R., SEKAR, R., CHOI, M. Y., ZHU, J., KANG, J. & BAE, C. 2001. Detailed Characterization of Morphology and Dimensions of Diesel Particulates Via Thermophoretic Sampling. *SAE Paper 2001-01-3572*, September 2001.

- LEE, R., PEDLEY, J. & HOBBS, C. 1998. Fuel quality impact on heavy duty diesel emissions—a literature review. *SAE Paper 982649*.
- LEE, S. C. & TIEN, C. L. 1981. Optical constants of soot in hydrocarbon flames. *Symp. (Int.) Combust., (Proc.) ; 18. combustion symposium; 17 Aug 1980; Waterloo, Canada*, 1159-1166.
- LEHRE, T., JUNGFLEISCH, B., SUNTZ, R. & BOCKHORN, H. 2003a. Size Distributions of Nanoscaled Particles and Gas Temperatures from Time-Resolved Laser-Induced-Incandescence Measurements. *Applied Optics*, 42, 2021-2030.
- LEHRE, T., JUNGFLEISCH, B., SUNTZ, R. & BOCKHORN, H. 2003b. Size Distributions of Nanoscaled Particles and Gas Temperatures from Time-Resolved Laser-Induced-Incandescence Measurements. *Appl. Opt.*, 42, 2021-2030.
- LEHRE, T., SUNTZ, R. & BOCKHORN, H. 2005. Time-resolved two-color LII: size distributions of nano-particles from gas-to-particle synthesis. *Proceedings of the Combustion Institute*, 30, 2585-2593.
- LEIDER, H. R., KRIKORIAN, O. H. & YOUNG, D. A. 1973. Thermodynamic properties of carbon up to the critical point. *Carbon*, 11, 555-563.
- LIU, F., DAUN, K. J., R., S. D. & J., S. G. 2006a. Heat conduction from a spherical nano-particle: status of modeling heat conduction in laser-induced incandescence *Applied Physics B: Lasers and Optics*, 83, 355-382.
- LIU, F., DAUN, K. J., SNELLING, D. R. & SMALLWOOD, G. J. 2006b. Heat conduction from a spherical nano-particle: status of modeling heat conduction in laser-induced incandescence. *Applied Physics B: Lasers and Optics*, 83, 355-382.
- LIU, F., GUO, H., SMALLWOOD, G. J. & GÜLDER, Ö. L. 2002. Effects of gas and soot radiation on soot formation in a coflow laminar ethylene diffusion flame. *Journal of Quantitative Spectroscopy and Radiative Transfer*, 73, 409-421.

- LIU, F., THOMSON, K. A. & SMALLWOOD, G. J. 2008. Effects of soot absorption and scattering on LII intensities in laminar coflow diffusion flames. *Journal of Quantitative Spectroscopy and Radiative Transfer*, 109, 337-348.
- MALLAMO, F., BADAMI, M. & MILLO, F. 2002. Analysis of multiple injection strategies for the reduction of emissions, noise and BSFC of a DI Cr small displacement non-road diesel engine. . *SAE Paper 2002-01-2672*.
- MANZELLO, S. L., LENHERT, D. B., YOZGATLIGIL, A., DONOVAN, M. T., MULHOLLAND, G. W., ZACHARIAH, M. R. & TSANG, W. 2007. Soot particle size distributions in a well-stirred reactor/plug flow reactor. *Proceedings of the Combustion Institute*, 31, 675-683.
- MARICQ, M. M. 2004. Size and charge of soot particles in rich premixed ethylene flames. *Combustion and Flame*, 137, 340-350.
- MATHIS, U., MOHR, M., KAEGI, R., BERTOLA, A. & BOULOUCOS, K. 2005. Influence of Diesel Engine Combustion Parameters on Primary Soot Particle Diameter. *Environmental Science & Technology*, 39, 1887 -1892.
- MCCOY, B. J. & CHA, C. Y. 1974. Transport phenomena in the rarefied gas transition regime. *Chemical Engineering Science*, 29, 381-388.
- MELLOR, A. M. & CHEN, S. K. 2002. Multiple injections with EGR effects on NO_x emissions for DI diesel engines analyzed using an engineering model. . *SAE Paper 2002-01-2774*.
- MELTON, L. A. 1984a. Soot diagnostics based on laser heating. *Appl. Opt.*, 23, 2201-2208.
- MELTON, L. A. 1984b. Soot Diagnostics Based on Laser Heating. *Applied Optics*, 23, 2201-2208.
- MERCIER, X., THERSSEN, E., PAUWELS, J. F. & DESGROUX, P. 2005. Measurements of absolute concentration profiles of C₂ in non-sooting and sooting

diffusion flames by coupling cavity ring-down spectroscopy and laser induced fluorescence. *Proceedings of the Combustion Institute*, 30, 1655-1663.

MEWES, B. & SEITZMAN, J. M. 1997. Soot volume fraction and particle size measurements with laser-induced incandescence. *Applied Optics*, 36, 709-717.

MICHELSEN, H. A. 2003. Understanding and predicting the temporal response of laser-induced incandescence from carbonaceous particles. *The Journal of Chemical Physics*, 118, 7012-7045.

MICHELSEN, H. A. 2006. Laser-induced incandescence of flame-generated soot on a picosecond time scale. *Applied Physics B: Lasers and Optics*, 83, 443-448.

MICHELSEN, H. A., LIU, F., KOCK, B. F., BLADH, H., BOIARCIUC, A., CHARWATH, M., DREIER, T., HADEF, R., HOFMANN, M., REIMANN, J., WILL, S., BENGTSSON, P. E., BOCKHORN, H., FOUCHER, F., GEIGLE, K. P., MOUNAÏM-ROUSSELLE, C., SCHULZ, C., STIRN, R., TRIBALET, B. & SUNTZ, R. 2007a. Modeling laser-induced incandescence of soot: a summary and comparison of LII models. *Applied Physics B: Lasers and Optics*, 87, 503-521.

MICHELSEN, H. A., TIVANSKI, A. V., GILLES, M. K., VAN POPPEL, L. H., DANSSON, M. A. & BUSECK, P. R. 2007b. Particle formation from pulsed laser irradiation of soot aggregates studied with a scanning mobility particle sizer, a transmission electron microscope, and a scanning transmission x-ray microscope. *Appl. Opt.*, 46, 959-977.

MICHELSEN, H. A., WITZE, P. O., KAYES, D. & HOCHGREB, S. 2003. Laser-Induced Incandescence of Soot: The Influence of Experimental Factors and Microphysical Mechanisms. *Applied Optics*, 42, 5577-5590.

MIE, G. 1908. Considerations on the optics of turbid media, especially colloidal metal sols. *Ann. d. Physik*.

- MILLER, J. A. & MELIUS, C. F. 1992. Kinetic and thermodynamic issues in the formation of aromatic compounds in flames of aliphatic fuels. *Combustion and Flame*, 91, 21-39.
- MIYAMOTO, N., OGAWA, H., SHIBUYA, M., ARAI, K. & ESMILAIRE, O. 1994. Influence of the molecular structure of hydrocarbon fuels on diesel exhaust emissions. *SAE Paper 940676*.
- MONTGOMERY, D. T. & REITZ, R. D. 1996. Six-mode cycle evaluation of the effect of EGR and multiple injections on particulate and NO_x emissions from a D.I. diesel engine. *SAE Paper 960316*.
- MOOSMÜLLER, H., CHAKRABARTY, R. K. & ARNOTT, W. P. 2009. Aerosol light absorption and its measurement: A review. *Journal of Quantitative Spectroscopy and Radiative Transfer*, 110, 844-878.
- MUELLER, M. E. & PITSCH, H. 2012. LES model for sooting turbulent nonpremixed flames. *Combustion and Flame*.
- MUSCULUS, M. P. B. & PICKETT, L. M. 2005. Diagnostic considerations for optical laser-extinction measurements of soot in high-pressure transient combustion environments. *Combustion and Flame*, 141, 371-391.
- NI, T., PINSON, J. A., GUPTA, S. & SANTORO, R. J. 1995a. Two-dimensional imaging of soot volume fraction by the use of laser-induced incandescence. *Applied Optics*, 34, 7083.
- NI, T., PINSON, J. A., GUPTA, S. & SANTORO, R. J. 1995b. Two-dimensional imaging of soot volume fraction by the use of laser-induced incandescence. *Appl. Opt.*, 34, 7083-7091.
- OBERDÖRSTER, G. 2000. Pulmonary effects of inhaled ultrafine particles. *International Archives of Occupational and Environmental Health*, 74, 1-8.

- OH, C. & SORENSEN, C. M. 1997. Light scattering study of fractal cluster aggregation near the free molecular regime. *Journal of Aerosol Science*, 28, 937-957.
- OLSON, D. B., PICKENS, J. C. & GILL, R. J. 1985. The effects of molecular structure on soot formation II. Diffusion flames. *Combustion and Flame*, 62, 43-60.
- OLTMANN, H., REIMANN, J. & WILL, S. 2010. Wide-angle light scattering (WALS) for soot aggregate characterization. *Combustion and Flame*, 157, 516-522.
- PARK, C., KOOK, S. & BAE, C. 2004. Effects of multiple injections in a HSDI diesel engine equipped with common-rail injection system. *SAE Paper 2004-01-0127*.
- PFEFFERLE, L. D., BERMUDEZ, G. & BOYLE, J. 1994. Benzene and Higher Hydrocarbon Formation During Allene Pyrolysis. *Springer Series in Chemical Physics*, Springer Verlag KG, 25-49.
- PICKETT, L. M. & SIEBERS, D. L. 2004. Soot in diesel fuel jets: effects of ambient temperature, ambient density, and injection pressure. *Combustion and Flame*, 138, 114-135.
- PIERPONT, D. A., MONTGOMERY, D. T. & REITZ, R. D. 1995. Reducing particulate and NO_x using multiple injections and EGR in a D.I. diesel. *SAE Paper 950217*.
- PINSON, J. A., MITCHELL, D. L., SANTORO, R. J. & LITZINGER, T. A. 1993. Quantitative, Planar Soot Measurements in a D.I. Diesel Engine Using Laser-induced Incandescence and Light Scattering. *SAE*, 932650.
- PINSON, J. A., NI, T. & LITZINGER, T. A. 1994. Quantitative Imaging Study of the Effects of Intake Air Temperature on Soot Evolution in An Optically-Accessible D.I. Diesel Engine. *SAE Paper 942044*.
- PON, R. M. & HESSLER, J. P. 1984. Spectral emissivity of tungsten: analytic expressions for the 340-nm to 2.6- μ m spectral region. *Appl. Opt.*, 23, 975-976.

- PRICE OT, ASGHARIAN B, MILLER FJ, CASSEE FR & DE, W.-S. R. 2002. Multiple Path Particle Dosimetry model (MPPD v1.0): A model for human and rat airway particle dosimetry. *RIVM rapport 650010030*.
- PURI, R., RICHARDSON, T. F., SANTORO, R. J. & DOBBINS, R. A. 1993. Aerosol dynamic processes of soot aggregates in a laminar ethene diffusion flame. *Combustion and Flame*, 92, 320-333.
- QUAY, B., LEE, T. W., NI, T. & SANTORO, R. J. 1994a. Spatially resolved measurements of soot volume fraction using laser-induced incandescence. *Combustion and Flame*, 97, 384-392.
- QUAY, B., LEE, T. W., NI, T. & SANTORO, R. J. 1994b. Spatially resolved measurements of soot volume fraction using laser-induced incandescence. *Combustion and Flame* 97, 3-4.
- RANNER, H., LACKNER, M. & WINTER, F. 2007. Laser cleaning of optical windows in internal combustion engines. *opt. Eng.*, 46.
- RAYLEIGH, L. 1871. On the scattering of light by small particles. *Philosophical Magazine*.
- REIMANN, J., KUHLMANN, S. A. & WILL, S. 2009. 2D aggregate sizing by combining laser-induced incandescence (LII) and elastic light scattering (ELS). *Applied Physics B: Lasers and Optics*, 96, 583-592.
- ROHLFING, E. A. 1988. Optical emission studies of atomic, molecular, and particulate carbon produced from a laser vaporization cluster source. *The Journal of Chemical Physics*, 89, 6103-6112.
- ROTH, P. & FILIPPOV, A. V. 1996. In situ ultrafine particle sizing by a combination of pulsed laser heatup and particle thermal emission. *Journal of Aerosol Science*, 27, 95-104.

- SANTORO, R. J. & MILLER, J. H. 1987. Soot particle formation in laminar diffusion flames. *Langmuir*, 3, 244-254.
- SANTORO, R. J., SEMERJIAN, H. G. & DOBBINS, R. A. 1983. Soot particle measurements in diffusion flames. *Combustion and Flame*, 51, 203-218.
- SANTORO, R. J., YEH, T. T., HORVATH, J. J. & SEMERJIAN, H. G. 1987. The Transport and Growth of Soot Particles in Laminar Diffusion Flames. *Combustion Science and Technology*, 53, 89-115.
- SATO, H., TREE, D. R., HODGES, J. T. & FOSTER, D. E. 1990. A study on the effect of temperature on soot formation in a jet stirred reactor. In: Proceedings of the 23rd international symposium on combustion. The Combustion Institute. 1469–1475.
- SCHOEMAECCKER-MOREAU, C. 2002. Diagnostics Laser dans une flamme de diffusion : imagerie quantitative de nanoparticules de suies et d'espèces majoritaires et minoritaires. *Université des Sciences et Technologies de Lille*.
- SCHOEMAECCKER-MOREAU, C., THERSSEN, E., MERCIER, X., PAUWELS, J. F. & DESGROUX, P. 2004. Two-color laser-induced incandescence and cavity ring-down spectroscopy for sensitive and quantitative imaging of soot and PAHs in flames. *Applied Physics B: Lasers and Optics*, 78, 485-492.
- SCHOEMAECCKER MOREAU, C., THERSSEN, E., MERCIER, X., PAUWELS, J. F. & DESGROUX, P. 2004. Two-color laser-induced incandescence and cavity ring-down spectroscopy for sensitive and quantitative imaging of soot and PAHs in flames. *Applied Physics B: Lasers and Optics*, 78, 485-492.
- SCHRAML, S., DANKERS, S., BADER, K., WILL, S. & LEIPERTZ, A. 2000. Soot temperature measurements and implications for time-resolved laser-induced incandescence (TIRE-LII). *Combustion and Flame*, 120, 439-450.
- SCHULZ, C., KOCK, B. F., HOFMANN, M., MICHELSEN, H., WILL, S., BOUGIE, B., SUNTZ, R. & G., S. 2006. Laser-induced incandescence: recent trends and current questions. *Applied Physics B: Lasers and Optics*, 83.

- SHADDIX, C. R. & SMYTH, K. C. 1996. Laser-induced incandescence measurements of soot production in steady and flickering methane, propane, and ethylene diffusion flames. *Combustion and Flame*, 107, 418-452.
- SHOBA, T. 2011. *The effects of Diesel fuel composition on atomisation and combustion*. PhD Thesis, University of Brighton.
- SIEBERS, D. L. & HIGGINS, B. S. 2001. Flame Lift-Off on Direct-Injection Diesel Sprays Under Quiescent Conditions. *SAE*, SAE2001-01-0530.
- SMALLWOOD, G. J., CLAVEL, D., GAREAU, D., SAWCHUK, R. A., SNELLING, D. R., WITZE, P. O., AXELSSON, B., BACHALO, W. D. & GÜLDER, Ö. L. 2002. Concurrent Quantitative Laser-Induced Incandescence and SMPS Measurements of EGR Effects on Particulate Emissions from a TDI Diesel Engine. *SAE TECHNICAL PAPER SERIES*, 2002-01-2715.
- SMALLWOOD, G. J., SNELLING, D. R., LIU, F. & GULDER, O. L. 2001. Clouds Over Soot Evaporation: Errors in Modeling Laser-Induced Incandescence of Soot. *Journal of Heat Transfer*, 123, 814-818.
- SMITH, O. 1981. Fundamentals of Soot Formation in Flames with Application to Diesel Engine Particulate Emissions. *Progress in Energy and Combustion Science*.
- SMYTH, K. C., SHADDIX, C. R. & EVEREST, D. A. 1997. Aspects of soot dynamics as revealed by measurements of broadband fluorescence and flame luminosity in flickering diffusion flames. *Combustion and Flame*, 111, 185-194.
- SNELLING, D., LINK, O., THOMSON, K. & SMALLWOOD, G. 2011. Measurement of soot morphology by integrated LII and elastic light scattering. *Applied Physics B: Lasers and Optics*, 1-13.
- SNELLING, D. R., LIU, F., SMALLWOOD, G. J. & GÜLDER, Ö. L. 2004. Determination of the soot absorption function and thermal accommodation coefficient using low-fluence LII in a laminar coflow ethylene diffusion flame. *Combustion and Flame*, 136, 180-190.

- SNELLING, D. R., SMALLWOOD, G. J., CAMPBELL, I. G., MEDLOCK, J. E. & GÜLDER, Ö. L. 1997. Development and Application of Laser-Induced Incandescence (LII) as a Diagnostic for Soot Particulate Measurements. *AGARD Conference Proceedings 598, Advanced Non-Intrusive Instrumentation for Propulsion Engines, Brussels, Belgium.*, 23, 1-9.
- SNELLING, D. R., SMALLWOOD, G. J., GÜLDER, Ö., BACHALO, W. & SANKAR, S. 2000. Soot Volume Fraction Characterization Using the Laser-Induced Incandescence Detection Method. *The 10th International Symposium on Applications of Laser Techniques to Fluid Mechanics, Lisbon, Portugal.*
- SNELLING, D. R., SMALLWOOD, G. J., LIU, F., GULDER, O. L. & BACHALO, W. D. 2005a. A calibration-independent laser-induced incandescence technique for soot measurement by detecting absolute light intensity. *Applied Optics*, 44, 6773-6785.
- SNELLING, DAVID R., SMALLWOOD, GREGORY J., LIU, F., GÜLDER, ÖMER L. & BACHALO, WILLIAM D. 2005b. A calibration-independent laser-induced incandescence technique for soot measurement by detecting absolute light intensity. *Appl. Opt.*, 44, 6773-6785.
- SNELLING, D. R., THOMSON, K. A., SMALLWOOD, G. J. & GÜLDER, Ö. L. 1999. Two-Dimensional Imaging of Soot Volume Fraction in Laminar Diffusion Flames. *Appl. Opt.*, 38, 2478-2485.
- SOID, S. N. & ZAINAL, Z. A. 2011. Spray and combustion characterization for internal combustion engines using optical measuring techniques – A review. *Energy*, 36, 724-741.
- SONG, J., SONG, C., TAO, Y., LV, G. & DONG, S. 2011. Diesel soot oxidation during the late combustion phase. *Combustion and Flame*, 158, 446-451.
- SORENSEN, C. M. 2001. Light Scattering by Fractal Aggregates: A Review. *Aerosol Science and Technology*, 35, 648-687.

- SORENSEN, C. M., CAI, J. & LU, N. 1992. Light-scattering measurements of monomer size, monomers per aggregate, and fractal dimension for soot aggregates in flames. *Appl. Opt.*, 31, 6547-6557.
- STARKE, R., KOCK, B. F. & ROTH, P. 2003. Nano-particle sizing by laser-induced-incandescence (LII) in a shock wave reactor. *Shock Waves*, 12.
- STIPE, C. B., CHOI, J. H., LUCAS, D., KOSHLAND, C. P. & SAWYER, R. F. 2004. Nanoparticle production by UV irradiation of combustion generated soot particles. *Journal of Nanoparticle Research*, 5, 467-477.
- STUMPF, M., VELJI, A., SPICHER, U., JUNGFLEISCH, B., SUNTZ, R. & BOCKHORN, H. 2005. Investigations on Soot Emission Behavior of A Common-Rail Diesel Engine during Steady and Non-Steady Operating Conditions by Means of Several Measuring Techniques.
- SUNDERLAND, P. B. & FAETH, G. M. 1996. Soot formation in hydrocarbon/air laminar jet diffusion flames. *Combustion and Flame*, 105, 132-146.
- TAIT, N. P. & GREENHALGH, D. A. 1993a. PLIF imaging of fuel fraction in practical devices and LH imaging of soot *BER BUNSENGES PHYS CHEM.*, 97, 1619-1625.
- TAIT, N. P. & GREENHALGH, D. A. 1993b. PLIF Imaging of Fuel Fraction in Practical Devices and LII Imaging of Soot. *Berichte der Bunsengesellschaft für physikalische Chemie*, 97, 1619-1624.
- TAO, F., GOLOVITCHEV, V. I. & CHOMIAK, J. 2001. Application of complex chemistry to investigate combustion zone structure of DI diesel sprays under engine-like conditions. *COMODIA 2001*, 92-100.
- TAO, F., SRINIVAS, S., REITZ, R. D. & FOSTER, D. E. 2005. Comparison of Three Soot Models Applied to Multi-Dimensional Diesel Combustion Simulations. *SME International Journal Series B*, 48, 671-678.

- THOMSON, K. A., R.; S. D., J.; S. G. & LIU, F. 2006. Laser induced incandescence measurements of soot volume fraction and effective particle size in a laminar co-annular non-premixed methane/air flame at pressures between 0.5–4.0 MPa *Applied Physics B: Lasers and Optics*, 83, 469-475.
- TOW, T. C., PIERPONT, D. A. & R.D., R. 1994. Reducing particulate and NO_x emissions by using multiple injections in a heavy duty D.I. diesel engine. *SAE Paper 940897*.
- TREE, D. R. & FOSTER, D. E. 1994. Optical Measurements of Soot Particle Size, Number Density, and Temperature in a Direct Injection Diesel Engine as a Function of Speed and Load. *SAE Paper 940270*.
- TREE, D. R. & SVENSSON, K. I. 2007. Soot processes in compression ignition engines. *Progress in Energy and Combustion Science*, 33, 272-309.
- ULLMAN, T. 1989. Investigation of the effects of fuel composition on heavy-duty diesel engine emissions. *SAE Paper 892072*.
- ULLMAN, T. L., SPREEN, K. B. & MASON, R. L. 1994. Effects of cetane number, cetane improver, aromatics, and oxygenates on 1994 heavy-duty diesel engine emissions. *SAE Paper 941020*.
- VAN-HULLE, P., TALBAUT, M., WEILL, M. & COPPALLE, A. 2002. Inversion method and experiment to determine the soot refractive index: application to turbulent diffusion flames. *Measurement Science and Technology*, 375.
- VAN DE HULST, H. C. 1957. Light scattering by small particles. *Wiley, New York*.
- VAN GULIJK, C., MARIJNISSEN, J. C. M., MAKKEE, M., MOULIJN, J. A. & SCHMIDT-OTT, A. 2004. Measuring diesel soot with a scanning mobility particle sizer and an electrical low-pressure impactor: performance assessment with a model for fractal-like agglomerates. *Journal of Aerosol Science*, 35, 633-655.

- VANDER WAL, R. L. 1998. Soot precursor carbonization: Visualization using LIF and LII and comparison using bright and dark field TEM. *Combustion and Flame*, 112, 607-616.
- VANDER WAL, R. L., BERGER, G. M., TICICH, T. M. & PATEL, P. D. 2002. Application of Laser-Induced Incandescence to the Detection of Carbon Nanotubes and Carbon Nanofibers. *Appl. Opt.*, 41, 5678-5690.
- VANDER WAL, R. L. & JENSEN, K. A. 1998. Laser-Induced Incandescence: Excitation Intensity. *Appl. Opt.*, 37, 1607-1616.
- VANDER WAL, R. L., TICICH, T. M. & BROCK STEPHENS, A. 1999. Can soot primary particle size be determined using laser-induced incandescence? *Combustion and Flame*, 116, 291-296.
- VANDER WAL, R. L. & WEILAND, K. J. 1994. Laser-induced incandescence: Development and characterization towards a measurement of soot-volume fraction. *Applied Physics B: Lasers and Optics*, 59, 445-452.
- VANDER WAL, R. L., ZHOU, Z. & CHOI, M. Y. 1996. Laser-induced incandescence calibration via gravimetric sampling. *Combustion and Flame*, 105, 462-470.
- VELJI, A., YEOM, K., WAGNER, U., SPICHER, U., ROSSBACH, M., SUNTZ, R. & BOCKHORN, H. 2010. Investigations of the Formation and Oxidation of Soot Inside a Direct Injection Spark Ignition Engine Using Advanced Laser-Techniques.
- VIOLI, A., D'ANNA, A. & D'ALESSIO, A. 1999. Modeling of particulate formation in combustion and pyrolysis. *Chemical Engineering Science*, 54, 3433-3442.
- VOGEL, S., HASSE, C., GRONKI, J., ANDERSSON, S., PETERS, N., WOLFRUM, J. & SCHULZ, C. 2005. Numerical simulation and laser-based imaging of mixture formation, ignition, and soot formation in a diesel spray. *Proceedings of the Combustion Institute*, 30, 2029-2036.

- WAINNER, R. T., SEITZMAN, J. M. & MARTI, S. R. 1999. Soot Measurements in a Simulated Engine Exhaust Using Laser-Induced Incandescence. *AIAA Journal* 1999 0001-1452, 37, 738-743.
- WANG, H. & FRENKLACH, M. 1997. A detailed kinetic modeling study of aromatics formation in laminar premixed acetylene and ethylene flames. *Combustion and Flame*, 110, 173-221.
- WENTZEL, M., GORZAWSKI, H., NAUMANN, K. H., SAATHOFF, H. & WEINBRUCH, S. 2003. Transmission electron microscopical and aerosol dynamical characterization of soot aerosols. *Journal of Aerosol Science*, 34, 1347-1370.
- WESTBLOM, U., BENGTSSON, P. E. & ALDÉN, M. 1991. Carbon atom fluorescence and emission detected in fuel-rich flames using a UV laser. *Applied Physics B: Lasers and Optics*, 52, 371-375.
- WILL, S., SCHRAML, S., BADER, K. & LEIPERTZ, A. 1998. Performance characteristics of soot primary particle size measurements by time-resolved laser-induced incandescence. *Applied Optics*, 37, 5647-5658.
- WILL, S., SCHRAML, S. & LEIPERT, A. 1996. Comprehensive two-dimensional soot diagnostics based on laser-induced incandescence (LII). *Symposium (International) on Combustion*, 26, 2277-2284.
- WILL, S., SCHRAML, S. & LEIPERTZ, A. 1995a. Two-dimensional soot-particle sizing by time-resolved laser-induced incandescence. *Opt. Lett.*, 20, 2342-2344.
- WILL, S., SCHRAML, S. & LEIPERTZ, A. 1995b. Two-dimensional soot-particle sizing by time-resolved laser-induced incandescence. *Optics Letters.*, 20, 2342.
- WILLIAMS, M. M. R. & LOYALKA, S. K. 1991. *Aerosol Science: Theory and Practice.* , Pergamon Press, Oxford (1991).

WORLD HEALTH ORGANIZATION 2004. Health Aspects of Air Pollution. *Results from the WHO project "Systematic review of health aspects of air pollution in Europe"*.

XU, F. & FAETH, G. M. 2001. Soot formation in laminar acetylene/air diffusion flames at atmospheric pressure. *Combustion and Flame*, 125, 804-819.

YANG, B., MELLOR, A. M. & CHEN, S. K. 2002. Multiple injections with EGR effects on NO_x emissions for DI diesel engines analyzed using an engineering model. *SAE Paper 2002-01-2774*.

ZHAO, B., UCHIKAWA, K. & WANG, H. 2007. A comparative study of nanoparticles in premixed flames by scanning mobility particle sizer, small angle neutron scattering, and transmission electron microscopy. *Proceedings of the Combustion Institute*, 31, 851-860.

ZHAO, H. & LADOMMATOS, N. 1998. Optical diagnostics for soot and temperature measurement in diesel engines. *Progress in Energy and Combustion Science*, 24, 221-255.

ZUR LOYE, A. O. 1990. 2-D soot imaging in a direct injection diesel engine using laser-induced incandescence. *International symposium COMODIA 90*, 523-528.

10 APPENDIX

10.1 Appendix A – Emission Standards

EU emission standards are summarized in the following tables. All dates listed in the tables refer to new type approvals. The EC Directives also specify a second date—one year later, unless indicated otherwise—which applies to first registration (entry into service) of existing, previously type-approved vehicle models. The emissions standards were sourced from diesel.net.

Tier	Date	CO	HC	HC+NO _x	NO _x	PM
Compression Ignition (Diesel)						
Euro 1†	1992.07	2.72 (3.16)	-	0.97 (1.13)	-	0.14 (0.18)
Euro 2, IDI	1996.01	1.0	-	0.7	-	0.08
Euro 2, DI	1996.01 ^a	1.0	-	0.9	-	0.10
Euro 3	2000.01	0.64	-	0.56	0.50	0.05
Euro 4	2005.01	0.50	-	0.30	0.25	0.025
Euro 5	2009.09 ^b	0.50	-	0.23	0.18	0.005 ^e
Euro 6	2014.09	0.50	-	0.17	0.08	0.005 ^e
Positive Ignition (Gasoline)						
Euro 1†	1992.07	2.72 (3.16)	-	0.97 (1.13)	-	-
Euro 2	1996.01	2.2	-	0.5	-	-
Euro 3	2000.01	2.30	0.20	-	0.15	-
Euro 4	2005.01	1.0	0.10	-	0.08	-
Euro 5	2009.09 ^b	1.0	0.10 ^c	-	0.06	0.005 ^{d,e}
Euro 6	2014.09	1.0	0.10 ^c	-	0.06	0.005 ^{d,e}

Figure A-1 – EU emissions standards for passenger cars (category M1), g.km⁻¹

* At the Euro 1.4 stages, passenger vehicles > 2,500 kg were type approved as Category N₁ vehicles

† Values in brackets are conformity of production (COP) limits

a - until 1999.09.30 (after that date DI engines must meet the IDI limits)

b - 2011.01 for all models

c - and NMHC = 0.068 g/km

d - applicable only to vehicles using DI engines

e - 0.0045 g/km using the PMP measurement procedure

Category†	Tier	Date	CO	HC	HC+NO _x	NO _x	PM
Compression Ignition (Diesel)							
N₁, Class I ≤1305 kg	Euro 1	1994.10	2.72	-	0.97	-	0.14
	Euro 2, IDI	1998.01	1.0	-	0.70	-	0.08
	Euro 2, DI	1998.01 ^a	1.0	-	0.90	-	0.10
	Euro 3	2000.01	0.64	-	0.56	0.50	0.05
	Euro 4	2005.01	0.50	-	0.30	0.25	0.025
	Euro 5	2009.09 ^b	0.50	-	0.23	0.18	0.005 ^e
N₁, Class II 1305-1760 kg	Euro 6	2014.09	0.50	-	0.17	0.08	0.005 ^e
	Euro 1	1994.10	5.17	-	1.40	-	0.19
	Euro 2, IDI	1998.01	1.25	-	1.0	-	0.12
	Euro 2, DI	1998.01 ^a	1.25	-	1.30	-	0.14
	Euro 3	2001.01	0.80	-	0.72	0.65	0.07
	Euro 4	2006.01	0.63	-	0.39	0.33	0.04
N₁, Class III >1760 kg	Euro 5	2010.09 ^c	0.63	-	0.295	0.235	0.005 ^e
	Euro 6	2015.09	0.63	-	0.195	0.105	0.005 ^e
	Euro 1	1994.10	6.90	-	1.70	-	0.25
	Euro 2, IDI	1998.01	1.5	-	1.20	-	0.17
	Euro 2, DI	1998.01 ^a	1.5	-	1.60	-	0.20
	Euro 3	2001.01	0.95	-	0.86	0.78	0.10
N₂	Euro 4	2006.01	0.74	-	0.46	0.39	0.06
	Euro 5	2010.09 ^c	0.74	-	0.350	0.280	0.005 ^e
	Euro 6	2015.09	0.74	-	0.215	0.125	0.005 ^e
	Euro 5	2010.09 ^c	0.74	-	0.350	0.280	0.005 ^e
	Euro 6	2015.09	0.74	-	0.215	0.125	0.005 ^e

Positive Ignition (Gasoline)

Category†	Tier	Date	CO	HC	HC+NOx	NOx	PM
N ₁ , Class I ≤1305 kg	Euro 1	1994.10	2.72	-	0.97	-	-
	Euro 2	1998.01	2.2	-	0.50	-	-
	Euro 3	2000.01	2.3	0.20	-	0.15	-
	Euro 4	2005.01	1.0	0.1	-	0.08	-
	Euro 5	2009.09 ^b	1.0	0.10 ^f	-	0.06	0.005 ^{d,e}
	Euro 6	2014.09	1.0	0.10 ^f	-	0.06	0.005 ^{d,e}
N ₁ , Class II 1305-1760 kg	Euro 1	1994.10	5.17	-	1.40	-	-
	Euro 2	1998.01	4.0	-	0.65	-	-
	Euro 3	2001.01	4.17	0.25	-	0.18	-
	Euro 4	2006.01	1.81	0.13	-	0.10	-
	Euro 5	2010.09 ^c	1.81	0.13 ^g	-	0.075	0.005 ^{d,e}
	Euro 6	2015.09	1.81	0.13 ^g	-	0.075	0.005 ^{d,e}
N ₁ , Class III >1760 kg	Euro 1	1994.10	6.90	-	1.70	-	-
	Euro 2	1998.01	5.0	-	0.80	-	-
	Euro 3	2001.01	5.22	0.29	-	0.21	-
	Euro 4	2006.01	2.27	0.16	-	0.11	-
	Euro 5	2010.09 ^c	2.27	0.16 ^h	-	0.082	0.005 ^{d,e}
	Euro 6	2015.09	2.27	0.16 ^h	-	0.082	0.005 ^{d,e}
N ₂	Euro 5	2010.09 ^c	2.27	0.16 ^h	-	0.082	0.005 ^{d,e}
	Euro 6	2015.09	2.27	0.16 ^h	-	0.082	0.005 ^{d,e}

Figure A-2 – EU emissions standards for light commercial vehicle [g.km⁻¹]

† For Euro 1/2 the Category N₁ reference mass classes were Class I ≤ 1250 kg, Class II 1250-1700 kg, Class III > 1700 kg.

a - until 1999.09.30 (after that date DI engines must meet the IDI limits)

b - 2011.01 for all models

c - 2012.01 for all models

d - applicable only to vehicles using DI engines

e - 0.0045 g/km using the PMP measurement procedure

f - and NMHC = 0.068 g/km

g - and NMHC = 0.090 g/km

h - and NMHC = 0.108 g/km

For particle number emissions, a particle number emission limit of $6 \times 10^{11} \text{ km}^{-1}$ (PMP method, NEDC test) becomes effective at the Euro 5/6 stage for all categories of diesel vehicles (M, N₁, N₂). The particle number limit must be met in addition to the PM mass emission limits listed in the above tables. A particle number emission limit for gasoline vehicles is to be defined by 1 September 2014.

Durability: useful vehicle life for the purpose of emission regulations is:

- Euro 3 stage—80,000 km or 5 years (whichever occurs first); in lieu of an actual deterioration run, manufacturers may use the following deterioration factors:
 - Positive ignition: 1.2 for CO, HC, NO_x
 - Compression ignition: 1.1 for CO; 1.0 for NO_x and for HC+NO_x; 1.2 for PM
- Euro 4 stage—100,000 km or 5 years, whichever occurs first.
- Euro 5/6 stage—in-service conformity: 100,000 km or 5 years; durability testing of pollution control devices for type approval: 160,000 km or 5 years (whichever occurs first); in lieu of a durability test, manufacturers may use the following deterioration factors:
 - Positive ignition: 1.5 for CO; 1.3 for HC; 1.6 for NO_x; 1.0 for PM
 - Compression ignition, Euro 5: 1.5 for CO; 1.1 for NO_x and for HC+NO_x; 1.0 for PM. Euro 6 deterioration factors to be determined.

The regulations include several additional provisions, such as:

- EU Member States may introduce tax incentives for early introduction of vehicles that comply with future emission standards.
- Requirement for low temperature emission test (-7°C) for gasoline vehicles effective 2002 [*Directive 2001/100/EC*]. The limits for cars are 15 g/km for CO and 1.8 g/km for HC, measured over the urban part of the test only.
- Onboard diagnostic (OBD) requirements for emission systems.

10.2 Appendix B – Fitting coefficients for soot sublimation rate properties

The coefficients of soot sublimation properties are expressed through polynomial coefficients. The fitting coefficients for the vapour pressure [atm], mean molecular weight [Kg.mol⁻¹] and the heat of vaporization [J.K⁻¹.mol⁻¹] (Leider et al, 1973) are listed in

Table A-18:

<i>i</i>	<i>p_i</i>	<i>m_i</i>	<i>h_i</i>
0	-122.96	0.017179	205398
1	9.0558×10^{-2}	6.8654×10^{-7}	736.6
2	-2.7637×10^{-5}	2.9962×10^{-9}	-0.40713
3	4.1754×10^{-9}	-8.5954×10^{-13}	1.1992×10^{-4}
4	-2.4875×10^{-13}	1.0486×10^{-16}	-1.1795×10^{-8}
5	0	0	1.0717×10^{-12}

Table A-18 – Fitting coefficients for the vapour pressure [atm], mean molecular weight [Kg.mol⁻¹] and the heat of vaporization [J.K⁻¹.mol⁻¹] (Leider et al, 1973)

10.3 Appendix C – Burner’s drawings

The drawings used for the conception of the Santoro burner come from: <http://www.liiscience.org/08Workshop/SantoroDrwg2.PDF>; based from the burner used by NIST.

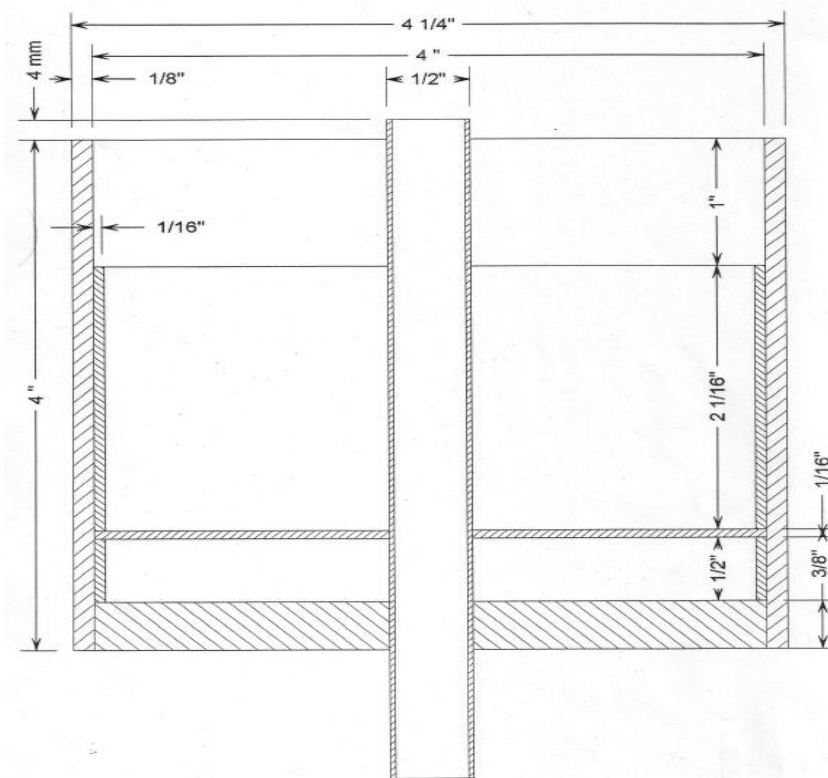
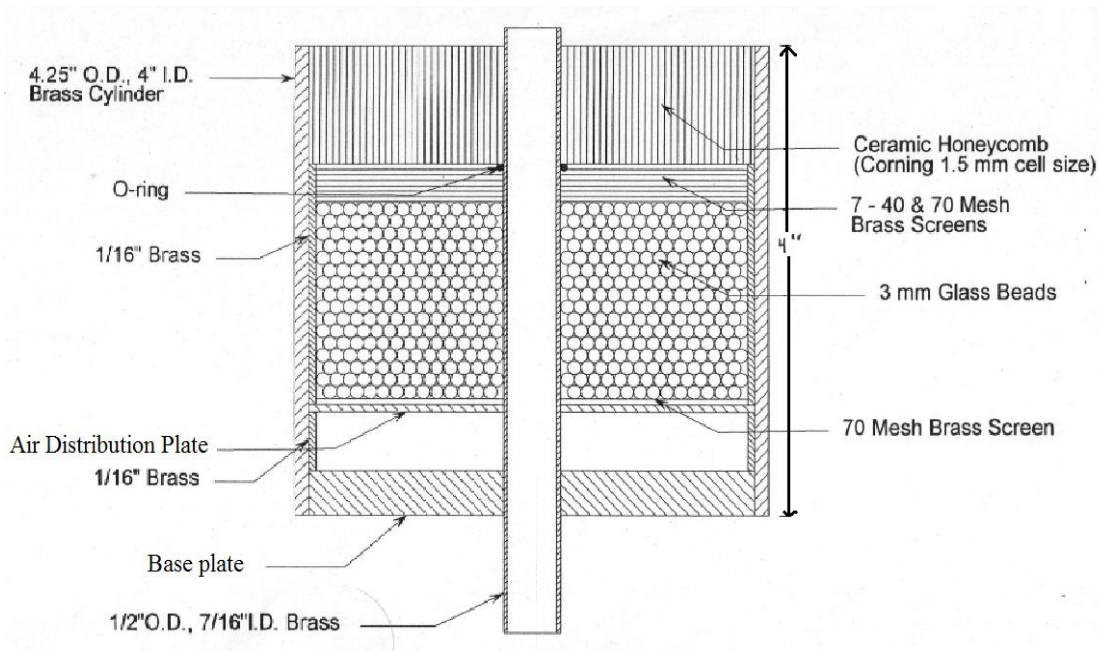


Figure A-3 – Schematics of the Santoro burner

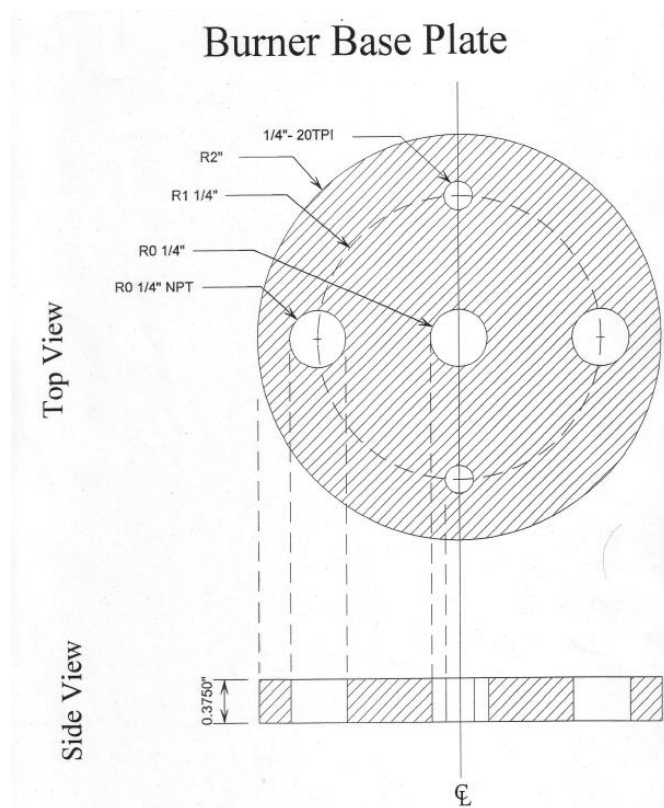
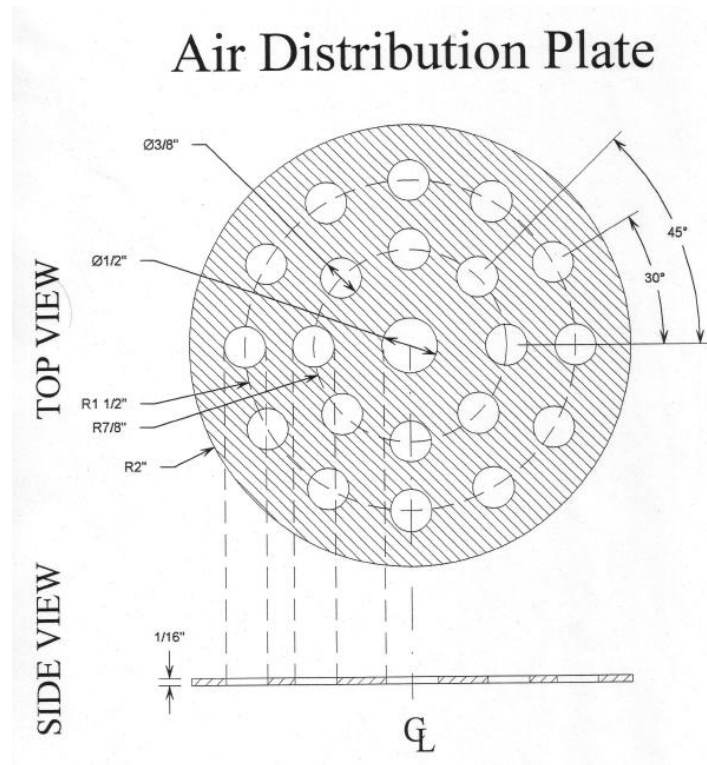


Figure A-4 – Schematic of the Santoro burner - Plates

10.4 Appendix D – Heat Release Rate

The first principle of thermodynamics applied to a quasi-static volume formed by the combustion chamber is expressed as:

$$\frac{dQ}{dt} - P \cdot \frac{dV}{dt} + \sum_i m_i \cdot h_i = \frac{dU}{dt} \quad \text{Equation 100}$$

With:

$\frac{dQ}{dt}$ heat transfer rate across the system boundary

$P \cdot \frac{dV}{dt}$ rate of work transfer done by the system

m_i Mass flow rate through the boundaries of species i

h_i Enthalpy of species i

U Internal energy of the system

In the case of direct-injection engines, the mass flows are the fuel and the crevice flow. The crevice flow can be neglected compare to the fuel flow. From this first assumption, the first law is simplified to:

$$\frac{dQ}{dt} - P \cdot \frac{dV}{dt} + m_f \cdot h_f = \frac{dU}{dt} \quad \text{Equation 101}$$

The cylinder contents are considered to have a uniform temperature in any instant of the combustion process. U and h_f are taken to be sensible internal energy of the cylinder contents and sensible enthalpy of the injected fuel ($U=U(T)-U(298K)$ and $h_f=h_f(T)-h_f(298K)$).

Since $h_f(t) \approx 0$, the equation becomes:

$$\frac{dQ_n}{dt} - P \cdot \frac{dV}{dt} = \frac{dU}{dt} \quad \text{Equation 102}$$

$\frac{dQ_n}{dt}$ net-heat release rate equivalent to the gross heat release minus the heat lost at the walls.

The content of the combustion chamber is assumed to follow the ideal gas law:

$$\frac{dU}{dt} = m \cdot c_v \frac{dT}{dt} = \frac{1}{\gamma - 1} V \frac{dP}{dt} - \frac{1}{\gamma - 1} P \frac{dV}{dt}$$

Equation 103

γ ratio of the specific heats c_p/c_v

Therefore Equation 102 becomes:

$$\frac{dQ_n}{dt} = \frac{\gamma}{\gamma - 1} P \cdot \frac{dV}{dt} + \frac{1}{\gamma - 1} V \cdot \frac{dP}{dt}$$

Equation 104

10.5 Appendix E – Santoro burner data in the literature

The data published by NIST and available at this address: <http://www.fire.nist.gov/fire/flamedata/datafiles/C2h4-s-41.txt>, are illustrated in Figure A-5. The LII measurements were calibrated against extinction results using $m=1.57-0.56i$ as refractive index.

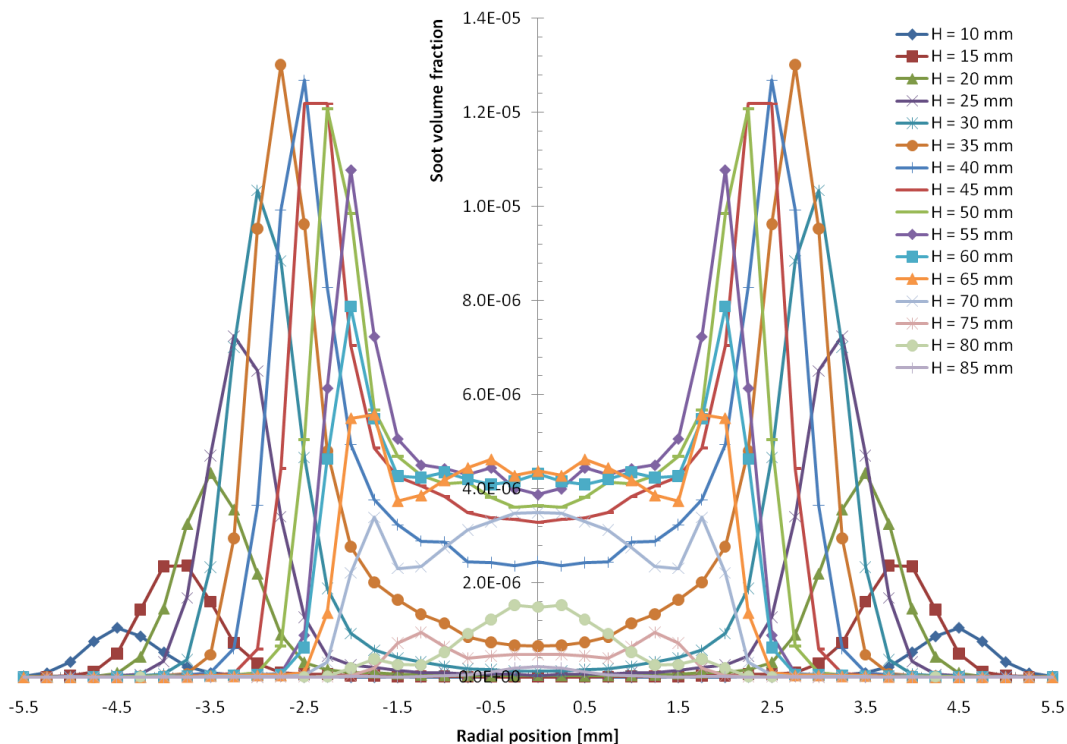


Figure A-5 – Soot volume fraction profiles for Santoro burner from NIST

Independent soot volume fraction measurements were carried out on the Santoro burner present at Brighton University. Results from extinction measurements are presented on Figure A-6 (Lebourgeois, 2010).

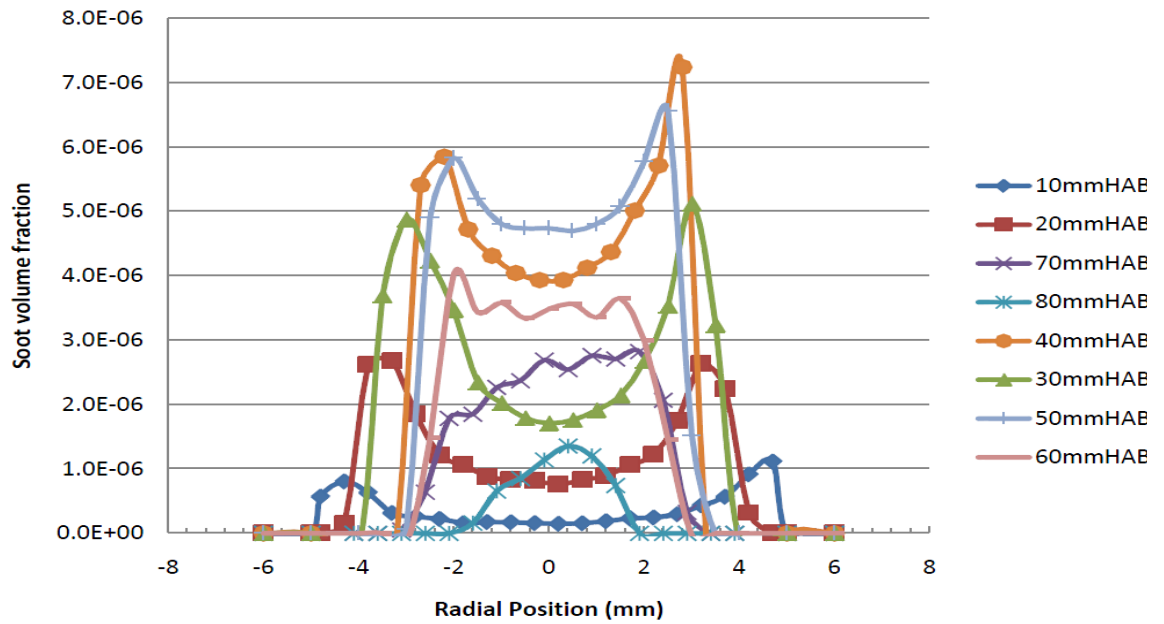
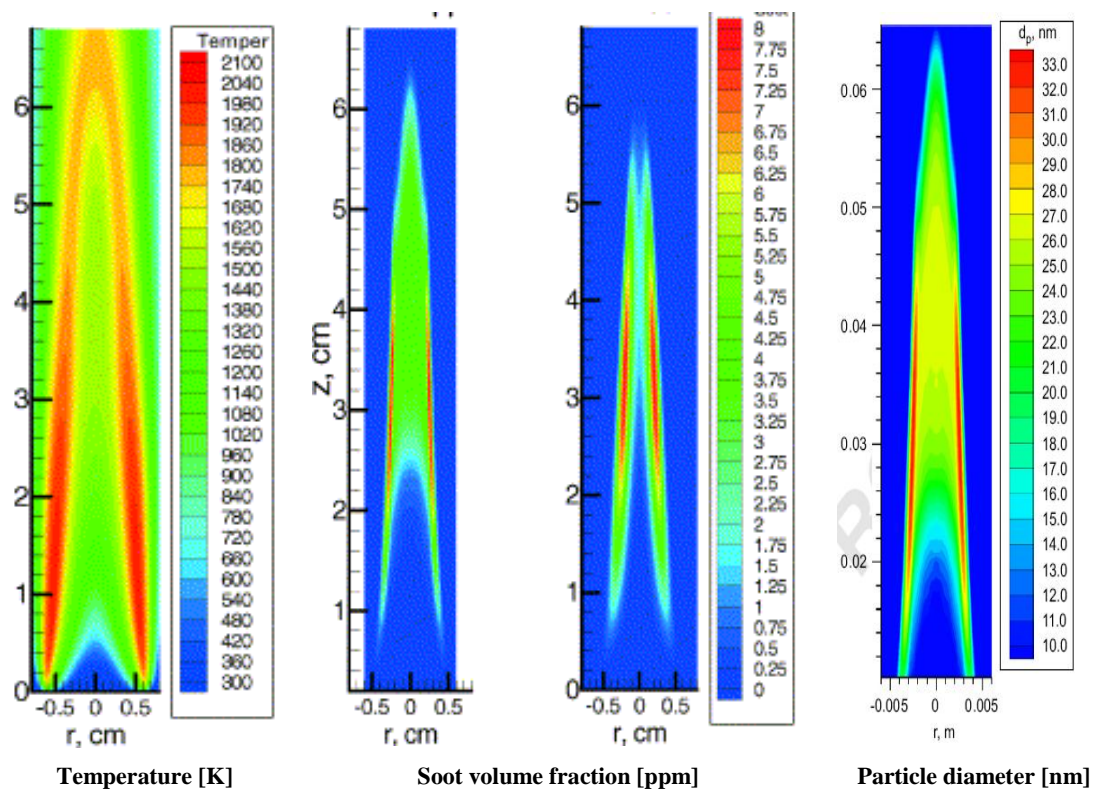


Figure A-6 – Soot volume fraction profiles for Santoro burner (Lebourgeois, 2010)

The CFD of a laminar diffusion flame was published by the NRC group, CFD computation allows to have more details on the combustion processes. The data presented below are for a Gülder burner, flows and design are different from a Santoro burner. However being laminar diffusion flames, the structure of these flames is relatively similar except for the data scales.



LEFT: experimental - RIGHT: CFD

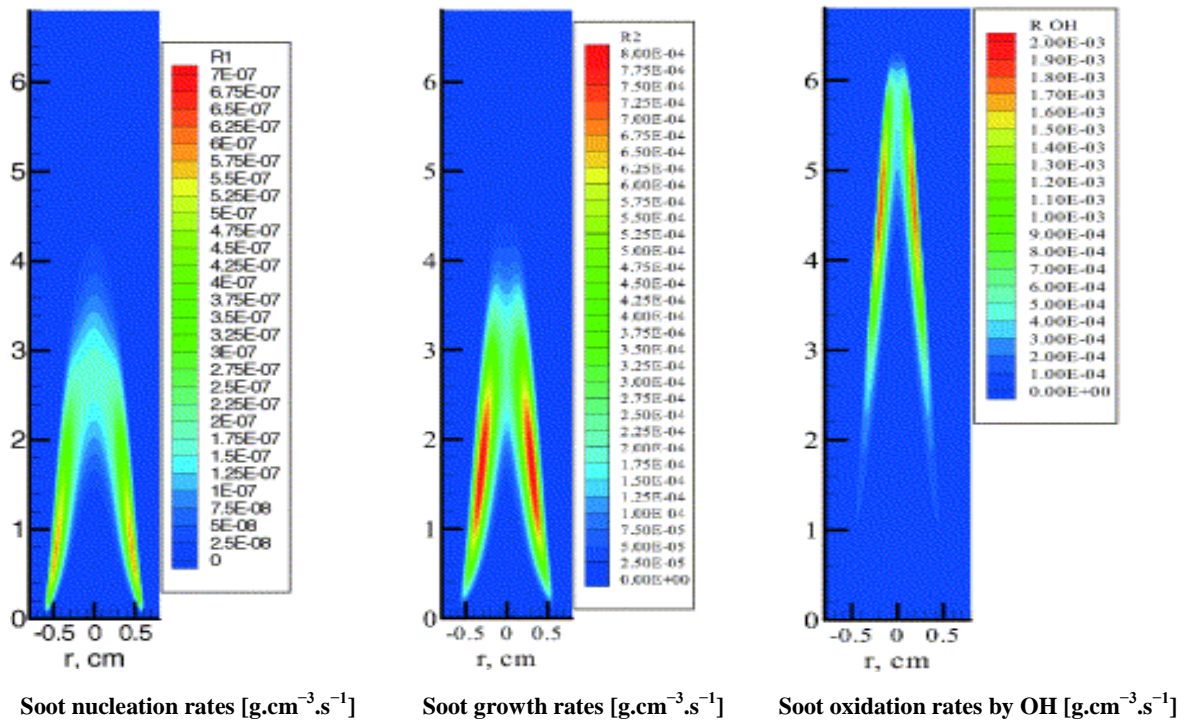


Figure A-7 – CFD simulations and experimental results from NRC group

